Multifractal Properties of Tribonacci Chains

Master Thesis

Utrecht University

Utrecht University
Institute for Theoretical Physics
Mathematical Institute

Author:
Julius (J.P.J.) Krebbekx

Supervisors:
Prof. Dr. Cristiane de Morais Smith
Dr. Karma Dajani
Anouar Moustaj MSc

July 6, 2023

Abstract

The description of electrons in solids using Bloch's theorem has allowed for a profound understanding of the electronic band structure of regular crystalline materials. An example of its success is the understanding of topological insulators and superconductors, and their invariants, via the reciprocal space. Aperiodic systems on the other hand, which are systems that break translational symmetry but possess long-range order, cannot be studied using the same tools, rendering their topological nature ambiguous. In this thesis, we review some physical and mathematical properties of aperiodic systems, and discuss some experimental realisations. We introduce two 1D tight-binding models based on the Tribonacci substitution, the hopping and on-site Tribonacci chains, which generalize the Fibonacci chain. For both hopping and on-site models, a perturbative real-space renormalization procedure is developed. We show that the two models are equivalent at the fixed point of the renormalization group flow, and that the renormalization procedure naturally gives the Local Resonator Modes. Additionally, the Rauzy fractal, inherent to the Tribonacci substitution, is shown to serve as the analog of conumbering for the Tribonacci chain. Our work provides new insight into how the internal space of a cut-and-project quasicrystal is used to describe the eigenstates, and can in principle be applied to any cut-and-project quasicrystal. Finally, we construct a Rice-Mele charge pump from the Tribonacci word, which exhibits multilevel topological pumping due to the multifractal nature of the Tribonacci chain's energy spectrum. This is a first step towards studying the topological properties of the Tribonacci chain.

Acknowledgements

First of all, want to express my gratitude to my three supervisors, Cristiane, Karma and Anouar. My very first meeting was with Cristiane and Anouar, together with Rodrigo, a former PhD student of Cristiane, where we would discuss some possible topics for a master thesis. We ended up talking for more than an hour about various options, and I left the meeting with a good feeling about the group. From that moment onwards, our regular meetings with the four of us often took more than an hour, and were at least as much fun as they were productive. Cristiane, being a busy professor, often has the tightest schedule, and has many responsibilities to look after. Despite all that, she always managed to make time for our meetings, reading my work and contribute to the project, which I take as a sign of respect for her students. Most striking is the passion and personal care Cristiane has for me as one of her students.

Being surrounded by three physicists in a project, I respect Karma for her interest and efforts to understand the physics behind our project, and her extremely valuable mathematical insights. In the eventful meeting where Karma proposed to look at the Tribonacci substitution, the main direction of the project, in hindsight, was determined. Besides all that, I want to thank Karma for her flexibility, often giving *very* quick replies to emails, and always thoroughly dissecting the mathematical elements of my work.

Anouar, being the daily supervisor of the project, probably had to endure most of my questions. Oftentimes, I was surprised by his insightful answers and deep knowledge. It would be a great personal achievement for me if I could be at the same level of intellectual maturity as him in three years time, as it is something that keeps surprising me. Besides being a very helpful and smart supervisor, Anouar has also become a friend during the project. Probably the highlight of our year was the winter school in Florence, where we had a lot of fun together with Lumen.

I have also had invaluable support from other people in my personal life, most notably my girlfriend Rhea. Naturally, I sometimes had to complain and discuss about my research project with someone besides my supervisors, which was often Rhea. I also want to thank all my fellow student friends, with whom I had enjoyable coffee breaks and discussions. Finally, the support of my parents and family during my educational endeavours has been invaluable, and without them, most of it would not have been possible.

Contents

1. Introduction

The description of electrons in solids using Bloch's theorem has allowed for a profound understanding of the electronic band structure of regular crystalline materials [1]. The discovery of quasicrystals [2], aperiodic structures that break translational symmetry, has pushed the field forward. The Penrose tilings [3] or the aperiodic mono-tile discovered recently by Smith et al. [4, 5] are some of the typical examples that have fascinated physicists and mathematicians for years. Quasi-crystalline lattices have been also experimentally realised using different quantum-simulator platforms, such as ultracold atoms [6] or photonics [7].

The advent of topological insulators has reiterated the importance of periodicity in solids because translation invariance is at the core of the topological classification of these materials [8–11]. It remains an open question how the notion of topology translates to aperiodic structures such as quasicrystals, where translation invariance is often replaced by scale invariance [12]. The topological aspects of quasicrystals have been recently investigated [12–16], but methods are often tailored to each model, and a general framework to study topology in these systems is lacking.

Arguably the most investigated quasicrystal is the Fibonacci chain [17], a one-dimensional model based on the Su-Schrieffer-Heeger (SSH) model [18]. The latter is a tight-binding model in which alternating weak and strong hopping parameters lead to a topological or trivial phase, depending on whether the last bond in the chain corresponds to a weak or strong hopping, respectively. The Fibonacci chain is a natural extension of the SSH model to the aperiodic domain [19], in which the weak and strong hopping parameters are distributed according to a Fibonacci word. This 1D tight-binding chain hosts many interesting properties, such as a multifractal energy spectrum and eigenstates [20–22]. In particular, a description of the system in terms of conumbers [23] has revealed hidden symmetries in Hilbert space and allowed for a systematic prediction of the influence of random disorder based on a renormalisation group (RG) scheme [19]. The interpretation of the system in terms of local symmetries has also led to a more profound understanding of its physical properties [24]. In addition, it was shown to be equivalent to the Harper model [25], from which it inherits its topological properties, which can be viewed as the starting point of topology in quasicrystals.

The motivation of the work in this thesis is to advance the knowledge of topology in quasicrystalline matter. We go beyond the realm of dimerised models, such as the SSH and Fibonacci chain, and introduce a quantum chain based on the Tribonacci substitution. More specifically, two tight-binding chains, the hopping Tribonacci Chain (HTC) and the on-site Tribonacci Chain (OTC), are defined analogously to the Fibonacci chain. These chains are closely linked to the Rauzy fractal, a well-known compact domain with fractal boundary [26]. One immediate consequence for the Tribonacci chain is that the method used by Kraus and Zilberberg [25] for studying topology is no longer applicable. Despite this important difference, we show that the Tribonacci chain shares many features with the Fibonacci chain. An RG scheme for the HTC and OTC is developed along the lines proposed by Niu and Nori [19]. This allows for the same interpretation of the spectrum as a multifractal set as for the Fibonacci chain [20]. The RG scheme is also used to render the HTC and OTC equivalent at the RG fixed point. We show how the Rauzy fractal orders the lattice points according to their local environment, in analogy with the conumbering scheme. Furthermore, the RG procedure provides a natural way to enumerate all structures in the Local Resonator Mode framework [24]. We also compute the multifractal dimensions of the energy spectrum and eigenstates of the HTC, and compare them with the Fibonacci chain. These results indicate that the Tribonacci chains are critical in terms of Anderson localization. Finally, we

apply the Tribonacci modulation to a Thouless pump, and study the topological charge pumping behaviour.

In Chapter 2 of this thesis, we begin by presenting the concept of a quasicrystal, providing its definition in both physics and mathematics. Moving on to Chapter 3, we delve into the mathematical foundations of aperiodic structures, exploring topics such as substitution sequences, Cut-and-Project Schemes (CPS), and (multi)fractals. Following this mathematical exploration, we briefly discuss the relevance and some experimental realisations of aperiodic structures in Chapter 4. The core of this thesis is Chapter 5, where we present the Tribonacci chain, and all related results. The key outcomes of this chapter are summarised in a publication Ref. [27]. In Chapter 6, we introduce topology in physics, serving as a bridge between the mathematical and physics approaches. We conclude the thesis by giving our final remarks in Chapter 7, and motivating directions for further research while offering potential starting points for pursuing those topics. Lastly, we present an overview of all original work in Appendix C.

2. Introduction to Quasicrystals

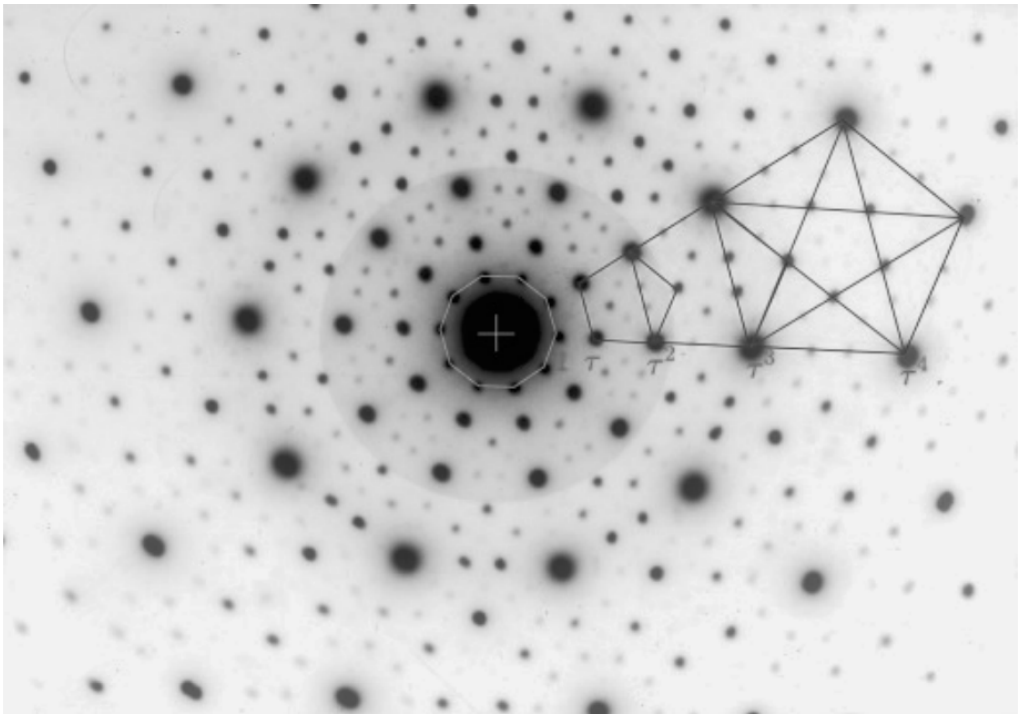

Figure 2.1.: Tenfold symmetric diffraction pattern with scaling symmetry (figure from Ref. [28]).

Classical crystals, obeying two-, three-, four- or sixfold rotational symmetry, are the cornerstone of modern day solid state matter. Until 1982, the vast majority of the scientific community believed that *periodic* crystals were the only kind of highly ordered solid state matter that could be called crystals. In that year, Dan Shechtman [2] discovered a tenfold rotational symmetry in the diffraction pattern of an AlMn sample. Not much later, the term *quasicrystals* was coined for such materials with "non-crystallographic" symmetries. The scientific community despised Shechtman's work so much that he had only reached the level of assistant professor at the time the Nobel Prize committee considered him a candidate in 2011. The fact that it took Shechtman so many years to convince his peers, and that he was disregarded as a scientist until he received his Nobel Prize in 2011, indicates that his findings did not fit in with the scientific paradigm of the time.

2.1. Regular Crystals

Before the concept of a quasicrystal can be introduced, classical crystals need to be discussed first. By a *regular* or *classical* crystal, we mean forms of matter where the atoms are positioned in a periodic arrangement. This periodic arrangement is often called the *lattice*, which is a set of points $\Gamma \subset \mathbb{R}^d$, where $d = 1, 2, 3$ is the dimension of the lattice. The lattice Γ is generated by the linearly independent primitive vectors $\mathbf{a}_i$, such that any two points $\mathbf{x}, \mathbf{y} \in \Gamma$ are related by $\mathbf{y} = \mathbf{x} + \mathbf{R}$

where the *lattice translation* is given by $\mathbf{R} = \sum_{i=1}^{d} n_i \mathbf{a}_i$ with $n_i \in \mathbb{Z}$. Such a lattice is also known as a Bravais lattice.

There are three important reasons why classical crystals are widely studied in physics.

1. From an experimental perspective, the strictly periodic arrangement gives rise to discrete diffraction spectra (see Section 2.2). This spectrum enables experimentalists to determine the crystal structure from a scattering experiment.
2. The separation between planes acts as a "ruler" that allows one to measure distances as small as a few ångstroms.
3. Since the arrangement is periodic under lattice translations $\mathbf{R}$, the single-particle potential $U(\mathbf{r})$ is periodic, i.e. $U(\mathbf{r} + \mathbf{R}) = U(\mathbf{r})$. This periodic property of the potential allows for Bloch's theorem to be derived, which is essential for studying electronic and transport properties of classical crystals.

Although the points above are important, there is much more to classical crystals than is touched upon here. One last essential element of the theory of classical crystals is the *crystallographic restriction theorem*, which is the well-known result that classical crystals can only display two-, three-, four- or sixfold rotational symmetry.

Theorem 2.1 (Crystallographic Restriction)**.** *A lattice $\Gamma \subset \mathbb{R}^d$ with $d = 2, 3$ can have n-fold rotational symmetry at most for $n \in \{1, 2, 3, 4, 6\}$ (Corollary 3.1 in Baake and Grimm [29])*

Finally, we note that the lattice Γ encodes only the periodicity of a crystal. To fully describe the atomic configuration of a crystal, the concept of a *unit cell* is required. The unit cell is the smallest portion of the crystal that is repeated, which consists of at least one atom (not infinitely many).

2.2. Diffraction

The *diffraction spectrum* plays a central role in the classification of (quasi)crystals and aperiodic order in general. The diffraction spectrum originates from physics experiments where electrons (or photons) hit a material with momentum $\mathbf{k}_{\text{in}}$ and scatter elastically off the sample in a direction $\mathbf{k}_{\text{out}}$. In principle, the scattered particles can fly off in any direction, and, in experiments, the intensity in each direction is measured. For a difference $\mathbf{q} = \mathbf{k}_{\text{out}} - \mathbf{k}_{\text{in}}$, the scattered intensity is (up to a constant factor) measured as the *structure factor* $S(\mathbf{q})$. If the material consists of identical atoms at locations $\mathbf{r}_i$, the structure factor can be computed as

$$S(\mathbf{q}) = \frac{1}{N} \sum_{j,k} e^{i\mathbf{q}\cdot(\mathbf{r}_j - \mathbf{r}_k)}. \tag{2.1}$$

Note that $S(\mathbf{q})$ is simply the modulus squared of the Fourier transform (FT) of the lattice $\{\mathbf{r}_i\}_i$. Even though the lattice and the diffraction spectrum are related via the FT, the inverse problem of finding the lattice corresponding to a particular diffraction pattern is generally not well-posed (no solution or not unique).

2.3. Quasicrystals and Aperiodicity

One of the most direct and earliest classifications of a quasicrystal departing from classical crystals is by Levine and Steinhardt [30]:

> "*A quasicrystal is the natural extension of the notion of a crystal to structures with quasiperiodic, rather than periodic, translational order.*"

As an example of a quasiperiodic function, Levine and Steinhardt take the function

$$f(x) = \sin x + \sin \pi x, \tag{2.2}$$

which clearly has no true period, since π is irrational. A quasicrystal of two unit cells A, B can be constructed by inserting A if the sign of $f(n)$ is positive and B if it is negative, labelling the cell with integers n. Note that Eq. 2.2 can be obtained by taking the "cut" $y = \pi x$ in the domain of the function $f(x, y) = \sin x + \sin y$. The cut $y = \pi x$ in the x, y-plane is visualised as a blue plane in Fig. 2.2, with the resulting quasiperiodic function that lies on the blue plane plotted on the right. This is perhaps the simplest and crudest example of a CPS that can be used to generate a quasicrystal lattice. The formal definition of a CPS is given in Section 3.2.

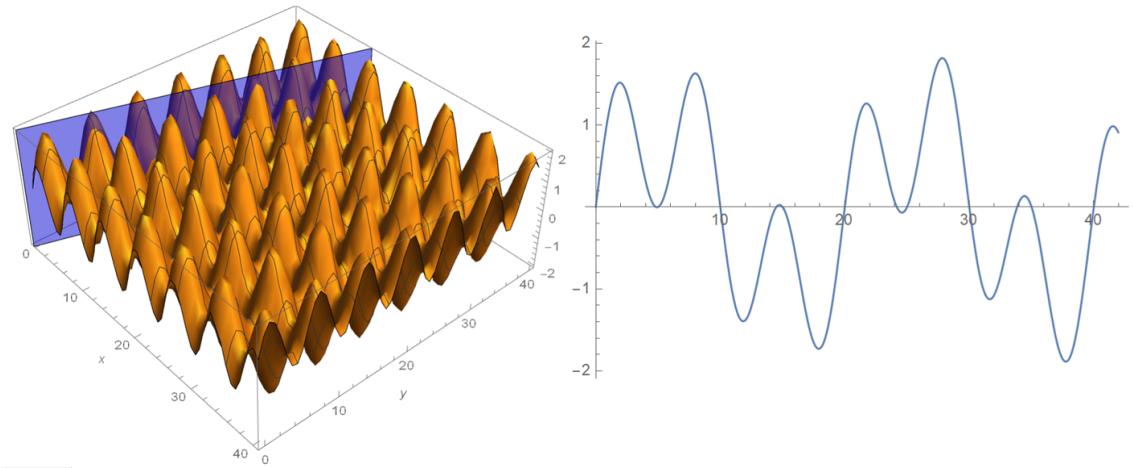

Figure 2.2.: The cut $y = \pi x$ that gives the quasiperiodic function Eq. 2.2.

This method became popular when the Dutch mathematician De Bruijn [3] used CPS to obtain 2D Penrose tilings from a 5D hypercubic lattice. Another feature of CPS is that the diffraction pattern of the resulting lattice is always discrete, provided that the original higher-dimensional lattice has a discrete diffraction pattern [31]. This feature motivates the mathematical definition of a crystal to be the result of a CPS [29]. If the result is a periodic lattice, one has a classical crystal; otherwise, the result is a quasicrystal.

From a physics perspective, it seems tempting to define quasicrystals as crystals that have non-crystallographic symmetries in the diffraction pattern, since a non-crystallographic symmetry is the central property in Shechtman's discovery from 1982. However, there exist non-periodic materials with allowed crystallographic symmetries and a discrete diffraction pattern. Therefore, the International Crystallographic Union updated the definition of a crystal in 1991 as follows [28]:

> "*In the following by 'crystal' we mean any solid having an essentially discrete diffraction diagram, and by 'aperiodic crystal' we mean any crystal in which three-dimensional lattice periodicity can be considered to be absent.*"

Note that this definition does not define what a quasicrystal is and places the ability to diffract central to the crystal property. An appropriate long-range order is a general property of ordered solid-state matter, it would seem, since only short-range order would not be sufficient to create a discrete diffraction spectrum. We will see later on that there are also systems with long-range order that do *not* have a discrete diffraction pattern.

3. Aperiodic Order

This chapter explores various topics from the vast field of aperiodic structures in mathematics. The emphasis is placed on generating aperiodic 1D structures, but most methods can be used to generate higher-dimensional structures as well. Section 3.5 treats an application of aperiodic systems in physics to conclude this chapter.

3.1. Substitution Rules

One widely used method to create highly-ordered systems, especially one-dimensional, is the method of substitution rules. The mathematical framework to study substitution rules is known as symbolic dynamics.

3.1.1. Basic Symbolic Dynamics

This section follows the book by Brin and Stuck [32]. Let $\mathcal{A}_m = \{a_0, \dots, a_{m-1}\}$ be a finite alphabet of $m \in \mathbb{N}$ symbols and $\mathcal{A}_m^*$ be the set of all finite words that can be made by concatenating elements from the alphabet. Furthermore, we define $\Sigma_m = \mathcal{A}_m^{\mathbb{Z}}, \Sigma_m^+ = \mathcal{A}_m^{\mathbb{N}}$ as the set of infinite two- and one-sided sequences, respectively. Arguably, the most important operator is the *shift operator* σ, which acts on a one- or two-sided sequence x as $\sigma(x)_i = x_{i+1}$, which is only invertible on Σ_m, not Σ_m^+. The pairs (Σ_m, σ) and (Σ_m^+, σ) are called the *full two-sided shift* and the *full one-sided shift*, respectively. The metric

$$d(x, y) = 2^{-l}, \qquad l = \min\{|i| \mid x_i \neq y_i\} \tag{3.1}$$

generates the product topology on $\Sigma_m^{(+)}$, which gives us a tractable notion of convergence of sequences.

A substitution rule is then a function $\rho : \mathcal{A}_m \to \mathcal{A}_m^*$ that assigns to each symbol a finite word. The rule ρ can be applied to some word $w \in \mathcal{A}_m^*$, where $w = x_0 x_1 \cdots x_n, x_i \in \mathcal{A}_m$ as the map

$$x_0 x_1 \cdots x_n \mapsto \rho(x_0)\rho(x_1) \cdots \rho(x_n).$$

A useful tool in studying substitutions is the *substitution matrix* $\mathbf{M}$. Consider the word w_n after n applications of some substitution ρ. Let $N_l^{(n)}$ be the amount of occurrences of some letter $l \subset \mathcal{A}_m$ in w_n. If $\mathbf{N}^{(n)} = (N_{a_0}^{(n)}, \dots, N_{a_{m-1}}^{(n)})^T$, then the matrix $\mathbf{M}$ relates

$$\mathbf{N}^{(n+1)} = \mathbf{M} \cdot \mathbf{N}^{(n)}.$$

The following definition makes the notion of a fixed point rigorous.

Definition 3.1. *(Fixed point) The one-sided fixed point $w \in \Sigma_m^+$ of a substitution ρ, starting from some seed w_0, satisfies $\rho(w) = \rho$. For the bi-infinite fixed point, the seed $w_{-1}|w_0$ must be a legal two-letter word of ρ.*

Oftentimes, a substitution ρ has no fixed fixed point, but a certain power $\sigma = \rho^k$ has, where $k \in \mathbb{N}$.

A particularly interesting class of substitutions are the *Pisot* type.

Definition 3.2. *(Pisot) A substitution ρ is called Pisot if and only if its substitution matrix* $\mathbf{M}$ *has one dominant eigenvalue $\alpha > 1$ and all other eigenvalues λ satisfy $|\lambda| < 1$.*

In other words, there is precisely one expanding eigenspace of dimension one and all other eigenspaces are contracting.

3.1.2. Sturmian Sequences

Before discussing particular substitution systems that generate words, we first discuss an important class of words, called *Sturmian words*. Fix some finite alphabet $\mathcal{A}$ for the remainder of this section. First, we introduce some useful definitions regarding words.

Definition 3.3. *(Factor) For a word $w = w_0 w_1 \cdots$ with $w_i \in \mathcal{A}$, a factor of length n is any subword $w_i \cdots w_{i+n-1} \subset \mathcal{A}^*$ where $i = 0, 1, \ldots$. The amount of distinct factors of length n in w is denoted by $p_n(w)$.*

Definition 3.4. *(Periodic) A word $w = w_0 w_1 \cdots$ is called eventually periodic if and only if*

$$\exists N, m > 0 : w_i = w_{i+m} \; \forall i \geq N.$$

If $N = 0$, w is simply called periodic. Equivalently, w is eventually periodic if and only if

$$\exists n > 0 : p_{n+1}(w) = p_n(w).$$

Definition 3.5. *(Aperiodic) A word $w = w_0 w_1 \cdots$ is called aperiodic if and only if it is not periodic nor eventually periodic.*

Now an important theorem by Morse and Hedlund [33], is the following.

Theorem 3.6. *(Morse-Hedlund) A given infinite word w is aperiodic if and only if $p_n(w) \geq n+1$ for all $n \geq 0$.*

This can be seen by noting that if $p_n(w) \leq n$ for some $n \in \mathbb{N}$, the word w is (eventually) periodic with period $k \leq n$. A special class of words, the *Sturmian* words, are precisely those for which $p_n(w) = n + 1$ is satisfied. Those can be seen as the words with minimal complexity that are still aperiodic.

Definition 3.7. *(Sturmian Sequence) An infinite word, also known as a sequence, is called Sturmian if $p_n(w) = n + 1$ for all $n = 1, 2, \ldots$.*

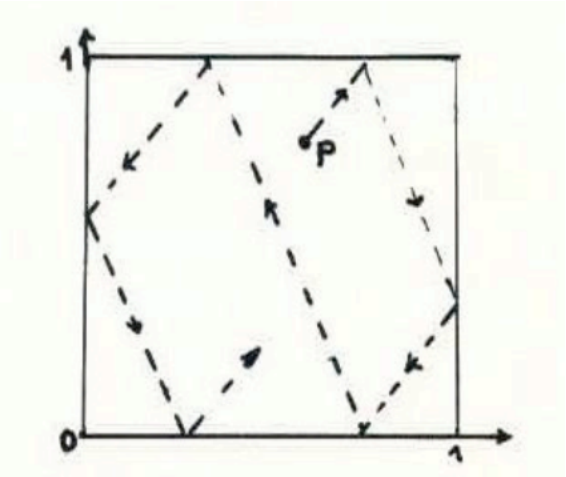

Figure 3.1.: Billiard construction of a Sturmian word (figure from Ref. [34]).

Another more intuitive way to construct the Sturmian words, only valid if $\mathcal{A}$ is binary, is the following. Consider the square $[0,1]^2 \subset \mathbb{R}^2$. Let a billiard ball start rolling at $P \in [0,1]^2$ in the direction $(1,\alpha)^T$, where α is irrational. Assuming no friction, the ball will bounce off the walls and roll forever in $[0,1]^2$. Any Sturmian word $w(P,\alpha)$ is constructed by appending a 0 to the sequence if the ball hits a vertical wall and a 1 if a horizontal wall is hit. This procedure is visualised in Fig. 3.1. Moreover, Coven and Hedlund [35] proved that the billiard construction is similar to Definition 3.7. Concerning binary words, there are two additional useful definitions. Let $|w|_s$ denote the amount of occurrences of symbol s in the finite word w.

Definition 3.8. *(Balanced) An infinite binary word w is balanced if for any two factors u, v of length n*

$$||u|_1 - |v|_1| \leq 1.$$

Definition 3.9. *(Completely balanced) Consider an infinite binary word w and let w_n denote the finite word consisting of the first n symbols of w. Then w is completely balanced if there exists a sequence $n_0 \leq n_1 \leq \cdots$ where $k, n_k \in \mathbb{N}$, $\lim_{k\to\infty} n_k = \infty$ such that $w = \lim_{k\to\infty} w_n$*

$$|w_{n_k}|_0 = |w_{n_k}|_1, \qquad \forall k \in \mathbb{N}.$$

In Section 3.2.4, we will show that all binary Sturmian sequences can be generated from a Cut-and-Project Scheme (CPS). The mathematical construction of the CPS ensures the diffraction pattern to be pure point, which makes Sturmian words natural quasicrystals. Another relevant question to ask is which Sturmian words can be constructed from a substitution rule. This question is answered in Section 3.2.4 as well.

3.1.3. Fibonacci Substitution

One well-known substitution rule is the *Fibonacci substitution*. On the binary alphabet $\mathcal{A}_2 = \{0,1\}$, one defines the rule

$$\rho : \begin{cases} 0 \mapsto 01, \\ 1 \mapsto 0. \end{cases} \tag{3.2}$$

Starting out with the symbol 1, the Fibonacci word is constructed by repeatedly applying Eq. 3.2, yielding:

$$1 \mapsto 0 \mapsto 01 \mapsto 010 \mapsto 01001 \mapsto 01001010 \mapsto 0100101001001 \mapsto \cdots$$

and similarly for the bi-infinite words

$$0|1 \mapsto 01|0 \mapsto 010|01 \mapsto 01001|010 \mapsto 01001010|01001 \mapsto 0100101001001|01001010 \mapsto \cdots$$

We label the words by the symbol $f_n^{(\mathrm{bi})}$ (F_n is reserved for the Fibonacci numbers), indicating the (bi-)finite Fibonacci word after n applications of the rule Eq. 3.2. There are many justifications for the name "Fibonacci" for this substitution rule. Recall the famous Fibonacci sequence

$$0, 1, 1, 2, 3, 5, 8, 13, 21, 34, 55, 89, 144, \cdots$$

starting with 0, 1 and subsequent numbers are the sum of the last two. Labelling the Fibonacci numbers by $F_{-1}, F_0, \cdots$ we have $F_{-1} = 0, F_0 = 1$ and $F_{n+2} = F_{n+1} + F_n$ for $n \in \mathbb{N}_0$.

The Fibonacci sequence appears as early as 450-200 BC in Indian mathematics [36], where it served the purpose of counting different patterns of long and short syllables. It became known as the Fibonacci sequence when in 1202 it appeared in the book *Liber Abaci* (Book of Calculation), written by Leonardo of Pisa, also known as Fibonacci. Fibonacci used the sequence to model a rabbit population. Denote the pairs of rabbits in month n by r_n. Each adult pair produces a pair of babies each month, and the babies take one month to become adults. If one starts with one pair of babies, $r_0 = 1$, then one month later they are adults, i.e. $r_1 = 1$. If one sees that the

amount of adults in generation n is given by r_{n-1}, and that r_n is equal to r_{n-1} plus the amount of parents in r_{n-1}, one obtains

$$r_n = r_{n-1} + r_{n-2},$$

which is the well-known Fibonacci sequence. Needless to say, there are many different ways to obtain the Fibonacci sequence, one of which the rabbit sequence is a mere example and by no means fundamental.

The golden ratio is obtained from the Fibonacci sequence as

$$\phi = \frac{1+\sqrt{5}}{2} = \lim_{n\to\infty} \frac{F_{n+1}}{F_n}.$$

Equivalently, suppose $F_{n+1}/F_n \xrightarrow{n\to\infty} x$ for some value x, dividing the equation $F_{n+2} = F_{n+1} + F_n$ by F_n gives us the equation $x^2 = x + 1$, which is precisely solved by ϕ.

It turns out that the length of the finite Fibonacci words $|f_n| = F_n$ obeys exactly the Fibonacci sequence (note we shifted the canonical numbering of Fibonacci numbers by one). This is true because of the property of the Fibonacci substitution that subsequent words can be produced by concatenating the previous two Fibonacci words [17]:

$$f_{n+2} = f_{n+1} f_n. \tag{3.3}$$

The infinite Fibonacci word $f = \rho^\infty(1)$ can be shown to be the limit of the sequence f_n by showing f_n is a Cauchy sequence. Let $n, m > N$ for some $N \in \mathbb{N}$ and w.l.o.g. $m > n$. Then

$$d(f_n, f_m) \leq \sum_{i=1}^{m-n} d(f_{n+i-1}, f_{n+i}) = \sum_{i=1}^{m-n} 2^{-F_{n+i}} \leq 1 - \sum_{i=1}^{F_n} 2^{-i} < 1 - \sum_{i=1}^{N} 2^{-i} = \epsilon(N),$$

where we first used the triangle inequality, then Eq. 3.1 with Eq. 3.3 for the equality, and $N < n \leq F_n$ in the last strict inequality. By choosing N large enough, $1 - \sum_{i=1}^{N} 2^{-i}$ becomes arbitrarily small by the geometric series. Since f_n is a Cauchy sequence it is convergent to f. The same can be shown for the bi-infinite word f^{bi}, but in this case one needs to consider applications of ρ^2 to get a converging word.

Having established the existence of the infinite Fibonacci f word in Σ_2^+, we will now discuss some relevant properties of f (see Ref. [34] for more background on claims made in the remainder of this section).

We can count the number of symbols $0, 1$ in a given word f_n by

$$\begin{bmatrix} N_0^{(n+1)} \\ N_1^{(n+1)} \end{bmatrix} = \begin{bmatrix} 1 & 1 \\ 1 & 0 \end{bmatrix} \begin{bmatrix} N_0^{(n)} \\ N_1^{(n)} \end{bmatrix},$$

such that $N_0^{(n+1)} = F_n, N_1^{(n+1)} = F_{n-1}$. The characteristic polynomial of the substitution matrix $x^2 - x - 1$ has ϕ and its conjugate as roots. By inspecting the substitution rule in Fig. 3.2, it is

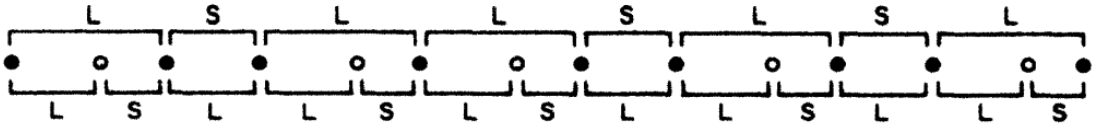

Figure 3.2.: Self-similarity of the Fibonacci quasicrystal (figure from [37]).

clear that the Fibonacci lattice is self-similar. This self-similarity allows the use of renormalisation schemes, i.e. schemes where the original system is described in terms of one or more copies of

itself with possibly different parameters, to quantitatively analyse systems based on the Fibonacci word.

The Fibonacci word $f^{(\mathrm{bi})}$ is also Sturmian [34]. This implies that it is aperiodic. From Section 3.2.2 we can conclude that it results from a CPS and the resulting lattice has a discrete diffraction pattern.

Since the Fibonacci word is aperiodic and the lattice has a discrete spectrum, it is an aperiodic crystal according to the physics classification. Mathematically, we speak of a quasicrystal because it originates from a CPS. Additionally, we see self-similarity, a property shared among many relevant quasicrystals in physics.

3.1.4. Thue-Morse Substitution

Another famous binary sequence that arises from a substitution rule is the Thue-Morse (TM) sequence. The Norwegian mathematician Axel Thue found this sequence when looking for a binary sequence without squares, i.e. two consecutive identical blocks. The TM sequence turns up in wildly different corners of mathematics [38], so we will focus on its properties that are of interest to us.

The substitution rule on the binary alphabet $\mathcal{A}_2 = \{0, 1\}$

$$\rho_{\mathrm{TM}} : \begin{cases} 0 \mapsto 01, \\ 1 \mapsto 10 \end{cases} \tag{3.4}$$

uniquely generates the Thue Morse sequence $(t_n)_{n\in N}$ from the seed 0. The first few iterations of the rule are given by

$$0 \mapsto 01 \mapsto 0110 \mapsto 01101001 \mapsto 0110100110010110 \mapsto \cdots$$

Inspecting these words more closely, one can observe that each subsequent word can be obtained from the previous word by appending the bitwise negated previous word. If one defines on $\mathcal{A}_2$ the negation map $\overline{0} = 1, \overline{1} = 0$, which is applied by the same rules as a substitution rule, one can generate the finite TM words T_n as follows.

$$\begin{aligned} T_0 &= 0, \\ T_1 &= 0\overline{0} = 01, \\ T_2 &= 01\overline{01} = 0110, \\ T_3 &= 0110\overline{0110} = 01101001, \\ T_4 &= 01101001\overline{01101001} = 0110100110010110. \end{aligned}$$

Observe that the negation map preserves palindromes, and T_2 is a palindrome. Hence, for $n \geq 2$ the TM word T_n is a palindrome. Similarly, the infinite TM word $t := T_\infty$ (the TM sequence $(t_n)_{n\in\mathbb{N}}$) is an infinite palindrome. It is also true that the negation map swaps amount of 0's and 1's, so when appending the negation of some word w to itself, the amount of 0's and 1's in $w\overline{w}$ is always equal. Observe that the length of the nth TM word is $|T_n| = 2^n$. This means that the amount of 1's in T_n, the *Hamming weight*, is equal to the amount of 0's $|T_n|_0$ and is given by

$$|T_n|_0 = |T_n|_1 = 2^{n-1}, \qquad \forall n > 0.$$

This means by Definition 3.9 that the TM word is *completely balanced*.

There are two ways to see that the TM sequence is not Sturmian. Firstly, by counting factors of length two, it is clear that the TM sequence is not Sturmian: $p_2(t) = 4 \neq 3$. The second method uses the completely balanced property and argues by contradiction. Suppose the TM sequence

is Sturmian, denoted $w(P, \alpha)$, where α irrational. For the sequence to be completely balanced, $\alpha = \pm 1$ is required. This contradictions shows that the TM sequence cannot be Sturmian. From Section 3.2.4 we can conclude that the TM sequence cannot arise from a CPS.

The TM sequence is not considered a quasicrystal. This is due to the fact that the Fourier transform of the lattice is not a pure point spectrum [38], which implies that the TM sequence cannot be constructed from a CPS. Despite all that, the TM sequence is ordered, aperiodic, balanced, and has a high degree of self-similarity. Suppose that one has the infinite TM sequence t. By the substitution rule Eq. 3.4, the word $t_{2i}t_{2i+1}$ is either 01 or 10. Hence we can define the *deflation rule* $01 \mapsto 0, 10 \mapsto 1$, i.e. ρ_{TM}^{-1}. This maps the TM sequence t to another sequence t' by $t'_n = t_{2n}$. Since $\rho_{\mathrm{TM}}(t) = t$ and we can invert ρ_{TM}, we have $t' = \rho_{\mathrm{TM}}^{-1}(t) = t$. Self-similarity is directly obtained via the substitution rule as a renormalisation step with scaling factor 2, since ρ_{TM} maps each symbol to a word of the same length.

To illustrate its fractal properties, one can show that the TM sequence can be used to generate the Koch snowflake [39]. Drawing an infinite line in the plane using certain rules, also known as *turtle graphics*, one obtains the Koch snowflake in the limit $n \to \infty$ from the rules:

- If $t_n = 0$, move ahead one unit,
- If $t_n = 1$, turn by $\pi/3$ radians.

In Fig. 3.3, various finite generations of the snowflake are shown that are proven to converge to the Koch snowflake by Ma et al. [39].

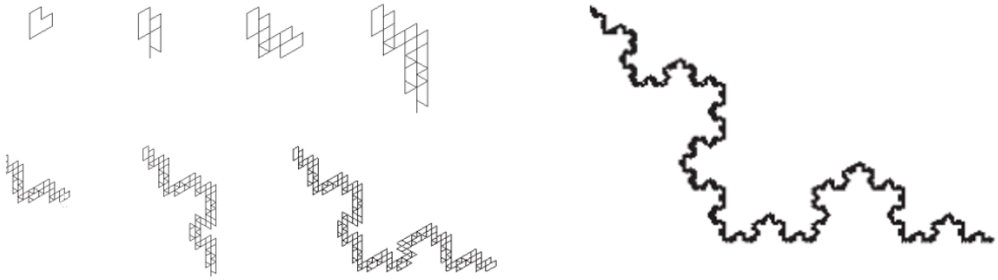

Figure 3.3.: Koch snowflake emerging from turtle graphics (figure from Ref. [39]).

3.1.5. Tribonacci Substitution

A well-known generalisation of the Fibonacci sequence is obtained by summing the last three numbers

$$T_n = T_{n-1} + T_{n-2} + T_{n-3}$$

where $T_{-2} = 0, T_{-1} = T_0 = 1$. The Tribonacci words W_n^T are generated by the substitution ρ_T on the alphabet $\mathcal{A}_3$

$$\rho_{\mathrm{T}} : \begin{cases} 0 \mapsto 01, \\ 1 \mapsto 02, \\ 2 \mapsto 0 \end{cases} \tag{3.5}$$

starting with the seed $W_0^T = 0$. Similar to the Fibonacci words, subsequent words are obtained by concatenating the previous *three* words

$$W_n^T = W_{n-1}^T W_{n-2}^T W_{n-3}^T. \tag{3.6}$$

The number of symbols for a given word can also be counted,

$$\begin{bmatrix} N_0^{(n+1)} \\ N_1^{(n+1)} \\ N_2^{(n+1)} \end{bmatrix} = \begin{bmatrix} 1 & 1 & 1 \\ 1 & 0 & 0 \\ 0 & 1 & 0 \end{bmatrix} \begin{bmatrix} N_0^{(n)} \\ N_1^{(n)} \\ N_2^{(n)} \end{bmatrix}$$

from which we can read off $N_0^{(n+1)} = T_n, N_1^{(n+1)} = T_{n-1}$ and $N_2^{(n+1)} = T_{n-2}$. For example take $W_3^T = 0102010$, then $N_0^3 = T_2 = 4, N_1^3 = T_1 = 2$ and $N_2^3 = T_0 = 1$. The characteristic polynomial of the substitution matrix above is $\lambda^3 - \lambda^2 - \lambda - 1$. In fact, the Fibonacci and Tribonacci can be generalised as a k-bonacci sequence

$$K_n = \sum_{i=1}^{k} K_{n-i}, \qquad K_0 = \cdots = K_{k-2} = 0, K_{k-1} = 1$$

and the corresponding substitution rule ρ_k on $\mathcal{A}_k$

$$\rho_k : \begin{cases} 0 \mapsto 01, \\ 1 \mapsto 02, \\ \cdots \\ (k-2) \mapsto 0(k-1), \\ (k-1) \mapsto 0, \end{cases}$$

starting with the seed word 0. The corresponding characteristic polynomial is then

$$\lambda^k - \sum_{i=0}^{k-1} \lambda^i. \tag{3.7}$$

The Fibonacci, Tribonacci and general k-bonacci substitutions can thus be viewed as the substitutions corresponding to the hierarchy of the characteristic polynomials Eq. 3.7. It is known that all k-bonacci substitutions are of Pisot type [40].

One particular choice of seed for the bi-infinite word is the seed $2|0 = \rho_{\mathrm{T}}^{-1}(0)|0$. The substitution for which a fixed point can be obtained is $\sigma = \rho_{\mathrm{T}}^3$, i.e. three consecutive applications of the Tribonacci substitution. Then, the Tribonacci word stabilises from the right hand side as well:

$$\rho_{\mathrm{T}}^3 : \begin{cases} 0 \mapsto 0102010, \\ 1 \mapsto 010201, \\ 2 \mapsto 0102. \end{cases} \tag{3.8}$$

From Eq. 3.6 it can also be seen that every three applications to W_n, the right side of the word is the original word W_n. The bi-infinite Tribonacci word is then the limit $W^T|W^T = \lim_{N\to\infty} \rho_{\mathrm{T}}^{3N-1}(0)|\rho_{\mathrm{T}}^{3N}(0)$. Another choice of seed could have been $1|0$, $0|0$, or $0|2$.

3.2. Cut-and-Project Schemes

Since CPS is often used as the definition of (quasi)crystals, its mathematical structure will be explained in this section. Conumbering and the connection to Sturmian sequences is treated as well, with the Fibonacci quasicrystal as leading example.

3.2.1. Mathematical Construction

To make the discussion appropriately precise, we introduce some definitions (see Ref. [29] for more details).

Definition 3.10 (Delone Set)**.** *A point set $\Lambda \subset \mathbb{R}^d$ is called Delone if it is discrete and relatively dense. In other words, there exist $0 < r < R \in \mathbb{R}$ such that for all $x \in \Lambda$:*

$$(\Lambda \setminus \{x\}) \cap B_r(x) = \emptyset, \qquad (\Lambda \setminus \{x\}) \cap B_R(x) \neq \emptyset,$$

where $B_r(x)$ denotes the open ball of radius r centered at x.

Intuitively, any lattice should be a Delone set, as atoms cannot be arbitrarily close but also not too far apart in a solid. The next definition is essential for the CPS.

Definition 3.11 (Point Lattice)**.** *A point set $\Gamma \subset \mathbb{R}^d$ is a point lattice if there exist d linearly independent vectors $b_1, \ldots, b_d$, such that*

$$\Gamma = \mathbb{Z}b_1 \oplus \cdots \oplus \mathbb{Z}b_d := \Big\{ \sum_{i=1}^{d} m_i b_i \mid m_i \in \mathbb{Z} \Big\}.$$

Now, we are ready to define the general CPS.

Definition 3.12 (Cut-and-Project Scheme)**.** *A CPS is a triple $(\mathbb{R}^d, H, \mathcal{L})$ where $H = \mathbb{R}^m$ for some $m \geq 0$ and $\mathcal{L} \subset \mathbb{R}^d \times H$ is a point lattice, together with the natural projections $\pi : \mathbb{R}^d \times H \to \mathbb{R}^d$ and $\pi_{int} : \mathbb{R}^d \times H \to H$ such that $\pi|_{\mathcal{L}}$ is injective and $\pi_{int}(\mathcal{L})$ lies dense in H. To define which points in $\mathcal{L}$ are projected onto $\mathbb{R}^d$, an acceptance set $A \subset H$ is provided.*

Here, we explain the general CPS procedure to obtain some point set Λ, which will turn out to be Delone. Denote $L = \pi(\mathcal{L})$ and $L^\star = \pi_{\text{int}}(\mathcal{L})$, and define the map $\star : L \to L^\star$ as

$$x \mapsto x^\star := \pi_{\text{int}} \left((\pi|_{\mathcal{L}})^{-1} (x) \right),$$

where $(\pi|_{\mathcal{L}})^{-1}(x)$ is the unique point in $\mathcal{L} \cap \pi^{-1}(x)$. Since $\pi|_{\mathcal{L}}$ is injective, $L^\star = \pi_{\text{int}}(\mathcal{L})$ holds. The following diagram summarises the procedure.

$$\begin{array}{ccccc}
\mathbb{R}^d & \xleftarrow{\ \pi\ } & \mathbb{R}^d \times H & \xrightarrow{\ \pi_{\text{int}}\ } & H \\
\cup & & \cup & & \cup \quad \text{dense} \\
\pi(\mathcal{L}) & \xleftarrow{\ 1-1\ } & \mathcal{L} & \longrightarrow & \pi_{\text{int}}(\mathcal{L}) \\
\| & & & & \| \\
L & & \xrightarrow{\qquad\star\qquad} & & L^\star
\end{array} \tag{3.9}$$

To ultimately obtain the point set Λ from the CPS, the acceptance set $A \subset H$ together with the projections are used. One selects all points $(x, y) \in \mathbb{R}^d \times H$, such that $y \in A$. Then $\pi(x, y)$ is added to Λ. This can be summarised as

$$\Lambda(A) := \{x \in L \mid x^\star \in A\}. \tag{3.10}$$

Such a set Λ arising from a CPS is called a *model set*. The requirement in Definition 3.12 that $\pi_{\text{int}}(\mathcal{L})$ be dense in H is only necessary for generating aperiodic structures. This can be seen by considering $\mathcal{L} \subset \mathbb{R}^2$ and $H = \mathbb{R}$. Then, an irrational cut will give a dense $\pi_{\text{int}}(\mathcal{L})$, whereas a rational slope of L in R^2 will not.

We are now in a position to state some useful results regarding model sets without proof, which can be found in Ref. [29].

Theorem 3.13. *If Λ is a model set, it is also a Delone set.*

This theorem ensures that any CPS will generate a physically reasonable lattice. In order to talk about the diffraction pattern of a set Λ, we define its *autocorrelation measure*. The autocorrelation measure γ_Λ of some point set Λ is defined to be the volume-averaged autocorrelation of its Dirac comb $\delta_\Lambda = \sum_{x\in\Lambda} \delta_x$:

$$\gamma_\Lambda = \lim_{R\to\infty} \gamma_\Lambda^{(R)} := \lim_{R\to\infty} \frac{\delta_{\Lambda\cap B_R} \star \delta_{\Lambda\cap B_R}}{\mathrm{vol}(B_R)},$$

where $\star$ denotes the autocorrelation operation and the limit exists for every Delone set [29]. Before proceeding, we briefly review the definition of the autocorrelation for functions and measures. The autocorrelation between two functions $f, g : \mathbb{R}^d \to \mathbb{C}$ is defined by

$$(f \star g)(\mathbf{x}) = \int_{\mathbb{R}^d} f(\mathbf{x}+\mathbf{y})\overline{g(\mathbf{y})}\mathrm{d}^d\mathbf{y},$$

where the overline indicated complex conjugation. Similarly, the autocorrelation measure of two measures μ, ν is defined as (see Ch. 9 of Ref. [29])

$$(\mu * \nu)(A) = \int_{\mathbb{R}^d\times\mathbb{R}^d} 1_A(\mathbf{x}-\mathbf{y})\mathrm{d}\mu(\mathbf{x})\overline{\mathrm{d}\nu(\mathbf{y})},$$

where 1_A is the indicator function, and the complex-conjugation of a complex measure μ is defined as $\int_A \overline{\mathrm{d}\mu(\mathbf{x})} = \overline{\mu(A)}$.

As discussed in Section 2.2, the diffraction pattern of a lattice is described by the structure factor $S(\mathbf{q})$ in Eq. 2.1. Before stating the main result of this section, the relation between the structure factor $S(\mathbf{q})$ and the autocorrelation measure γ_Λ needs to be established.

Recall that $S(\mathbf{q})$ was the modulus squared of the FT of the lattice. To make this more rigorous, let $\delta_\Lambda(\mathbf{x}) = \sum_{\mathbf{y}\in\Lambda} \delta(\mathbf{x}-\mathbf{y})$ be the Dirac comb of delta functions, instead of Dirac measures, that describes the lattice $\Lambda \subset \mathbb{R}^d$. Note that the measure δ_Λ is recovered by

$$\delta_\Lambda(A) = \int_A \delta_\Lambda(\mathbf{x})\, d^d\mathbf{x},$$

where $A \subset \mathbb{R}^d$ and we used the fact that for delta functions, the Riemann integral is defined. Using the definition of the Fourier transform

$$\widehat{f}(\mathbf{q}) = \int_{\mathbb{R}^d} f(\mathbf{x}) e^{-2\pi i\mathbf{q}\cdot\mathbf{x}}\, \mathrm{d}^d\mathbf{x}, \qquad f(\mathbf{x}) = \int_{\mathbb{R}^d} \widehat{f}(\mathbf{q}) e^{2\pi i\mathbf{q}\cdot\mathbf{x}}\, \mathrm{d}^d\mathbf{q},$$

the structure factor can be written as

$$S(\mathbf{q}) = \frac{1}{N}\left|\widehat{\delta_\Lambda}(\mathbf{q})\right|^2 = \frac{\widehat{(\delta_\Lambda \star \delta_\Lambda)}(\mathbf{q})}{N}, \tag{3.11}$$

where N is the amount of lattice sites in Λ and where the well-known result is used that for the autocorrelation of a function $f : \mathbb{R}^n \to \mathbb{R}$, $\widehat{(f\star f)}(\mathbf{q}) = |\widehat{f}(\mathbf{q})|^2$ holds. Since $S(\mathbf{q})$ is the FT of the autocorrelation function, we need to take the FT of the autocorrelation measure. The FT of a measure μ is defined as (see Ch. 8 of Ref. [29])

$$\widehat{\mu}(\mathbf{q}) = \int_{\mathbb{R}^d} e^{-2\pi i\mathbf{q}\cdot\mathbf{x}}\mathrm{d}\mu(\mathbf{x}), \tag{3.12}$$

which is a function on $\mathbb{R}^d$. Choose any radius $R \in [0,\infty)$, then there are finitely many $N(R)$ points in $\Lambda \cap B_R$ (assuming Λ is Delone). Then Eq. 3.11 can be rewritten as

$$S(\mathbf{q}) = \int_{\mathbb{R}^d} e^{-2\pi i\mathbf{q}\cdot\mathbf{x}} \lim_{R\to\infty} \frac{(\delta_{\Lambda\cap B_R} \star \delta_{\Lambda\cap B_R})(\mathbf{x})}{N(R)}\mathrm{d}^d\mathbf{x} = \int_{\mathbb{R}^d} e^{-2\pi i\mathbf{q}\cdot\mathbf{x}} \lim_{R\to\infty} \mathrm{d}\mu^{(R)}(\mathbf{x}), \tag{3.13}$$

and the FT of the autocorrelation measure can be rewritten as

$$\widehat{\gamma_\Lambda}(\mathbf{q}) = \int_{\mathbb{R}^d} e^{-2\pi i \mathbf{q}\cdot\mathbf{x}} \lim_{R\to\infty} \mathrm{d}\gamma_\Lambda^{(R)}(\mathbf{x}), \tag{3.14}$$

where we introduced the measure $\mu^{(R)}$ defined by

$$\mu^{(R)}(A) = \int_A \frac{(\delta_{\Lambda\cap B_R} \star \delta_{\Lambda\cap B_R})(\mathbf{x})}{N(R)} \mathrm{d}^d\mathbf{x}.$$

We will now show that for every value of R, the measures $\mu^{(R)}$ and $\gamma^{(R)}$ are related by a constant $\rho(R)$. Let $A \subset \mathbb{R}^d$ be any set and denote $\Lambda \cap B_R = \Lambda'$, then

$$\begin{aligned}
\mu^{(R)}(A) &= \frac{1}{N(R)} \int_A \mathrm{d}^d\mathbf{x} \int_{\mathbb{R}^d} \mathrm{d}^d\mathbf{y} \delta_{\Lambda'}(\mathbf{y})\delta_{\Lambda'}(\mathbf{x}+\mathbf{y}) \\
&= \frac{1}{N(R)} \int_{\mathbb{R}^d\times\mathbb{R}^d} 1_A(\mathbf{x})\delta_{\Lambda'}(\mathbf{y})\delta_{\Lambda'}(\mathbf{x}+\mathbf{y})\mathrm{d}^d\mathbf{x}\mathrm{d}^d\mathbf{y} \\
&= \frac{1}{N(R)} \int_{\mathbb{R}^d\times\mathbb{R}^d} 1_A(\mathbf{x}-\mathbf{y})\mathrm{d}\delta_{\Lambda'}(\mathbf{x})\mathrm{d}\delta_{\Lambda'}(\mathbf{y}) \\
&= \frac{1}{N(R)}(\delta_{\Lambda'} \star \delta_{\Lambda'})(A) = \frac{\mathrm{vol}(B_R)}{N(R)}\gamma_\Lambda^{(R)}(A) = \frac{1}{\rho(R)}\gamma_\Lambda^{(R)}(A).
\end{aligned} \tag{3.15}$$

By plugging Eq. 3.15 into Eqs. 3.13 and 3.14, we can conclude $\widehat{\gamma_\Lambda}(\mathbf{q}) = \rho S(\mathbf{q})$, where $\rho = \lim_{R\to\infty}\rho(R)$ can be interpreted as the average density over the whole lattice Λ. This limit exists since Λ is assumed to be Delone. The relation between the structure factor and the autocorrelation measure is now established, where $S(\mathbf{q})$ is related by the FT of the autocorrelation measure by the constant ρ.

We can now state the most important result, Theorem 9.4 from Ref. [29], which is the following theorem.

Theorem 3.14. *Let Λ be a model set for some CPS as given in Definition 3.12. The autocorrelation measure γ_Λ exists and its Fourier transform $\widehat{\gamma_\Lambda}$ is a positive definite, pure point measure.*

We have shown that each lattice originating from a CPS has pure point diffraction spectrum. In many cases, this spectrum is self-similar and has some rotational symmetry, which need not be crystallographic. It is known that finding the real space lattice corresponding to some pure point diffraction pattern is generally ill-posed. An interesting question, which to the best of our knowledge is unanswered, is the following:

"*Upon imposing a certain rotational symmetry and scale invariance on a pure point diffraction pattern, is the problem of finding its real space lattice well-defined?*"

We will now show how to apply the formal CPS in Eq. 3.9 to some examples.

3.2.2. Fibonacci Quasicrystal

We want to construct the 1D Fibonacci quasicrystal, so $d = 1$. Take $H = \mathbb{R}$ and start with a cubic lattice in $\mathbb{R}^2$. Next, we draw a line L with slope $\alpha = 1/\phi$, where ϕ is the golden ratio, see Fig. 3.4. We choose a basis in $\mathbb{R}^2$ such that cubic lattice is spanned by the canonical basis vectors $\mathbf{e}_1 = (1,0)^T$ and $\mathbf{e}_2 = (0,1)^T$. The acceptance set A is the strip of width $\frac{1+\alpha}{\sqrt{1+\alpha^2}}$ perpendicular to the line, such that $L \times A$ is the region traced out by a unit cube sliding along L, see Fig. 3.5. Projecting all lattice points in $L \times A$ onto the line L, the horizontal line in Fig. 3.4, yields the Fibonacci quasicrystal. Long and short intervals correspond to a 0 and 1, respectively, in the Fibonacci word $1f$ (note the 1 appended). The points in $L \times A$ are equivalently obtained from the word $1f$. For the first m symbols, the mth point in $L \times A$ is given by

$$\mathbf{x}_m = (n_0^m, n_1^m)^T,$$

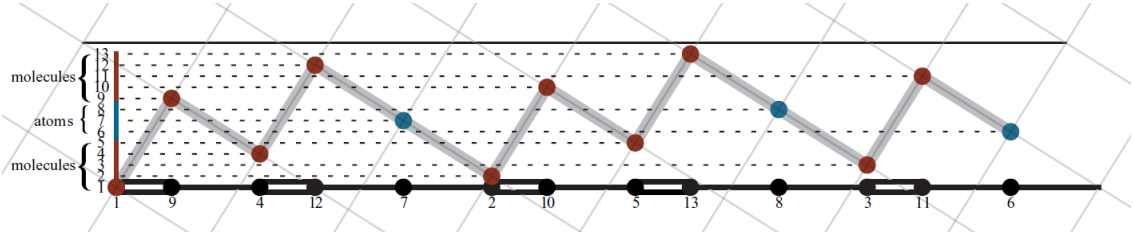

Figure 3.4.: Fibonacci quasicrystal by means of CPS (figure from Ref. [22]). Red dots represent sites that have one 0 and one 1 as neighbours in the Fibonacci word. Blue dots represent sites that have two 0's as neighbours in the Fibonacci word.

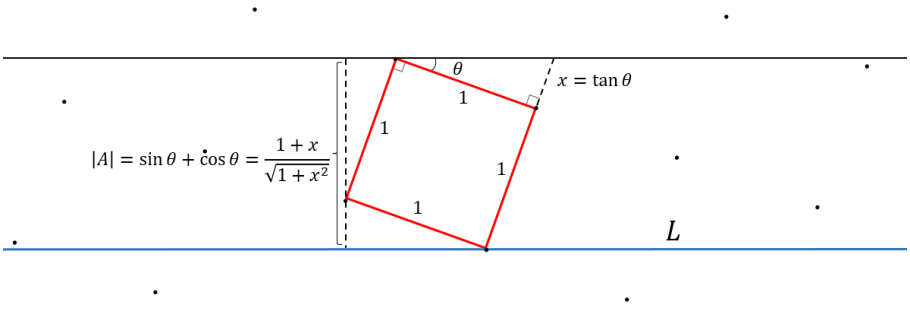

Figure 3.5.: Geometry of the sliding unit cube.

where n_l^m are the amount of occurrences of letter l in the first m letters of $1f$.

If we approximate $\phi_n = F_{n-1}/F_{n-2}$ and let the slope be $1/\phi_n$, we obtain a periodic lattice with unit cells of F_n sites. In Fig. 3.4, the unit cell contains $F_6 = 13$ sites and the slope is given by $F_4/F_5 = 5/8$. Approaching the irrational slope by rational numbers and considering the periodic lattice for increasing n is a conventional way to study aperiodic CPS lattices.

Finally, we mention the *conumbering* method for approximant Fibonacci words. As seen in Fig. 3.4 the points can be numbered according to their ordering in H-space. It turns out that this precisely orders the Fibonacci lattice points according to their *local* environment. Define bonding between two consecutive points $\mathbf{x}, \mathbf{y}$ as weak if $\mathbf{y} - \mathbf{x} = \mathbf{e}_1$, i.e. horizontal, and strong if $\mathbf{y} - \mathbf{x} = \mathbf{e}_2$, i.e. vertical. Weak and strong bonds are depicted in Fig. 3.4 as single and double lines, respectively. The conumbering scheme groups points surrounded by weak-strong, weak-weak and strong-weak as adjacent couplings. It turns out that conumbering often reveals symmetries of the system that are not manifest in the real-space ordering of lattice points [22]. Furthermore, given a real-space index i, the corresponding conumber is given by

$$c(i) = F_{n-1} i \bmod F_n, \tag{3.16}$$

which will be proven below.

Conumbering

In the special case $H = \mathbb{R}$, Sire et al. [23] developed conumbering as an alternative way to label the lattice points in Λ. Suppose we cut the d-dimensional hyperplane $\mathcal{P}$ spanned by

$$\mathbf{a}_i = (0, \ldots, 0, p_i, 0, \ldots, 0, -r_i), \qquad p_i, r_i \in \mathbb{R},$$

in $\mathbb{R}^{d+1}$, where $1 \leq i \leq d$ and p_i is the ith entry. The resulting lattice obtained by projecting points on the plane is quasiperiodic in all directions if $p_i/r_i = \alpha_i \notin \mathbb{Q}$ for all i, i.e. the plane

cuts irrationally. Often, the quasicrystal is approximated by $\alpha_i' = p_i'/q_i'$, where $p_i', q_i' \in \mathbb{Z}$. The lattice that results from projecting on this approximate hyperplane $\mathcal{P}'$, called the *approximant*, is periodic with a unit cell consisting of N points. The conumbering scheme labels points in the unit cell according to their distance from $\mathcal{P}'$ before projecting. More precisely, Sire et al. showed that all $\mathbf{x}_j \in \mathbb{R}^{d+1}$ in the unit cell are obtained from a generator $\mathbf{h}$ as

$$\mathbf{x}_j = j\mathbf{h} \bmod [\mathbf{a}_1, \ldots, \mathbf{a}_n], \qquad 0 \leq j < n,$$

where the modulo is taken w.r.t. the $\mathbb{Z}$-module spanned by $\mathbf{a}_1, \ldots, \mathbf{a}_n$. Conumbering provides a 1D description of a d-dimensional quasicrystal. It turns out that it orders the points according to their local environment. We will discuss the conumbering scheme in detail for the Fibonacci quasicrystal in the remainder of this section.

Consider the CPS for the Fibonacci approximant chain in Fig. 3.4, where the line L is spanned by $\mathbf{a} = (8, 5)$. One obtains the conumbers by projecting the points on the orthogonal axis and labeling them from closest to furthest away from L. We will now explicitly construct a generator $\mathbf{h}_n$ for every nth approximant, such that

$$\mathbf{x}_j^{(n)} = \mathbf{h}_n j \mod \mathbf{a}_n, \qquad 0 \leq j < F_n \tag{3.17}$$

and the conumber $c(j)$ for each point $\mathbf{x}_j^{(n)}$ is given by

$$c(j) = jF_{n-1} \bmod F_n.$$

In general, for the approximant with F_n sites in a unit cell one has $\mathbf{a}_n = (F_{n-1}, F_{n-2})$, so $\alpha_n = F_{n-2}/F_{n-1}$. For a point $\mathbf{x} = (x, y)$ to lie in $L \times A$, it must satisfy

$$0 \leq y - \alpha_n x < 1 + \alpha_n. \tag{3.18}$$

On the other hand, for the unit cell to be constructed as in Eq. 3.17, we need $\{\mathbf{a}_n, \mathbf{h}_n\}$ to be a basis of $\mathbb{Z}^2$. This is equivalent to

$$\det \begin{bmatrix} F_{n-1} & h_n^x \\ F_{n-2} & h_n^y \end{bmatrix} = F_{n-1}h_n^y - F_{n-2}h_n^x = \pm 1$$

by Pick's theorem. If we want $\mathbf{h}_j$ to lie in $L \times A$ for all $j = 0, \ldots, F_n - 1$, we will require the points $x = jh_n^x$ on the line with slope h_n^y/h_n^x to satisfy Eq. 3.18. This yields

$$0 \leq F_{n-1}h_n^y - F_{n-2}h_n^x \leq 1,$$

which allows us to conclude $F_{n-1}h_n^y - F_{n-2}h_n^x = 1$. We will now show that either $\mathbf{h}_n = (F_{n-2}, F_{n-3})$ or $\mathbf{h}_n = (F_{n-3}, F_{n-4})$, depending on the parity of n. For this we need Vadja's identity, which for our definition of the Fibonacci numbers reads:

$$F_{n+i}F_{n+j} - F_nF_{n+i+j} = (-1)^{n+1}F_{i-1}F_{j-1}.$$

We rewrite it in a more useful form

$$F_nF_{n+i+j} - F_{n+i}F_{n+j} = (-1)^nF_{i-1}F_{j-1}$$

and relabel $n + i + j \to n - 1$ to get

$$F_{n-1-i-j}F_{n-1} - F_{n-1-j}F_{n-1-i} = (-1)^{n-1-i-j}F_{i-1}F_{j-1}.$$

Note that we can only pick $i, j = 1, 2$ to have $F_{i-1}F_{j-1} = 1$. Now, we want to solve $F_{n-1}h_n^y - F_{n-2}h_n^x = 1$. Hence, w.l.o.g. we set $j = 1$ to get

$$F_{n-2-i}F_{n-1} - F_{n-2}F_{n-1-i} = (-1)^{n-i} \tag{3.19}$$

from which we can read off the solution

$$\mathbf{h}_n = \begin{cases} (F_{n-3}, F_{n-4}) & \text{if } n \bmod 2 = 0, \\ (F_{n-2}, F_{n-3}) & \text{else.} \end{cases} \tag{3.20}$$

Let us recap what we have established so far. For every nth approximant, we have shown that all $\mathbf{x}_j^{(n)}$ are found by Eq. 3.17 using the generator Eq. 3.20. Additionally, Eq. 3.20 was derived with the constraint that all $\mathbf{x}_j^{(n)}$ lie on a line in $L \times A$ that starts at the origin. Hence, $\mathbf{x}_j^{(n)}$ will be ordered from close to far away from L, starting from $j = 0$ to $j = F_n - 1$.

Suppose that we relabel $\mathbf{x}_j$ as $\mathbf{x}'_i$, where $i = 0, \ldots, F_n - 1$ labels the points from left to right according to their location projected on L. By the pigeonhole principle, we should be able to find a function c that maps one labeling to the other. The key to finding this function is to note that if $\mathbf{x}_j = (a, b)$ for some $a, b \in \mathbb{N}$, then $i = a + b$, i.e. the sum of the amount of horizontal and vertical steps in the cubic lattice. Thus, given a conumber $j =: c(i)$, the corresponding lattice label i is found by

$$i = c^{-1}(j) = x_j + y_j = j(h_n^x + h_n^y) \bmod F_n = \begin{cases} jF_{n-2} \bmod F_n & \text{if } n \bmod 2 = 0, \\ jF_{n-1} \bmod F_n & \text{else.} \end{cases}$$

Even more useful is the function $c(i)$, which gives the conumber $\mathbf{x}_{c(i)}$ corresponding to some site $\mathbf{x}'_i$. By inverting the above, we obtain $c(i)$.

Start by multiplying both sides with F_{n-1} and taking modF_n to get

$$F_{n-1}i \bmod F_n = F_{n-1}(h_n^x + h_n^y)j \bmod F_n = \begin{cases} jF_{n-2}F_{n-1} \bmod F_n & \text{if } n \bmod 2 = 0, \\ jF_{n-1}^2 \bmod F_n & \text{else.} \end{cases}$$

If n is even, we have $F_{n-2}F_{n-1} = F_{n-3}F_n + 1$, by Eq. 3.19. Similarly if n is odd, we have $F_{n-1}^2 = F_{n-2}F_n + 1$. This reduces the above equation to

$$c(i) = F_{n-1}i \bmod F_n,$$

where now $j = c(i)$, which is valid for all n. This concludes our proof of Eq. 3.16.

3.2.3. Tribonacci Quasicrystal

To construct the 1D Tribonacci quasicrystal we take $d = 1$ and $H = \mathbb{R}^2$. Points in $\mathbb{Z}^3 \subset \mathbb{R}^3$ are given by

$$\mathbf{x}_m = (n_0^m, n_1^m, n_2^m)^T,$$

where n_l^m counts the occurrences of letter l in the first m letters of the Tribonacci word. The line L is defined by

$$L = \{x\mathbf{e}_L \mid x \in \mathbb{R}\}, \qquad \mathbf{e}_L = \lim_{m\to\infty} \frac{\mathbf{x}_m}{\|\mathbf{x}_m\|},$$

i.e. the asymptotic direction of $\mathbf{x}_m$ in $\mathbb{R}^3$. The line L coincides with the eigenspace of the largest eigenvalue of the substitution matrix, which is guaranteed to be 1D because the Tribonacci substitution is Pisot, i.e. it has only one expanding direction. We can thus write $\mathbb{R}^3 = L \oplus H$. The projection operator $\pi : L \oplus H \to L$ is given by $x \oplus y \mapsto x$.

To study the acceptance set A, label each $\mathbf{x}_m$ as 0,1, or 2 by using $\Delta_m = \mathbf{x}_m - \mathbf{x}_{m-1}$ with the rule

$$\begin{cases} 0 \text{ if } & \Delta_m = (1,0,0)^T, \\ 1 \text{ if } & \Delta_m = (0,1,0)^T, \\ 2 \text{ if } & \Delta_m = (0,0,1)^T. \end{cases}$$

Projecting these points using $\pi_{\text{int}} : L \oplus H \to H$ as $x \oplus y \mapsto y$ into $H = \mathbb{R}^2$ results in the acceptance set A, the Rauzy Fractal (up to an affine transformation, see Section 5.3.1 for details). This procedure is visualised in Fig. 3.6a where $0, 1, 2$ correspond to red, green and blue. The Rauzy fractal is equal to three scaled copies of itself, as depicted in Fig. 3.6b. The scaling factor is $1/\beta$ where $\beta \approx 1.8392$ is the Tribonacci constant. The three copies are scaled by $1/\beta, 1/\beta^2, 1/\beta^3$, respectively.

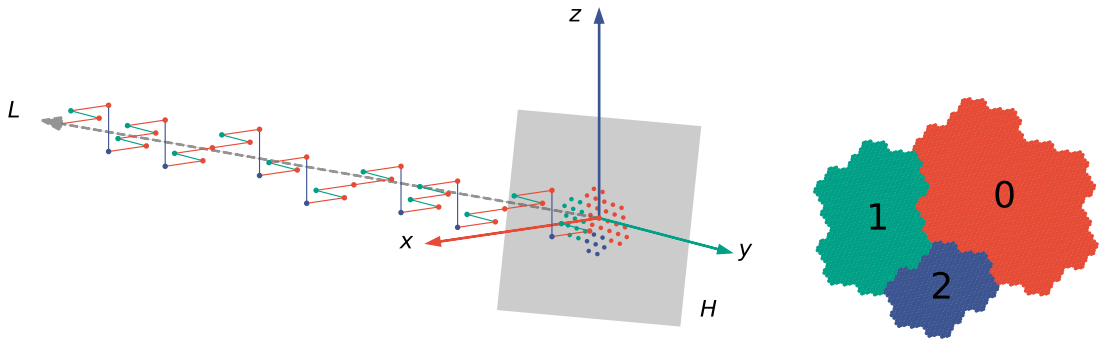

(a) Construction of the Rauzy fractal.

(b) Numbered Rauzy fractal.

Figure 3.6.: The Rauzy fractal as acceptance set $A \subset H$ of the Tribonacci word.

3.2.4. Sturmian Sequences Revisited

We encountered the Sturmian words in Section 3.1.2. It turns out that an infinite word is Sturmian if and only if it originates from a CPS with irrational cut [33]. This will be shown in this section for Sturmian sequences on a binary alphabet.

Recall the alternative definition of Sturmian sequences as a billiard ball bouncing off the walls in Section 3.1.2. This is the same as letting the ball roll in $\mathbb{R}^2/\mathbb{Z}^2$ in a straight line and append 0 or 1 by the same rules, which is again similar to a CPS with $L = \mathbb{R}$ and a projection set $A = [-\frac{\alpha}{\sqrt{1+\alpha^2}}, \frac{1}{\sqrt{1+\alpha^2}}]$. This set arises from letting $L \times A$ be the result of tracing a unit cube of the cubic lattice along L with the lower left vertex located on L. The value ρ where L intersects the x-axis is called the *intercept* of L.

If $\alpha \in \mathbb{Q}$, the orbit of the ball is periodic, and so will the word $w(P, \alpha)$ be. If α is irrational, the word will be aperiodic. Any Sturmian word is aperiodic, hence we require α irrational. We conclude with the following theorem:

Theorem 3.15. *A binary word is Sturmian if and only if it can be built from a CPS with $L = H = \mathbb{R}$, where the slope α is irrational.*

Another interesting question is which Sturmian words can be generated by a substitution rule. Since the Sturmian words and CPS words are 1-to-1, we can similarly ask which CPS words can be constructed by a substitution rule. Yasutomi et al. [41] proved the following theorem.

Theorem 3.16. *A CPS (viz. Sturmian) word can be constructed by a substitution rule if and only if α is a quadratic irrational and the intercept $\rho \in \mathbb{Z}[\alpha]$.*

This precisely answers the question.

3.2.5. Higher-Dimensional Tilings

So far, we have discussed applications of a CPS that yielded a 1D lattice. The advantage was that the mathematical details remained tractable, except for a constructive description of the Rauzy fractal, and the total space $\mathbb{R}^d \times H$ has been a 2- or 3D space, which is something humans can visualise. The two tilings discussed in this section, the Ammann-Beenker (see Fig. 3.7a) tiling and the Penrose tiling (see Fig. 3.7b), are examples where geometric intuition is less helpful, as the total spaces are 4- and 5D, respectively. We discuss the details of CPS for the Amman-Beenker tiling, as this is the most tractable tiling, but the technical methods for the Penrose tiling are the same.

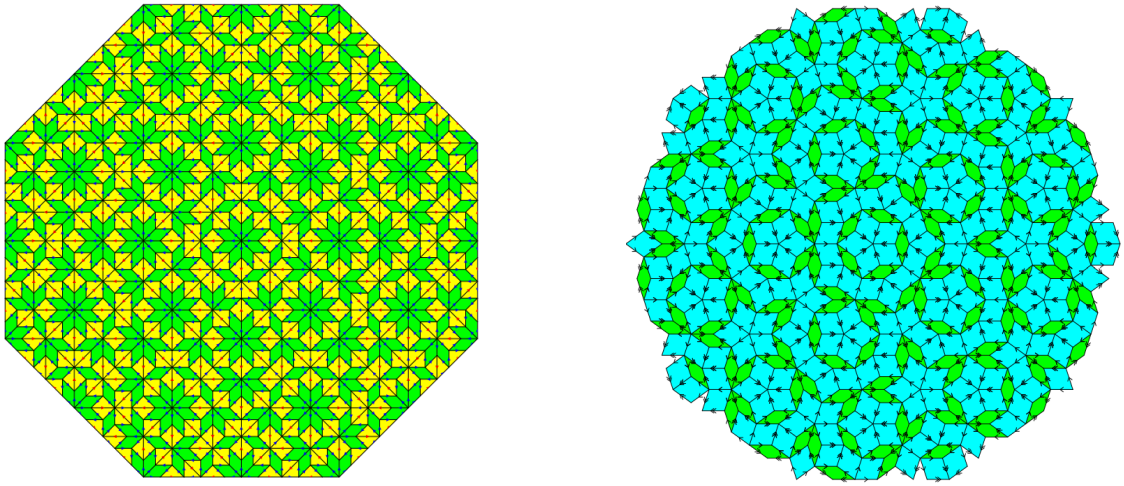

(a) The Ammann-Beenker tiling. (b) Penrose.

Figure 3.7.: Tilings with local matching rules (figures from Ref. [42]).

Ammann-Beenker

The Ammann-Beenker tiling, as depicted in Fig. 3.7a, is a 8-fold rotationally symmetric tiling of the plane. It is a quasicrystal in the sense that its diffraction spectrum, when taking the vertices as atoms, is pure point, which can be seen as a consequence of the fact that it can be constructed from a CPS.

One way to construct the Ammann-Beenker tiling is the *inflation method*. Consider the top two tiles in Fig. 3.8. After inflating both tiles with a factor $1+\sqrt{2}$, the tiles can be subdivided into its original parts. Starting with a square, which is made of two yellow triangles, the inflation rules are applied repeatedly in Fig. 3.8b to obtain the Ammann-Beenker tiling in Fig. 3.7a. Note the blue, red and black markers on the sides and corners of the tiles. Those are called *matching rules*, which ensure that the tiling can extend to infinity. It is well-known that for any aperiodic tiling with matching rules, any violation of those rules destroys the possibility of extending the pattern to infinity [42].

It is also true that any finite patch occurs infinitely often in the tiling [42], which can be proven using the inflation construction of the Ammann-Beenker tiling as follows. Suppose one obtains some pattern $\mathcal{P}$ after n iterations of inflation rules on a seed tile t. After another n iterations of the inflation rules, the pattern $\mathcal{P}$ will occur once for every $t \in \mathcal{P}$. So if t occurs at least twice in $\mathcal{P}$, the pattern occurs infinitely often.

Following the inflation rule ensures the matching rules to be satisfied, which ensures the tiling to be aperiodic [42]. However, it turns out that the matching rules do not provide enough information to

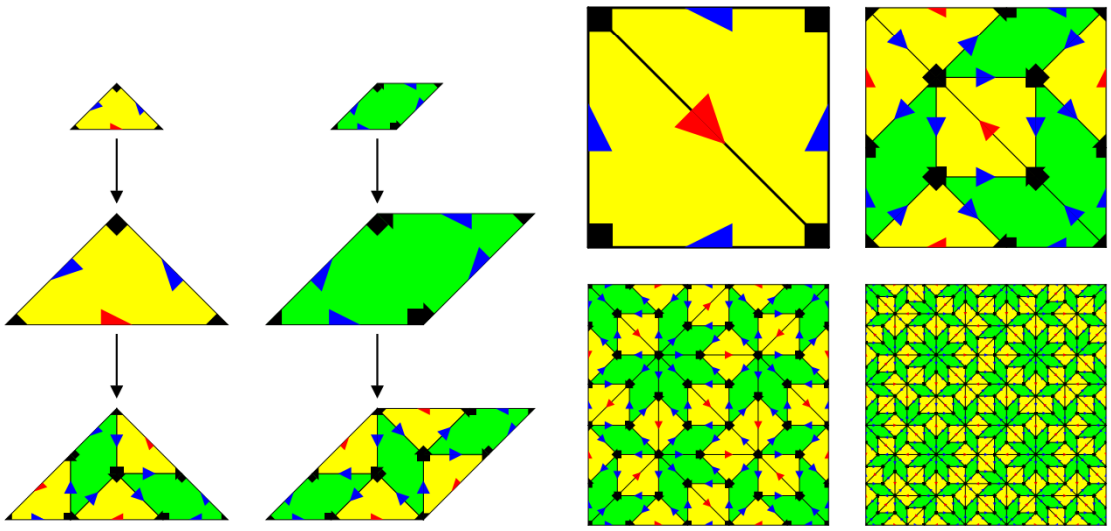

(a) Inflation with matching rules. (b) Repeated rules.

Figure 3.8.: The inflation rules of the Ammann-Beenker tiling and repeated application of them (figures from Ref. [42]).

tile the plane, one tile at a time, such that all matching rules are satisfied. This can be conceptually explained as follows. It is known that any finite patch of the Ammann-Beenker/Penrose tiling repeats itself infinitely often in the infinite tiling. So suppose one is tiling the plane and only a finite portion, call it $\mathcal{P}$, is finished. Continuing the tiling, the same portion $\mathcal{P}$ would turn up again. If matching rules would uniquely define a tiling, the same pattern must be tiled around the copy of $\mathcal{P}$. This results in a periodic tiling, which contradicts the statement that a tiling with satisfied matching rules is aperiodic.

Note that tiling the plane tile-by-tile is possible. The matching rules give a good indication on what tile to choose. However, at some points, more than one option is possible. If the choice was wrong, one will get stuck at some points (no tiles fit at some point). This means that tiling tile-by-tile will be a tedious trial-and-error process.

The fact that inflation rules only generate a finite portion and tiling the plane tile-by-tile is not uniquely defined, another way of defining aperiodic tilings is desired. This is precisely the role played by CPS, since it is a mathematically rigorous framework that uniquely determines the infinite tiling with a finite set of rules. We will now show how the Ammann-Beenker tiling is obtained from a CPS.

The remainder of this section summarises details of a work by Baake et al. [42]. Consider the unit vectors in Fig. 3.9. More specifically, they read

$$\begin{aligned}
\mathbf{a}_1 &= (1,0)^T, \qquad \mathbf{a}_1^* = (1,0)^T, \\
\mathbf{a}_2 &= \frac{1}{\sqrt{2}}(1,1)^T, \qquad \mathbf{a}_2^* = \frac{1}{\sqrt{2}}(-1,1)^T, \\
\mathbf{a}_3 &= (0,1)^T, \qquad \mathbf{a}_3^* = (0,-1)^T, \\
\mathbf{a}_4 &= \frac{1}{\sqrt{2}}(-1,1)^T, \qquad \mathbf{a}_4^* = \frac{1}{\sqrt{2}}(1,1)^T.
\end{aligned}$$

These vectors have the property that $(\mathbf{a}_i \oplus \mathbf{a}_i^*) \cdot (\mathbf{a}_j \oplus \mathbf{a}_j^*) = 2\delta_{i,j}$, from which we can conclude that $\{\frac{1}{\sqrt{2}}\mathbf{a}_i \oplus \mathbf{a}_i^* \mid i = 1,2,3,4\}$ is a orthonormal basis of $\mathbb{R}^4$. Denote $\mathbf{a} = (\mathbf{a}_1, \mathbf{a}_2, \mathbf{a}_3, \mathbf{a}_4)^T$ and let

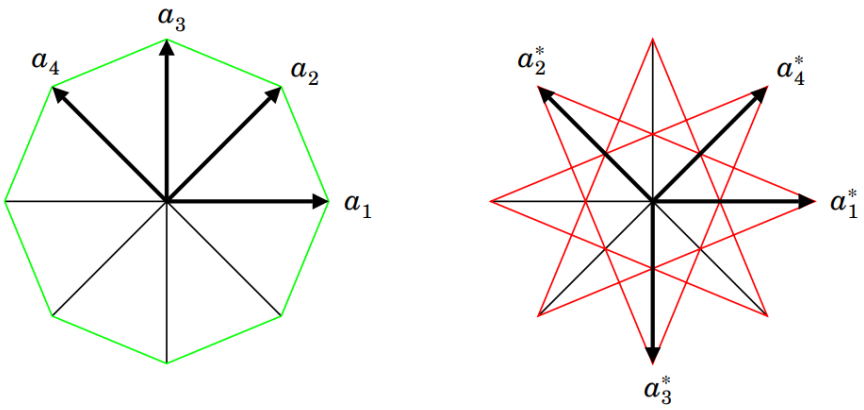

Figure 3.9.: Unit vectors in $\mathbb{R}^2$ for the CPS of the Ammann-Beenker tiling (figure from Ref. [42]).

$\mathbf{u} \in \mathbb{Z}^4$, one can construct a hypercubic lattice, with lattice constant $\sqrt{2}$ as

$$\mathcal{L} = \{x \oplus x^* \mid x = \mathbf{u} \cdot \mathbf{a}, x^* = \mathbf{u} \cdot \mathbf{a}^*, \mathbf{u} \in \mathbb{Z}^4\}.$$

Now we have all our ingredients for the CPS for the Ammann-Beenker tiling. We have $d = 2, H = \mathbb{R}^2$ and our hypercubic lattice $\mathcal{L}$ in $\mathbb{R}^4$. The projections are simply $\pi(x \oplus y) = x, \pi_{\text{int}}(x \oplus y) = y$. The acceptance set A is an octagon with unit edges. The vertices of the Ammann-Beenker tiling are

$$\Lambda(A) = \{x = \mathbf{u} \cdot \mathbf{a} \mid x^* = \mathbf{u} \cdot \mathbf{a}^* \in A, \mathbf{u} \in \mathbb{Z}^4\} \subset \pi(\mathcal{L}).$$

This concludes our discussion of the construction of the Ammann-Beenker tiling from a CPS. Note that the methods presented in this section are also applicable to Penrose tilings.

Penrose

To generate the Penrose tiling, see Fig. 3.7, one can use both an inflation scheme or CPS. These are very similar to those of the Ammann-Beenker tiling. Therefore, we focus on a third method to generate the Penrose tiling, called the *pentagrid method*. This method was developed by the Dutch mathematician Nicolaas Govert de Bruijn [3]. The pentagrid method has a few advantages:

- From the Pentagrid method, the non-periodicity of the Penrose tiling can be read off,
- The pentagrid offers an easy way of generating a finite patch of the Penrose tiling at hand.

Now let us describe the Pentagrid method as a recipe to obtain Penrose tilings, where our discussion is based on Ref. [43]. First, one takes five unit vectors $\mathbf{e}_i$ in $\mathbb{R}^2$, which are at an angle of 72°, as depicted in Fig. 3.10a. For each unit vector $\mathbf{e}_i$, define a set of lines V_i that are perpendicular to that unit vector, with a unit vector spacing. More specifically,

$$L_i = \{\mathbf{x} \in \mathbb{R}^2 \mid \mathbf{x} \cdot \mathbf{e}_i = 0\}, \qquad V_i = \{V_i + n\mathbf{e}_i \mid n \in \mathbb{Z}\},$$

where a set V_i is shown in Fig. 3.10b.

Now, one picks five real numbers $\gamma_i \in \mathbb{R}$, and translates the sets of lines with $\mathbf{e}_i\gamma_i$. The numbers γ_i must satisfy the requirement that not more than two lines intersect at each intersection of lines. Each choice of γ_i that satisfies this requirement is called a Penrose tiling, and there are uncountably many. Such a set of lines is depicted in Fig. 3.11a.

It is a curious fact of Penrose tilings that they are made up of ribbons, as shown in Fig. 3.11b. De Bruijn showed [3] each ribbon is in one-to-one correspondence with a line in the pentagrid. This can be understood in the following way. Consider the two highlighted lines in Fig. 3.11a

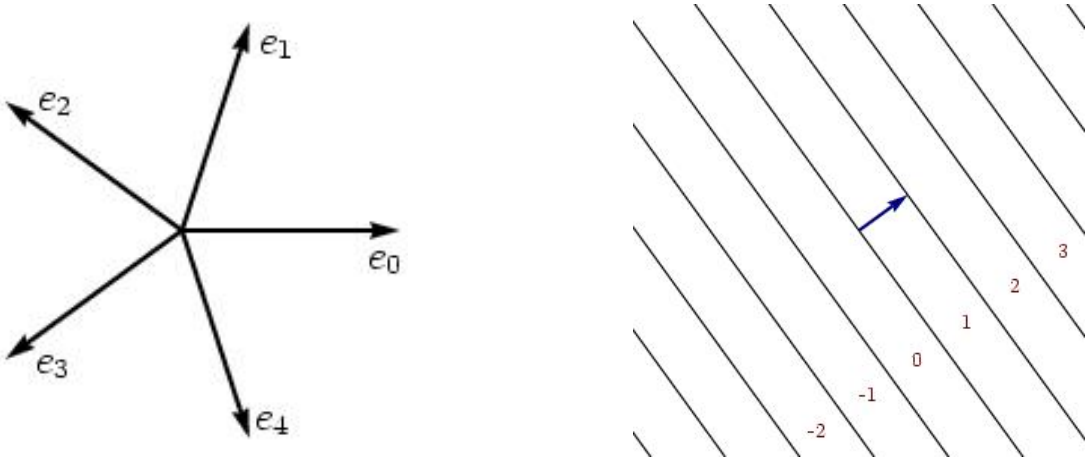

(a) The unit vectors $\mathbf{e}_i$.

(b) Set of lines V_i.

Figure 3.10.: Unit vectors and their parallel lines (figures from Ref. [43]).

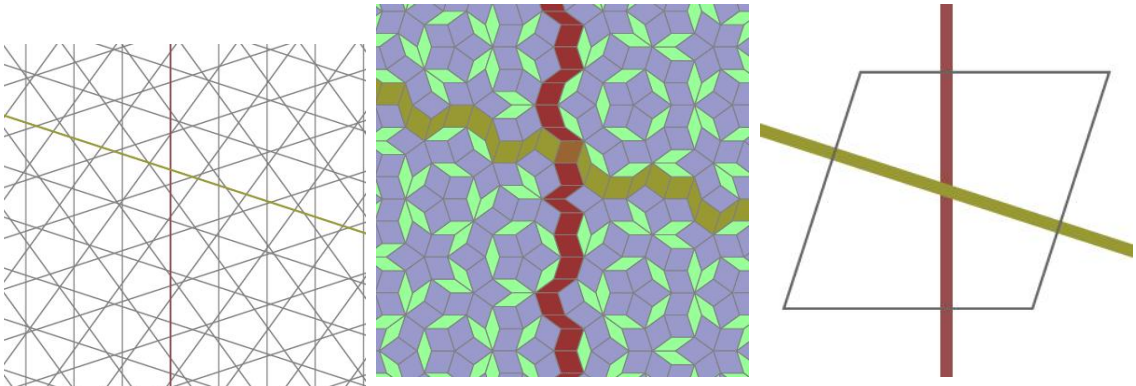

(a) A pentagrid.

(b) A Penrose tiling with two highlighted ribbons.

(c) A tile constructed at the intersection of two pentagrid lines.

Figure 3.11.: A pentagrid with the corresponding Penrose tiling, where the highlighted lines in the pentagrid correspond to the highlighted ribbons (figures from Ref. [43]).

that intersect. One can then construct a tile at this intersection as in Fig. 3.11c, by drawing lines perpendicular to the pentagrid lines. Using this construction of a tile, one can determine the sequence of tiles along any ribbon in the Penrose tiling.

Now it is clear why the pentagrid is useful for generating an arbitrary patch of a Penrose tiling, since one simply studies the type of intersection between pentagrid lines to decide what the next tile in a ribbon should be. Additionally, to see why the Penrose tiling must be non-periodic, we show that the ratio of thick and thin rhombs converges to the golden ratio. Take an arbitrary line in the pentagrid, then the interval between intersections with another pentagrid line defining a thick rhomb is $\sin 72$ and for a thin rhomb $\sin 36$. Therefore, the ratio of thick and thin rhombs is

$$\frac{\#\text{ thin rhombs}}{\#\text{ thick rhombs}} = \frac{1/\sin 36}{1/\sin 72} = \frac{1+\sqrt{5}}{2},$$

which is precisely the golden ratio. If the Penrose tiling were periodic, this fraction would be rational, from which we can conclude the Penrose tiling is non-periodic. Note, however, that the converse implication is not necessarily true: there exists non-periodic tilings with a rational ratio between the type of tiles. An example is the Thue-Morse word, which has exactly the same amount

of zeros and ones.

3.3. Fractality

As previously discussed, quasicrystals often display scaling symmetry in their diffraction pattern. This symmetry is inherited from the self-similarity of the quasicrystalline lattice in real space. In this section, a quick introduction to self-similarity, fractality, and multifractality is given. The Cantor set will be the guiding example.

3.3.1. Cantor Set

We do not really need measures right now, but it is useful to start working in their language from now on. Measures will prove to be a useful way to define a function on a set. Functions $f : A \to B$ assign an element $b \in B$ to some $a \in A$; *measures* assign a value in $[0, \infty]$ to subsets of A.

To make this more precise, we first define the σ-algebra of sets on which a measure is defined.

Definition 3.17. *(σ-algebra) A σ-algebra $\mathcal{A}$ on a set X is a family of subsets of X with the following properties*

$$X \in \mathcal{A},$$
$$A \in \mathcal{A} \Rightarrow A^c \in \mathcal{A},$$
$$(A_i)_{i\in\mathbb{N}} \subset \mathcal{A} \Rightarrow \bigcup_{i\in\mathbb{N}} A_i \in \mathcal{A}.$$

The formal definition of a measure reads as follows.

Definition 3.18. *(Measure) A measure μ on X is a map $\mu : \mathcal{A} \to [0, \infty]$, defined a σ-algebra $\mathcal{A}$, which satisfies*

$$\mu(\emptyset) = 0,$$

and, for a countable family of disjoint sets $(A_i)_{i\in\mathbb{N}} \subset \mathcal{A}$,

$$\mu\left(\bigcup_{i\in\mathbb{N}} A_i\right) = \sum_{i\in\mathbb{N}} \mu(A_i).$$

Moreover, μ is called a probability measure if $\mu(X) = 1$.

For theoretical details on measures, see Ref. [44]. The most intuitive σ-algebra is the *Borel σ-algebra*, which is obtained by taking the smallest σ-algebra containing the open sets in $\mathbb{R}^n$. Correspondingly, the most natural measure on the real numbers is the Lebesgue measure λ. For an interval $[a, b)$, $\lambda([a, b)) = b - a$.

The *Cantor Set* $\mathcal{C} = \lim_{n\to\infty} C_n$ is constructed by starting with $C_0 = [0, 1]$. Each subsequent set C_n is obtained by cutting out the middle third of each interval in C_{n-1}, see Fig. 3.12a. This is the same as scaling C_{n-1} by $1/3$ and appending a copy of that shifted by $2/3$, i.e.

$$C_n = \frac{C_{n-1}}{3} \cup \left(\frac{2}{3} + \frac{C_{n-1}}{3}\right). \tag{3.21}$$

Like this, C_n will consist of 2^n intervals of Lebesgue measure 3^{-n}. Thus, the measure of the Cantor set $\lambda(\mathcal{C}) = \inf_n \lambda(C_n) = \lim_{n\to\infty} \lambda(C_n) = 0$. In this sense, the Cantor set has *measure zero*. This might strike the reader as obvious, since the Lebesgue measure of a point is zero. It turns out that $\mathcal{C}$ has the same cardinality as $\mathbb{R}$, i.e. the continuum $\mathfrak{c}$.

The Cantor set $\mathcal{C}$ has other remarkable properties. Firstly it is a closed set. It can be seen from Eq. 3.21 that every C_n is closed, and $\mathcal{C} = \cap_n C_n$ is the intersection of closed sets, hence closed.

Secondly, $\mathcal{C}$ *contains no isolated points*, i.e. for all $x \in \mathcal{C}, \epsilon > 0$, there is some $y \in \mathcal{C}$ such that $|x - y| < \epsilon$. By realising that the endpoints of C_0 in fact never get removed, pick n such that $1/3^n < \epsilon$ and one of the 2^{n+1} endpoints will lie within ϵ from x. Finally, since $\mathcal{C}$ cannot contain any open interval, its interior is empty. From this, we can conclude that $\overline{\mathcal{C}} = \mathcal{C}$ has empty interior, hence is *nowhere dense*. Another type of Cantor set, the Smith-Volterra-Cantor set $\mathcal{S}$ in Fig. 3.12b

(a) Ternary Cantor set. (b) Smith-Volterra-Cantor set.

Figure 3.12.: Two different Cantor sets (figures from Wikipedia).

is generated from $S_0 = [0, 1]$ by removing the middle 1/4th of each interval. This set seems to be the same as $\mathcal{C}$, but if we compute the removed amount, we see that every step removes 2^n times an interval of width $1/4^{n+1}$, which sums to

$$\sum_{n=0}^{\infty} \frac{2^n}{2^{2n+2}} = \frac{1}{4} \sum_{n=0}^{\infty} \frac{1}{2^n} = \frac{1}{2},$$

i.e. the Cantor set $\mathcal{S}$ has Lebesgue measure $\lambda(\mathcal{S}) = 1/2$. Yet the same arguments as above can be applied to show that $\mathcal{S}$ is closed, nowhere dense and contains no isolated points. Since we can interpret the Lebesgue measure as a 1D volume, the set $\mathcal{S}$ has nonzero volume, yet empty interior, hence it must have a boundary with nonzero volume. This shows how bizarre sets in a space as simple as $\mathbb{R}$ can be. Therefore measures are the right tool to analyse functions on them.

3.3.2. Fractals

There is no universal definition of what constitutes a fractal. However, one can point to two properties that set aside fractals from regular geometric objects: *self-similarity* and its anomalous *dimension*. Self-similarity demands that an object, when scaled by a certain factor, looks the same as (a part of) the original version. An anomalous dimensions occur naturally in the boundary of fractal sets. Usually, one thinks of a boundary of a set in 2D to be a line, i.e. a 1D object. However, many boundaries of fractals have dimension greater than 1. A notorious example is the boundary of the Mandelbrot set, which has dimension 2. This explains why defining a fractal by a non-integer dimension is inadequate.

The dimension of a fractal is most intuitively described via "box-counting". If we would cover a compact, open set of $\mathbb{R}^n$ (e.g. a ball or cube) with hypercubes with sides l, the amount of cubes needed would scale as l^{-n}. From this, we can read off that the dimension of the space is n. The amount of boxes to cover a line in $\mathbb{R}^n$ scales as $1/l$, so the dimension of a line is $d = 1$. Generally

$$D_{\text{box}} = \lim_{l \downarrow 0} \frac{\log \#\text{boxes of size } l}{\log 1/l}. \tag{3.22}$$

This formula becomes even simpler when the object is self-similar [45]. If one scales the object by a factor S and N copies of the fractal of original size emerge, the *Hausdorff dimension* is

$$D_{\text{hd}} = \frac{\log N}{\log S}. \tag{3.23}$$

Eq. 3.23 is only a special case of the Hausdorff dimension, which can be defined for any subset $S \subset X$ of a metric space (X, d), where d is a metric. For any $U \subset X$, define its *diameter* as $\text{diam}(U) = \sup\{d(x, y \mid x, y \in U)\}$, where $\text{diam}(\emptyset) = 0$ is taken. Suppose we want to study some

set $S \subset X$, take any $\delta > 0$ and define the *Hausdorff* measure

$$H_\delta^D(S) := \inf\left\{\sum_{i\in I}(\mathrm{diam}(U_i))^D \mid (U_i)_{i\in I} \text{ countable cover of } S, \mathrm{diam}(U_i) < \delta\right\},$$

$$H^D(S) = \lim_{\delta\downarrow 0} H_\delta^D(S).$$

Intuitively, the Hausdorff measure raises the characteristic length of covering sets to some power D, and sums the result. Depending on D, this can be length, area, volume, etc. As $\delta \downarrow 0$, a small value of D causes the measure to diverge, and if D is very large, the measure converges to zero. The *Hausdorff dimension* is then defined as

$$D_{\mathrm{hd}}(S) := \inf\{D \in \mathbb{R} \mid H^D(S) = 0\},$$

which takes the form of Eq. 3.23 for self-similar sets [46]. The idea of taking a real-valued dimension, determined by the scaling behaviour of increasingly smaller sets that cover S, is the same as the box-counting dimension. In fact, in many cases $D_{\mathrm{box}}(S) = D_{\mathrm{hd}}(S)$ holds. It is the mathematical construction of the Hausdorff dimension that results in more favourable and consistent results when $D_{\mathrm{box}}(S) \neq D_{\mathrm{hd}}(S)$. For all strange sets that we study in this thesis, the box-counting dimension does coincide with the Hausdorff dimension, so we need not explore the differences.

We will show that the Cantor set is a fractal in the sense that it is self-similar and has an anomalous dimension. By inserting the Cantor set $\mathcal{C}$ into Eq. 3.21 we see that $\mathcal{C}$ is equal to two copies of itself scaled by $1/3$, which shown self-similarity. So if we scale $\mathcal{C}$ by a factor of 3, we obtain two copies of $\mathcal{C}$, hence by Eq. 3.23 $D_{\mathrm{hd}} = \frac{\log 2}{\log 3}$. If we count intervals of length l required to cover $\mathcal{C}$, one needs 2^n intervals of length $l = 1/3^n$ to cover $\mathcal{C}$, so by Eq. 3.22 $D_{\mathrm{box}} = \lim_{l\downarrow 0} \frac{\log 2^n}{\log 3^n} = D_{\mathrm{hd}}$. Note $0 < D_{\mathrm{hd}} < 1$, which shows the anomalous dimension of $\mathcal{C}$.

3.3.3. Multifractals

The Cantor set $\mathcal{C}$ is a *monofractal*, a fractal with only one dimension dictated by Eq. 3.21 that is locally the same for every point in $\mathcal{C}$. It turns out that most interesting fractal objects contain more than one fractal dimension, arising from different local scaling behaviour throughout the fractal. The notion of local scaling, instead of global scaling like in Eq. 3.23, will be made precise in this section.

Following the work by Halsey, Jensen, and Kadanoff [47] we want to define a measure μ on a set $\mathcal{S}$ such that $\mu(\mathcal{S}) = 1$. Assuming $\mathcal{S} \subset \mathbb{R}^n$ bounded, we can cover it with finitely many hypercubes K_i with sides l. Define μ such that if we pick a random point in $x \in \mathcal{S}$, the probability that it lies in K_i is $\mu(K_i)$. We call it the *mass* of K_i and it can have multiple interpretations. Now, we vary l and study the scaling behaviour

$$\mu(K_i) \propto l^\alpha.$$

The defining feature of *multifractals*, as opposed to monofractals, is that $\alpha = \alpha(x)$, i.e. the scaling behaviour varies locally instead of being a global constant. If $\mathcal{S}$ is covered by boxes of with sides l, one can count the amount of boxes where $\alpha \in [\alpha', \alpha' + \delta)$, denoted by $N(\alpha', l, \delta)$ where $\delta << 1$. The ansatz by Halsey et al. [47] is that this amount can be written as

$$N(\alpha', l, \delta) \propto l^{-f(\alpha')}\delta.$$

The function $f(\alpha)$ is the *dimension* of the set of points that locally scale as α. To see $f(\alpha)$ is indeed a dimension, compare this with the density of hypercubes $\rho(l) = l^{-n}$, where n is clearly the dimension. To summarise, α and $f(\alpha)$ describe a multifractal object in the following sense:

- $\alpha = \alpha(x)$ is the local scaling behaviour of a point $x \in \mathcal{S}$,

- $f(\alpha)$ is the fractal dimension of the subset $\mathcal{S}_\alpha \subset \mathcal{S}$ that scales as α.

Hentschel et al. [48] showed that there is an infinite number of dimensions D_q that characterise a set

$$D_q = \lim_{l \downarrow 0} \frac{1}{q-1} \frac{\log \sum_i \mu(K_i)^q}{\log l}. \tag{3.24}$$

Note that for $q = 0$, we precisely obtain Eq. 3.22. Evaluating Eq. 3.24 is generally cumbersome, so Halsey et al. [47] developed the following method. Let $S_1, \ldots, S_N$ partition $\mathcal{S}$ and each S_i be contained in a ball of radius $l_i < l$. Then, the partition function

$$\Gamma(q, \tau, \{S_i\}, l) = \sum_{i=1}^{N} \frac{\mu(S_i)^q}{l^\tau} \tag{3.25}$$

as $l \downarrow 0$ neither goes to zero nor infinity, also commonly referred to as Γ being "of order unity", if precisely $\tau = (q-1)D_q$ holds. We note that $\alpha, f(\alpha)$ and $q, \tau(q)$ are thermodynamically conjugate and hence related by a Legendre transform. The relations read [47]:

$$\alpha(q) = \frac{\mathrm{d}}{\mathrm{d}q}\tau(q),$$
$$f(\alpha(q)) = q\alpha(q) - \tau.$$

Let us apply the formalism from this section to the ternary Cantor set. We can cover C_n with 2^n intervals $K_i^{(n)}$ of width $l_n = 3^{-n}$, so $\mu(K_i^{(n)}) = 2^{-n}$. Since all these intervals are identical, we can conclude for any $x \in \mathcal{C}$ that $\alpha(x) = \alpha$. This means that the local scaling is uniform, with α determined by

$$\mu(K_i^{(n)}) = 2^{-n} = \left(3^{-n}\right)^\alpha \quad \Rightarrow \quad \alpha = \frac{\log 2}{\log 3},$$

which coincides with the box-counting and Hausdorff dimension of $\mathcal{C}$. One of the easiest examples of a multifractal is the two-scale Cantor set [47]. For example, start with $T_0 = [0, 1]$ and remove the second 1/4th interval. In general

$$T_n = \frac{1}{4}T_{n-1} \cup \left(\frac{1}{2} + \frac{1}{2}T_{n-1}\right), \qquad T_0 = [0, 1].$$

The resulting two-scale cantor set is $\mathcal{T} = \cap_n T_n$, see Fig. 3.13. It is clear from the recursive relation

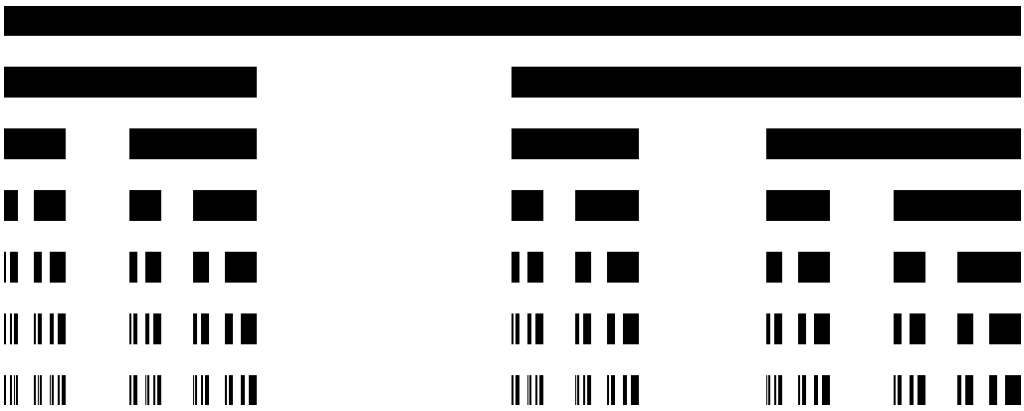

Figure 3.13.: The two-scale Cantor set $\mathcal{T}$ (figure from Wikipedia).

that $0, 1 \in \mathcal{T}$. To compute $\alpha(0)$, cover T_n in intervals of $l_n = 4^{-n}$. Using $\lambda(T_n) = (3/4)^n$, we have for the interval $K_1^{(n)}$ containing $x = 0$ that

$$\mu(K_1^{(n)}) = \frac{l_n}{\mu(T_n)} = \frac{4^{-n}}{(3/4)^n} = 3^{-n} = l_n^{\alpha(0)} \quad \Rightarrow \quad \alpha(0) = \frac{\log 3}{\log 4} \approx 0.79.$$

Similarly, around $x = 1$ let $l_n = 2^{-n}$ such that

$$\mu(K_{2^n}^{(n)}) = \frac{l_n}{\mu(T_n)} = \frac{2^{-n}}{(3/4)^n} = l_n^{\alpha(1)} \quad \Rightarrow \quad \alpha(1) = \frac{\log 3/2}{\log 2} \approx 0.58,$$

which shows that indeed in $\mathcal{T}$, the local scaling is not homogeneous, i.e. it is a multifractal.

Ultimately, one is interested in the multifractal dimension D_q. Suppose our set of interest is partitioned like in Eq. 3.25. We decimate the scale $l \to l^2$. If our set is constructed by repeatedly taking the union of scaled and shifted versions of itself, like the Cantor sets, the partition function for l^2 becomes

$$\Gamma(q, \tau, l^2) = \sum_{i=1}^{N} \sum_{j=1}^{N} \frac{[\mu(S_i)\mu(S_j)]^q}{(l_i l_j)^\tau} = [\Gamma(q, \tau, l)]^2.$$

For Γ to be of order unity as $l \downarrow 0$, it is evident that $\Gamma(q, \tau(q), l) = 1$ must hold for any l. Now, it is easy to determine D_q for the ternary Cantor set:

$$\Gamma(q, \tau, 1/3) = 2\frac{(1/2)^q}{(1/3)^\tau} = 1 \quad \Rightarrow \quad \tau = (q-1)\frac{\log 2}{\log 3} \quad \Longleftrightarrow \quad D_q = \frac{\log 2}{\log 3} \;\; \forall q,$$

which is equal to the exponent α for $\mathcal{C}$. For the two-scale Cantor set, we have for $N = 2$ the following details: $S_1 = [0, 1/4], S_2 = [1/2, 1], \mu(S_1) = 1/3, \mu(S_2) = 2/3$ so

$$\Gamma(q, \tau, 1/2) = \frac{(1/3)^q}{(1/4)^\tau} + \frac{(2/3)^q}{(1/2)^\tau} = 1.$$

At $q = 0$, the above holds for $\tau = -\frac{\log\left(\sqrt{5}-1\right)/2}{\log 2}$ so $D_0 = \log\phi/\log 2 \approx 0.694$. However, D_q varies with q, so the two-scale Cantor set is clearly a multifractal.

Numerical Approximations of the Multifractal Dimensions

In this section, the method from Refs. [49,50] for numerically computing the multifractal dimension Eq. 3.24 is explained. Throughout this section, denote $S = \{s_i \mid i = 1, \ldots, N\} \subset \mathbb{R}^n$ as the set of N points in n dimensions, for which one wants to evaluate Eq. 3.24. Each point can be written in the canonical basis as $s_i = \sum_{\delta=1}^{n} s_i^\delta e_\delta$, where $s_i^\delta \in \mathbb{R}$. The steps of the algorithm are as follows.

1. Compute the largest scale using the infinity norm

$$E_{\max} = \max_{i,j} \|s_i - s_j\|_\infty := \max_{i,j,\delta} |s_i^\delta - s_j^\delta|.$$

2. Map the set S into the n-dimensional hypercube by the affine transformation

$$s_i \to \tilde{s}_i = \frac{s_i}{E_{\max} + \epsilon},$$

   where ϵ is a small number such that $|s_i| < 1$ is always true within machine precision.

3. Compute the smallest scale of the scaled set S'

$$E_{\min} = \min_{i \neq j} \|\tilde{s}_i - \tilde{s}_j\|_2 := \min_{i \neq j} \sqrt{\sum_{\delta=1}^{n} (\tilde{s}_i^\delta - \tilde{s}_j^\delta)^2}.$$

   Note that now the Euclidean norm is used instead of the infinity norm.

4. Construct a set of M rational decompositions of the unit cube, which decreases exponentially in size. To this end, define

$$k_m := \lfloor E_{\min}^{-m/M} \rfloor, \qquad m = 0, 1, \ldots, M,$$

where each integer m labels a decomposition of the unit cube in boxes with length $E_m = 1/k_m$, which are roughly linearly spaced on a logarithmic scale. Furthermore, label the boxes K_ν that partition the hypercube in the mth generation by an integer $\nu = 1, \ldots, N(E_m)$, where $N(E_m) = k_m^n$ is the total amount of boxes.

5. For each m, compute the fraction of points from S that lie in each box

$$p_\nu(E_m) = \frac{|\{x \in \tilde{S} \mid x \in K_\nu\}|}{|S|},$$

and compute the "partition function"

$$Z_m(q) = \sum_{\nu=1}^{N(E_m)} [p_\nu(E_m)]^q,$$

for a desired range of values $q \in \mathbb{R}$.

6. For each value of q, define the dataset

$$\{(x_m, y_m) = (\ln E_m, \ln Z_m(q)/[q-1]) \mid m = 0, 1, \ldots, M\},$$

and use simple linear regression to fit the relation $y_m = a_q x_m$, where the parameter $a_q = D_q$ approximates the multifractal dimension.

Using the numerical recipe above, one obtains a reasonable approximation for the multifractal dimension, provided $q \geq 0$. For $q < 0$, the numerical method is shown to be unstable [50]. Additionally, the numerical method has no rigorously proven guarantees on convergence. Therefore, this method is appropriate for qualitative exploration of multifractal properties, which is satisfactory for the research in this thesis. For more quantitative investigation, one should explore more rigorous methods.

3.4. L-Systems

Yet another mathematical formalism to generate aperiodic, and most of the time fractal structures, is the Lindenmayer system, or L-system for short. It was introduced in 1968 by the Hungarian plant biologist Aristid Lindenmayer [51], who was working at Utrecht University at the time. Lindenmayer developed the framework to model the growth process of fungi and bacterial colonies. The key assumption is that the behaviour of cells, which multiply by growth and division, can be described by a *formal grammar*, which is a well-defined mathematical notion. See the book by Rozenberg and Salomaa [52] for the mathematical theory of L-systems.

Let us first give the definition of an L-system, and discuss applications later. Similar to symbolic dynamics, we start with a finite alphabet $\mathcal{A}$. This alphabet now consists of two types of symbols:

- *variables*: symbols that can be replaced by production rules,
- *constants*: symbols that cannot be replaced.

Now there is a set ρ of *production rules*, which describe how variables are replaced by some finite string of symbols from $\mathcal{A}$. Finally, there is an *axiom* $\omega \in \mathcal{A}^*$, where $\mathcal{A}^*$ denotes the set of finite words with symbols in $\mathcal{A}$. The mathematical definition of an L-system reads:

Definition 3.19. *(L-System) An L-system is defined as the triple*

$$L = (\mathcal{A}, \omega, \rho),$$

where $\mathcal{A}$ is a finite alphabet, $\omega \in \mathcal{A}^*$ the axiom, i.e. the starting block of the production rule, and $\rho : \mathcal{A} \to \mathcal{A}^*$ the set of production rules. A symbol $s \in \mathcal{A}$ is a constant if $\rho(s) = s$, else it is a variable.

One can immediately see the similarity with the substitution rules as defined in Section 3.1.1. The existence of an axiom is formally the only difference between the L-system and a substitution rule. In practice however, substitution rules often do not have constants in the sense of L-systems. Now, we will discuss applications of L-systems.

3.4.1. Algae

The starting point for Lindenmayer to model algae growth, perhaps based on Fibonacci's rabbit sequence (see Section 3.1.3), is the L-system with the following motivation. Suppose there exist adult algae (A) and child algae (B). Every generation, adult algae produce a child and child algae grow up to become adults. Suppose the first generation consists of one child. This amounts to the L-system

$$L_{\text{algae}} = (\mathcal{A}, \omega, \rho) = (\{A, B\}, B, \{A \to AB, B \to A\}).$$

Note that there are no constants, and the above L-system generates

$$B \to A \to AB \to ABA \to ABAAB \to ABAABABA \to \cdots,$$

which is exactly the Fibonacci substitution from Section 3.1.3. In fact, the Fibonacci, Thue-Morse and Tribonacci sequences are defined as substitution rules with an axiom, which makes them all equivalent to an L-system.

3.4.2. Cantor Set

To generate the Cantor set, take

$$L_{\text{cantor}} = (\{A, B\}, A, \{A \to ABA, B \to BBB\}).$$

If the axiom is called the 0th generation, then for subsequent generations

$$A \to ABA \to ABABBBABA \to ABABBBABABBBBBBBBBABABBBABA, \cdots$$

If A means "draw a line of length l_n" and B "move l_n forward without drawing", where $l_n = 3^{-n}$, the L-system above precisely generates the ternary Cantor set in Fig. 3.12a. If n is the amount of times that the production rules are applied, then the segments A correspond to the black lines in Fig. 3.12a, and B to the blank spaces in the same figure.

3.4.3. Sierpinski Triangle

Now we come to the first example of an L-system that uses constants. Consider the L-system given by

$$L_{\text{sierpinski}} = (\{F, G, +, -\}, F - G - G, \{F \to F - G + F + G - F, G \to GG\})$$

The interpretation of the symbols is as follows.

- F or G: draw one unit forward,
- $\pm$: turn counterclockwise by $\pm 120°$ ($2\pi/3$ radians).

Using this interpretation, the axiom $F-G-G$ is a simple triangle, which is the $n=0$ generation. The difference between F and G is the following: sides G simply double in length in the next generation, whereas the side F fills the triangle with a smaller one, see Fig. 3.14a. Subsequent even generations are depicted in Fig. 3.14b.

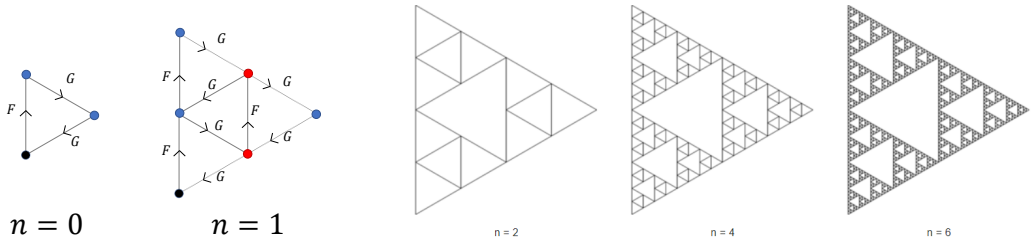

(a) Generation 0 and 1.

(b) Generations $n = 2, 4, 6$.

Figure 3.14.: The L-system for the Sierpinski triangle. In a), the black dot is the starting point, red (blue) dots denote + (-), and the dotted lines in $n = 1$ denote the result of ρ on the elements G in $n = 0$.

3.4.4. Fractal Plants

Arguable the most beautiful use of L-systems is the generation of fractal, plant-like structures. We first show in detail how a plant structure is generated in the fractal binary tree, and then show a few complicated structures without discussing its L-system.

Consider the L-system given by

$$L_{\text{tree}} = (\{0, 1, [,]\}, 0, \{0 \to 1[0]0, 1 \to 11\}).$$

It is clear that [and] are the constants. The interpretation of symbols reads:

- 0: draw a leaf (endpoint of a tree),
- 1: draw a line segment,
- [: save current position and angle, and turn left by 45°,
-]: restore position and angle associated to the corresponding [bracket, and turn right by 45°.

In the language of abstract data types, the brackets [,] define a push and pop operation, respectively, on a last-in-first-out data stack. The the axiom and first four generations of the fractal tree are depicted in Fig. 3.15.

For generating more complicated fractal plant-like structures (see Fig. 3.16), the mechanism of constant symbols that read/write locations and angles turns out to be an essential tool [52].

Finally, we would like to point out that fractal plant-like structured can be generated by other means. Examples of those are the Barnsley Fern and the Pythagoras tree. Those are examples of an *iterated function system*. These are not necessarily related to L-systems, they rather give another perspective on generating self-similar structures.

3.5. The Fibonacci Chain

In this section, we will introduce our first quantum mechanical model, the Fibonacci Chain (FC). We will study the single-particle states for aperiodic 1D tight-binding models.

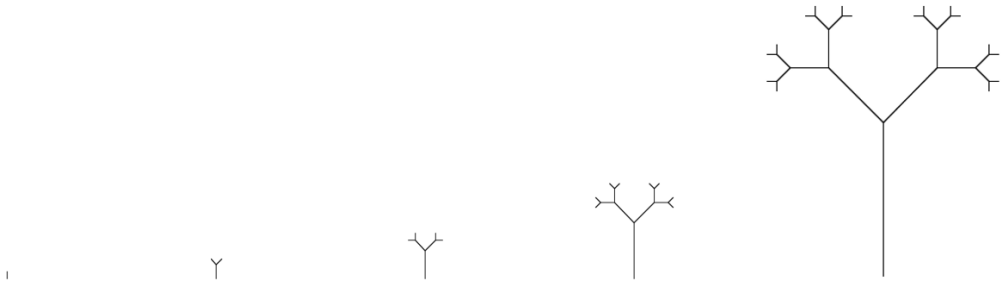

Figure 3.15.: Axiom and first four generations of the binary tree (figures from Wikipedia).

Figure 3.16.: Fractal plants (figure from Ref. [53]).

3.5.1. Finite Fibonacci Chain

The system is defined by the tight-binding Hamiltonian

$$H = \sum_{n=1}^{F_N} t_n \big(|n\rangle \langle n+1| + |n+1\rangle \langle n| \big), \qquad t_n = \begin{cases} t_w & \text{if } (f_N)_n = 0, \\ t_s & \text{if } (f_N)_n = 1, \end{cases}$$

with the couplings t_n determined by the Fibonacci word f_N, where $|f_N| = F_N$. Solving the time-independent Schrödinger equation

$$H |\psi\rangle = E |\psi\rangle \tag{3.26}$$

boils down to a linear algebra problem once a basis is chosen. For example if $N = 4$, we have $f_4 = 01001$. When writing the state $|\psi\rangle = \sum_{n=1}^{F_N} \psi_n |n\rangle$ in the position basis $\{|n\rangle\}_n$, the Hamiltonian

H becomes the matrix

$$H_{\mathrm{PBC}} = \begin{bmatrix} 0 & t_1 & 0 & 0 & t_5 \\ t_1 & 0 & t_2 & 0 & 0 \\ 0 & t_2 & 0 & t_3 & 0 \\ 0 & 0 & t_3 & 0 & t_4 \\ t_5 & 0 & 0 & t_4 & 0 \end{bmatrix}, \qquad H_{\mathrm{OBC}} = \begin{bmatrix} 0 & t_1 & 0 & 0 & 0 \\ t_1 & 0 & t_2 & 0 & 0 \\ 0 & t_2 & 0 & t_3 & 0 \\ 0 & 0 & t_3 & 0 & t_4 \\ 0 & 0 & 0 & t_4 & 0 \end{bmatrix},$$

where we treat both periodic BCs (PBC) and open BCs (OBC). Solving Eq. 3.26 is a problem of finding the eigenvalues and eigenvectors of the matrices above. Alternatively, one can write Eq. 3.26 as the discretised version

$$(H\psi)_n = t_{n-1}\psi_{n-1} + t_n\psi_{n+1}, \qquad n = 1, \ldots, F_N, \tag{3.27}$$

where the basis $\{|n\rangle\}_n$ is assumed. Since the Hamiltonians above correspond to a finite open and closed chain, the spectrum consists of finitely many points. This is fine for studying edge-state wavefunctions, but to study the gap structure of the energy spectrum we need to study the infinite Fibonacci chain.

3.5.2. Infinite Fibonacci Chain

If we consider the bi-infinite Fibonacci word $f^{(\mathrm{bi})}$, then the bi-infinite 1D quantum chain has Hamiltonian

$$(H\psi)_n = t_{n-1}\psi_{n-1} + t_n\psi_{n+1}, \qquad n \in \mathbb{Z}, \qquad t_n = \begin{cases} t_w & \text{if } (f^{(\mathrm{bi})})_n = 0, \\ t_s & \text{if } (f^{(\mathrm{bi})})_n = 1, \end{cases} \qquad \forall n \in \mathbb{Z}.$$

The discretised Schrödinger equation will read

$$(H\psi)_n = E\psi_n, \qquad \forall n \in \mathbb{Z}, \tag{3.28}$$

where H is an operator on $\psi \in l^2(\mathbb{Z}) := \{x \in \mathbb{C}^{\mathbb{Z}} \mid \|x\|_2^2 = \sum_{x\in\mathbb{Z}} |x(n)|^2 < \infty\}$, i.e. all square-summable bi-infinite complex sequences. Often, the bi-infinite chain is approximated by f_N as a periodic crystal with f_N defining the couplings in the unit cell. Whereas the finite chain yielded a discrete spectrum with F_N points, we now obtain a spectrum of F_N separated energy bands upon applying Bloch's theorem [1].

Let us briefly explain how Bloch's theorem is applied to periodic tight-binding chains. Let us label each unit cell containing L sites with an integer $n \in \mathbb{Z}$. The situation for $L = 3$ is depicted in Fig. 3.17. One way to label a site $|m\rangle$ in the chain is by the tensor product $|m\rangle = |n\rangle \otimes |r\rangle$. The expression for a general tight-binding Hamiltonian with zero on-site energies then reads

$$H = -\sum_{n\in\mathbb{Z}} \left(t_0 \,|n-1\rangle\,|L-1\rangle\,\langle n|\,\langle 0| + |n\rangle\,\langle n| \sum_{r=1}^{L-1} t_r \,|r-1\rangle\,\langle r| \right) + H.c., \tag{3.29}$$

where $H.c.$ stands for Hermitian conjugate of the whole expression. Since the Hamiltonian is periodic in n, one uses the FT

$$|n\rangle = \int_{-\pi}^{\pi} \frac{e^{ikn}}{\sqrt{2\pi}} |k\rangle \, \mathrm{d}k, \qquad |k\rangle = \sum_{n\in\mathbb{Z}} \frac{e^{-ikn}}{\sqrt{2\pi}} |n\rangle$$

to derive the identity

$$\sum_n |n - n_0\rangle\,\langle n| = \int_{-\pi}^{\pi} e^{-ikn_0} |k\rangle\,\langle k| \, \mathrm{d}k.$$

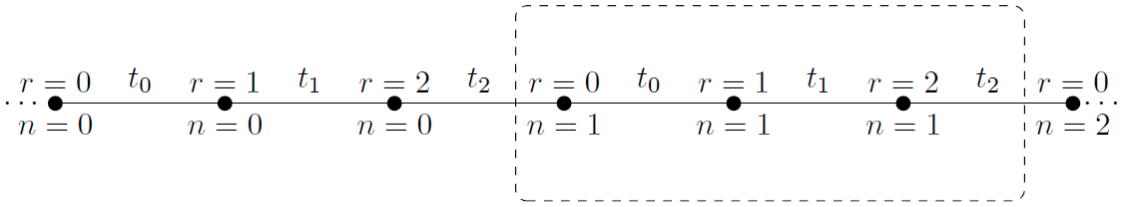

Figure 3.17.: Labeling of a periodic chain (figure from Ref. [54].)

The above identity is used to rewrite the Hamiltonian Eq. 3.29 as

$$H = -\int_{-\pi}^{\pi} |k\rangle \langle k| \left(t_0 e^{-ik} |L-1\rangle \langle 0| + \sum_{r=1}^{L-1} t_r |r-1\rangle \langle r| \right) \mathrm{d}k + H.c.,$$

which can be rewritten using $|\mathbf{r}\rangle = (|0\rangle, |1\rangle, \ldots, |L-1\rangle)^T$ as

$$H = -\int_{-\pi}^{\pi} |k\rangle |\mathbf{r}\rangle h(k) \langle \mathbf{r}| \langle k| \, \mathrm{d}k, \tag{3.30}$$

where $h(k)$ is an $L \times L$ matrix. From Eq. 3.30 we can read off that any eigenstate of H in momentum space has the form

$$|\psi_a\rangle = |u_{a,k}\rangle |k\rangle,$$

where $a = 1, \ldots, L$ labels the eigenstates $|u_{a,k}\rangle$ of $h(k)$ with eigenvalue (energy) $E_a(k)$. Depending on H, the energy bands $E_a(k)$ can have the same values for different values of a and/or k. The study of $E_a(k)$ is commonly referred to as *band theory*, and is one of the earliest triumphs of theoretical condensed matter physics.

3.5.3. Spectrum

Bellissard et al. [55] showed that all Hamiltonians on $l^2(\mathbb{Z})$ of the form

$$(H\psi)_n = \psi_{n+1} + \psi_{n-1} + \lambda v(n)\psi_n \tag{3.31}$$

where $v(n)$ is a Sturmian potential $v(n) = \chi_{[1-\alpha,1)}(x + n\alpha \mod 1)$ have a "Cantor set of zero Lebesgue measure" for $\lambda > 0, \alpha \notin \mathbb{Q}$. In this section, we will elaborate on what this precisely means and how this follows from the substitution rules Eq. 3.2. In particular, the spectrum of the Fibonacci chain will be shown to generally be a multifractal set.

What Bellissard et al. [55] mean by a Cantor set of Lebesgue measure zero is the following. The spectrum is a subset of $\mathbb{R}$ that contains no isolated points, is nowhere dense and has zero Lebesgue measure, just as the ternary Cantor set in Section 3.3.1. Note that the spectrum need not be the Cantor set, it simply shares the above three properties. Furthermore, a Cantor set can be mono- or multifractal, depending on the decimation rules.

To discuss the fractal properties of the spectrum of the Fibonacci chain, we will use the renormalisation scheme by Niu and Nori [19] (see Ref. [22] for more details on this scheme). The idea is to consider $\rho = t_w/t_s << 1$, in which limit one can approximate the Nth Fibonacci approximant Hamiltonian as

$$H_N = (zH_{N-2} - t_s) \oplus (\bar{z}H_{N-3}) \oplus (zH_{N-2} + t_s) + \mathcal{O}(\rho^4) \tag{3.32}$$

where $z = \rho/2$ and $\bar{z} = \rho^2$. For the Fibonacci chain approximants, we consider the infinitely extended crystal where each unit cell is the approximant, such that one has energy bands. The energy bands for $N = 0, 1$ are both single bands with widths $2t_s, 2t_w$, respectively, and for $N = 2$

there are two bands. All other spectra are unions of scaled and shifted versions of these according to Eq. 3.32. By the same equation, it is clear that different parts of the spectrum (left, middle or right) scale differently. This is analogous to the multifractal Cantor set in Section 3.3.3. One would only expect Eq. 3.32 to yield a monofractal if all parts of the spectrum scale with the same rate, i.e. $z^{1/2} = \bar{z}^{1/3}$ or equivalently $\rho = 1/8$. This turns out to be true only in the renormalisation regime [17]. Rüdinger and Piéchon [56] showed, using the trace map formalism, that the exact spectrum is never a monofractal. Finally, it is well-established that the hopping and on-site models like Eq. 3.31 of the Fibonacci chain are equivalent in the $n \to \infty$ limit [17]. We conclude that the spectrum of Eq. 3.28 is a nowhere dense set that contains no isolated points, has Lebesgue measure zero and is multifractal for any ρ.

For future purposes, we note that a renormalisation scheme as done by Niu and Nori [19] is not possible for any aperiodic chain. For example, Qin et al. [57] applied the idea by Niu and Nori of defining atoms and molecules to perform renormalisation for the Thue-Morse chain, but showed that it did not allow for an approximation such as Eq. 3.32 of the Hamiltonian. This was due to the fact that the atomic/molecular deflation rules did not yield a TM sequence again.

3.5.4. Gap-Labelling Theorem

Mace et al. [22] studied a systematic way of labeling the energy gaps of the Fibonacci chain spectrum, introduced by Bellissard [58]. This method concerns the *integrated density of states* IDOS(E), which is the fraction of energy states below some energy E. Mace showed that

$$\mathrm{IDOS}(E \in \mathrm{gap}) = \frac{n}{1+\alpha} \bmod 1,$$

where n is called the *gap label*. The derivation of the formula is simplified by using coprime approximants F_{N-1}/F_N to the Fibonacci slope $\alpha = 1/\phi$ and by the recursive structure Eq. 3.32 realising that each band has equal IDOS. The gap label $n \in \mathbb{Z}$ orders the gaps in the spectrum in decreasing width as $|n|$ increases.

4. Quasicrystals in Experiments

This chapter will motivate why quasicrystals are relevant to study in physics. Additionally, we give an overview of some experiments that realise quasicrystals.

4.1. Introduction: Relevance of Quasicrystals

Since the introduction function decomposition by Joseph Fourier in 1822 using sinusoidal functions for a heat problem, the ubiquitous Fourier transform (FT) has become a dominant tool in physics. For its implementation in physics, one requires translational invariance, or discrete periodicity. Therefore, the majority of tools developed in physics, being based on the FT, turned translationally invariant systems into the most widely studied class of systems. For condensed matter, this translates to regular crystals, where the cornerstone is Bloch's theorem, which in turn relies on the FT. Bloch's theorem tells us that electron wavefunctions are sine waves, i.e. they are *extended* throughout the system.

On the other hand, in totally disordered systems there is translational invariance too by isotropy. Here, the well-known mechanism of Anderson localisation tells us that the electron wavefunctions are *localised*, i.e. they are peaked at various locations but zero elsewhere.

Quasicrystals are neither translationally invariant nor disordered. The result is that the wavefunctions are *critical*, i.e. neither extended nor localised. This makes the quantum properties of quasicrystals interesting. Because they lack translational invariance, many computational tools are not available, and it is therefore difficult obtain analytic results for quasicrystals.

The remainder of this chapter introduces a few recent experiments that reproduced some signatures for quasicrystals that were predicted theoretically. One of the main challenges is that in an experiment, no system is truly infinite. It is therefore the question if theoretically predicted properties for infinite quasicrystals are still present if only a finite portion of the system is considered.

4.2. Photonic Quantum Simulator

The first physical model of a quasicrystal that we considered, the finite Fibonacci chain from Section 3.5.1, was realised in an experiment by Baboux et al. [59] in 2017. The setup is a photonic crystal, where the occupation of each site in the Fibonacci chain is modeled by the presence of a cavity polariton: a quantum of light-matter (photon-dipole) interaction where a photon polarises dielectric matter. Since the geometry of the system can be chosen to emulate a quantum chain, this is an example of a photonic quantum simulator, i.e. a system where the quantum properties of light injected into the material are exploited to emulate some quantum system.

Baboux et al. generate the Fibonacci word using the alternative method

$$\chi_j = \mathrm{sgn}[\cos(2\pi j\sigma^{-1} + \phi) - \cos(\pi\sigma^{-1})],$$

where $\sigma = (1+\sqrt{5})/2$ and ϕ is a degree of freedom called the *phason*. The Fibonacci quasicrystal is then constructed by letting the jth site be 0 if $\chi_j = 1$ and 1 else. The reason for choosing this construction of the Fibonacci chain is that once can continuously vary ϕ from 0 to 2π and arrive at the same system. The experimental setup for various values of ϕ is displayed in Fig. 4.1. Note

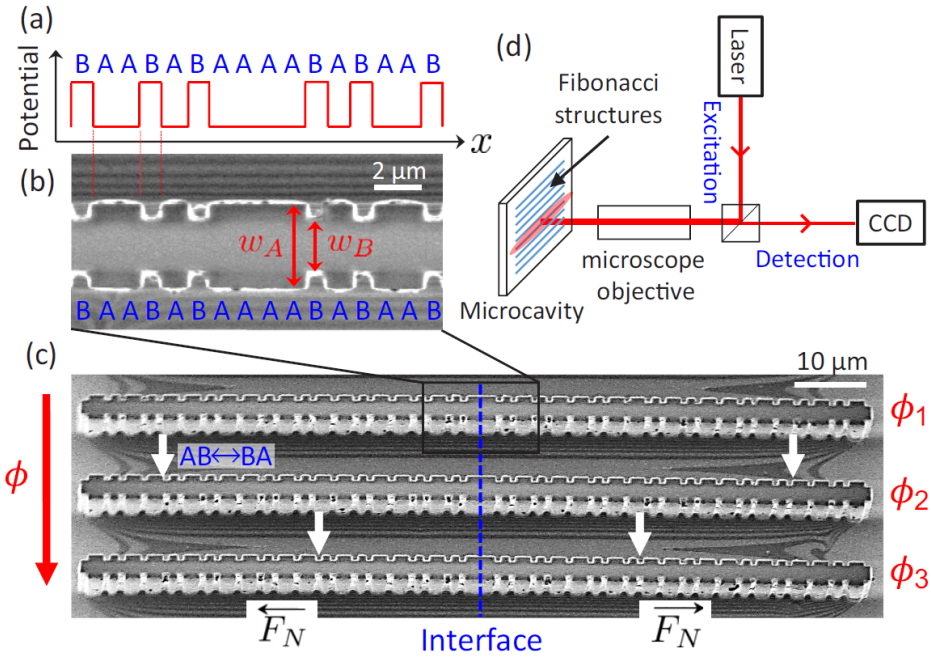

Figure 4.1.: The Fibonacci photonic quasicrystal (figure from Ref. [59]).

that the cavity polaritons implement the on-site model of the Fibonacci chain

$$(\hat{H}\psi)_n = t(\psi_{n-1} + \psi_{n+1}) + \epsilon_n \psi_n,$$

where now the hopping parameters t are constant and the on-site energy ϵ_n is either high or low according to the Fibonacci word (1 or 0 respectively).

The experiment measures gapped states and reveals their topological properties. To this end, the emitted radiation, displayed in Fig. 4.2a, is studied in both real and momentum space. From the

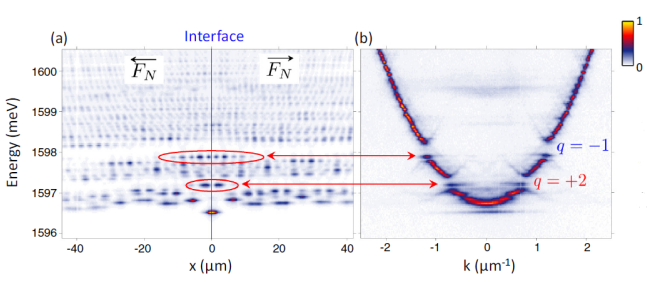

(a) Real space and Fourier spectrum.

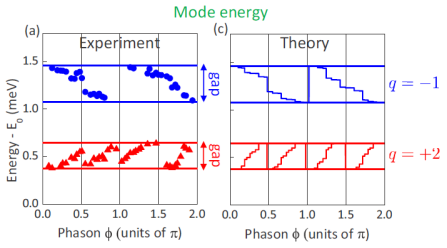

(b) Energy of the gapped modes $q = -1, 2$ as the phason varies.

Figure 4.2.: Experimental results (figures from Ref. [59]).

spectra in Fig. 4.2a, one can identify two gapped states. Baboux et al. [59] identify these states using the momentum space gap label $k = \frac{\pi}{a}(p + q\sigma^{-1})$, where q is argued to be the gap topological number. To each of these states $|\psi_q\rangle$ with $q = -1, 2$, an energy is associated by $\hat{H}|\psi_q\rangle = E_q|\psi_q\rangle$. As the phason ϕ is changed, this energy can vary and this is precisely what is measured and displayed in Fig. 4.2b, juxtaposed with the theoretical prediction. From Fig. 4.2b, one can count the amount of times that the energy "winds" around the gap and this corresponds precisely to the theoretical prediction of the winding number $\mathcal{W} = 2q$.

This experiment is an example of a quasicrystal realised in experiment where the wavefunctions, the spectrum and the topological properties of certain states can be studied. For an extensive review on the field of topological photonic materials see Ozawa et al. [60].

4.3. Ultracold Atom Quantum Simulator

Another widely used method of implementing quantum models are optical traps for ultracold atoms. Suppose a quantum system of either bosons or fermions is described by a potential $V(\mathbf{r})$. The idea of quantum simulation is to artificially create a potential landscape that reproduces $V(\mathbf{r})$, and load the appropriate quantum particles into the potential landscape. This section deals with optical lattices, i.e. the potential landscape is a field of light and the quantum particles are atoms which are ultracold such that their quantum behaviour dominates. For an extensive review on the field of cold atoms in optical lattices, see Bloch et al. [61]. We will focus on experimental realisations of aperiodic optical lattices, such as the fivefold symmetric lattice by Corcovilos et al. [62] and the eightfold by Schneider et al. [6], which is similar to the Ammann-Beenker tiling from Section 3.2.5.

Before discussing a specific experiment, we briefly explain the principles of an optical trap for cold atoms. Consider a plane wave electric field

$$\mathbf{E}_{\mathbf{k}}(\mathbf{x}, t) = E\hat{\mathbf{n}}e^{i(\mathbf{k}\cdot\mathbf{x}-\omega t)}, \tag{4.1}$$

where $\hat{\mathbf{n}}$ is the polarisation unit vector, E is the electric field strength, $\mathbf{k}$ the wavevector and ω its angular frequency. If we superimpose another plane wave on top of Eq. 4.1 that propagates in exactly the opposite direction, we obtain

$$\mathbf{E}(\mathbf{x}, t) = \mathbf{E}_{\mathbf{k}}(\mathbf{x}, t) + \mathbf{E}_{-\mathbf{k}}(\mathbf{x}, t) = 2E\hat{\mathbf{n}}\cos(\mathbf{k}\cdot\mathbf{x})e^{-i\omega t},$$

i.e. a standing wave. Using the phasor representation, time-averaged intensity reads

$$I(\mathbf{x}) = \frac{1}{2Z_0}\left\langle |\mathbf{E}(\mathbf{x}, t)|^2 \right\rangle = 2E^2\cos^2(\mathbf{k}\cdot\mathbf{x}),$$

where Z_0 is the vacuum impedance. To use the intensity profile as potential landscape, one can put neutral particles with nonzero dipole moment into the system. The force resulting from the potential is the dipole force [61]

$$\mathbf{F} \propto \nabla I(\mathbf{x}),$$

where ∇ is the gradient operator. The attractive or repulsive nature of the force is dependent on the laser frequency ω and on the atomic resonant frequency ω_0. Often, one chooses the laser frequency such that the force is attractive towards the peaks of the intensity ($\omega < \omega_0$). This allows one to re-interpret the intensity $I(\mathbf{x})$ as the potential (up to a constant) of an atom with nonzero dipole moment in the electric field. The challenge is now to generate the desired intensity $I(\mathbf{x})$ that resembles some Hamiltonian by letting electric fields interfere.

Corcovilos et al. [62] constructed a fivefold symmetric 2D optical potential by taking five 850nm laser beams that nearly propagate in parallel. These five beams are equally placed around a circle and point slightly inwards towards the common axis, see Fig. 4.3a. The setup used by Schneider to create the eightfold quasicrystal is slightly different, as it uses a large angle between the beams (see Fig. 4.3b). In the region where they intersect, a quasicrystalline lattice is created with eightfold symmetry.

The experimental result of the fivefold quasicrystal where dark regions indicate potential wells in Fig. 4.4a, matches very well their numerical simulation. Additionally, the relative phases of the five laser beams can be tuned at will. By changing two of these, e.g. ϕ_1 and ϕ_2, and varying them in a loop in configuration space, see Fig. 4.4b, a potential well is displaced in the lattice. This

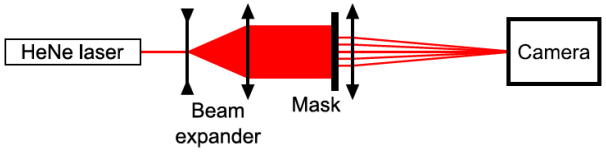

(a) Fivefold quasicrystal by Corcovilos et al. [62].

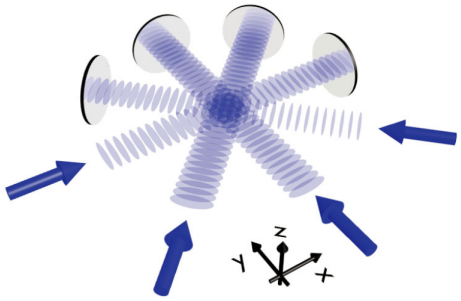

(b) Eightfold quasicrystal by Schneider et al. [6].

Figure 4.3.: Experimental setups (figures extracted from Refs. [6, 62]).

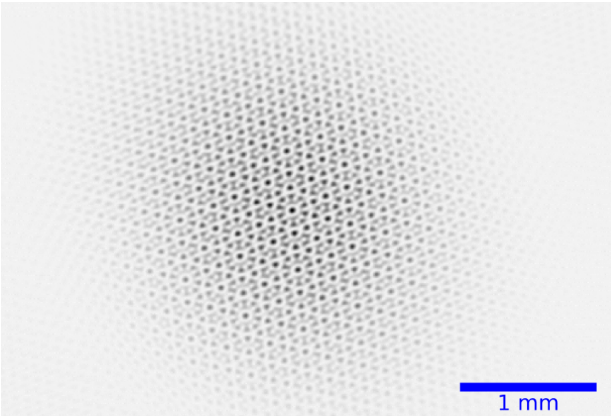

(a) Real space potential landscape.

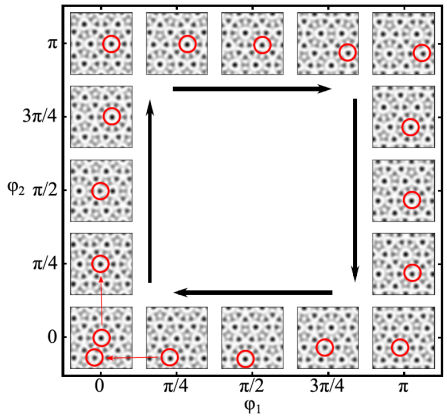

(b) Geometric pumping.

Figure 4.4.: Experimental results (figures from Ref. [62]).

phenomenon is called *geometric pumping* and allows the experimentalist to force transport in an optical lattice by periodically changing relative phases.

Optical lattices are useful simulating many quantum phenomena, of which emulating quasicrystals is merely an example. To name a few [61]: Bose-Einstein condensation, superfluid to Mott insulator transition, dynamics near quantum phase transitions, rotating quantum gases, BCS-BEC crossovers and out-of-equilibrium quantum dynamics.

4.4. Twisted Bilayer Graphene

The last experimental realisation of quasicrystals that we discuss is not a quantum simulator, in the sense that it provides a flexible way of implementing various Hamiltonians. Instead, it is a byproduct of the modern and popular field of *twisted bilayer graphene*. Before discussing the way it implements quasicrystals, we explain the basics of twisted bilayer graphene.

The study of graphene has been around in the 20th century as a byproduct of research on graphite, a material that is known to be a stack of graphene layers held together by Van der Waals forces. However, it was not until 2004 that graphene was correctly isolated and fully characterised by Geim and Novoselov, for which they received the Nobel Prize in physics in 2010. Graphene is a 2D layer of carbon atoms that form a honeycomb lattice. In Fig. 4.5a, a finite part of a graphene sheet is shown. Here, both white and blue atoms are carbon atoms, but the colouring is applied

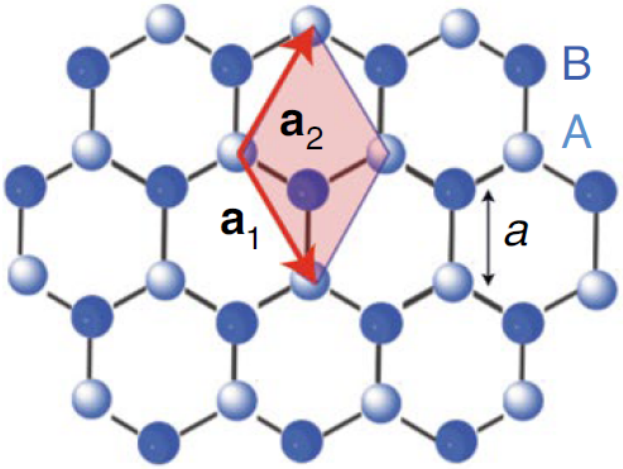

(a) Unit cell (figure from Ref. [63]).

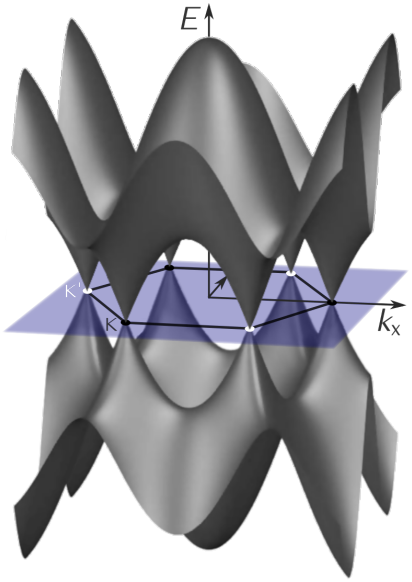

(b) The Brillouin zone with energy bands (figure from Wikipedia).

Figure 4.5.: Graphene in real- and momentum space.

to emphasise that the unit cell of the graphene lattice consists of two inequivalent carbon atoms because they have different neighbors. The vectors $\mathbf{a}_1 = (1/2, \sqrt{3}/2)^T a_0, \mathbf{a}_2 = (1/2, -\sqrt{3}/2)^T a_0$ span the Bravais lattice, which is triangular in this case with lattice constant a_0. For completeness, in Fig. 4.5b, the Brillouin zone (blue) is shown with the energy bands (grey). At six points in momentum space, the bands touch as tips of a cone. These points are called *Dirac cones*, for the behaviour of electrons resemble relativistic electrons. There are actually just two inequivalent Dirac cones, indicated by either a white or black dot. These arise because the unit cell contains two atoms. All three copies of each colour are then equivalent by the threefold symmetry of the triangular lattice.

One might wonder why the unit cell cannot simply contain one carbon atom and define the honeycomb structure as the lattice? This question is easily answered by the observation that there exist no primitive vectors $\mathbf{a}_1, \mathbf{a}_2$ that can produce each point of the honeycomb as a linear combination of the primitive vectors.

Suppose that one stacks two layers of graphene in a way that a blue atom sits on top of a white atom in Fig. 4.5a. Unlike in graphite, let the top layer twist with an angle θ around some blue atom sitting on top of a white one, see Fig. 4.6. This material is commonly referred to as *twisted bilayer graphene* (TBG).

One can see that an emergent pattern, a so-called Moiré pattern, is formed. That is again a honeycomb lattice, at a much larger scale. In fact, the angles θ_i at which different Moiré patterns form can be labeled by an integer [65] and computed by

$$\cos\theta_i = \frac{3i^2 + 3i + 1/2}{3i^2 + 3i + 1}, \qquad i = 0, 1, 2, \ldots .$$

Furthermore, the lattice constant of the Bravais lattice of the Moiré pattern is given by $\sqrt{3i^2 + 3i + 1}a_0$. These angles are just the angles that give a *commensurate* bilayer, in the sense that the stacked lattice is periodic. Any other angle will also give rise to a Moiré pattern, but the lattice configuration is not exactly periodic. Fig. 4.8 shows an example of this with incommensurate angle

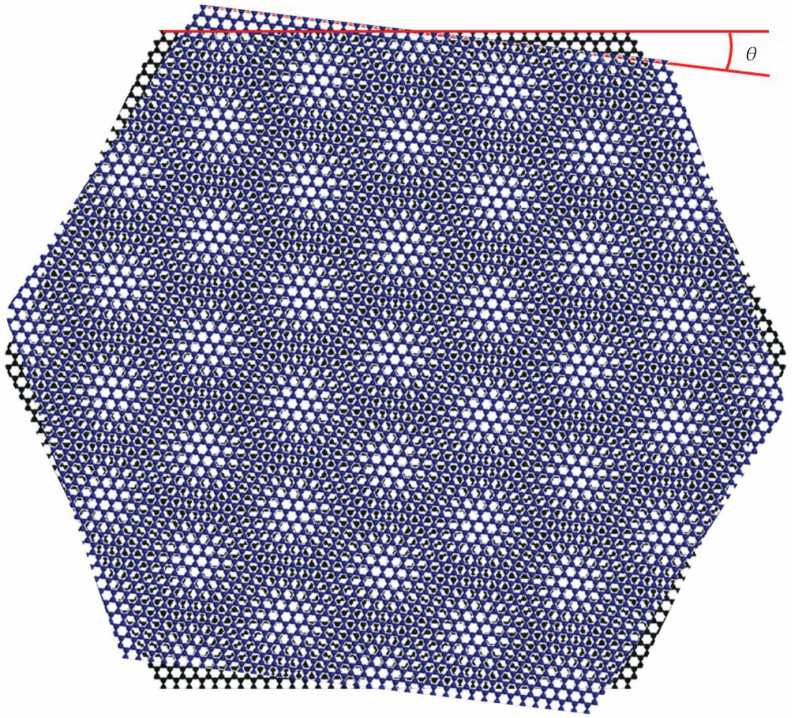

Figure 4.6.: Twisted bilayer graphene and its Moiré pattern (figure from Ref. [64]).

$\theta = 30°$. This is precisely what gives rise to quasicrystals in TBG, which in this case is a dodecagonal quasicrystal [66]. Moreover, this quasicrystal has a manifest sixfold rotational symmetry in real space. In Fig. 4.8b, six nonparallel lines are drawn in the same way as one does for the pentagrid method mentioned in Section 3.2.5. The correspondence between nonparallel lines and real space symmetry shows a remarkable resemblance to the pentagrid for the Penrose tiling. Finally, to confirm that TBG indeed produces true quasicrystals as defined in Section 2.3, one needs to perform diffraction experiments. From a mathematical perspective, it is not yet established that TBG structures can arise from a CPS.

It turns out that there exist incommensurate *magic angles* in TBG, at which the material has remarkable properties. These properties mainly concern the geometry of the band structure. Most notably, flat bands and superconductivity are hallmarks of TBG [63]. Another noteworthy feature of TBG is the similarity of its phase diagram with high-temperature (cuprate) superconductors. This resemblance could be pure coincidence or indeed give insights into the unknown physics of

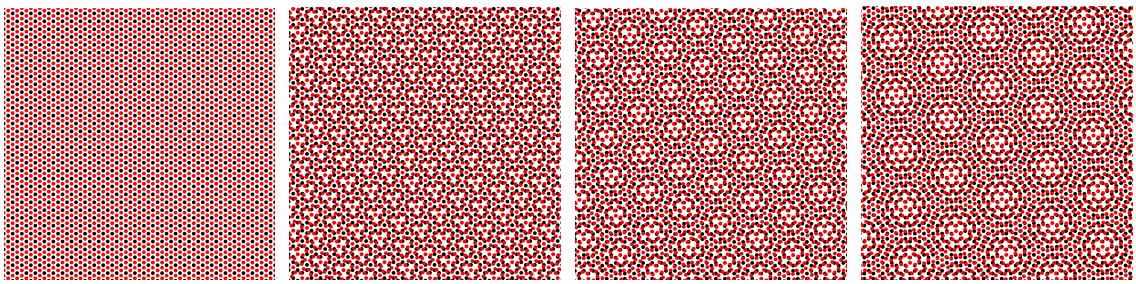

(a) $i = 0$. (b) $i = 1$. (c) $i = 2$. (d) $i = 3$.

Figure 4.7.: TBG at commensurate angles θ_i.

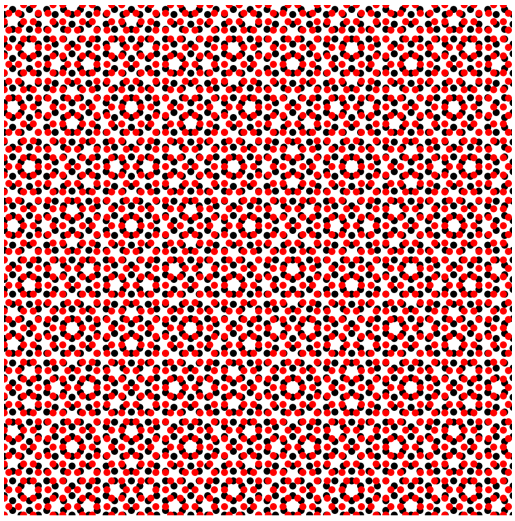

(a) Aperiodic Moiré pattern.

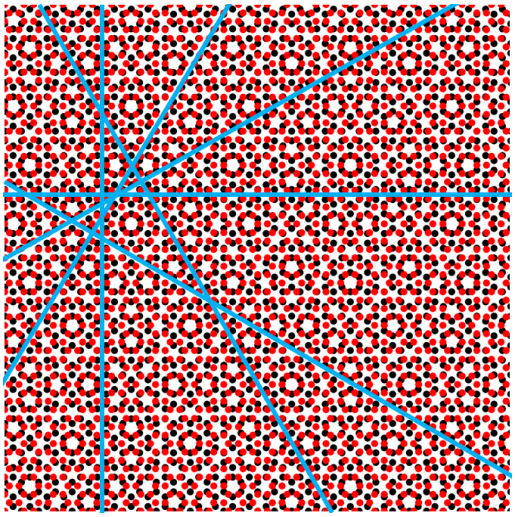

(b) A grid construction.

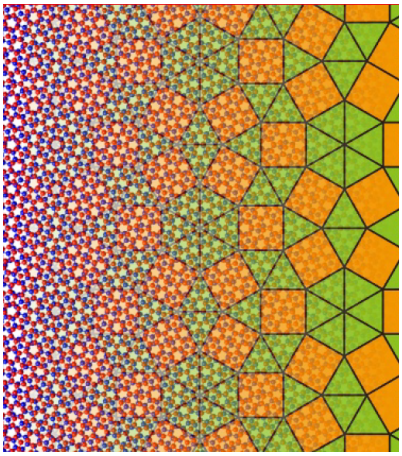

(c) Dodecagonal quasicrystal (figure from Ref. [66]).

Figure 4.8.: TBG at the incommensurate angle of 30°.

high-temperature superconductors. Andrei et al. [63] point out that this debate is still to be settled.

5. The Tribonacci Chain[1]

In Section 3.5, a quantum chain was studied that is based on the Fibonacci substitution from Section 3.1.3, which was shown in Section 3.2.2 to yield a quasicrystalline structure. It is a model that features critical eigenstates, and the Fibonacci substitution gives it a rich structure: multifractal spectrum [20], multifractal wavefunctions [21], renormalisation via the Fibonacci substitution [19], gap-labelling [58] and conumbering [23]. See the review paper by Jagannathan [17] for an overview of the Fibonacci chain.

The Fibonacci chain is a *binary* chain, that is, it contains two different hopping parameters, or equivalently, on-site energies [19]. There are many well-studied binary chains based on substitution rules, such as the (generalised) Thue-Morse chain [67, 68], the metallic mean chains [69, 70] and the Rudin-Shapiro chain [71, 72], to name a few. The advantage is that binary systems can be parameterised by one parameter. For hopping models, this parameter $\rho = t_0/t_1$ is the ratio between the two hopping parameters t_0 and t_1. For on-site models, it is the so-called resolution $\rho = |\epsilon_0 - \epsilon_1|/t$, where ϵ_0, ϵ_1 are the two different on-site energies and t is a constant hopping strength between adjacent sites.

In this chapter we introduce a new quantum chain, which is based on a substitution over an alphabet of *three* letters, the Tribonacci substitution from Section 3.1.5. Even though we deviate from the simpler case of a binary chain, we will see that similar techniques, such as renormalisation, can be applied. Additionally, we will see that the internal space of the Tribonacci CPS, the Rauzy fractal, plays a similar role as the conumbering scheme for the Fibonacci chain. The work in this chapter has lead to a publication, see Ref. [27], which summarises the most important results.

5.1. The Model

Analogous to the Fibonacci quasicrystal, we can construct a quantum chain using the Tribonacci substitution. Since the Tribonacci word contains three letters $0, 1, 2$, we require three bonding strengths t_0, t_1, t_2 for the hopping model. Using the bi-infinite Tribonacci word

$$\cdots w_{-2}w_{-1}|w_0w_1\cdots = W^T|W^T,$$

we define the hopping Tribonacci Chain (HTC) Hamiltonian as

$$H = \sum_{n\in\mathbb{Z}} t_{w_n} |n+1\rangle\langle n| + H.c.. \tag{5.1}$$

One can also define a finite hopping chain with periodic boundary conditions from a Tribonacci approximant W_N^T, defined by

$$H_N = \sum_{n=0}^{T_N-1} t_{w_n} |n+1 \bmod T_N\rangle\langle n| + H.c., \tag{5.2}$$

for which the energy spectrum is plotted in Fig. 5.1a. The model can be parameterised using two parameters, for instance t_0/t_2 and t_1/t_2. Inspired by Niu and Nori [19], we use only one parameter ρ for the system by setting $t_0/t_1 = t_1/t_2 = \rho$. More generally, we denote $H^{(p,q)}$ as the

[1] This chapter is original work, and lead to the publication Ref. [27].

Tribonacci Hamiltonian with $t_0/t_1 = \rho^p, t_1/t_2 = \rho^q$, where p, q are positive real numbers. It is common practice to choose one energy scale and write all other parameters in units thereof. In this case, we could write $t_0/t_2 = \rho^{p+q}$ and $t_1/t_2 = \rho^q$. The reason for defining p, q in this way is that the formulas of the renormalisation process in Section 5.2 become more intuitive to handle. Also analogous to Niu and Nori [19], one defines atoms/molecules based on the local environment of a lattice site. The atoms are sites that are coupled on both sides with t_0. Molecules of type 1 consist of two sites coupled by t_1 and molecules of type 2 are two sites coupled by t_2. By the nature of the Tribonacci word W^T, molecules are surrounded by a t_0 bond on both sides. Physically, this means that the chain splits up into isolated dimers (the molecules of type 1 and 2), and isolated monomers (atoms) upon setting $t_0 = 0$.

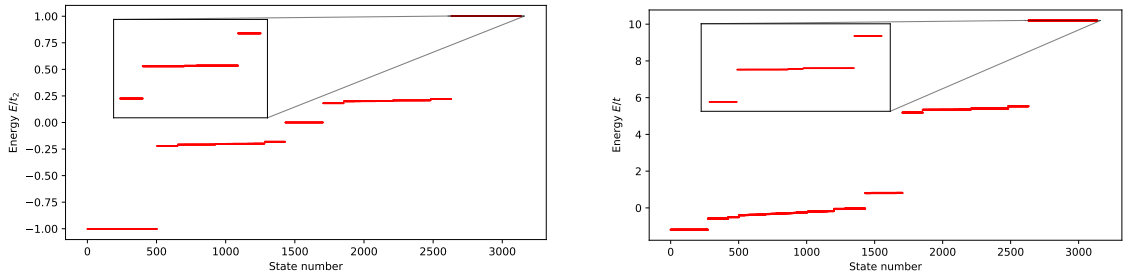

(a) The HTC with $\rho = 0.2$.

(b) The OTC with $c = 5$.

Figure 5.1.: The energy spectrum for both the HTC and OTC of $T_{13} = 3136$ lattice sites and periodic boundary conditions.

The HTC Hamiltonian possesses a symmetry called *chiral* (or sublattice) symmetry. The physical interpretation of this symmetry is that the system can be split up into two non-interacting systems that mutually interact. In the case of Eq. 5.1, the system can be split up into even and odd numbered sites, where it is clear that even (odd) sites do not interact. The mathematical formulation of chiral symmetry is that there exists an operator Γ such that $\Gamma H \Gamma = -H$ and $\Gamma^2 = 1$, which in this case reads

$$\Gamma = \sum_{n\in\mathbb{Z}} |2n\rangle \langle 2n| - \sum_{n\in\mathbb{Z}} |2n+1\rangle \langle 2n+1| .$$

A direct consequence of chiral symmetry is a symmetric spectrum around $E = 0$. This can be seen by taking some solution $H|\psi\rangle = E|\psi\rangle$, then $|\phi\rangle = \Gamma|\psi\rangle$ is also a solution since $H|\phi\rangle = H\Gamma|\psi\rangle = -\Gamma H|\psi\rangle = -E|\phi\rangle$. So for every energy E, there is a corresponding state with energy $-E$. See Appendix B.1 for more details on chiral symmetry and its connection to tridiagonal matrices.

We can also define an on-site model using Tribonacci modulation of on-site potentials, with a constant tunneling parameter t between sites. The on-site Tribonacci Chain (OTC) Hamiltonian reads

$$H^o = \sum_{n\in\mathbb{Z}} \epsilon_{w_n} |n\rangle \langle n| - t \sum_{n\in\mathbb{Z}} |n+1\rangle \langle n| + H.c.. \tag{5.3}$$

One can also define a finite on-site chain with periodic boundary conditions from a Tribonacci approximant W_N^T, defined by

$$H_N^o = \sum_{n=0}^{T_N-1} \epsilon_{w_n} |n\rangle \langle n| - t\big(|n+1 \bmod T_N\rangle \langle n| + H.c.\big), \tag{5.4}$$

for which the energy spectrum is plotted in Fig. 5.1b. Note that w.l.o.g. we can set $\epsilon_0 = 0$, and the model can be parameterised using two variables: $c_1 = (\epsilon_1 - \epsilon_0)/t$ and $c_2 = (\epsilon_2 - \epsilon_0)/t$ such that $c_2 - c_1 = (\epsilon_2 - \epsilon_1)/t$. In the future we will be interested in the weak coupling regime, in other words $|c_1|, |c_2|, |c_2 - c_1| \gg 1$. One has a lot of freedom in choosing such c_1, c_2. We use the particular choice of $c_1 = c_2/2 = c \gg 1$ to compare the on-site model with the hopping model.

Later, we will see that the equivalence is not dependent on the choice of parameterisation of the on-site model.

Finally, we would like to point out that there exists a quasiperiodic 2D tiling, the Rauzy tiling, which is based on the Tribonacci numbers and is a cut-and-project set from a 3D space [73]. Several physical properties of tight-binding models on these lattices have been studied [74, 75], in particular the effect of a magnetic field [13, 14, 76]. The generalized Rauzy tiling extends this construction to arbitrary dimension, being a CPS from a d-dimensional periodic lattice to a $(d-1)$-dimensional real space quasicrystal, and this family of tilings can be viewed as a generalization of the Fibonacci chain [73]. In the light of these works, the Tribonacci chain generalises the Fibonacci chain in the complementary direction. Instead of keeping the codimension of the CPS fixed at one, we keep the real space dimension fixed at one and increase the dimensionality of the internal space of the CPS.

5.1.1. Non-perturbative methods: Trace Map

For quantum chains that are based on substitution rules, the method of *trace maps* can be used to derive exact results for the spectrum and wavefunctions. Baake et al. [77] point out that for binary chains, the machinery of trace maps is well-understood. They also argue that generalisation to substitutions with more than two letters is not straightforward. In this section, we give a short introduction to the method of trace maps and derive the trace map dynamical system for the Tribonacci chains.

Let $|\psi\rangle$ be a solution to the Schrödinger equation $H|\psi\rangle = E|\psi\rangle$, with $E \in \mathbb{R}$ and $|\psi\rangle = \sum_{n\in\mathbb{Z}} \psi_n |n\rangle$, where $\psi := (\psi_n)_{n\in\mathbb{Z}} \in l^2(\mathbb{Z}) := \{x \in \mathbb{C}^{\mathbb{Z}} \mid \|x\|_2^2 = \sum_{n\in\mathbb{Z}} |x(n)|^2 < \infty\}$, i.e. all square-summable bi-infinite complex sequences. This can be used to write the Schrödinger equation for the HTC Eq. 5.1 as

$$(H\psi)_n = t_{n-1}\psi_{n-1} + t_n\psi_{n+1} = E\psi_n, \tag{5.5}$$

and similarly for the on-site model Eq. 5.3

$$(H\psi)_n = \epsilon_n\psi_n - t\psi_{n-1} - t\psi_{n+1} = E\psi_n. \tag{5.6}$$

If one defines $\Psi_n = (\psi_n, \psi_{n-1})^T$, then Ψ_{n+1} for the hopping model can be obtained as

$$\Psi_{n+1} = T_n\Psi_n, \qquad T_n = \begin{pmatrix} E/t_n & -t_{n-1}/t_n \\ 1 & 0 \end{pmatrix}, \tag{5.7}$$

where T_n can be found by solving Eq. 5.5 for ψ_{n+1}. One defines the matrix $M_n = T_{n-1}T_{n-2}\cdots T_0$, such that $\Psi_n = M_n\Psi_0$. Because of Eq. 3.6, the matrices M_n themselves obey the recurrence relation $M_{n+1} = M_{n-2}M_{n-1}M_n$. By taking a trace of the matrices M_n, hence the name *trace map*, one can study recurrence relations of these traces that describe the system. The trace map can be used to describe the spectrum: as $n \to \infty$, the values of E that make the system not diverge, belong to the spectrum [78]. For a finite system, the boundary conditions at the beginning and end of the chain, $\psi_0/\psi_1 = t_0/E$ and $\psi_{N_1}/\psi_{N-2} = t_{N-2}/E$, determines the spectrum uniquely.

Our partial result for the trace map dynamical system for the Tribonacci chain reads

$$x_{n+1} = 2x_ny_n - x_{n-3}, \tag{5.8}$$
$$y_{n+1} = 2x_nx_{n-1} - y_{n-1}, \tag{5.9}$$

where $x_n = \mathrm{Tr}\{M_n\}/2, y_n = \mathrm{Tr}\{M_{n-2}M_{n-1}\}/2$. To prove this, we require the Cayley-Hamilton theorem for $\mathrm{SL}(2,\mathbb{C})$ matrices, which implies for any $A \in \mathrm{SL}(2,\mathbb{C})$

$$A^2 = \mathrm{Tr}\{A\}A - \mathrm{Id}, \tag{5.10}$$
$$A + A^{-1} = \mathrm{Tr}\{A\}\,\mathrm{Id} \Rightarrow \mathrm{Tr}\{A^{-1}\} = \mathrm{Tr}\{A\}. \tag{5.11}$$

For the Tribonacci transfer matrices we have the relations

$$M_n = M_{n-3}M_{n-2}M_{n-1} \Rightarrow M_{n-3}^{-1} = M_{n-2}M_{n-1}M_n^{-1}$$
$$M_{n+1} = M_{n-2}M_{n-1}M_n,$$

which can be added together to yield

$$M_{n+1} = M_{n-2}M_{n-1}\left(M_n + M_n^{-1}\right) - M_{n-3}^{-1}. \tag{5.12}$$

Now, taking the trace of Eq. 5.12 and applying Eq. 5.11, we obtain

$$\mathrm{Tr}\{M_{n+1}\} = \mathrm{Tr}\{M_{n-2}M_{n-1}\}\,\mathrm{Tr}\{M_n\} - \mathrm{Tr}\{M_{n-3}\},$$

which is exactly the first relation in Eq. 5.8. The second equation is easier to obtain. By adding M_nM_{n-1} to both sides of the equation

$$M_nM_{n-1}^{-1} = M_{n-3}M_{n-2},$$

one obtains

$$M_n\,\mathrm{Tr}\{M_{n-1}\} = M_{n-3}M_{n-2} + M_nM_{n-1}, \tag{5.13}$$

where we used Eq. 5.11 in the first term. Taking the trace of Eq. 5.13, and using the cyclic property of the trace, one obtains

$$\mathrm{Tr}\{M_{n-1}M_n\} = \mathrm{Tr}\{M_n\}\,\mathrm{Tr}\{M_{n-1}\} - \mathrm{Tr}\{M_{n-3}M_{n-2}\},$$

which is exactly the second relation in Eq. 5.8.

5.1.2. Non-Perturbative Methods: Zero Energy Wavefunction

Before we discuss the perturbative treatment of the HTC Eq. 5.1, we will show how to solve the $E = 0$ state exactly.

Now assuming $E = 0$ is an eigenvalue, by Eq. 5.5 the wavefunction must satisfy

$$t_n\psi_n + t_{n+1}\psi_{n+2} = 0, \qquad \forall n.$$

If we label even (or odd) sites $2m = n$ with an integer m, we can write

$$\psi_{2(m+1)} = -\rho^{A(m)}\psi_{2m}, \qquad A(m) = \begin{cases} +2 & (02) \\ +1 & (01) \\ 0 & (00) \\ -1 & (10) \\ -2 & (20) \end{cases},$$

analogous to Macé [54]. The value of $A(m)$ depends on $t_{2m}/t_{2m+1} = t_i/t_j$, where ij can read $00, 01, 10, 02, 20$, i.e. the possible factors of W^T of length two. In the case of the bi-infinite chain Eq. 5.1, the $E = 0$ is doubly degenerate, since the odd and even eigenstates are linearly independent solutions. By setting $\psi_0 = 1$, the unnormalised wavefunction reads

$$\psi_{2m} = (-1)^m e^{h(m)\log\rho}, \qquad h(m) = \sum_{i=0}^{m-1} A(i),$$

in accordance with the result by Kalugin and Katz [79]. They found that the many-body ground state at half-filling for a general quasicrystal has the form

$$\psi_m = C(m)e^{\kappa h(m)},$$

where $\kappa \in \mathbb{R}$ and m labels the sites of the quasicrystal, which need not be one-dimensional.

In the case of a finite chain, the existence of an $E = 0$ state depends on the parity of the chain. Consider a chain with N sites, labeled by $n = 0, 1, \ldots, N-1$. The $E = 0$ state would demand

$$(H\psi)_0 = t_0\psi_1 = 0, \qquad (H\psi)_{N-1} = t_{N-2}\psi_{N-2} = 0.$$

From $\psi_1 = 0$, we can already see that the wavefunction must be zero on all odd sites. Additionally, the wavefunction must be zero on sites with the same parity as $N-2$. If N were even, this would mean $\psi = 0$, which means a $E = 0$ state cannot exist. Only if N is odd, we have one $E = 0$ state, which is consistent with the chiral symmetry of finite hopping Hamiltonians, as explained in Appendix B.1. This wavefunction has only support on the even sites $n = 0, 2, \ldots, N-1$.

5.1.3. Multifractality

In this section, the multifractal properties of the HTC are studied and compared to those of the Fibonacci chain, which are mainly taken from Ref. [54]. The Fibonacci chain was discussed in Section 3.5.1, and we are now interested in the finite chain with periodic boundary conditions

$$H_N^F = \sum_{n=0}^{F_N-1} t_{w_n^F} \left|n+1 \bmod F_N\right\rangle \langle n| + H.c., \tag{5.14}$$

where the hopping parameters t_0, t_1 are related by $t_0/t_1 = \rho$ and w_n^F denotes the nth letter of the infinite Fibonacci word. Finally, the numerical method to reliably approximate multifractal dimensions is explained in Section 3.3.3.

The first step in the analysis is numerical computation of the multifractal dimension D_q, given by Eq. 3.24, for both the Fibonacci and the HTC. The results are plotted in Fig. 5.2(a), with the particular choice of $\rho = 0.2$, such that the results can be compared with Ref. [54].

From Fig. 5.2(a), one can conclude that the Tribonacci has a multifractal energy spectrum, with a generally lower fractal dimension than the Fibonacci chain. This can be seen as a consequence of the fact that the Tribonacci chain's renormalisation scheme contains factors with larger powers of ρ (see Section 5.2.2) than the Fibonacci chain, resulting in stronger scaling.

As done for the Fibonacci chain in Ref. [22], one can compute the average multifractal dimension D_q^ψ for the wavefunctions as well. The results for $\rho = 0.2$ are plotted in Fig. 5.2(b). Again, the conclusion is that the multifractal dimension is generally lower, and decays faster as a function of q.

From the point of view of the quantum chain, it is not strange that the multifractal dimension of the HTC wavefunctions is smaller. The HTC contains weaker bonds of $\mathcal{O}(\rho^2)$ than the Fibonacci chain, which has $\mathcal{O}(\rho)$ as weakest bond strengths. These weaker links in the HTC make it more difficult for particles to traverse the chain. Since it is known that the average multifractal dimension is related to diffusive properties in the system [80, 81], a lower value for the HTC is expected. An averaged multifractal dimension strictly between zero and one is also an indicator of critical states and Anderson localisation [81], but one should study the inverse participation ratio as done in Ref. [82] to strengthen this claim. The study of the inverse participation ratio is a topic for further research.

5.2. Perturbative Renormalisation

A perturbative renormalisation (RG) analysis of the HTC Eq. 5.1 and OTC Eq. 5.3 can be carried out, analogous to the one performed by Niu and Nori [19] for the Fibonacci chain. We start in Section 5.2.1 by working out the self-similar properties of the Tribonacci word, and how these

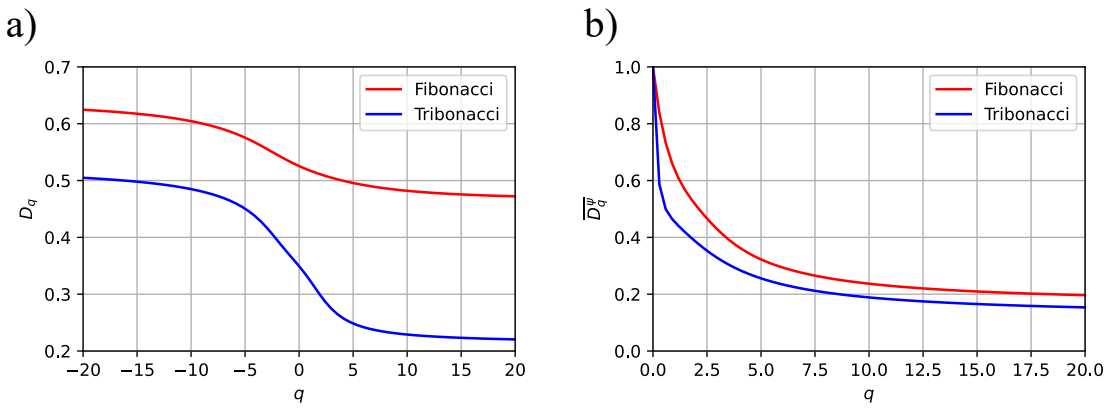

Figure 5.2.: Multifractal properties of the Fibonacci chain Eq. 5.14 and the HTC, at $\rho = 0.2$. (a) The multifractal dimensions of the energy spectrum for the Fibonacci chain H_{19}^F and the HTC H_{13}. The size of the chain is chosen such that they have approximately the same maximum number of points in K_i in Eq. 3.24. (b) The average multifractal dimensions of the eigenstates of the Fibonacci chain H_{14}^F and the HTC H_{10}. The size of the chains is chosen such that they have approximately the same number of lattice sites.

lead to a perturbative RG scheme for the HTC and OTC. Sections 5.2.2 and 5.2.3 carry out the calculations that lead to the perturbative RG schemes Eqs. 5.33 and 5.36 for the HTC and OTC, respectively. Finally, in Section 5.2.5 the RG schemes are used to prove that the HTC and OTC are equivalent models in the limit of applying the RG scheme infinitely many times.

5.2.1. The Renormalisation Scheme

A key property of the Tribonacci W^T word is its self-similarity [83]. Take any finite string $s = s_1 \cdots s_N$ of length N that occurs somewhere in W^T. We say that s occurs at position i in W^T if $s_1 \cdots s_N = w_i \cdots w_{i+N}$. Let $i_1, i_2, \ldots$ denote the places where s occurs in W^T. Then, the words $r_j = w_{i_j} \cdots w_{i_{j+1}}$ between occurrences of s have useful properties. Firstly, for any choice s, the word $r_j \in \{r^{(0)}, r^{(1)}, r^{(2)}\}$ takes one of three values. Secondly, if we label $r^{(l)}$ such that $r^{(0)}$ occurs most often, $r^{(1)}$ second most often and $r^{(2)}$ least often, then the map $\kappa : r^{(l)} \mapsto l.$ where $l = 0, 1, 2$, maps the string $r_1 r_2 \cdots$ back to W^T. In other words

$$\kappa(r_1)\kappa(r_2)\cdots = W^T, \tag{5.15}$$

where $r_i \in \{r^{(0)}, r^{(1)}, r^{(2)}\}$ are the words between subsequent occurrences of s in W^T. This also works if s occurs in a Tribonacci approximant W_N^T. By applying periodic boundary conditions when determining r_j, the map κ results in

$$\kappa(r_1)\kappa(r_2)\cdots = W_{N-k}^T, \tag{5.16}$$

where k depends on the choice of s. Eqs. 5.15 and 5.16 are the foundation of the perturbative RG scheme presented in this section, for which the proof is given in Section 5.2.4.

For the RG scheme, it is convenient to consider the Nth HTC approximant Eq. 5.2. Furthermore, the Hamiltonian is split up in two parts

$$H_N = H_{0,N} + H_{1,N}, \tag{5.17}$$

where $H_{1,N}$ contains only the terms with a t_0 hopping, such that $H_{0,N}$ can be regarded as the unperturbed Hamiltonian. Note that $H_{0,N}$ has only five highly degenerate energy levels $E =$

Table 5.1.: For W_N^T and particular strings $s = 0, 1, 2, 00$, the occurrences between s can be one of $r^{(i)}$, and map to W_{N-k}^T under the map $\kappa : r^{(i)} \mapsto i$, $i = 0, 1, 2$.

s	$r^{(0)}$	$r^{(1)}$	$r^{(2)}$	maps W_N^T to
0	1	2	$\emptyset$	W_{N-1}^T
1	020	00	0	W_{N-2}^T
2	010010	01010	010	W_{N-3}^T
00	10201010201	102010201	10201	W_{N-4}^T

$0, \pm t_1, \pm t_2$. The $E = 0$ states are the atoms, which are isolated sites, corresponding to 00 in W^T. Type-1 molecules are the $E = \pm t_1$ states, corresponding to 010 in W^T. These are isolated dimers, consisting of two neighboring sites coupled by a t_1 bond, on which an eigenstate can either bond ($E = t_1$) or anti-bond ($E = -t_1$). Similarly, the $E = \pm t_2$ states correspond to 020 in W^T, and are called type-2 molecules.

Upon setting t_0 nonzero, the atoms/molecules start to interact. If one considers one type of atom or molecule as a lattice site, one can compute the effective coupling between subsequent sites using Brillouin-Wigner perturbation theory. Fig. 5.1a depicts the spectrum of Eq. 5.2, where one can see five branches around $E = 0, \pm t_1, \pm t_2$ that would become fully degenerate upon setting $t_0 = 0$.

Now, we explain the simplest case, the type-1 molecule, in detail. The procedure for the other bonds is exactly the same, but with longer computations. Consider the Tribonacci approximant

$$W_6^T = 0\overset{r_1}{\underline{10}}\overset{r_2}{2}\overset{r_3}{0}\overset{r_4}{1}\overset{r_5}{0}\overset{r_6}{2}\overset{r_7}{0}\overset{r_8}{1}\overset{r_9}{0}\overset{r_{10}}{2}\overset{r_{11}}{0}\overset{r_{12}}{1}\overset{r_{13}}{0}2\underline{0}. \tag{5.18}$$

The first step is to tabulate all words r_i occurring between 1's in W_6, starting after the first occurrence of 1, and considering periodic boundary conditions. The possibilities are $020, 00$ and 0, which occur $7, 4$ and 2 times, respectively. Therefore

$$\begin{gathered}\{r\} = \{r_1 = r^{(0)}, r_2 = r^{(1)}, r_3 = r^{(0)}, \ldots, r_{13} = r^{(1)}\}, \\ r^{(0)} = 020, r^{(1)} = 00, r^{(2)} = 0.\end{gathered} \tag{5.19}$$

Finally, upon applying the map $\kappa : r^{(l)} \mapsto l$, the Tribonacci approximant W_4^T is obtained as

$$W_4^T = \kappa(r_1)\kappa(r_2)\cdots\kappa(r_{13}) = 0102010010201, \tag{5.20}$$

which has $k = 2$ in Eq. 5.16. The procedure in Eqs. 5.18, 5.19, and 5.20, which is the $s = 1$ case, can be carried out for any s. This is done for $s = 0, 1, 2, 00$ in Table 5.1. We note that if *open boundary conditions* are enforced on the approximants W_N^T, the last word r_{13} would be dropped in Eq. 5.18, resulting in W_4^T with the last symbol removed. Since the last symbol of W_N^T is not used in the HTC (OTC) Eq. 5.1 (Eq. 5.3) when enforcing open boundary conditions, the RG scheme for the Tribonacci word works equally well for the Tribonacci chain with open and periodic boundary conditions.

To proceed with the renormalisation scheme, consider $H_{0,N}$, which is Eq. 5.2 with $t_0 = 0$. Since each occurrence of 1 or 2 in any Tribonacci word is both preceded and followed by a 0, the chain consists of non-interacting atoms and molecules, which results in the energy spectrum

$$\sigma(H_{0,N}) = \{-t_2, -t_1, 0, t_1, t_2\}. \tag{5.21}$$

The amount of t_2 bonds is T_{N-3} and the amount of t_1 bonds is T_{N-2}. Therefore, the energies $E = \pm t_2$ and $E = \pm t_1$ are each T_{N-3}-fold and T_{N-2}-fold degenerate, respectively. All other $T_N - 2T_{N-2} - 2T_{N-3} = T_{N-4}$ states have $E = 0$, which is exactly the amount of atoms in the approximant chain. Upon setting $t_0 > 0$, the degeneracies will be lifted and five energy bands form, one around each value in the spectrum Eq. 5.21. As we work in the perturbative limit, we

can keep $t_0/t_1 \ll 1$ such that bands from two different values from the unperturbed spectrum do not approach each other. Ultimately, this motivates us to look for an approximation where

$$H_N \approx (H_{-t_2} - t_2) \oplus (H_{-t_1} - t_1) \oplus H_{t_0} \oplus (H_{t_1} + t_1) \oplus (H_{t_2} + t_2), \tag{5.22}$$

where each individual Hamiltonian is unknown and has $|\sigma(H_{(\cdot)})| \ll t_1$.

We will now show how the self-similarity of the Tribonacci words can be applied to the Hamiltonian. For this, we focus on the first four columns of Table 5.1. At $t_0 = 0$, we denote an eigenstate of $H_{0,N}$ as $|E, i, t_0 = 0\rangle$, where $E = \pm t_2, \pm t_1, 0$ and i labels the ith occurrence of an atom/molecule on which the eigenstate is localised. We assume that these eigenstates vary continuously with t_0, which they do since the degeneracies in the spectrum are lifted for $t_0 > 0$. Upon setting $t_0 > 0$, the isolated atoms and molecules start to couple, and we can compute the generally nonzero elements $\langle E, i, t_0| H_N |E', i', t_0\rangle$. The key idea of the renormalisation scheme is to define *five* new chains that together form the original HTC. These are:

- The atomic chain. Here, the lattice sites are the 00-atoms in H_N and the couplings between them are $t_i^{00} = \langle E = 0, i, t_0| H_N |E = 0, i+1, t_0\rangle$. It has no on-site energy terms. This chain has T_{N-4} sites and periodic boundary conditions.
- The type-1 molecular bonding chain. The lattice sites are the 010 molecules and their adjacent coupling is $t_i^1 = \langle E = t_1, i, t_0| H_N |E = t_1, i+1, t_0\rangle$. Additionally, the chain has on-site energies $\epsilon_i = E = t_1$. It has T_{N-2} sites and periodic boundary conditions.
- The type-1 molecular anti-bonding chain. This is the same as the molecular 1 bonding chain, but now with $E = -t_1$.
- The type-2 molecular bonding chain. The lattice sites are the 020 molecules and their adjacent coupling is $t_i^2 = \langle E = t_2, i, t_0| H_N |E = t_2, i+1, t_0\rangle$. Additionally, the chain has on-site energies $\epsilon_i = E = t_2$. It has T_{N-3} sites and periodic boundary conditions.
- The type-2 molecular anti-bonding chain. This is the same as the molecular 2 bonding chain, but now with $E = -t_2$.

Up to now, we have made no approximation, and one can check that all chains combined describe all $2T_{N-2} + 2T_{N-3} + T_{N-4} = T_N$ states of H_N. The reason to start using perturbation theory from now on, is that $|E, i, t_0\rangle$ is unknown for $t_0 \neq 0$. Using perturbation theory, we will see in Section 5.2.2 that $t_i^{(\cdot)}$ will depend only on the couplings connecting the subsequent atoms/molecules. For each chain, there are exactly three different strings of couplings as dictated by Table 5.1, which are visualised in Fig. 5.3, where a single line denotes a t_0 coupling, double line a t_1 and a triple line a t_2. Since we have shown, by constructing Table 5.1, that these strings of couplings map to a Tribonacci word themselves, we can conclude that each of the five atomic/molecular chains is a HTC with unknown t_0, t_1 and t_2. The perturbative expression of H_N in terms of five different HTCs, with different hopping parameters and on-site energies, allows us to improve the ansatz in Eq. 5.22 to

$$H_N \approx (z_2 H_{N-2}^{(p_2,q_2)} - t_2) \oplus (z_1 H_{N-3}^{(p_1,q_1)} - t_1) \oplus z_0 H_{N-4}^{(p_0,q_0)} \oplus (z_1 H_{N-3}^{(p_1,q_1)} + t_1) \oplus (z_2 H_{N-2}^{(p_2,q_2)} + t_2), \tag{5.23}$$

where z_i, p_i and q_i for $i = 0, 1, 2$ remain to be determined from perturbation theory.

5.2.2. Brillouin-Wigner Perturbation Theory for the Hopping Model

This section explains how perturbation theory can be applied to H_N to compute the values of z_i, p_i and q_i in the ansatz Eq. 5.23. Canonical Rayleigh-Schrödinger time-independent perturbation theory cannot be applied here because of the degeneracy of the $H_{0,N}$ energy levels. This problem also arose in the case of the Fibonacci chain, for which Brillouin-Wigner perturbation theory

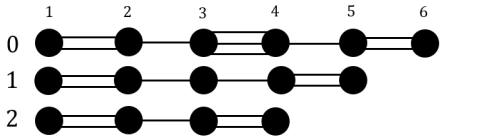

(a) Molecular-1 chain segments.

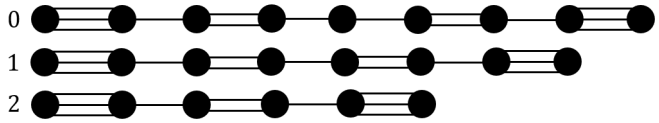

(b) Molecular-2 chain segments.

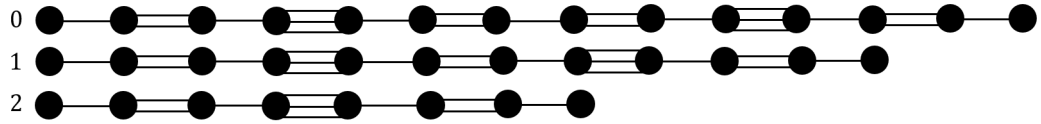

(c) Atomic chain segments.

Figure 5.3.: Atomic and molecular chains.

(BWPT) was used. The framework of BWPT is now briefly introduced, after which we apply it to the HTC. We start by writing the Hamiltonian as

$$H = H_0 + H_1,$$

where H_0, H_1 are the unperturbed and perturbing part, respectively. Denote Q as the projection operator on the eigenspace of E_0, which is spanned by all $|\psi_0\rangle$ such that $H_0 |\psi_0\rangle = E_0 |\psi_0\rangle$. The goal is to derive some effective Hamiltonian H_{eff} that agrees with H on Q, for each of the five unperturbed energy levels $E_0 = \pm t_2, \pm t_1, 0$.

We start by fixing some $|\psi\rangle, E$ that satisfy $H |\psi\rangle = E |\psi\rangle$. Additionally, define P as

$$P = \mathrm{Id} - Q,$$

i.e. the projection orthogonal to Q. Rewriting the Schrödinger equation we obtain

$$(E - H_0) |\psi\rangle = H_1 |\psi\rangle . \tag{5.24}$$

Using Eq. 5.24, one can check that

$$P |\psi\rangle = P \frac{1}{E - H_0} H_1 |\psi\rangle \tag{5.25}$$

holds. We denote the inverse of an operator $\mathcal{O}$ as $\mathcal{O}^{-1} = \frac{1}{\mathcal{O}}$ for clarity in future computations. By noting that $H_0 P = P H_0$ such that

$$(E - H_0) P |\psi\rangle = P H_1 |\psi\rangle , \tag{5.26}$$

and using $P^2 = P$ and Eqs. 5.24 5.26, one can check that the following equalities:

$$P |\psi\rangle = P \frac{1}{E - H_0} H_1 |\psi\rangle = \frac{1}{E - H_0} P H_1 |\psi\rangle = P \frac{1}{E - H_0} P H_1 |\psi\rangle . \tag{5.27}$$

Note that $\frac{1}{E - H_0}$ is ill-defined (division by zero) on the kernel of P, so every time one needs to find an expression for $P \frac{1}{E - H_0}$, the well-defined expression for $\frac{1}{E - H_0} P$ can be used instead. Using P and Q we write $|\psi\rangle$ as

$$|\psi\rangle = (Q + P) |\psi\rangle = Q |\psi\rangle + P \frac{1}{E - H_0} H_1 |\psi\rangle . \tag{5.28}$$

Realising that Eq. 5.28 is a self-consistent equation for $|\psi\rangle$, one can sum all the terms that arise from iterating that equation to get

$$|\psi\rangle = \left[\sum_{n=0}^{\infty} \left(P \frac{1}{E - H_0} H_1 \right)^n \right] Q |\psi\rangle . \tag{5.29}$$

To obtain an expression for H_{eff}, one needs to multiply Eq. 5.29 with QH which yields

$$EQ\left|\psi\right\rangle = \underbrace{\left[QH_0 + QH_1 \sum_{n=0}^{\infty} \left(P\frac{1}{E-H_0}H_1\right)^n\right]}_{H_{\text{eff}}} Q\left|\psi\right\rangle .$$

Using $Q^2 = Q$, the expression for H_{eff} can be written as

$$H_{\text{eff}} = QH_0Q + QH_1\left[\sum_{n=0}^{\infty}\left(P\frac{1}{E-H_0}H_1\right)^n\right]Q. \tag{5.30}$$

Note that during the whole derivation, there was no need to pick a certain unperturbed energy E_0, which is strictly needed to define the projectors P, Q. Suppose one now chooses some E_0, one might wonder what value to insert for E, which is the unknown energy of the full system. It turns out that the energy E_0 of the unperturbed system can be used, as long as H_{eff} is used at the lowest non-vanishing order in H_1 for that particular computation.

In Fig. 5.3a, the three possible words between occurrences of a t_1 bond are depicted. The application of BWPT starts by writing down the eigenstates of H_0, which is in this case the Hamiltonian of a chain in Fig. 5.3a, with $t_0 = 0$. Focusing on the chain with six sites, labeled 0 in Fig. 5.3a, the (un)perturbed Hamiltonians read

$$\begin{aligned} H_0 &= t_1\left|1\right\rangle\left\langle 2\right| + t_2\left|3\right\rangle\left\langle 4\right| + t_1\left|5\right\rangle\left\langle 6\right| + H.c.,\\ H_1 &= t_0(\left|2\right\rangle\left\langle 3\right| + \left|4\right\rangle\left\langle 5\right|) + H.c., \end{aligned}$$

and the six eigenstates of H_0 are

$$\begin{aligned} \left|\pm\right\rangle_1 &= \frac{1}{\sqrt{2}}\left(\left|1\right\rangle \pm \left|2\right\rangle\right), \qquad E_0 = \pm t_1,\\ \left|\pm\right\rangle_2 &= \frac{1}{\sqrt{2}}\left(\left|3\right\rangle \pm \left|4\right\rangle\right), \qquad E_0 = \pm t_2,\\ \left|\pm\right\rangle_3 &= \frac{1}{\sqrt{2}}\left(\left|5\right\rangle \pm \left|6\right\rangle\right), \qquad E_0 = \pm t_1. \end{aligned}$$

The renormalised coupling t_0', i.e. the hopping amplitude between adjacent lattice sites $\left|+\right\rangle_1$ and $\left|+\right\rangle_3$ (or $\left|-\right\rangle_1$ and $\left|-\right\rangle_3$) of the molecular 1 (anti-)bonding chain, is then computed by

$$t_0' = \left\langle\pm\right|_1 H_{\text{eff}}\left|\pm\right\rangle_3 ,$$

where the subscript 0 refers to the fact that the subword that determines the couplings in the chain is mapped to the symbol 0 in the HTC, as dictated by Table 5.1. Moreover, H_{eff} should be of lowest order in H_1 such that t_0' is non-vanishing. In general, we denote the renormalised couplings by t_i', where the subscript indicates it plays the role of a t_i bond in the renormalised chain. If the amount of t_0 bonds in a chain is k, then one can see that H_{eff} must be at least of order k in H_1. We denote $H_{\text{eff}}^{(k)}$ as the effective Hamiltonian Eq. 5.30 up to and including the kth order in H_1. Proceeding with the computation of t_0', we have

$$\begin{aligned} \left\langle\pm\right|_1 H_{\text{eff}}^{(0)}\left|\pm\right\rangle_3 &= \left\langle\pm\right|_1 H_0\left|\pm\right\rangle_3 = \pm t_1\left\langle\pm\right|_1\left|\pm\right\rangle_3 = 0,\\ \left\langle\pm\right|_1 H_{\text{eff}}^{(1)}\left|\pm\right\rangle_3 &= \left\langle\pm\right|_1 H_{\text{eff}}^{(0)} + H_1\left|\pm\right\rangle_3 = \pm\frac{t_0}{\sqrt{2}}\left\langle 3|\pm\right\rangle_3 = 0. \end{aligned}$$

It turns out that the second order in H_1 is nonzero:

$$\begin{aligned} \left\langle\pm\right|_1 H_{\text{eff}}^{(2)}\left|\pm\right\rangle_3 &= \left\langle\pm\right|_1 H_{\text{eff}}^{(1)} + H_1 P\frac{1}{\pm t_1 - H_0}H_1\left|\pm\right\rangle_3\\ &= \pm\frac{t_0^2}{2}\left\langle 3\right| P\frac{1}{\pm t_1 - H_0}\left|4\right\rangle , \end{aligned}$$

Table 5.2.: For general p, q in the HTC given by $H^{(p,q)}$ (or $H_N^{(p,q)}$), the renormalised couplings $t_i' = c_i(p,q)t_i$ are shown.

E_0	t_0'	$c_0(p,q)$	t_1'	$c_1(p,q)$	t_2'	$c_2(p,q)$	$\lvert t_0'/t_1'\rvert$	$\lvert t_1'/t_2'\rvert$
0	$\frac{t_0^7}{t_1^4 t_2^2}$	ρ^{6p+2q}	$-\frac{t_0^6}{t_1^3 t_2^2}$	ρ^{6p+2q}	$-\frac{t_0^4}{t_1^2 t_2}$	ρ^{4p+2q}	ρ^p	ρ^{2p+q}
$\pm t_1$	$\mp\frac{t_0^2 t_2}{2(t_2^2-t_1^2)}$	$\rho^{p+q}/2$	$\frac{t_0^2}{2t_1}$	$\rho^{2p}/2$	$\pm\frac{t_0}{2}$	$\rho^{p+q}/2$	ρ^q	ρ^p
$\pm t_2$	$\frac{t_0^4 t_1^2}{2t_2(t_1^2-t_2^2)^2}$	$\rho^{3p+5q}/2$	$\pm\frac{t_0^3 t_1^2}{2(t_1^2-t_2^2)^2}$	$\rho^{3p+4q}/2$	$\pm\frac{t_0^2 t_1}{2(t_2^2-t_1^2)}$	$\rho^{2p+3q}/2$	ρ^{p+q}	ρ^{p+2q}

and by noting $|4\rangle = \pm\frac{|\pm\rangle_2 - |\mp\rangle_2}{\sqrt{2}}$ we can proceed as

$$\langle\pm|_1 H_{\text{eff}}^{(2)} |\pm\rangle_3 = \frac{t_0^2}{2\sqrt{2}} \langle 3| P \frac{1}{\pm t_1 - H_0}(|\pm\rangle_2 - |\mp\rangle_2).$$

Now using the operators

$$\begin{aligned} P &= |\mp\rangle_1 \langle\mp|_1 + |\pm\rangle_2 \langle\pm|_2 + |\mp\rangle_2 \langle\mp|_2 + |\mp\rangle_3 \langle\mp|_3 , \\ \frac{1}{\pm t_1 - H_0} P &= \frac{1}{\pm 2t_1} |\mp\rangle_1 \langle\mp|_1 + \frac{1}{\pm t_1 \mp t_2} |\pm\rangle_2 \langle\pm|_2 + \frac{1}{\pm t_1 \pm t_2} |\mp\rangle_2 \langle\mp|_2 + \frac{1}{\pm 2t_1} |\mp\rangle_3 \langle\mp|_3 , \end{aligned}$$

we can complete the computation by using Eq. 5.27:

$$\begin{aligned} \langle\pm|_1 H_{\text{eff}}^{(2)} |\pm\rangle_3 &= \frac{t_0^2}{2\sqrt{2}} \langle 3| \frac{1}{\pm t_1 - H_0} P(|\pm\rangle_2 - |\mp\rangle_2) \\ &= \pm \frac{t_0^2}{2\sqrt{2}} \langle 3| \left(\frac{1}{t_1 - t_2} |\pm\rangle_2 - \frac{1}{t_1 + t_2} |\mp\rangle_2 \right) \\ &= \mp \frac{t_0^2}{4} \frac{2t_2}{t_2^2 - t_1^2} = \mp \frac{t_0^2}{2t_2} \left(1 + \mathcal{O}\left(\frac{t_1^2}{t_2^2} \right) \right) \approx \mp \frac{t_0^2}{2t_2} = \mp \frac{\rho^{p+q}}{2} t_0 = \mp \frac{\rho^2}{2} t_0. \end{aligned}$$

This computation is carried out for all possible words in Figs. 5.3a, 5.3c and 5.3b. The results of the computation of the renormalised couplings are summarised in Table 5.2. By chiral symmetry of the HTC, see Appendix B.1, the sign of t_i' has no influence on the spectrum, as was also the case for the Fibonacci chain. Coefficients c_i, which are taken only at leading order in ρ, describe the renormalisation such that $t_i' = c_i t_i$. To represent the results in Table 5.2 in a analogous way as Niu and Nori [19] did, we write RG of the HTC into five chains as

$$\{t_0, t_1, t_2\} = \begin{cases} \{t_0', t_1', t_2'\} = \left\{ \frac{t_0^4 t_1^2}{2t_2(t_1^2-t_2^2)^2}, + \frac{t_0^3 t_1^2}{2(t_1^2-t_2^2)^2}, + \frac{t_0^2 t_1}{2(t_2^2-t_1^2)} \right\}, \\ \{t_0', t_1', t_2'\} = \left\{ -\frac{t_0^2 t_2}{2(t_2^2-t_1^2)}, \frac{t_0^2}{2t_1}, + \frac{t_0}{2} \right\}, \\ \{t_0', t_1', t_2'\} = \left\{ \frac{t_0^7}{t_1^4 t_2^2}, -\frac{t_0^6}{t_1^3 t_2^2}, -\frac{t_0^4}{t_1^2 t_2} \right\}, \\ \{t_0', t_1', t_2'\} = \left\{ + \frac{t_0^2 t_2}{2(t_2^2-t_1^2)}, \frac{t_0^2}{2t_1}, -\frac{t_0}{2} \right\}, \\ \{t_0', t_1', t_2'\} = \left\{ \frac{t_0^4 t_1^2}{2t_2(t_1^2-t_2^2)^2}, -\frac{t_0^3 t_1^2}{2(t_1^2-t_2^2)^2}, -\frac{t_0^2 t_1}{2(t_2^2-t_1^2)} \right\}. \end{cases} \tag{5.31}$$

By filling in the results from Table 5.2 into the ansatz Eq. 5.23, we can approximate the nth Tribonacci Hamiltonian as

$$H_N \approx (z_2 H_{N-3}^{(2,3)} - t_2) \oplus (z_1 H_{N-2} - t_1) \oplus (z_0 H_{N-4}^{(1,3)}) \oplus (z_1 H_{N-2} + t_1) \oplus (z_2 H_{N-3}^{(2,3)} + t_2), \tag{5.32}$$

where $z_0 = \rho^6, z_1 = \rho^2/2, z_2 = \rho^5/2$. The spectrum of the finite HTC with periodic boundary conditions is plotted in Fig. 5.1a, where the branching structure of Eq. 5.32 is apparent.

Note that as long as $p > 0$ and $q \geq 0$, the renormalisation scheme results in Table 5.2 can be used. For general (p, q), one can derive from the last three columns of Table 5.2 that

$$\begin{aligned} H_N^{(p,q)} \approx &(z_2 H_{N-3}^{(p+q,p+2q)} - t_2) \oplus (z_1 H_{N-2}^{(q,p)} - t_1) \\ &\oplus (z_0 H_{N-4}^{(p,2p+q)}) \oplus (z_1 H_{N-2}^{(q,p)} + t_1) \oplus (z_2 H_{N-3}^{(p+q,p+2q)} + t_2), \end{aligned} \tag{5.33}$$

where $t_0/t_1 = \rho^p, t_1/t_2 = \rho^q$ and $z_0 = \rho^{4p+2q}, z_1 = \rho^{p+q}/2, z_2 = \rho^{2p+3q}/2$. Since the Tribonacci word W^T maps to itself when counting occurrences between $1, 2$ or 00, we can rephrase Eq. 5.33 for the infinite HTC as

$$\begin{aligned} H^{(p,q)} \approx &(z_2 H^{(p+q,p+2q)} - t_2) \oplus (z_1 H^{(q,p)} - t_1) \\ &\oplus (z_0 H^{(p,2p+q)}) \oplus (z_1 H^{(q,p)} + t_1) \oplus (z_2 H^{(p+q,p+2q)} + t_2), \end{aligned} \tag{5.34}$$

where all coefficients are the same as in Eq. 5.33. Finally, it is necessary to comment on the error of the approximation in Eq. 5.34. The error is directly determined by the order at which the perturbation theory is performed, which is different in the five blocks of the Hamiltonian. The error in each block is determined by the next-to-leading order of z_i, i.e.

$$\begin{aligned} H^{(p,q)} = &(z_2 H^{(p+q,p+2q)} - t_2 + \mathcal{O}(\rho^2 z_2)) \oplus (z_1 H^{(q,p)} - t_1 + \mathcal{O}(\rho^2 z_1)) \\ &\oplus (z_0 H^{(p,2p+q)} + \mathcal{O}(\rho^2 z_0)) \oplus (z_1 H^{(q,p)} + t_1 + \mathcal{O}(\rho^2 z_1)) \\ &\oplus (z_2 H^{(p+q,p+2q)} + t_2 + \mathcal{O}(\rho^2 z_2)). \end{aligned} \tag{5.35}$$

The spectrum of the HTC is compared with the spectrum of the approximate RG scheme Eq. 5.32 in Fig. 5.4a. This is a numerical check that the RG scheme is a good approximation to the energy spectrum of the HTC.

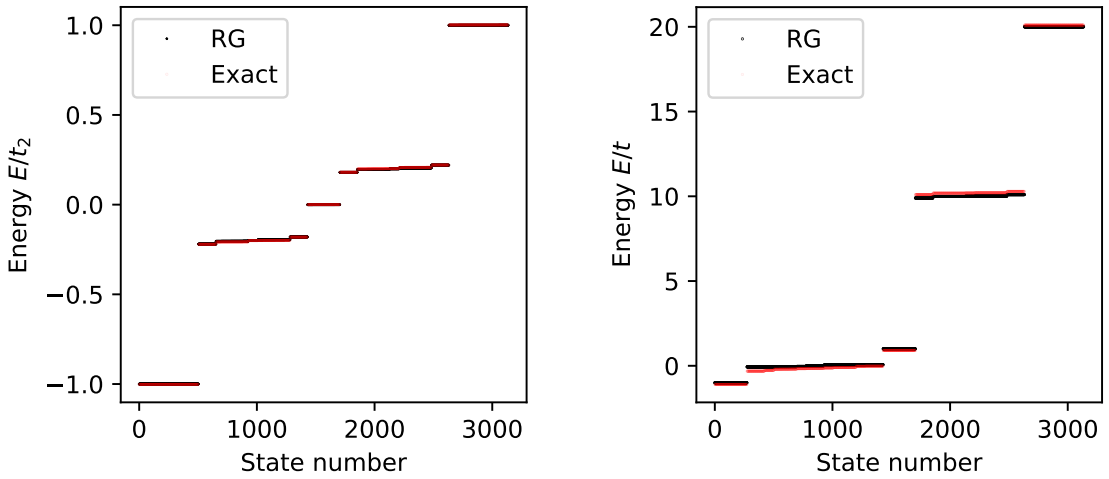

(a) The HTC H_{13} with $\rho = 0.2$.

(b) The OTC H_{13}^o with $c = 10$.

Figure 5.4.: The energy spectrum for both the HTC and OTC of $T_{13} = 3136$ lattice sites and periodic boundary conditions, compared with the approximate RG scheme Eq. 5.33 and 5.33.

5.2.3. Brillouin-Wigner Perturbation Theory for the On-Site Model

Consider the on-site model Eq. 5.3, and define

$$H_0 = \sum_{n\in\mathbb{Z}} \epsilon_n |n\rangle \langle n|, \qquad \epsilon_n = \begin{cases} \epsilon_0 & \text{if } (w)_n = 0, \\ \epsilon_1 & \text{if } (w)_n = 1, \\ \epsilon_2 & \text{if } (w)_n = 2. \end{cases}$$
$$H_1 = -t \sum_{n\in\mathbb{Z}} |n+1\rangle \langle n| + H.c.,$$

such that we can apply exactly the same BWPT formulas as in Section 5.2.2. In the case of the on-site model, we need the words occurring between subsequent occurrences of the symbols $0, 1$ and 2 in W^T, which are given in the first three rows of Table 5.1. The key result of BWPT is that the on-site Hamiltonian can be written as a block diagonal of three Hamiltonians of the *hopping model*, as will be shown in the remainder of this section. This fact plays a crucial role in the argument of Section 5.2.5, that shows the equivalence of the HTC and OTC.

Carrying out the BWPT calculations for the on-site model is less cumbersome than it was for the hopping model, since the unperturbed Hamiltonian H_0 is diagonal. Note that H_0 is a chain with three kinds of non-interacting atoms. We call them the atomic chains $0, 1, 2$, where each chain consists of the sites with energy ϵ_0, ϵ_1 and ϵ_2, respectively. Starting with the atomic 0 chain, the most frequent occurrence between 0's is the word 1, as one can see from Table 5.1. In this case, we have

$$H_0 = \epsilon_0 |1\rangle \langle 1| + \epsilon_1 |2\rangle \langle 2| + \epsilon_0 |3\rangle \langle 3|,$$
$$H_1 = -t \left(|1\rangle \langle 2| + |2\rangle \langle 3| + H.c. \right),$$

with unperturbed eigenstates

$$\begin{aligned} |1\rangle, |3\rangle, \quad & E = \epsilon_0, \\ |2\rangle, \quad & E = \epsilon_1. \end{aligned}$$

The two adjacent lattice sites of the atomic 0 chain that we are considering are $|1\rangle, |3\rangle$, and the effective coupling between them is computed as

$$t_0' = \langle 1| H_{\text{eff}} |3\rangle,$$

where H_{eff} should be of lowest order in H_1 such that t_0' is non-vanishing. For the zeroth and first order, the result vanishes, but for the second order

$$H_{\text{eff}}^{(2)} = QH_0Q + QH_1Q + QH_1P\frac{1}{E - H_0}H_1Q = H_{\text{eff}}^{(1)} + QH_1P\frac{1}{E - H_0}H_1Q,$$

the result of the computation reads

$$t_0' = \langle 1| H_{\text{eff}}^{(2)} |3\rangle = \langle 1| H_1P\frac{1}{\epsilon_0 - H_0}H_1 |3\rangle = t^2 \langle 2| \frac{1}{\epsilon_0 - H_0} |2\rangle = \frac{t^2}{\epsilon_0 - \epsilon_2}.$$

All effective couplings are computed in similar fashion in Appendix A.2, and the results are tabulated in Table 5.3.

Using the fact that the on-site chain renormalises to three HTCs with couplings given in Table 5.3, we make the ansatz that the on-site Tribonacci Hamiltonian can be approximated as

$$H_N^{\circ} \approx (z_0 H_{N-1}^{(p_0,q_0)} + \epsilon_0) \oplus (z_1 H_{N-2}^{(p_1,q_1)} + \epsilon_1) \oplus (z_2 H_{N-3}^{(p_2,q_2)} + \epsilon_2), \tag{5.36}$$

where z_i, p_i and q_i are unknown constants, that depend on c_1 and c_2 of the on-site model. The spectrum of eigenvalues of Eq. 5.36 is depicted in Fig. 5.1b, where the branching into three HTC spectra, each around the dimensionless energy ϵ_i/t, becomes apparent.

Table 5.3.: Effective hopping parameters for the OTC, part I.

E_0	t'_0	t'_1	t'_2
ϵ_0	$t^2/(\epsilon_0-\epsilon_1)$	$t^2/(\epsilon_0-\epsilon_2)$	t
ϵ_1	$t^4/(\epsilon_1-\epsilon_0)^2(\epsilon_1-\epsilon_2)$	$t^3/(\epsilon_1-\epsilon_0)^2$	$t^2/(\epsilon_1-\epsilon_0)$
ϵ_2	$t^7/(\epsilon_2-\epsilon_0)^4(\epsilon_2-\epsilon_1)^2$	$t^6/(\epsilon_2-\epsilon_0)^3(\epsilon_2-\epsilon_1)^2$	$t^4/(\epsilon_2-\epsilon_0)^2(\epsilon_2-\epsilon_1)$

Table 5.4.: Effective hopping parameters for the OTC, part II.

E_0	$a_i=\lvert t'_0/t'_1\rvert$	$b_i=\lvert t'_1/t'_2\rvert$
ϵ_0	$\lvert c_2/c_1\rvert$	$1/\lvert c_2\rvert$
ϵ_1	$1/\lvert c_2-c_1\rvert$	$1/\lvert c_1\rvert$
ϵ_2	$1/\lvert c_2\rvert$	$1/\lvert c_2(c_2-c_1)\rvert$

The values of p_i, q_i in Eq. 5.36 can be determined by computing the absolute value of the ratios $t'_0/t'_1=\rho^p, t'_1/t'_2=\rho^q$ and using the identity $a=\rho^{\log a/\log\rho}$ for any $a>0$. This results in the values $z_0=t, z_1=t/c_1, z_2=t/[c_2^2(c_2-c_1)]$ and $p_i=\log a_i/\log\rho, q_i=\log b_i/\log\rho$ for $i=0,1,2$. The values of a_i, b_i are tabulated in Table 5.4, and the fact that $0<a_i,b_i,\rho<1$ ensures that $p_i, q_i>0$. Finally, we want to point out that the renormalisation for the infinite OTC reads

$$H^{\text{on-site}} \approx (z_0 H^{(p_0,q_0)}+\epsilon_0)\oplus(z_1 H^{(p_1,q_1)}+\epsilon_1)\oplus(z_2 H^{(p_2,q_2)}+\epsilon_2), \tag{5.37}$$

where the coefficients are the same as in Eq. 5.36.

The spectrum of the OTC is compared with the spectrum of the approximate RG scheme Eq. 5.36 in Fig. 5.4b. This is a numerical check that the RG scheme is a good approximation to the energy spectrum of the OTC.

5.2.4. Proof of Renormalisation Scheme

In this section we will prove that the renormalisation in Table 5.1 is correct.

Theorem 5.1. *For each of the strings* 1, 2 *and* 00*, there are exactly three distinct words that occur between subsequent occurrences of these strings in the Tribonacci word* W^T*. These words are given by Table 5.1. Moreover, for each string, if one maps the longest word to* 0*, the shortest word to* 2 *and the other to* 1*, the order of the words reproduces the Tribonacci word* W^T*. Finally, if one considers the finite Tribonacci word* W_n^T*, the sequence of words mapped to* $0,1,2$ *generates another finite Tribonacci word of lower order when considering periodic boundary conditions. For* $1,2$ *and* 00*, these words are* W_{n-2}^T, W_{n-3}^T *and* W_{n-4}^T*, respectively.*

Proof. We will first prove the infinite case and then make a few adjustments to prove the finite case. Throughout this proof, let ρ denote the Tribonacci substitution on the alphabet $\mathcal{A}_3=\{0,1,2\}$.

- *Infinite case:* The proof will be split up in the cases 1, 2 and 00.
  - *Case 1:* Consider $w_0^1=\rho^2(0)=0102, w_1^1=\rho^2(1)=010$ and $w_2^1=\rho^2(2)=01$. To study all possible words between occurrences of 1 in W^T, it is sufficient to study $w_i^1 01=01x1$ for $i=0,1,2$ since $\rho^2(W^T)=W^T$ and each w_i^1 starts with 01. One can see x can only read $s_0^1=020, s_1^1=00$ or $s_2^1=0$. This proves that there are exactly three possible words between 1's in W^T.
  - *Case 2:* Consider $w_0^2=\rho^3(0)=0102010, w_1^2=\rho^3(1)=010201$ and $w_2^2=\rho^3(2)=0102$. To study all possible words between occurrences of 2 in W^T, it is sufficient to study $w_i^2 0102=0102x2$ for $i=0,1,2$ since $\rho^3(W^T)=W^T$ and each w_i^2 starts with 0102.

One can see x can only read $s_0^2 = 010010, s_1^2 = 01010$ or $s_2^2 = 010$. This proves that there are exactly three possible words between 2's in W^T.

– *Case 00:* Consider $w_0^{00} = \rho^4(0) = 0102010010201, w_1^{00} = \rho^4(1) = 01020100102$ and $w_2^{00} = \rho^4(2) = 0102010$. To study all possible words between occurrences of 00 in W^T, it is sufficient to study $w_i^{00}w_j^{00} = 01020100x00y$ for $i, j = 0, 1, 2$ since $\rho^4(W^T) = W^T$ one can see that both x and y contain no 00. An important note is that the above holds since the word 22 does not occur in W^T. One can see x can only read $s_0^{00} = 10201010201, s_1^{00} = 102010201$ or $s_2^{00} = 10201$. This proves that there are exactly three possible words between 00's in W^T.

So we see that the words s_i^l occur in a Tribonacci sequence, we introduce the map $\sigma : s_i^l \to i \in \mathcal{A}_3$, where $l = 1, 2, 00$. From the above, we saw that under ρ^2 (ρ^3 or ρ^4), any $i \in \mathcal{A}_3$ in W^T that is mapped to w_i^1 (w_i^2 or w_i^{00}), leads to the occurrence of the word s_i^1 (s_i^2 or s_i^{00}). Therefore, by mapping all s_i^1 (s_i^2 or s_i^{00}) in W^T back to $\mathcal{A}_3$ using σ, one exactly recovers W^T.

- *Finite case:*

  – *Case 1:* Note that for $n > 0$, the finite Tribonacci word reads $W_n^T = 01\cdots$, and we need $n > 1$ for $n - 2 \geq 0$. From the proof of the finite case above, we know that for each $i \in \mathcal{A}_3$ in W_{n-2}^T, the word s_i^1 is completed by appending any next word w_j^1 to $\rho^2(i)$, since any word reads $w_j^1 = 01\cdots$. Therefore, to form all words s_i^1 corresponding to symbols i in W_{n-2}^T, one needs to append 01 to W_n^T, which is the same as taking periodic boundary conditions, i.e. attaching the begin and end of W_n^T to form a ring. By doing this one obtains exactly W_{n-2}^T by counting words between 1's in W_n^T, using periodic boundary conditions, and mapping $\sigma : 020 \to 0, 00 \to 1, 0 \to 0$.

  – *Case 2:* Note that for $n > 1$, the finite Tribonacci word reads $W_n^T = 0102\cdots$, and we need $n > 2$ for $n - 3 \geq 0$. From the proof of the finite case, we know that for each $i \in \mathcal{A}_3$ in W_{n-3}^T, the word s_i^2 is completed by appending any next word w_j^2 to $\rho^3(i)$, since any word reads $w_j^2 = 0102\cdots$. Therefore, to form all words s_i^2 corresponding to symbols i in W_{n-3}^T, one needs to append 0102 to W_n^T, which is the same as taking periodic boundary conditions, i.e. attaching the begin and end of W_n^T to form a ring. By doing this one obtains exactly W_{n-3}^T by counting words between 2's in W_n^T, using periodic boundary conditions, and mapping $\sigma : 010010 \to 0, 01010 \to 1, 010 \to 0$.

  – *Case 00:* Note that for $n > 3$, the finite Tribonacci word reads $W_n^T = 01020100\cdots$, and we need $n > 3$ for $n - 4 \geq 0$. From the proof of the finite case, we know that for each $i \in \mathcal{A}_3$ in W_{n-4}^T, the word s_i^{00} is completed by appending any next word w_j^{00} to $\rho^4(i)$, since any word reads $w_j^{00} = 01020100\cdots$, or $w_2^{00} = 0102010$ but then appending any other word $w_k^{00} = 0\cdots$ creates a 00. When appending 01020100 to W_n^T, and mapping the words s_i^{00} between 00's in W^T to $\mathcal{A}_3$ exactly recovers W_{n-4}^T.

□

The final goal would be to prove the theorem above, for any k-bonacci word W^K, or find the proof in literature. We noted in simulations of the 4-bonacci words, it is possible that different words between occurrences of some factor have the same length, which was not the case for the Fibonacci and Tribonacci word. They do still map to the $4-$bonacci word when mapping the *frequencies* of the words to symbols $0, ..., 3$ from highest to lowest. This works perfectly by taking periodic boundary conditions, which recovers a previous generation approximant of W_N^4. In fact, this procedure works for all k-bonacci words checked in simulations. The fact that this procedure works is proven by Berthé et al. [84] for a broad class of infinite words called the Arnoux-Rauzy words, in which the Tribonacci word W^T is contained.

5.2.5. Hopping and On-site Model Equivalence

Having established the renormalisation of the Tribonacci hopping and on-site chains using perturbation theory (see Eq. 5.34 and Eq. 5.37), we are in shape to argue that the hopping and on-site model are equivalent. By *equivalence* we mean that by applying the renormalisation Eq. 5.34 for the hopping model infinitely often, it tends to the same RG fixed point as it does for the on-site model Eq. 5.37.

To make our argument more tractable, we introduce the *renormalisation depth* $N \geq 0$, which counts how often the renormalisation equations are applied to the hopping and on-site Hamiltonians. Starting with the hopping Hamiltonian $H^{(1,1)}$, note that Eq. 5.34 can be applied to $H^{(1,1)}$ to obtain five blocks, and to each of these blocks Eq. 5.34 can be applied again. This process can be continued indefinitely, where the amount of blocks for the hopping model as function of N is given by $B^{\text{hop}}(N) = 5^N$.

Now consider the on-site Hamiltonian Eq. 5.3. We can apply Eq. 5.37 once, yielding three blocks of hopping Hamiltonians. To each of these three blocks, the procedure for the hopping model can be applied. Therefore, the amount of blocks as function of N is given by $B^{\text{o-s}}(N) = \max\{1, 3 \cdot 5^{N-1}\}$.

Let us now focus on Eq. 5.34, where each block $(z_i^{(N)} H^{(p_i^{(N)}, q_i^{(N)})} - t_i^{(N)})$ at renormalisation depth $N > 0$ is described by two relevant parameters: $p_i^{(N)}, q_i^{(N)}$, where $i = 1, 2, \ldots, 5^N$. The other values are less interesting since $z_i^{(N)} \xrightarrow{N\to\infty} 0$ exponentially fast and $\lim_{N\to\infty} t_i^{(N)} \in \sigma(H)$, i.e. contains the same information as the spectrum. Denote the set of all $p_i^{(N)}, q_i^{(N)}$ as I_N such that

$$I_N = \{p_1^{(N)}, q_1^{(N)}, p_2^{(N)}, q_2^{(N)}, \ldots, p_{5^N}^{(N)}, q_{5^N}^{(N)}\}.$$

For each N, we define the probability measure μ_N on the measurable space $(I_N, 2^{I_N})$ by

$$\mu_N(A) = |A|/|I_N|,$$

where $A \subset I_N$ is any subset and $|\cdot|$ denotes the cardinality of a set. Furthermore, we introduce the set

$$J_N := \{x \in I_N \mid x \leq N\},$$

the set of $p_i^{(N)}, q_i^{(N)}$ that are less than, or equal to N. Our aim is to prove that

$$\lim_{N\to\infty} \mu_N(J_N) = 0, \tag{5.38}$$

which would imply that the RG fixed point of the Tribonacci chain, either hopping or on-site, is only described by HTCs with $p = q = \infty$, except for a part of the spectrum that has measure zero. We will also show that the RG fixed point is independent on the initial p, q in Eq. 5.34, which implies that the RG fixed points of the HTC and OTC are the same, rendering them equivalent models in the same sense as Niu and Nori [19].

The rest of this section is devoted to proving Eq. 5.38. The dynamical system on the values p, q generated by Eq. 5.34 can be represented by the map

$$f : \mathbb{R}^2 \to \mathbb{R}^{10}, \qquad (p, q) \mapsto \begin{Bmatrix} (p+q, p+2q) \\ (q, p) \\ (p, 2p+q) \\ (q, p) \\ (p+q, p+2q) \end{Bmatrix}. \tag{5.39}$$

We can modify Eq. 5.39 to the following function, that yields the same, or smaller values:

$$\tilde{f} : \mathbb{R}^2 \to \mathbb{R}^{10}, \qquad (p, q) \mapsto \begin{Bmatrix} (2\tilde{p}, 2\tilde{p}) \\ (\tilde{p}, \tilde{p}) \\ (\tilde{p}, \tilde{p}) \\ (\tilde{p}, \tilde{p}) \\ (2\tilde{p}, 2\tilde{p}) \end{Bmatrix}, \qquad \tilde{p} := \min\{p, q\} \tag{5.40}$$

Note that Eq. 5.40 is symmetric with respect to the permutation $p \leftrightarrow q$ in its arguments, as well as in each of the five tuples of the output, which allows us to write as a function of only one variable:

$$g : \mathbb{R} \to \mathbb{R}^5, \qquad \tilde{p} \mapsto \{2\tilde{p}, \tilde{p}, \tilde{p}, \tilde{p}, 2\tilde{p}\}. \tag{5.41}$$

Starting with any $p, q, \tilde{p} \in \mathbb{R}$, note that after N applications of f to p, q and g to $\tilde{p}$, it is true that $p_i^{(N)}, q_i^{(N)} \geq \tilde{p}_i^{(N)}$, for each $i = 1, 2, \ldots, 5^N$. Note that after N applications of g to some initial value $\tilde{p}$, we have a set I_N^g of 5^N different real values. Similarly, define $J_N^g := \{x \in I_N^g \mid x \leq N\}$, we can now rigorously show $\lim_{N\to\infty} |J_N^g|/|I_N^g| = 0$, which implies that Eq. 5.38 holds. Note that the map g leaves $3/5$ of its output constant and multiplies $2/5$ with a factor of two. For $x \in J_N^g$ to hold, it can be multiplied by a factor of two at most $\lfloor \log_2 N \rfloor$ times. By this argument, $|J_N^g|$ can exactly be computed by counting the possible ways that g can be successively applied to a single initial value $\tilde{p}_0 > 0$. First let $\tilde{n} = \lceil \log_2 \tilde{p}_0 \rceil$, such that $2^{\tilde{n}} \geq \tilde{p}_0$. An initial value $\tilde{p}_0$ lies in J_N^g if and only if it has been multiplied by 2 at most $\lfloor \log_2 N \rfloor - \tilde{n}$ times. Therefore, to count the number of values in J_N^g, we need to count the number of values in I_N^g that have been multiplied by 2 at most $\lfloor \log_2 N \rfloor - \tilde{n}$ times, or less. This is precisely given by the exact combinatorial argument

$$|J_N^g|/|I_N^g| = \sum_{n=0}^{\lfloor \log_2 N \rfloor - \tilde{n}} \binom{N}{n} (3/5)^{N-n} (2/5)^n < \sum_{n=0}^{\lfloor \log_2 N \rfloor} \binom{N}{n} (3/5)^{N-n} (2/5)^n,$$

which can be bounded from above as

$$\sum_{n=0}^{\lfloor \log_2 N \rfloor} \binom{N}{n} (3/5)^{N-n} (2/5)^n \leq \binom{N}{\log_2 N} (3/5)^N \log_2 N. \tag{5.42}$$

Now we need to approximate $\binom{N}{\log_2 N}$, for which we can use Stirling's approximation $\log n! = n \log n - n + \mathcal{O}(\log n)$:

$$\begin{aligned}
\log \binom{N}{\log_2 N} =& \log N! - \log(N - \log_2 N)! - \log(\log_2 N)! \\
=& N \log N - (N - \log_2 N) \log(N - \log_2 N) + \mathcal{O}(\log N) \\
=& N \log N - (N - \log_2 N) \left(\log N + \log\left(1 - \frac{\log_2 N}{N}\right)\right) + \mathcal{O}(\log N) \\
=& \frac{\log^2 N}{\log 2} + (N - \log_2 N) \left(\frac{\log_2 N}{N} + \mathcal{O}\left(\frac{\log_2^2 N}{N^2}\right)\right) + \mathcal{O}(\log N) \\
=& \frac{\log^2 N}{\log 2} + \mathcal{O}(\log N).
\end{aligned}$$

Since we are interested in the large N limit, it is enough to know the divergent behaviour of $\binom{N}{\log_2 N}$. We can now further approximate Eq. 5.42 as

$$\begin{aligned}
\binom{N}{\log_2 N} (3/5)^N \log_2 N =& e^{\log^2 N/\log 2 + \mathcal{O}(\log n)} e^{N(\log 3 - \log 5)} e^{\log \log_2 N} \\
=& e^{N(\log 3 - \log 5) + \mathcal{O}(\log^2 N)} \xrightarrow{N\to\infty} 0,
\end{aligned}$$

since $\log 3 - \log 5 < 0$. This means that

$$0 \leq |J_N|/|I_N| \leq |J_N^g|/|I_N^g| \xrightarrow{N\to\infty} 0,$$

proving the statement in Eq. 5.38.

5.3. The Rauzy Fractal

One of the tools to study the Fibonacci chain is the conumbering scheme, as explained in detail in Section 3.2.2. The conumbering scheme was obtained by projecting the Fibonacci staircase in the complementary space H. The useful property is that conumbering reorders the lattice sites according to their *local environment*. We will show in this section that the Rauzy fractal can be seen as a conumbering scheme for the Tribonacci chain. Since the Rauzy fractal plays such a central role in this section, we start off by explaining in detail what the Rauzy fractal is and how the two most common methods of generating the set are related.

5.3.1. Generating the Rauzy Fractal

There are two main ways of generating the Rauzy fractal: projecting on the contracting eigenspace of the Tribonacci substitution or using a valuation map. By using a bi-orthogonal basis of eigenvectors of the adjacency matrix of the Tribonacci substitution, we can derive the affine transformation that relates the two different methods of generating the Rauzy fractal. It turns out that the valuation map generates a Rauzy fractal where the domains are scaled versions of the whole fractal (see Fig. 5.5a), which is the canonical Rauzy fractal. The projection method yields a skewed version of this fractal (see Fig. 5.5c). It is worth noting that many sources (see Ref. [33], section 7.4.3, and Refs. [85–87]) claim that the canonical Rauzy fractal is obtained using the projection method, which is strictly speaking not the case.

The Rauzy fractal, as introduced in Section 3.2.3, was obtained by Rauzy in 1982 [26] by means of a *valuation map* E. Let $\mathcal{A} = \{0, 1, 2\}$ be the alphabet for the Tribonacci substitution ρ, then the valuation map $E : \mathcal{A}^* \to \mathbb{C}$ associates a complex number to each finite word. For any $u, v \in \mathcal{A}^*$, Rauzy demanded that $E(uv) = E(u) + E(v)$ and $E(\rho(u)) = \omega E(u)$ for some constant $\omega \in \mathbb{C}$. Note that since $\rho(W^T) = W^T$, it must be true that $E(W^T) = 0$. Denote $|u|_i$ the number of times that $i \in \mathcal{A}$ occurs in u. A crucial fact is that the Tribonacci substitution ρ is Pisot. This implies that the adjacency matrix

$$M = \begin{pmatrix} 1 & 1 & 1 \\ 1 & 0 & 0 \\ 0 & 1 & 0 \end{pmatrix},$$

defined by $M_{ij} = |\rho(j)|_i$, has one eigenvalue $|\beta| > 1$ and all other eigenvalues have $|\lambda| < 1$. The matrix M has one real eigenvalue $\beta = (1 + \sqrt[3]{19 + 3\sqrt{33}} + \sqrt[3]{19 - 3\sqrt{33}})/3 \approx 1.8392$, the Tribonacci constant, and two complex eigenvalues $\omega, \bar{\omega}$, which are complex conjugates of each other. The corresponding normalised right eigenvectors of M are denoted by $|v_\beta\rangle, |v\rangle, \overline{|v\rangle}$. The valuation map is given by

$$E(u) = \sum_{i \in \mathcal{A}} |u|_i v_i,$$

where $\langle v^t| = (v_0, v_1, v_2)$ is the left eigenvector of M, corresponding to the eigenvalue ω. The left eigenvector is obtained via the bi-orthogonal construction from Appendix B.2, which means it need not be normalised. We are now in shape to define the Rauzy fractal using the valuation map. Let $[W^T]_m$ denote the first m symbols of the Tribonacci word. The Rauzy fractal is the set

$$\mathfrak{R} := \overline{\{E([W^T]_m) \mid \forall m \in \mathbb{N})\}}, \tag{5.43}$$

which is displayed in Fig. 5.5a. This plot is made by taking the complex number $z = a + bi$, where $a, b \in \mathbb{R}$, and plotting it as a point $(a, b) \in \mathbb{R}^2$. This set can be partitioned in three domains $\mathfrak{R}_i$ where $i = 0, 1, 2$ (red, green, blue respectively), that are the same as $\mathfrak{R}$ up to a factor $\beta^{-(1+i)}$, a rotation and translation. These domains are defined by

$$\mathfrak{R}_i := \overline{\{E([W^T]_m) \mid w_m = i,\, m \in \mathbb{N})\}}, \tag{5.44}$$

where w_m denotes the mth symbol of W^T. See Ref. [88] for more details on generating the Rauzy fractal.

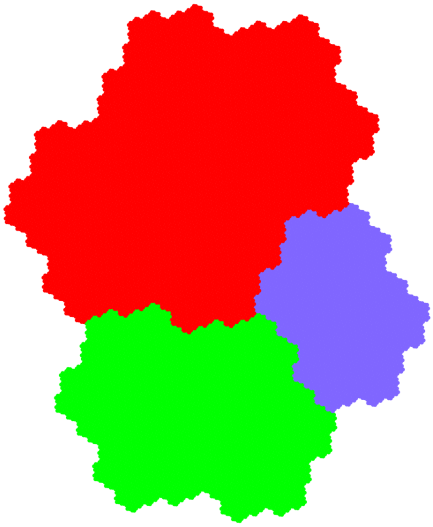

(a) Using the valuation map.

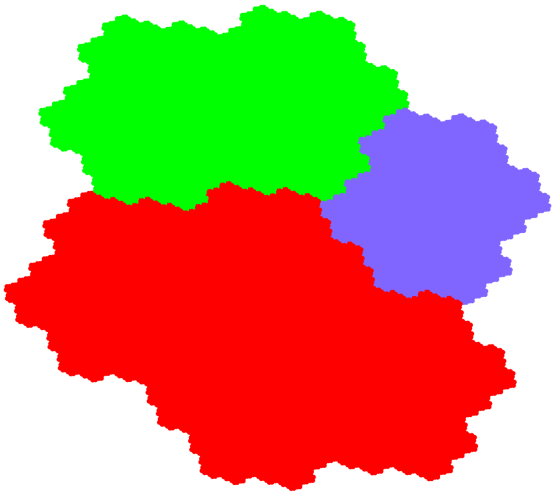

(b) Affine transformation of valuation map.

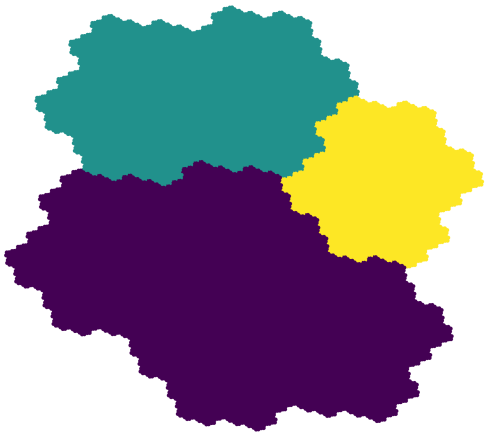

(c) Using the projection method.

Figure 5.5.: Two different Rauzy fractals.

The second method, which we refer to as the *projection method*, is the method explained in Section 3.2.3. Let the unstable eigenspace E^u of M be the one-dimensional real space spanned by $|v_\beta\rangle$, and the stable eigenspace E^s be spanned by $\{|\mathrm{re}\rangle, |\mathrm{im}\rangle\}$, where $|\mathrm{re}\rangle = \mathrm{Re}\{|v\rangle\}$ and $|\mathrm{im}\rangle = \mathrm{Im}\{|v\rangle\}$. Equivalently, one can define $E^s = \{c\,|v\rangle + \bar{c}|\overline{v}\rangle \mid c \in \mathbb{C}\} \subset \mathbb{R}^3$. Denote π the projection along E^u onto E^s. Any $|x\rangle \in \mathbb{R}^3$ can be uniquely decomposed as $|x\rangle = \gamma\,|v_\beta\rangle + c\,|v\rangle + \bar{c}|\overline{v}\rangle$ where $\gamma \in \mathbb{R}, c \in \mathbb{C}$. The map π then acts as $\pi\,|x\rangle = c\,|v\rangle + \bar{c}|\overline{v}\rangle$. Denoting the mth point in the staircase as $|x_m\rangle = \sum_{i=0}^{m} |e_{w_i}\rangle$, the projection method yields the Rauzy fractal

$$R = \overline{\{\pi\,|x_m\rangle \mid m \in \mathbb{N}\}},$$

which is displayed in Fig. 5.5c. One immediate connection between the valuation and the projection method, is the fact that the valuation map can be written as

$$E([W^T]_m) = \langle v^t | x_m \rangle = c,$$

where we used $|x_m\rangle = \gamma\,|v_\beta\rangle + c\,|v\rangle + \bar{c}|\overline{v}\rangle$ and the fact that $\{\langle v_\beta^t|, \langle v^t|, \overline{\langle v^t|}\}$ and $\{|v_\beta\rangle, |v\rangle, |\overline{v}\rangle\}$ form a bi-orthogonal system.

The question now is: how are the sets in Figs 5.5a and 5.5c related? We will derive an affine transformation that maps the former to the latter as points in $\mathbb{R}^2$. We first need a choice of basis to represent the points of $\mathfrak{R}$ and R in $\mathbb{R}^2$. For the complex numbers in $\mathfrak{R}$, we have the canonical representation $z = a + bi \mapsto (a, b) \in \mathbb{R}^2$. In associating E^s with $\mathbb{R}^2$, we have some freedom. By applying a Gram-Schmidt procedure to the real and imaginary parts of $|v\rangle$, we can define

$$\begin{aligned} |e_1\rangle &= |\mathrm{re}\rangle / \||\mathrm{re}\rangle\|, \\ |e_2\rangle &= |\mathrm{res}\rangle / \||\mathrm{res}\rangle\|, \qquad \text{where } |\mathrm{res}\rangle = |\mathrm{im}\rangle - \langle e_1|\mathrm{im}\rangle |e_1\rangle . \end{aligned} \tag{5.45}$$

Then we can represent any $|x\rangle = a' |e_1\rangle + b' |e_2\rangle \in E^s \subset \mathbb{R}^3$ as $(a', b') \in \mathbb{R}^2$.

We can now answer the question: for a given $|x_m\rangle$, how are (a, b) and (a', b') related? For a fixed $m \in \mathbb{N}$, we have seen that $E([W^T]_m) = c = a + bi$ and $\pi |x_m\rangle = c |v\rangle + \bar{c}|\overline{v}\rangle = a' |e_1\rangle + b' |e_2\rangle$. The answer is the matrix A that solves

$$\begin{pmatrix} a' \\ b' \end{pmatrix} = A \begin{pmatrix} a \\ b \end{pmatrix} . \tag{5.46}$$

By noting that

$$|x\rangle = c |v\rangle + \bar{c}|\overline{v}\rangle = 2a |\mathrm{re}\rangle - 2b |\mathrm{im}\rangle , \tag{5.47}$$

and inverting Eqs. 5.45 to obtain

$$\begin{aligned} |\mathrm{re}\rangle &= \||\mathrm{re}\rangle\| |e_1\rangle , \\ |\mathrm{im}\rangle &= \||\mathrm{res}\rangle\| |e_2\rangle + \langle e_1|\mathrm{im}\rangle |e_1\rangle , \end{aligned} \tag{5.48}$$

we can plug Eqs. 5.48 into Eq. 5.47 to obtain

$$|x\rangle = (2a\||\mathrm{re}\rangle\| - 2b \langle e_1|\mathrm{im}\rangle) |e_1\rangle - 2b\||\mathrm{res}\rangle\| |e_2\rangle ,$$

from which we can read off the matrix A as being given by

$$A = \begin{pmatrix} 2\||\mathrm{re}\rangle\| & -2 \langle e_1|\mathrm{im}\rangle \\ 0 & -2\||\mathrm{res}\rangle\| \end{pmatrix} . \tag{5.49}$$

To demonstrate the correctness of Eq. 5.46, the map in Eq. 5.49 is applied to $\mathfrak{R}$ in Fig. 5.5a, which yields the result in Fig. 5.5b. It is of no surprise that Figs. 5.5b and 5.5c are identical, since we have just derived the mathematical correspondence between the two.

5.3.2. The Rauzy Fractal vs. Conumbering

In this section, the Rauzy fractal will be proposed as a conumbering scheme for the Tribonacci chain. We will discuss many similarities with the conumbering scheme for the Fibonacci chain, and some essential differences.

First of all, the Rauzy fractal is obtained by projecting the Tribonacci staircase onto the internal space of the CPS, as demonstrated in Section 3.2.3. The result is the canonical Rauzy fractal up to an affine transformation, as shown in Section 5.3.1. So the Rauzy fractal and the conumbering scheme both order the lattice points in a compact set in the internal space of their CPS.

We saw in Eq. 5.44 that the Rauzy fractal can be decomposed into domains, where the mth point was classified by the local environment of the mth letter in the Tribonacci word W^T. Since the letters in W^T define the on-site potentials in the OTC Eq. 5.3, it is clear that the red, green and blue regions in Fig. 5.5a contain exactly the lattice points with on-site potential ϵ_0, ϵ_1 and ϵ_2, respectively.

To order the lattice points of the HTC Eq. 5.1, we need to partition $\mathfrak{R}$ in a different way. Note that around a lattice point, one can have three distinct local environments:

1. Red: 01 (t_0 on the left and t_1 on the right) or 10,

2. Green: 02 or 20,
3. Blue: 00.

Environments 1 and 2 indicate that the lattice point lies in the molecular type-1 (type-2) chain, and environment 3 is the atomic chain. Analogous to Eq. 5.44, we have the following partition:

$$\mathfrak{R}_\omega := \overline{\{E([W^T]_m) \mid w_{m-1}w_m = \omega,\, m \in \mathbb{N})\}}, \tag{5.50}$$

where $\omega = 00, 01, 10, 02, 20$. The resulting partition is depicted in Fig. 5.6, where $01, 10$ are red, $02, 20$ green and 00 blue, respectively. It is now clear how the Rauzy fractal can be used to order the lattice points, for both the hopping and on-site model, according to their local structure.

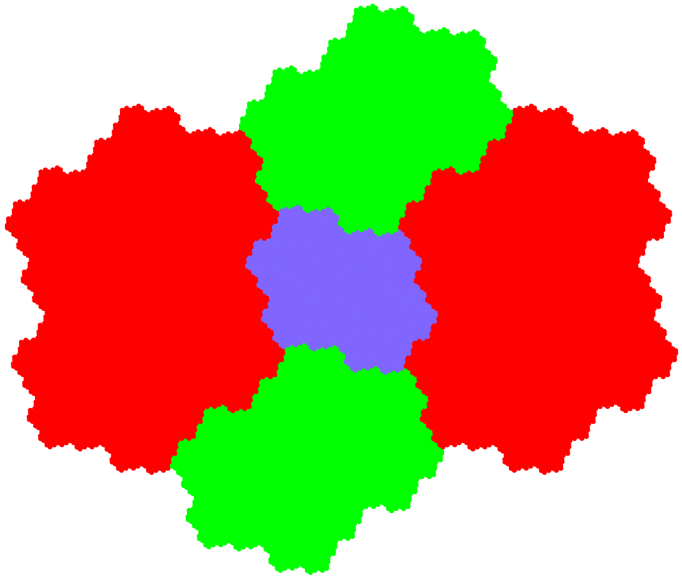

Figure 5.6.: Partition of the Rauzy fractal for the HTC Eq. 5.1.

One can go a step further, and consider the possible environments of the local structures discussed above. For example, if one takes the local structure 020 in W^T, what are the distinct local environments? First, because of the constraints of the Tribonacci substitution, the first few letters around 020 are predetermined, being 0102010. Now, we find the possible letters x, y such that the factor $x0102010y$ occurs in W^T. The possible values xy turn out to be:

$0 : xy = 01, 10,$

$1 : xy = 02, 20,$

$2 : xy = 00.$

For each label $0, 1$ and 2, the xy values *always* occur in pairs, in the sense that if $x = 01$ is the environment of the nth occurrence of 020 in W^T, then $x = 10$ must be the environment of the $(n+1)$th occurrence. Moreover, when determining xy for all occurrences of 020 in W^T, then if the pair (or single value for label 2) of xy values is mapped to its corresponding letter (0,1 or 2 as in the enumeration above), one exactly obtains W^T. We have no proof of this claim, but tested it extensively numerically, while all the time applying periodic boundary conditions to the Tribonacci approximants W_N^T.

For the factors $0, 00, 010$ and 020 of W^T, the possible environments are given in Table 5.5. The question that naturally arises is if one can keep iterating the process of finding the environments of environments, and so on. In Section 5.3.3, we will show that the RG scheme is enough to generate Table 5.5 and all subsequent environments for the Tribonacci word.

Table 5.5.: For every factor, the environments of the extended factor, due to the Tribonacci substitution constraints, are given, together with the corresponding label (0,1 or 2). The columns corresponding to $0, 010$ and 020 are used to subdivide the Rauzy fractal for the on-site model, and the columns $00, 010$ and 020 are used similarly for the hopping model.

Factor of W^T	0	00	010	020
Environments	$x0y$	$x01020100102010y$	$x010y$	$x0102010y$
0	$xy = 12, 21$	$xy = 12, 21$	$xy = 20, 02$	$xy = 01, 10$
1	$xy = 01, 10$	$xy = 01, 10$	$xy = 21, 12$	$xy = 02, 20$
2	$xy = 11$	$xy = 11$	$xy = 22$	$xy = 00$

Having discussed the similarities with the conumbering, we now turn to the essential differences between the Rauzy fractal and conumbering. As demonstrated by Macé et al. [22], the conumbering scheme is useful when plotting all eigenstates in a 2D grid, where one axis labels the conumbered sites, and the other axis the ordered energy levels. Since the Rauzy fractal orders the points of a 1D lattice in a compact set in two dimensions, it cannot be used to reorder the Tribonacci lattice sites in a meaningful way to make a similar 2D plot. Alternatively, one could plot the wavefunction onto the Rauzy fractal and study the stack of Rauzy fractals, where the stack is made up of one Rauzy fractal per energy level. The study of wavefunctions on the Rauzy fractal is carried out in the remainder of this chapter.

5.3.3. Wavefunctions on the Rauzy Fractal

In order to study wavefunctions on the Rauzy fractal, we take a finite Tribonacci chain and numerically compute the eigenvalues and wavefunctions. For an energy E_i in the spectrum, the wavefunction $|\psi\rangle_i$ has value $\psi_i(n) \in \mathbb{R}$ on site n. As discussed in the previous section, we project the lattice sites onto the internal space of the CPS to obtain the Rauzy fractal. An example wavefunction of the HTC and OTC is plotted on the Rauzy fractal in Fig. 5.7(a) and (c). More examples of the wavefunctions for the HTC and OTC are found in the Appendix A.5 Figs. A.15 and A.16, respectively.

The key observation is if E_i is from a certain band, the wavefunction ψ_i is localised primarily on lattice sites associated to that band. More precisely, the spectrum of the OTC splits up into three bands, one around each ϵ_i, as discussed in Section 5.2.3. Now if E_j is contained in the band around ϵ_i, then $\psi_j(k)$ has primarily support on lattice sites with on-site energy $\epsilon_{w_k} = \epsilon_i$. Equivalently, we saw in Section 5.2.2 that the spectrum of the HTC splits up into five bands, one centered around each $\pm t_2, \pm t_1, 0$. If E_i sits in a band associated to some atomic chain or molecular 1 (or 2) (anti-)bonding chain, the wavefunction $\psi_i(j)$ has primarily support on that particular chain. We would like to point out the similarity between the eigenstates $|\psi\rangle_0$ in Fig. 5.7(a) and in the red region in Fig. 5.7(d). This can be understood by the fact that the eigenstate $|\psi\rangle_0$ of the OTC H^o_{13} is approximately the eigenstate of the first block of Eq. 5.36, which is a HTC.

Upon subdividing the Rauzy fractal again according to Table 5.5, Figs. 5.7(b) and (d) are obtained. In view of th RG scheme Eqs. 5.33 and 5.36, the subdivision of the Rauzy fractal can be understood in two equivalent ways: 1) by determining the environments of the nearest neighbor structures of the lattice sites (which is Table 5.5), 2) By considering the nearest neighbors of the lattice sites of the renormalised atomic and molecular chains. Since one can keep applying the RG scheme, we have shown that *the RG scheme naturally gives the environments of a lattice site.*

Since the interaction between sites is finite, there are some nonzero amplitudes on the other regions of the Rauzy fractal. Finally, when looking at the plots of the wavefunctions, it seems that scaled down copies of the same pattern are repeated. These patterns correspond to the environments of lattice sites and can be explained from the local symmetries of the chain, as will be shown in

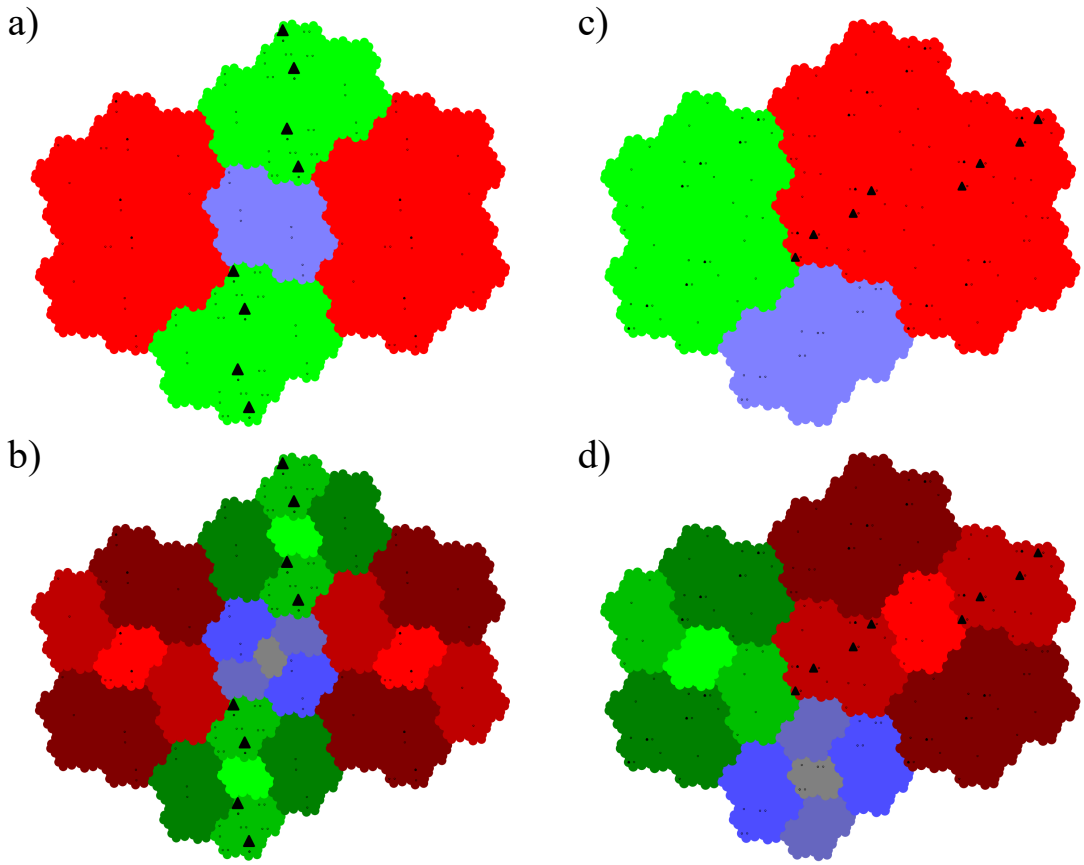

Figure 5.7.: The eigenstate $|\psi\rangle_0$ on the Rauzy fractal of $T_{13} = 3136$ points. The regions are colored according to the local environment of a lattice site n in the HTC (or OTC), and the length of the black triangles are proportional to $|\psi_0(n)|^2$. (a) $|\psi\rangle_0$ of the HTC H_{13} with coupling $\rho = 0.2$ and coloring according to nearest-neighbor bonds. (b) $|\psi\rangle_0$ of the HTC H_{13} with coupling $\rho = 0.2$ and coloring according to the five possible environments of the local structures in a). (c) $|\psi\rangle_0$ of the OTC H^o_{13} with coupling $c = 5$ and and coloring according the on-site potential of a lattice site. (d) $|\psi\rangle_0$ of the OTC H^o_{13} with coupling $c = 5$ and coloring according to the five possible environments of the lattice sites in c).

Section 5.3.4.

5.3.4. Local Resonator Modes

It is an interesting fact that all local environments are known from only the nearest-neighbor structures and the RG Eq. 5.33. This fact can be applied to elegantly categorize all Local Resonator Modes (LRMs) of the HTC and OTC. This LRM framework was developed by Röntgen et al. [24], and applied to the Fibonacci chain, among other chains. The LRM framework is used to perturbatively describe the eigenstates of a on-site model, based on the *local* structures of the chain, such as the environments given in Table 5.5. By the diagonal nature of an unperturbed on-site model, the theoretical underpinnings of the framework could be developed with relative ease. In principle, the framework could be developed for hopping models, but this would require an arduous development of the theory. Therefore, we focus on the OTC Eq. 5.3 first, and later show numerical evidence that the framework can be similarly applied to the HTC Eq. 5.1.

Consider the on-site model Eq. 5.3, which is parameterised as $c_1 = c_2/2 = c = 100$, such that the chain is at high contrast. Furthermore, we consider the chain with periodic boundary conditions and $T_7 = 81$ sites, depicted in Fig. 5.9. In the same way that the spectrum can be split up in three parts, see Eq. 5.36, one can identify three bands of eigenstates that are clustered around ϵ_0, ϵ_1 and ϵ_2 with T_6, T_5, T_4 states per band, respectively. In a band of eigenstates corresponding to ϵ_i, one can see that the states are primarily localised on the sites with potential ϵ_i (in agreement with Section 5.3.3). Furthermore, the arrangements of the wavefunctions on these sites is determined by the *local* structures of the OTC, as given in Table 5.5, which is precisely what the local resonator framework by Röntgen et al. [24] describes.

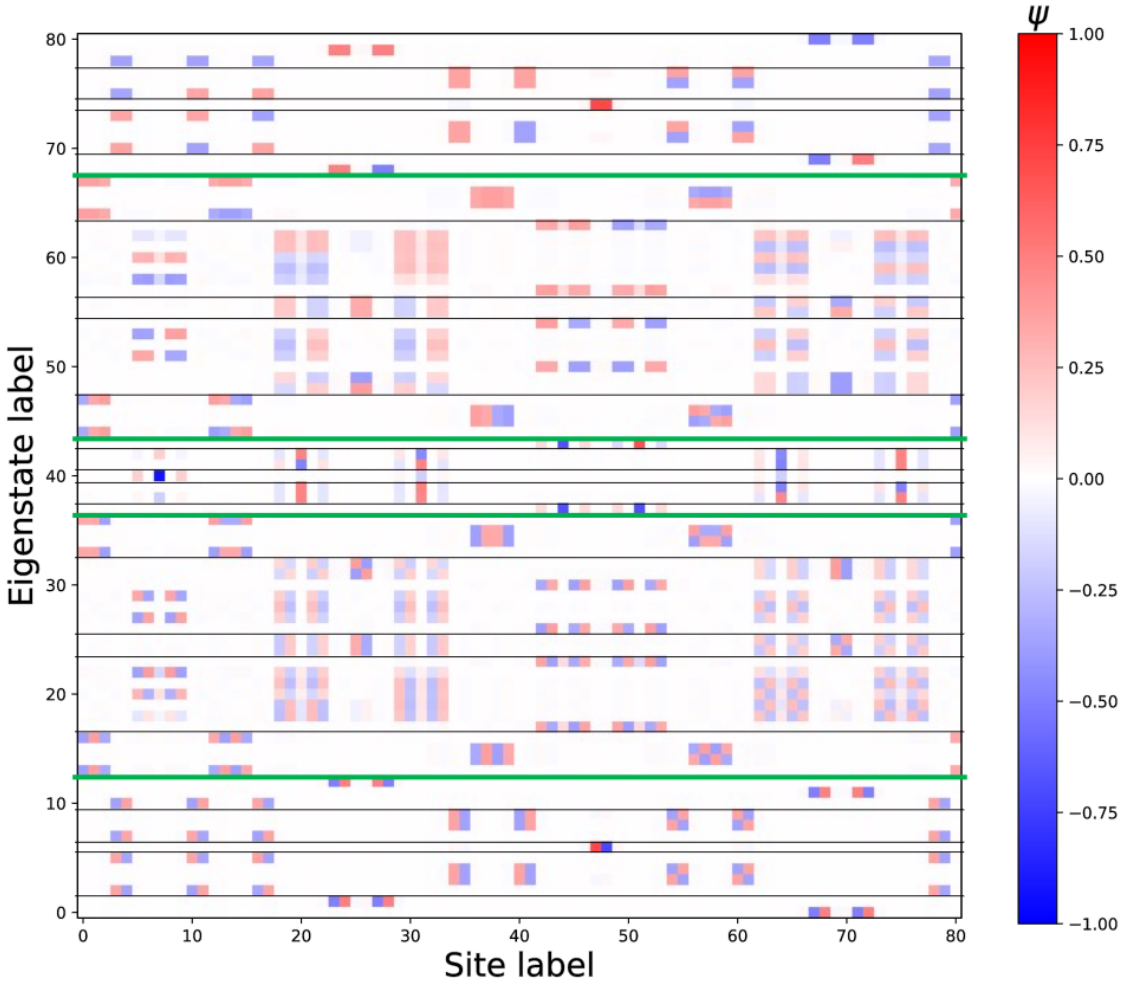

Figure 5.8.: The HTC eigenstates $|\psi\rangle_i$ of H_7, ordered such that $E_i < E_{i+1}$. The sign and magnitude on each site is represented by a color. The green lines denote the splitting after one RG step, the black lines denote two RG steps. Note that the states between two subsequent lines localize on similar local environments, which is more accurate for the black lines than for the green lines.

In similar fashion, one can take the HTC with periodic boundary conditions and $T_7 = 81$ sites at weak coupling, in this case $\rho = 0.1$ is taken. The eigenstates with their sign are compared to the Tribonacci chain structure in Fig. 5.8. Analogous to Eq. 5.33, we can identify five bands of eigenstates. Again, in each of these bands, the states primarily sit on the sites which belong to the corresponding atomic/molecular (anti)bonding chain. Here, the amount of states per block is exactly T_4, T_5, T_3, T_5, T_4, respectively. Finally, since each of the bands between the green lines in

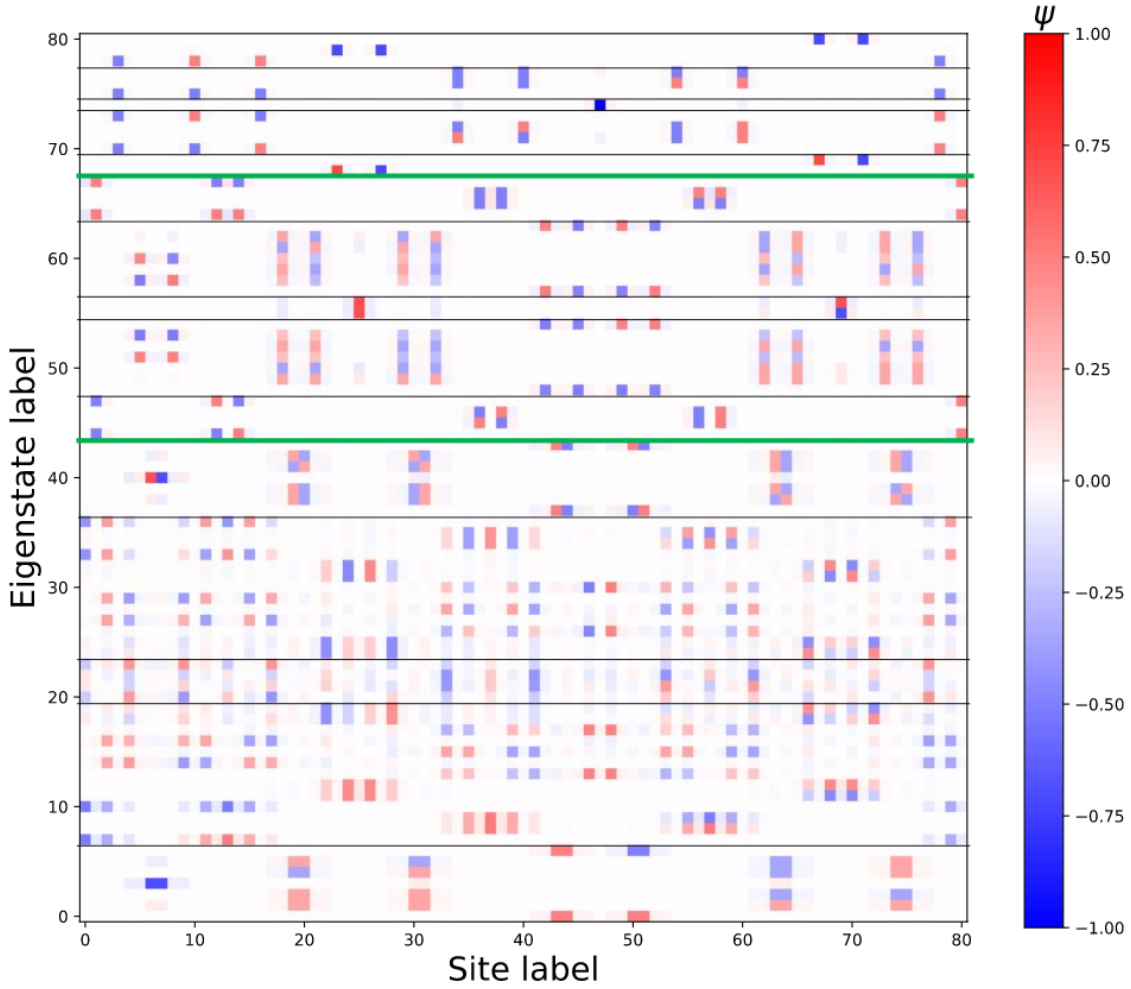

Figure 5.9.: The OTC eigenstates $|\psi\rangle_i$ of H_7^o. The colors and green/black lines have the same meaning as in Fig. 5.8.

Fig. 5.9 is approximately described by a HTC according to Eq. 5.36, these bands themselves have a comparable local resonator structure to that in Fig. 5.8.

The states between the green lines in Figs. 5.8 and 5.9 correspond to the same class of LRMs. Upon subdividing the area between these green bands, marked with black lines, the classes of LRMs become more refined. The key insight is that the refinement of the LRMs corresponds one-to-one with the refinement of environments of a lattice site in Table 5.5. We note that this correspondence is only shown to hold on a qualitative level, by counting the amount of eigenstates and studying their localisation, and should be proven and studied more quantitatively in future work.

The main conclusion of this section is that the wavefunctions of the Tribonacci chains can be described by the framework of LRMs, where the LRMs correspond to eigenstates that localise on one type lattice sites that have a particular environment. This means that the wavefunction is determined by the band in which the energy of the state lies, together with the local resonator structures of the sites/bonds belonging to that energy band. This is key to understanding the structure of the wavefunctions when plotted on the Rauzy fractal in Section 5.3.3: The RG scheme naturally gives all environments of a lattice site, and at the same time categorizes the LRMs. This simplification of the analysis is founded on the self-similarity of the Tribonacci word.

5.4. Edge States in the Tribonacci Chain

Up to now, we have studied the HTC and OTC models with exclusively periodic boundary conditions. Now, we impose open boundary conditions to the HTC in Eq. 5.1 which yields the Hamiltonian

$$\tilde{H}_{N,\Delta} = \sum_{n=0}^{T_N-2+\Delta} t_{w_n} |n+1\rangle \langle n| + H.c., \tag{5.51}$$

where the parameter $\Delta \in \mathbb{Z}$ can be set nonzero to tune the truncation of the chain. Adding or removing sites by varying Δ does not introduce disorder, since the added/removed bonds still follow the Tribonacci word. Note that one could also add/remove bonds at the beginning of the chain. However, we do not explore that here since there is a priori no reason why the left end is qualitatively different than the right end, and understanding the truncation behaviour of one side would enable us to understand the other side as well.

Upon choosing certain approximants N and truncation parameters Δ, the energy spectrum reveals in-gap modes. These modes indicate localisation since there is no state nearby, so they do not tunnel well into the bulk and therefore must localise. To study the edge modes, we fix some N, Δ and collect *all* modes that show exponential decay instead of looking only at pronounced in-gap modes.

We take $N = 8, \Delta = 0$, corresponding to Fig. 5.10a, and study all eigenstates. For these values, the Tribonacci word begins and ends as (up to the first difference) $0102 \cdots 0010$. The exponentially decaying edge modes are filtered out by checking if the logarithm is roughly linear. All left and right edge modes, together with their location in the spectrum, are displayed in Figs. 5.11 and 5.12, respectively. Note that we look only at states up to $E = 0$, as all $E > 0$ states are simply chiral partners of $E < 0$ energy states. First of all, we see that there are both left and right edge modes. Second of all, the amount of "noise" in the exponential decay seems to correlate with the gap size in which the mode lies. By "noise" we mean the deviation from a pure exponential decay. This deviation is not truly noise here, since it is a deterministic pattern that is determined by Tribonacci substitution.

To say more about the effect of choosing a different truncation, we take $N = 8, \Delta = 1$, which adds one bond to the chain. The left and right edge modes for this system are shown in Figs. 5.13 and 5.14, respectively. Firstly, note from Figs. 5.11 and 5.13 that the left edge modes are unaffected by changing the truncation of the right side of the chain. Moreover, note that the right edge mode for $N = 8, \Delta = 1$ in Fig. 5.14a decays much faster than the one for $N = 8, \Delta = 0$ in Fig. 5.12c, while the latter state lies in a bigger gap than the former. This means that the strength of the exponential decay is not necessarily related to the gap size in which the edge mode lies.

For $N = 8, \Delta = -2$ and $N = 9, \Delta = 0, 1, -2$, the same analysis as done in this chapter is carried out in Appendix A.4. The results of the full analysis regarding edge states in the HTC with open boundary conditions can be summarised as follows:

- The left edge states are unaffected by different truncations of the right hand side.
- Gap width or distance to a band seems not to be the guiding principle in determining the exponential decay.
- Because of chiral symmetry, each edge mode $|\psi\rangle$ has a chiral partner $\Gamma |\psi\rangle$.

5.5. Tribonacci Topological Charge Pump

In this section, we study the consequences of charge pumping on an Tribonacci chain. The charge pump will directly inherit the spectral properties of the Tribonacci chain, which determine the way in which charges (electrons) are transported. The work in this section is a generalisation of the Fibonacci charge pump in Ref. [89].

Firstly, the concept of a charge pump is explained in Section 5.5.1, after which the topological aspects of charge pumping are shown in Section 5.5.2. In Section 5.5.3 we consider the Tribonacci variant of the charge pump and in Section 5.5.4, the charge pump for general aperiodic modulations is studied.

5.5.1. Introduction to Charge Pumping

A charge pump, originally studied by Thouless et al. [90], is a one-dimensional system that is modulated periodically in time in an adiabatic fashion. The working principle can be qualitatively compared to the screw of Archimedes in Fig. 5.15(a): After each full rotation of the screw, a unit of water is pumped upwards and the screw is back to its original position. In an analogy with a charge pumping Hamiltonian, the screw represents the potential in the Hamiltonian and water represents the charges.

In a charge pumping Hamiltonian, there is often a background potential $U_0(x)$, which is static in time, and a time-varying periodic modulation $U_1(x,t)$, that has the same spatial period as U_0. This situation is depicted in Fig. 5.15(b), where charges are pumped by the movement of the modulating potential U_1. Note that U_1 is not necessarily strong enough to overcome the potential barrier of U_0 in a classical sense, but since we are working in a quantum mechanical regime, charge is pumped by particles tunneling to adjacent lattice sites.

The simplest model that captures the essential aspects of charge pumping is the Rice-Mele charge pump. Using the definition of the model from Ref. [89], the Rice-Mele Hamiltonian reads

$$\begin{aligned} H(t) = \sum_{n\in\mathbb{Z}} (\{[\Delta - (-1)^n \delta(t)]\,|n+1\rangle\langle n| + H.c.\} - (-1)^n h(t)\,|n\rangle\langle n|), \\ \delta(t) = \delta_0 \cos(2\pi t/T), \qquad h(t) = h_0 \sin(2\pi t/T), \end{aligned} \tag{5.52}$$

where Δ is a constant hopping term, representing the static potential, T the period of the temporal modulation and h_0, δ_0 real parameters. Instead of giving a full explanation of charge pumping, for which we refer the reader to chapters 4 and 5 of Ref. [92], we explain how charge pumping manifests itself in a single-particle model like Eq. 5.52.

Consider the spectrum of Eq. 5.52 with a finite number of sites and open boundary conditions in Fig. 5.16b for all values $t \in [0,T]$, where the Fermi level is taken to be $E_F/\Delta = 0$. The hallmark of charge pumping is that a single particle is pumped to one end of the chain, and that at the end this particle is pumped through the Fermi level, which must lie in a energy gap of the infinite system. The amount of charges that are pumped is equal to the number of energy levels that cross the Fermi level from below in one pumping cycle [92], which is one charge in the case of Fig. 5.16b. To respect the symmetries of the system, for each charged pumped upwards (the red line in Fig. 5.16b), there must be a corresponding charge being pumped downwards (the green line in Fig. 5.16b). Since this crossing is an effect that is only visible upon enforcing open boundary conditions, Fig. 5.16a gives us no information in that regard. However, in the next section we will show that charge pumping is a topological property than can be derived from the bulk system, i.e. the system with periodic boundary conditions.

5.5.2. Topological Aspects of Charge Pumping

In chapter 5 of Ref. [92], it is shown that the amount of pumped particles in Eq. 5.52 per cycle is given by a Chern number

$$C = \frac{1}{2\pi} \int_0^T \mathrm{d}t \int_0^{2\pi} \mathrm{d}k F(k,t), \tag{5.53}$$

with $F(k,t)$ the Berry curvature defined by

$$F(k,t) = \sum_{n\in\mathrm{occ}} i\big[\,\langle \partial_t u_n(k,t) | \partial_k u_n(k,t)\rangle - \langle \partial_k u_n(k,t) | \partial_t u_n(k,t)\rangle\,\big], \tag{5.54}$$

where $|u_n(k,t)\rangle$ are the eigenstates of the Bloch Hamiltonian (see Section 3.5.2 how to compute it) of Eq. 5.52 corresponding to the occupied bands. For $\Delta > |h_0|, |\delta_0|$, the Hamiltonian Eq. 5.52 is topological with $C = 1$ and pumps exactly one unit of charge per cycle [89,92]. The fact that the amount of charges is a topological invariant, a Chern number, means that the amount of pumped charges is quantised and constant under continuous deformations of Eq. 5.52 that leave the band gap finite in Fig. 5.16a. The band gap is required to remain finite, otherwise it is ambiguous which eigenstates correspond to the filled bands in Eq. 5.54.

As shown in Ref. [89], one can derive Eq. 5.53 for systems that lack translational invariance, which do not allow for the construction of a Bloch Hamiltonian. Suppose one has a rectangular lattice with L_x, L_y sites in the x- and y-direction, respectively. Let the Fermi projector

$$P = \sum_{n \in \text{occ}} |\psi_n\rangle \langle \psi_n| , \tag{5.55}$$

be the projector on the filled eigenstates $|\psi_n\rangle$. In order to make the position operators $\hat{x}, \hat{y}$ compatible with periodic boundary conditions $x \sim x + L_x, y \sim y + L_y$, we consider the operators

$$\begin{aligned} \begin{pmatrix} \mathbf{0}_{M,M} & \mathbf{0}_{M,N} \\ \mathbf{0}_{N,M} & U \end{pmatrix} &= P \exp\left\{ 2\pi i \frac{\hat{x}}{L_x} \right\} P = P_x, \\ \begin{pmatrix} \mathbf{0}_{M,M} & \mathbf{0}_{M,N} \\ \mathbf{0}_{N,M} & V \end{pmatrix} &= P \exp\left\{ 2\pi i \frac{\hat{y}}{L_y} \right\} P = P_y, \end{aligned} \tag{5.56}$$

where the basis of P_x, P_y is chosen to be the eigenstates $|\psi_n\rangle$ where $n = 1, \ldots, M$ label the empty states and $n = M+1, \ldots, L_x L_y$ label the filled states, of which there are a total of N. Furthermore, we denote $\mathbf{0}_{A,B}$ as a $A \times B$ matrix of zeros and U and V are $N \times N$ matrices. If λ_i denote the eigenvalues of $VUV^\dagger U^\dagger$, the *Bott index* is defined as

$$I_{\text{Bott}} = \frac{1}{2\pi} \sum_i \operatorname{Im} \ln \lambda_i = \frac{1}{2\pi} \operatorname{Im} \operatorname{Tr} \ln VUV^\dagger U^\dagger. \tag{5.57}$$

The Bott index is an object originating from K-theory, which measures the anti-commutativity of two operators U, V. In a physical setting, the Bott index operators U, V in Eq. 5.56 measures the geometric (Berry) phase that is picked up as the Hamiltonian is varied along a closed loop in parameter space. For a mathematical approach that bridges the gap with its application in physics, we recommend Ref. [93]. For a more physics-oriented approach, as used in this section, we refer the reader to Refs. [89,94,95].

We will now show exactly how the Bott index relates to the Chern number in Eq. 5.53 of the Rice-Mele model. As shown in Ref. [89], the unitary x-position operator $U^\dagger$ acts as

$$\exp\left\{ -2\pi i \frac{\hat{x}}{L_x} \right\} = \sum_{k_n} |k_n\rangle \left\langle k_n - \frac{2\pi}{L_x} \right|, \qquad |x\rangle = \frac{1}{\sqrt{L_x}} \sum_{k_n} e^{i k_n x} |k_n\rangle ,$$

where $k_n = 2\pi n / L_x$ and $n = 1, 2, \ldots, L_x$, and a similar result with $x \to y$ holds for the y-position operator. If one now assumes the Bloch Hamiltonian exists and considers some momentum eigenstate $|\psi(k_x, k_y)\rangle$, the operator $VUV^\dagger U^\dagger$ acts as an anti-clockwise translation of the eigenstate along the perimeter of the rectangle $[k_x, k_x + 2\pi/L_x] \times [k_y, k_y + 2\pi/L_y]$. Therefore, the eigenvalues λ_n of $VUV^\dagger U^\dagger$ are precisely the Berry phases $e^{i\gamma_n}$ of translating an eigenstate $|\psi_n\rangle$ along a rectangle in k-space. The final step is to identify the y-dimension with time $t \in [0, T]$. This has the effect of changing the action $V^\dagger : k_y \mapsto k_y + 2\pi/L_y$ to $V^\dagger : t \mapsto t + \Delta t$, where $\Delta t = T/L_y$ and L_y is an integer that parameterises the discretisation of the time domain. This change is directly implemented by taking $V^\dagger = e^{-iHt}$, the time-evolution operator.

By taking the imaginary part of the logarithm in Eq. 5.57, the Bott index is precisely the sum of all Berry fluxes γ_n. The key connection to the Chern number is that it is given by the sum of

Berry fluxes [92], and therefore the Bott index in Eq. 5.57 is proven to be equivalent to the Chern number in Eq. 5.53 in Refs. [93, 96].

Finally, we briefly explain the numerical method from Ref. [89] for evaluating the Bott index Eq. 5.57 that is used in Sections 5.5.3 and 5.5.4. For a general pump Hamiltonian $H(t)$ with L lattice sites and periodic boundary conditions, discretise the interval $[0, T]$ into N intervals of width $\Delta t = T/N$, where $\tilde{T} = \{0, \Delta t, \ldots, (N-1)\Delta t\}$ denotes the set of all time values. For every $t \in \tilde{T}$, the Schrödinger equation $H(t)\,|\psi_n(t)\rangle = E_n(t)\,|\psi_n(t)\rangle$ is solved. Each eigenstate is written in position basis as $|\psi_n(t)\rangle = \sum_{l=1}^{L} \psi_n(t)\,|l\rangle$, such that the operator $\exp\{2\pi i\hat{x}/L\}$ acts on a state as $\exp\{2\pi i\hat{x}/L\}\,|\psi_n(t)\rangle = \sum_{l=1}^{L} e^{2l\pi i/L}\psi_n(t)\,|l\rangle$. Using these definitions, one defines the $M \times M$ matrices $\tilde{U}_t, \tilde{V}_{t,t+\Delta t}$ for every $t \in \tilde{T}$ as

$$[\tilde{U}_t]_{n,m} = \langle\psi_n(t)|\exp\left\{2\pi i\frac{\hat{x}}{L}\right\}|\psi_m(t)\rangle\,, \qquad [\tilde{V}_{t,t+\Delta t}]_{n,m} = \langle\psi_n(t)|\psi_m(t+\Delta t)\rangle\,, \tag{5.58}$$

where the indices n, m run over the $M \leq L$ filled states of the system. The Bott index Eq. 5.57 is approximated by the formula

$$\tilde{I}_{\text{Bott}} = \frac{1}{2\pi}\sum_{t\in\tilde{T}} \operatorname{Im}\operatorname{Tr}\ln \tilde{V}_{t,t+\Delta t}\tilde{U}_{t+\Delta t}\tilde{V}^{\dagger}_{t,t+\Delta t}\tilde{U}^{\dagger}_{t}, \tag{5.59}$$

which recovers Eq. 5.57 in the limit $\Delta t \to 0$ [89].

5.5.3. The Tribonacci Charge Pump

In the work by Yoshii et al. [89], the Rice-Mele charge pump is modified using the Fibonacci word f from Section 3.1.3. This is done by replacing the terms $(-1)^n$ in Eq. 5.52, which represent an infinite periodic string $\cdots 01010101 \cdots$, with the term $(-1)^{(f^{(bi)})_n}$, where $(f^{(bi)})_n$ denotes the nth word of the bi-infinite Fibonacci word f. In this way, a weak bond corresponding to a 0 in f is mapped to $(-1)^0 = 1$ and a strong bond 1 in f is mapped to the value -1.

Since we have three letters $0, 1$ and 2 in the Tribonacci word, we cannot simply raise -1 to the power of a letter, since 0 and 2 would result in the same contribution. Since the t_2 bonds are stronger than the t_1 bonds in the Tribonacci chain, we choose the replacement

$$(-1)^n \to g(n) = \begin{cases} 1 & \text{if } w_n = 0, \\ -1 & \text{if } w_n = 1, \\ -2 & \text{if } w_n = 2. \end{cases}$$

in Eq. 5.52, where w_n is the nth letter of the bi-infinite Tribonacci word. Although this is a physically motivated choice, one can choose any three distinct values that are associated to the letters $0, 1$ and 2 in the Tribonacci word.

Before turning to our results, let us briefly explain the main results of the work in Ref. [89]. In the limit of infinite system size, the Rice-Mele charge pump in Eq. 5.52 has a time-dependent two-band Bloch Hamiltonian since the unit cell consists of two sites. Therefore, the only valid filling that one can choose is half-filling. In the case of an aperiodic Rice-Mele pump, such as the Fibonacci pump in Ref. [89], there is no well-defined unit cell, hence any filling can be chosen. Yoshii et al. [89] showed that the Fibonacci Rice-Mele pump with $\Delta > |h_0|, |\delta_0|$ can pump a charge at various filling levels, which they call *multilevel pumping*. The way to compute the amount of pumped charges for a given filling is to numerically evaluate the Bott index Eq. 5.59 for a finite system with periodic boundary conditions at the desired filling.

The first step in studying the pumping behaviour of the Tribonacci charge pump is to compute the energy levels during one cycle, which are displayed in Fig. 5.17. First, note that for any value

of $t \in [0, T]$, the energy spectrum in Fig. 5.17a can be divided into five bands, analogous to the spectrum of the HTC in Fig. 5.1a. Upon taking open boundary conditions in Fig. 5.17b, it is clear that lines emerge that traverse energy bands during one cycle. The open boundary spectrum is shown as well in Fig. 5.17c for $\Delta = 20$, in which case the model is a regular monoatomic hopping chain with a perturbative Rice-Mele modulation.

In order to see whether the models in Figs. 5.17b and 5.17c are in fact charge pumps, we numerically evaluate the Bott index Eq. 5.59. The results for a Tribonacci Rice-Mele charge pump with $T_6 = 44$ sites can be summarised as follows:

- For $\Delta = 2, 20, 200, 2000$, the Bott index is one for *all fillings except* $M = 0, 1$. This means that the system pumps precisely one charge for all fillings, except $M = 0, 1$, independent of Δ.
- The Fibonacci Rice-Mele model with $F_8 = 34$ and $F_9 = 55$ sites yields exactly the same results regarding the Bott indices.

There is one observation that is, to our best knowledge, not compatible with the working principle of the charge pump as explained by Asboth et al. in Ref. [92]. In Fig. 5.17c, there is clearly no energy level traversing the well-separated bands. This is consistent with the picture where the model is a regular hopping chain with a Rice-Mele modulation that weak. In that case, however, one would expect a zero Bott index for fillings that lie in between the separated bands in Fig. 5.17c. This is not the case for the numerically computed Bott indices using Eq. 5.59. In order to resolve this dichotomy, a starting point would be to numerically compute the location of Wannier centers during one full cycle and compare it with the result of the Bott index. As explained in Ref. [92], if these centers move one lattice site, this means one charge has been pumped.

5.5.4. General Aperiodic Charge Pumping

The multilevel pumping, found by Yoshii et al. [89] in the Fibonacci Rice-Mele model which is also present in the Tribonacci Rice-Mele model in Section 5.5.3, turns out to be a common feature of aperiodic Rice-Mele models. More specifically, we show the multilevel pumping behaviour of Rice-Mele models based on the Thue-Morse, Rudin-Shapiro, silver mean substitution.

The Thue-Morse substitution is a binary substitution explained in Section 3.1.4, yielding the binary Thue-Morse word $W^{TM} = \cdots w_{-1}^{TM} | w_0^{TM} w_1^{TM} \cdots$. The silver mean ρ_{SM} substitution is a generalisation of the Fibonacci substitution that reads

$$\rho_{SM} : 0 \mapsto 010, \quad 1 \mapsto 0, \tag{5.60}$$

for which we denote the fixed point word as $W^{SM} = \cdots w_{-1}^{SM} | w_0^{SM} w_1^{SM} \cdots$. The Rudin-Shapiro substitution ρ_{RS} is a four-letter substitution that reads

$$\rho_{RS} : 0 \mapsto 01, \quad 1 \mapsto 02, \quad 2 \mapsto 31, \quad 3 \mapsto 32, \tag{5.61}$$

resulting in the fixed point $\tilde{W}^{RS}$. The binary Rudin-Shapiro word $W^{RS} = \cdots w_{-1}^{RS} | w_0^{RS} w_1^{RS} \cdots$ is obtained by mapping $1 \mapsto 0$, $2 \mapsto 1$ and $3 \mapsto 1$ in $\tilde{W}^{RS}$. Using these aperiodic binary words, we study the Rice-Mele model where $(-1)^n \to (-1)^{w_n^x}$ is taken with a fixed $x \in \{TM, SM, RS\}$.

For the three aperiodic words, the energy levels of the corresponding Rice-Mele pump are displayed in Fig. 5.18. For each model, it is clear that there are energy levels that move from one band of energy levels to another during a cycle, which is an indication of charge pumping. We numerically compute the Bott index for the finite systems with periodic boundary conditions using Eq. 5.59. For $\Delta = 2, 20$ and $h_0 = \delta_0 = 1$, we obtain the following conclusions for the silver mean pump with 41 sites and both the Thue-Morse as well as the Rudin-Shapiro pump with 32 sites:

- The silver mean and Rudin-Shapiro systems have a Bott index of one for all fillings except the fillings $M = 0, 1$. This is precisely the same situation as for the Fibonacci and Tribonacci Rice-Mele pumps.

- The Thue-Morse system has a Bott index of one for all *even* fillings, independent of Δ. For odd fillings, the Bott index takes varying integers, which values depend on Δ.

In that sense, the three aperiodic chains display multilevel pumping as well, where for the Thue-Morse chain one should consider only even fillings. It is an interesting open question why the pumping behaviour of the silver mean and Rudin-Shapiro pumps, where the latter is not even a quasicrystal, is similar to the Fibonacci and Tribonacci case, but the Thue-Morse pump, also not a quasicrystal, is different.

The fact that the numerically computed Bott index is almost always equal to one for the Fibonacci, Tribonacci, Silver mean, and Rudin-Shapiro chain, especially in the absence of a band crossing, is an important topic for further research. If one was to further investigate this topic, we recommend the following courses of action:

1. First, attempt to analytically compute the Chern number Eq. 5.53 for the Rice-Mele model in Ref. [89], and look if this is always equal to one for $\delta_0 \neq 0$ and $h_0 \neq 0$, as they claim to be the case. If that is indeed true, then the model in Ref. [89] is an inappropriate model for topological charge pumping, since there would be charge pumping without an energy level crossing.
2. Study the finite-size effects on the result of the numerical computation of the Bott index. Because of limited computational resources and time, we have only studied aperiodic chains with ~ 100 lattice sites. It could be the case that the results become radically different if one increases the number of lattice sites.
3. Study the stability and correctness of the numerical scheme proposed in Ref. [89], which is used here as well. It could be the case that numerical artefacts cause the Bott index to be nonzero as we are not in the thermodynamic limit, hence the Bott index need not be equal to the Chern number.

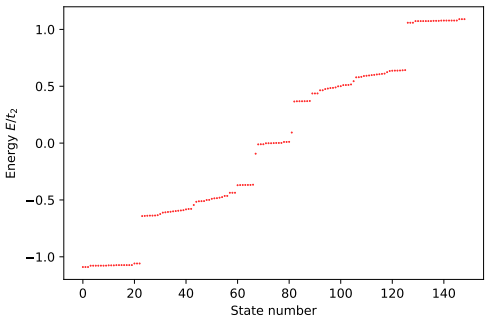

(a) $N = 8, \Delta = 0$.

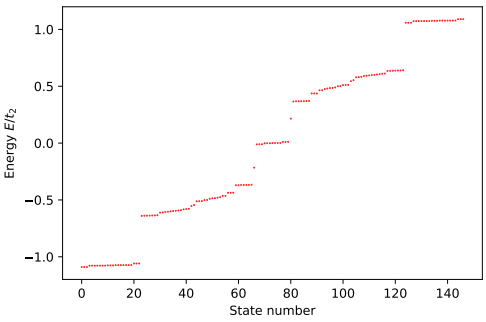

(b) $N = 8, \Delta = -2$.

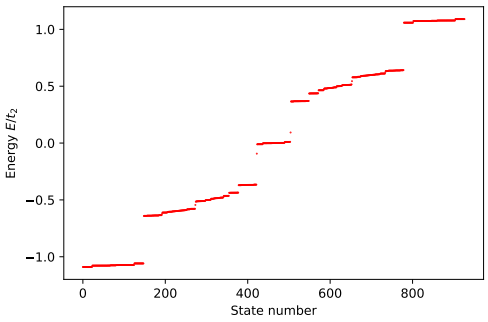

(c) $N = 11, \Delta = 0$.

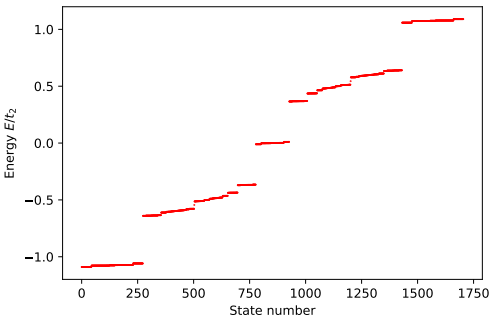

(d) $N = 12, \Delta = 0$.

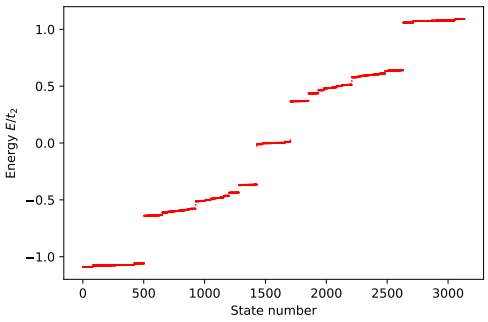

(e) $N = 13, \Delta = 0$.

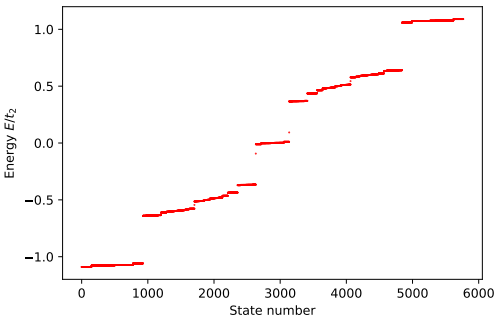

(f) $N = 14, \Delta = 0$.

Figure 5.10.: The energy spectrum of the HTC with open boundary conditions Eq. 5.51 for various N, Δ, where some exhibit pronounced in-gap modes.

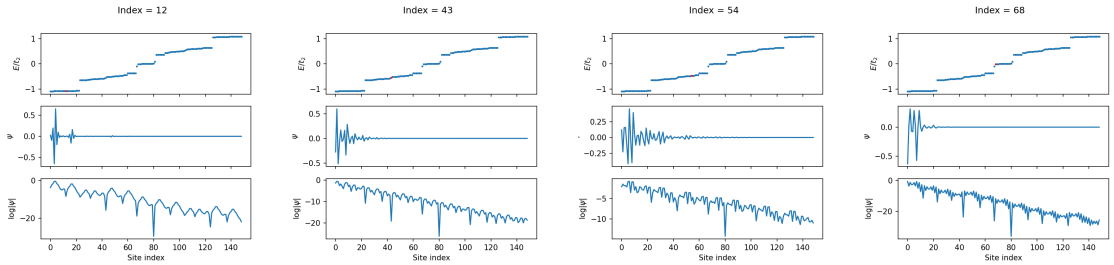

(a) (b) (c) (d)

Figure 5.11.: All left modes of $N = 8, \Delta = 0$.

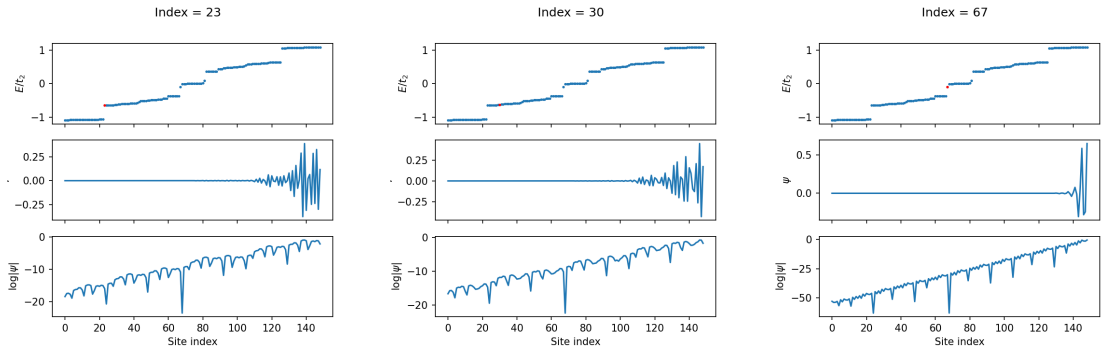

(a) (b) (c)

Figure 5.12.: All right edge modes of $N = 8, \Delta = 0$.

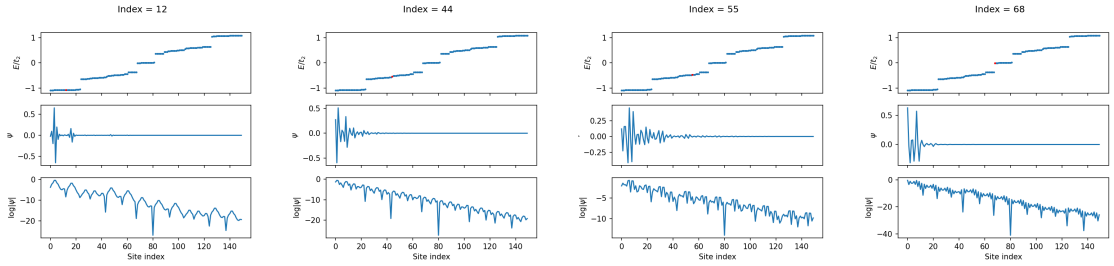

(a) (b) (c) (d)

Figure 5.13.: All left modes of $N = 8, \Delta = 1$.

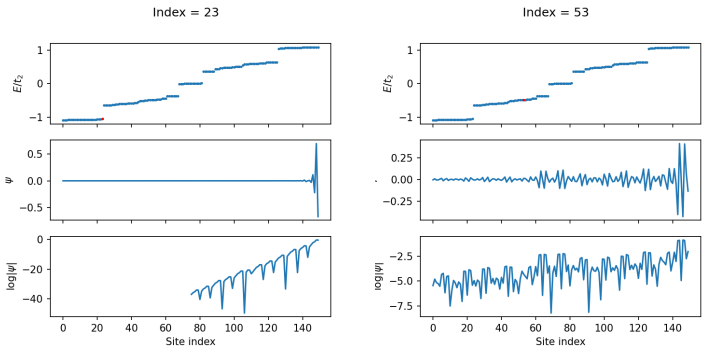

(a) (b) Questionable edge mode.

Figure 5.14.: All right edge modes of $N = 8, \Delta = 1$.

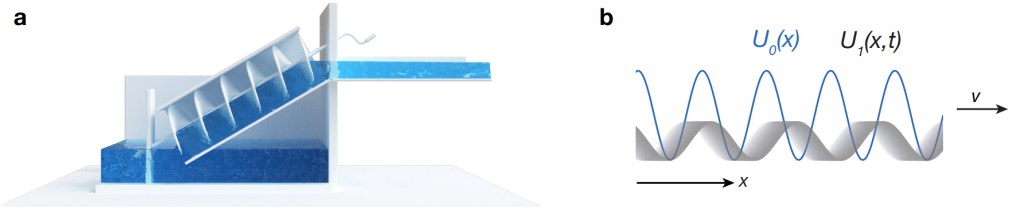

Figure 5.15.: a) Archimedes' screw: pumping water by periodic motion. b) The static potential U_0 and the modulating potential U_1 (figure from Ref. [91]).

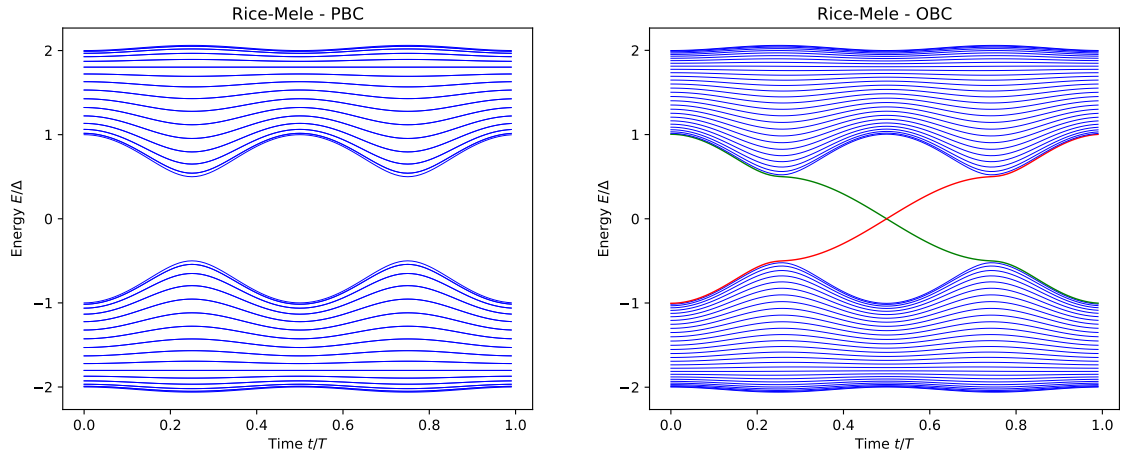

(a) Periodic boundary conditions.

(b) Open boundary conditions.

Figure 5.16.: The Rice-Mele charge pump spectrum for $\Delta = 2, \delta_0 = h_0 = 1$, and 60 lattice sites. The red line indicates a charged pumped to the upper band, and the green line indicates a charge pumped to the lower band.

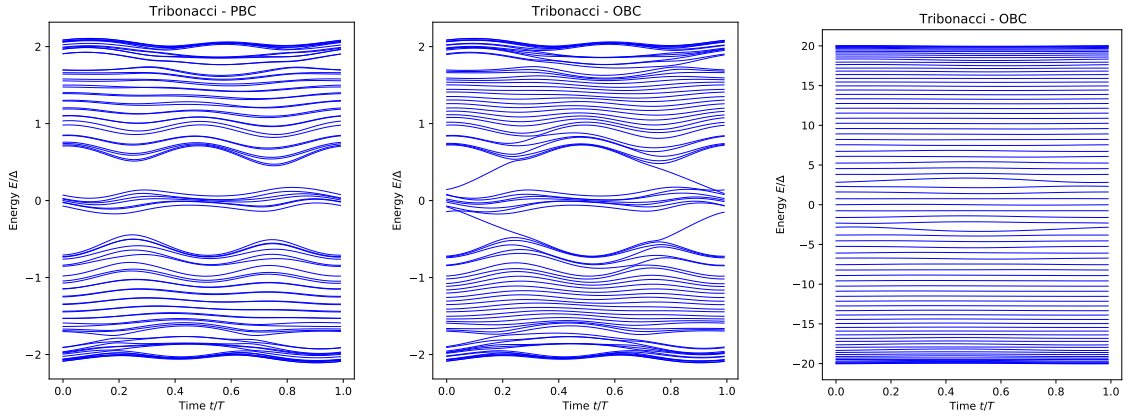

(a) Periodic boundary conditions, $\Delta = 2$.

(b) Open boundary conditions, $\Delta = 2$.

(c) Open boundary conditions, $\Delta = 20$.

Figure 5.17.: The energy levels during a full cycle of the Tribonacci Rice-Mele pump with $T_7 = 81$ sites, $h_0 = \delta_0 = 1$, and various Δ values.

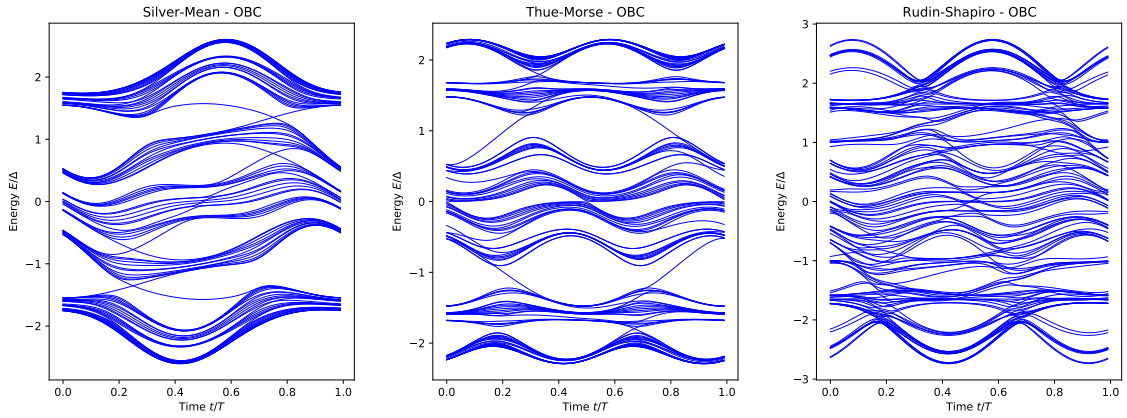

(a) Silver mean pump, 99 lattice sites.

(b) Thue-Morse pump, 128 lattice sites.

(c) Rudin-Shapiro pump, 128 lattice sites.

Figure 5.18.: The energy levels during a full cycle of three finite aperiodic Rice-Mele pumps with $\Delta = 2, h_0 = \delta_0 = 1$ and open boundary conditions.

6. Topology in Physics

The aim of this chapter is to introduce topology in physics from a viewpoint that is accessible to both physicists as well as mathematicians. While relying on the least amount of background knowledge from both physics and mathematics, we bridge the mathematical theory of topology and the classification of symmetry protected topological (SPT) states in a rigorous way. To achieve this goal, we introduce all necessary concepts from mathematics and physics in Section 6.1. Subsequently, we introduce the concept of topology in physics, and explain the bulk-boundary correspondence: a hallmark of topology in condensed matter. Subsequently, the mechanism of symmetry protected topology is explained in Section 6.3. Finally, in Section 6.4, the full tenfold way classification of translationally-invariant SPT states is given in the context of K-theory, which completes the bridge between topology in condensed matter and mathematical topology.

Central references on which this chapter is based are the review papers by Chiu et al. [11] and Ludwig [10].

6.1. Preliminaries

6.1.1. Mathematical Topology of Spaces and Maps

The mathematical subject of topology describes properties of objects "modulo" continuous deformations. If two objects can be deformed continuously into each other, they are topologically equivalent. The only properties of interest are those that are kept invariant under those continuous deformations, such as the amount of holes in a sheet, or the structure of a knot. These properties are called *topological invariants*. Perhaps the most famous example of a continuous deformation is the equivalence between the doughnut and the coffee mug, where the amount of holes (both have one) is kept invariant during the continuous deformation.

In this brief mathematical section, we review the mathematical concepts of topology that are used throughout this chapter. We start by defining what a topology is, and how it allows for the definition of a continuous map.

Definition 6.1. *(Topology, topological space, open set, neighborhood) Let X be a set and τ a family of subsets of X. The family τ is topology on X if and only if*

1. $\emptyset, X \in \tau$,
2. *For any collection $(A_\alpha)_{\alpha\in I}$ (I may be uncountable) where each $A_\alpha \in \tau$, the union $\bigcup_{\alpha\in I} A_\alpha \in \tau$ is a member of the topology,*
3. *For any finite collection $A_i \in \tau$, the intersection $\bigcap_i A_i \in \tau$.*

If τ is a topology, the tuple (X, τ) is a topological space. We often say that X is a topological space, by which we mean (X, τ).

Given a topological space (X, τ), we say that a subset $U \subset X$ is open if and only $U \in \tau$. Finally, a neighborhood of a point $x \in X$ is any set $V \subset X$ such that there exists an open set $U \in \tau$ for which $x \in U \subset V \subset X$ holds.

Since we will be working with topological spaces, let us briefly discuss the most important topologies that we will need. Firstly, if $X \subset \mathbb{R}^d$, we will *always* take the "natural" topology τ_d on the

real numbers. This topology is defined as the smallest topology that contains all open d-balls

$$B_d(x,r) = \{y \in X \mid d(x,y) < r\}, \qquad x \in X, \quad r > 0,$$

where $d(\cdot,\cdot)$ is the Euclidean metric. Secondly, if we have two topological spaces (X, τ_X) and (Y, τ_Y), the product topology on the space $X \times Y$ is defined by

$$\tau_{X\times Y} := \{D \subset X \times Y \mid \forall\,(x,y) \in D\ \exists U \in \tau_X, V \in \tau_Y \text{ such that } x \in U, y \in V, \text{ and } U \times V \subset D\}.$$

Unless specified otherwise, the topology of $X \times Y$, where X, Y are topological spaces, will be taken to be the product topology.

Definition 6.2. *(Continuous map) Let $f : X \to Y$ be a map between the topological spaces X, Y. The map f is continuous if and only if for every open set $V \subset Y$, the inverse image*

$$f^{-1}(V) = \{x \in X \mid f(x) \in V\} = U$$

is an open set. Furthermore f is said to be continuous at a point $x \in X$ if and only if $f^{-1}(V)$ is a neighborhood of x for every neighborhood V of $f(x) \in Y$.

A key notion in topology is the equivalence between two topological spaces.

Definition 6.3. *(Homeomorphism, topological equivalence, topological invariant) A homeomorphism between two topological spaces X, Y is a bijective continuous map $f : X \to Y$ with continuous inverse. If there exists a homeomorphism between two topological spaces X and Y, they are said to be topologically equivalent, denoted by $X \cong Y$.*

If X is a topological space and denote $p(X)$ as some property of X, then $p(X)$ is called a topological invariant if $p(X) = p(Y)$ for every Y such that $X \cong Y$.

Next, one can study the maps between topological spaces, and their equivalence.

Definition 6.4. *(Homotopy) Let $f : X \to Y$ be a continuous map between topological spaces X, Y. A homotopy of f is a family of continuous maps $(f_t)_{t\in[0,1]} : X \to Y$ such that:*

1. *$f_0 = f$,*
2. *The map $F : X \times [0,1] \to Y$ is continuous, where $F(x,t) := f_t(x)$.*

Furthermore, we say that f_0 and f_1 are homotopic, denoted by $f_0 \simeq f_1$. Two maps f, g are said to be homotopic if and only if there exists such a map F, satisfying the above properties, with $F(x,0) = f$ and $F(x,1) = g$.

Now, we are ready to introduce homotopy classes; the topologically distinct maps between topological spaces.

Definition 6.5. *(Homotopy Class) Let X and Y be any topological space. The set*

$$[X,Y] := \{f : X \to Y \mid f \text{ continuous}\}/\sim,$$

contains all equivalence classes of topologically distinct maps. The equivalence relation $\sim$ is defined on the set of continuous functions, where $f \sim g$ holds if and only if $f \simeq g$, i.e. they are homotopic.

Finally, we introduce the concept of path-connectedness and the set of path-connected components.

Definition 6.6. *(Path-connected, path-connected component) Two points $x, y \in X$ in a topological space X are said to be path-connected if and only if there exists a continuous function $f : [0,1] \to X$ such that $f(0) = x$ and $f(1) = y$, defining an equivalence relation. Denote $x \sim y$ as the equivalence relation, where two points are equivalent if they are path-connected. The set of points $y \in X$ that satisfy $x \sim y$ constitute the path-connected component of $x \in X$. The set of path-connected components is denoted*

$$\pi_0(X) = X/\sim .$$

A topological space X is path connected if $\pi_0(X) = \{1\}$, i.e. consists of one element, or equivalently $x \sim y$ for all $x, y \in X$.

Topology of Loops

A tractable setting to apply the above definitions is a loop in the punctured plane $P = \mathbb{R}^2 \setminus \{0\}$. Let $\mathbb{S}^1 = [0,1]/(0 \sim 1)$ denote the unit circle, i.e. the interval $[0,1]$ where the begin and end are glued together.

Definition 6.7. *(Loop) A loop in the space X is a continuous map $\gamma : \mathbb{S}^1 \to X$.*

Two loops γ_1 and γ_2 in any space X are homotopic if and only if there exists a family of loops $\gamma_{[t]}$ for $t \in [0,1]$, such that $\gamma_{[0]} = \gamma_1, \gamma_{[1]} = \gamma_2$, and the map $t \mapsto \gamma_{[t]}$ is continuous in the space of loops. We will now show why a loop cannot be "untied" from the origin in the punctured plane P in a continuous way. Consider the loops in P

$$\gamma_1(x) = \begin{pmatrix} \cos 2\pi x \\ \sin 2\pi x \end{pmatrix}, \qquad \gamma_2(x) = \begin{pmatrix} \cos 2\pi x - 2 \\ \sin 2\pi x \end{pmatrix}, \qquad \gamma_{[t]}(x) = \begin{pmatrix} \cos 2\pi x - 2t \\ \sin 2\pi x \end{pmatrix}, \tag{6.1}$$

where γ_1 encloses the puncture in P and γ_2 does not. By observing that $\gamma_{[1/2]}(0) = 0 \notin P$, it is clear that $\gamma_{[1/2]}$ is *not* a loop in P. Hence, γ_1 and γ_2 are not topologically equivalent. Note that this is not a proof, since one has to show that the loops cannot be deformed into each other for any choice of family $\gamma_{[t]}$. In similar fashion, one cannot continuously deform the two loops

$$\gamma_3(x) = \begin{pmatrix} \cos 4\pi x \\ \sin 4\pi x \end{pmatrix}, \tag{6.2}$$

and γ_1 into each other, since γ_1 wraps once around the punctured origin and γ_3 wraps two times.

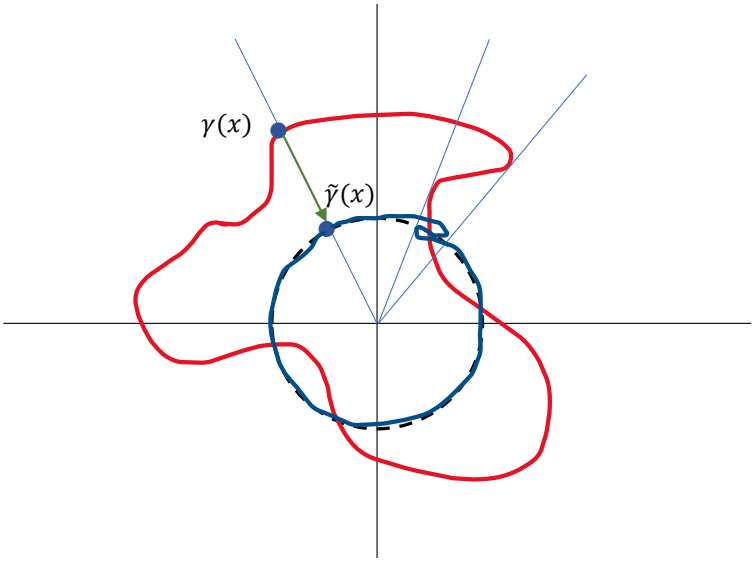

Figure 6.1.: Projecting a loop γ (red) onto the unit circle (dashed). The resulting projected loop $\tilde{\gamma}$ is schematically depicted in blue.

Instead of constructing explicit continuous maps between loops to study their topological equivalence, it is often useful to study properties that are kept invariant during continuous deformations: topological invariants. In the case of loops in the punctured plane P, the relevant topological invariant is the winding number ν [97]. The winding number counts the amount of times that the loop winds around the puncture, counting $+1$ for each anti-clockwise winding and -1 for each clockwise winding. To see why the winding number is a topological invariant, take any loop γ. Since the puncture is at the origin, each point on the loop can be projected onto the unit circle in P in a continuous way by the map $\gamma(x) \mapsto \gamma(x)/||\gamma(x)||_2 =: \tilde{\gamma}(x) = (\cos\phi(x), \sin\phi(x))^T$, where $\phi(x)$ is the phase that parameterises the unit circle (see Fig. 6.1). In fact, for any loop γ and its

projected version $\tilde{\gamma}$ are homotopic. The winding number is then the integral of the phase over $\mathbb{S}^1$, divided by the phase of one winding

$$\nu(\gamma) = \frac{1}{2\pi}\int_{\mathbb{S}^1} \mathrm{d}\phi(x) = \frac{1}{2\pi}\int_{\mathbb{S}^1} \frac{\mathrm{d}\phi}{\mathrm{d}x}\mathrm{d}x \in \mathbb{Z}, \tag{6.3}$$

which must be an integer [98]. Because ν is restricted to the discrete set $\mathbb{Z}$, the winding number reads $\nu(\gamma) = \nu(\gamma')$ for any pair of homotopic loops $\gamma \sim \gamma'$. The power of Eq. 6.3 is that it can immediately decide whether or not two loops are homotopic, without explicitly constructing a homotopy.

Note that the target space P is not homeomorhpic to $\mathbb{R}^2$, in which all loops are nullhomotopic. On the other hand, if we were to cut open the base space $\mathbb{S}^1$ to a regular interval, all images in P would be open strings, which are nullhomotopic. These examples show that the topology of both the base space as well as the target space influence the topological properties of the mapping between them.

For proofs, and more details regarding loops, we refer the reader to the books by Nakahara [99] and Hatcher [98], where the former is most suitable for physicists and the latter for mathematicians.

6.1.2. Quantum Mechanics

Model Definition

To be more precise, the physical systems that we consider are *gapped*, *non-interacting*, *fermionic second-quantised* Hamiltonians. These systems are described with fermionic creation (annihilation) operators $\hat{\psi}_I^\dagger$ ($\hat{\psi}_I$) where $I = i_1, \ldots, i_N$ in the case of N lattice sites, that act on the fermionic Fock space $\mathcal{H} := F_-(H)$, the many-body Hilbert space, where H is the single-particle Hilbert space. The indices $i_1, \ldots i_N$ are general multi-indices that can also have orbital or spin degrees of freedom. These operators obey the canonical fermionic anti-commutation relations

$$\hat{\psi}_I\hat{\psi}_J^\dagger + \hat{\psi}_J^\dagger\hat{\psi}_I =: \{\hat{\psi}_I, \hat{\psi}_J^\dagger\} = \delta_{IJ}, \qquad \{\hat{\psi}_I, \hat{\psi}_J\} = \{\hat{\psi}_I^\dagger, \hat{\psi}_J^\dagger\} = 0,$$

where I, J are the general multi-indices. The non-interacting property is reflected in the structure of the Hamiltonian, which contains only quadratic terms in the creation/annihilation operators. For non-superconducting systems, the second-quantised Hamiltonian has the form

$$\hat{H} = \sum_{I,J} \hat{\psi}_I^\dagger H_{IJ} \hat{\psi}_J \equiv \hat{\psi}^\dagger H \hat{\psi}, \tag{6.4}$$

where H_{IJ} is a $N \times N$ called the first-quantised Hamiltonian. For superconducting systems, define the Nambu spinors as

$$\hat{\Psi}^\dagger = (\hat{\psi}_1^\dagger, \ldots, \hat{\psi}_N^\dagger, \hat{\psi}_1, \ldots, \hat{\psi}_N).$$

The second-quantised Hamiltonian for superconducting systems has the form

$$\hat{H} = \frac{1}{2}\hat{\Psi}^\dagger H \hat{\Psi}, \tag{6.5}$$

where the $2N \times 2N$ matrix H is the first-quantised Hamiltonian, often referred to as a Bogoliubov-De Gennes (BdG) Hamiltonian. The gapped property will be explained in Section 6.1.2.

For further reference, we denote the set of all "allowed" single-particle Hamiltonians as $\mathcal{G}_\mathcal{H}$, where the notion of "allowed" is explained in Section 6.3.4.

The Bloch Hamiltonian

If the first-quantised Hamiltonian (viz. single-particle Hamiltonian) H is translationally invariant, Bloch's theorem [1] can be applied, as was done for 1D systems in Section 3.5.2. We refer the reader to the book by Kittel [100] for a general treatment of Bloch's theorem to any Bravais lattice in detail.

Here, the general method of obtaining the Bloch Hamiltonian is explained. We assume that the system is translationally invariant such that there is a Bravais lattice Γ, which hosts a unit cell of M atoms at each Bravais lattice point. In this way, each lattice point of H can be uniquely labeled by a tuple (x, i), where $x \in \Gamma$ and $1 \leq i \leq M$. An example is the graphene lattice in Fig. 4.5a, where the unit cell consists of two atoms A and B, and the Bravais lattice is spanned by the vectors $\mathbf{a}_1$ and $\mathbf{a}_2$. Define creation/annihilation operators $\hat{A}_i(\mathbf{R})$ for atom i in the unit cell at position $\mathbf{R}$. The only nonzero anti-commutator reads

$$\{\hat{A}_i(\mathbf{R}), \hat{A}_j^\dagger(\mathbf{R}')\} = \delta_{ij}\delta_{\mathbf{R},\mathbf{R}'}.$$

Since there is periodicity due to the Bravais lattice Γ, the operators $\hat{A}_i$ are Fourier transformed

$$\hat{A}_i(\mathbf{R}) = \frac{1}{\sqrt{N}} \sum_{\mathbf{k}\in BZ} \hat{A}_i(\mathbf{k}) e^{i\mathbf{k}\cdot\mathbf{R}},$$

where N is the number of lattice sites and BZ denotes the (first) Brillouin zone, the primitive cell of the reciprocal lattice of Γ. Analogous to the real-space operators, the Fourier space creation/annihilation operators obey anti-commutation relations where the only nonzero relation reads

$$\{\hat{A}_i(\mathbf{k}), \hat{A}_j^\dagger(\mathbf{k}')\} = \delta_{ij}\delta_{\mathbf{k},\mathbf{k}'}.$$

By using algebraic identities such as $\frac{1}{N}\sum_{\mathbf{R}} e^{i\mathbf{R}\cdot(\mathbf{k}-\mathbf{k}')} = \delta_{\mathbf{k},\mathbf{k}'}$, the second-quantised Hamiltonian can be rewritten as

$$\hat{H} = \sum_{\mathbf{k}} \hat{\psi}^\dagger(\mathbf{k}) H(\mathbf{k}) \hat{\psi}(\mathbf{k})(\mathbf{k}), \qquad \hat{\psi}(\mathbf{k}) = \left(\hat{A}_1(\mathbf{k}), \ldots, \hat{A}_n(\mathbf{k})\right)^T, \tag{6.6}$$

where $H(\mathbf{k})$ is a $M \times M$ matrix for every $\mathbf{k} \in BZ$, called the *Bloch Hamiltonian*.

Band Structures

The eigenvalue problem for the Bloch Hamiltonian reads $H(\mathbf{k})\,|u_a(\mathbf{k})\rangle = E_a(\mathbf{k})\,|u_a(\mathbf{k})\rangle$, where $1 \leq a \leq M$ denotes the energy band, $E_a(\mathbf{k})$ is the energy of the state in band a with momentum k and $|u_a(\mathbf{k})\rangle$ is the momentum eigenstate of band a. An important feature of bands is that they can be empty, filled, or partially filled. This can be understood in the simplest way by defining an energy E_F, the Fermi energy, and consider all states with $E_a(\mathbf{k}) \leq E_F$ to be filled, and the rest empty. In practice, the Fermi energy can be tuned by, e.g. by applying an external voltage. A schematic representation of a band structure of a 1D system is plotted in Fig. 6.2. In Fig. 4.5b, the two energy bands of graphene are plotted as two grey surfaces, and the Fermi level is indicated by the blue plane.

The band structure is important for the study of insulating systems, since the Fermi energy must always lie inside a gap for all $\mathbf{k} \in BZ$, as in Fig. 6.2. To ensure this is the case, a so-called *flat-band* Hamiltonian is constructed from $H(\mathbf{k})$:

$$Q(\mathbf{k}) = \sum_{a=1}^{n} |u_a(\mathbf{k})\rangle \langle u_a(\mathbf{k})| - \sum_{b=n+1}^{M} |u_b(\mathbf{k})\rangle \langle u_b(\mathbf{k})|,$$

where $|u_i(\mathbf{k})\rangle$ are the eigenstates of $H(\mathbf{k})$. This procedure is also known as "spectral flattening", and it is known that the deformation from $H(\mathbf{k})$ to the flat-band Hamiltonian is continuous for

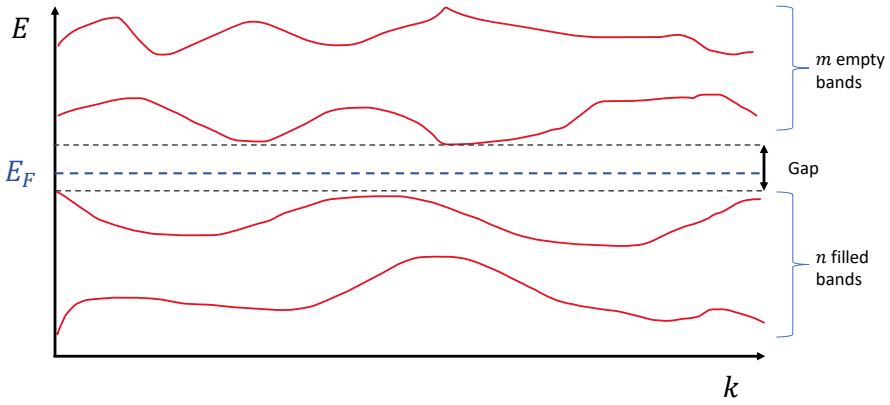

Figure 6.2.: Schematic band structure of n filled and m empty bands, divided by a gap (black dotted lines), in which the Fermi energy E_F (blue dotted line) lies (based on Ref. [10]). Since the x-axis is the BZ, periodic boundary conditions apply.

every $\mathbf{k} \in BZ$. In fact, the maps $\gamma : \mathbf{k} \mapsto Q(\mathbf{k})$ and $\gamma' : \mathbf{k} \mapsto H(\mathbf{k})$ are homotopic [10, 101]. From now on, unless explicitly indicated, when saying Bloch Hamiltonian, we refer to the map

$$\gamma : \mathbf{k} \mapsto Q(\mathbf{k}), \qquad \gamma \in \mathcal{G} = \{\text{allowed maps } \gamma : BZ \to G\}, \tag{6.7}$$

where G is the space of allowed flat-band Hamiltonians $G \subset \mathbb{C}^{M\times M}$. What "allowed" exactly means is discussed in Section 6.3.4.

6.2. Introduction to Topology in Physics

At first glance, topology seems to be an inappropriate tool for physicists, since the deformation of a physical system often yields a quantitatively different result. However, in modern condensed matter, simplified model systems such as tight-binding models are often used to describe a real-world material. If the real-world system can be obtained, at least to a good approximation, from the simplified model via a continuous deformation, the topological invariants of the model system carry over to the real-world system. One powerful feature of this approach is that the real-world system is "robust" to any kind of disorder that can be described as a continuous deformation, in the sense that properties connected to the topological invariant are unaffected.

6.2.1. Definition of Topology in Physics

We are now in shape to define the main essence of topology for non-interacting, second-quantised fermionic insulators or superconductors:

"*When talking about topology of a system $\hat{H} = \hat{\Psi}^\dagger H \hat{\Psi}$, we mean the topological properties of the space $\mathcal{G}_\mathcal{H}$ of allowed single-particle Hamiltonians. If H is path-connected to all other allowed $H' \in \mathcal{G}_\mathcal{H}$, the system is said to be topologically trivial, otherwise, the system is said to be topological.*"

The definition above can written more succinctly as follows.

Definition 6.8. *(Topology in Physics - General case) A system $H \in \mathcal{G}_\mathcal{H}$ is topologically trivial if and only if $\pi_0(\mathcal{G}_\mathcal{H}) = \{1\}$, i.e. has one path-connected component. Otherwise, H is said to be topological.*

Furthermore, $H, H' \in \mathcal{G}_{\mathcal{H}}$ are topologically equivalent if and only if H and H' are path-connected, i.e. they lie in the same path-connected component of $\mathcal{G}$.

When the system is translationally invariant, the definition above can be reformulated in terms of the Bloch Hamiltonian:

"*When talking about topology of a system $\hat{H}$, we mean the topological properties of the Bloch Hamiltonian $\gamma \in \mathcal{G}$ as a map from $BZ \to G$. Two systems described by $\gamma, \gamma' \in \mathcal{G}$ are called topologically equivalent if and only if γ and γ' can be continuously deformed into each other in $\mathcal{G}$* (i.e. γ, γ' are homotopic). If γ is homotopic to all other allowed $\gamma' \in \mathcal{G}$, the system is said to be topologically trivial, otherwise, the system is said to be topological."

The definition for translationally invariant systems can written more succinctly as follows.

Definition 6.9. *(Topology in Physics - Translationally invariant case) A system $\gamma \in \mathcal{G}$ is topologically trivial if and only if $\pi_0(\mathcal{G}) = \{1\}$, i.e. has one path-connected component. Otherwise, γ is said to be topological.*

Furthermore, $\gamma, \gamma' \in \mathcal{G}$ are topologically equivalent if and only if $\gamma \simeq \gamma'$, i.e. they are homotopic and therefore lie in the same path-connected component of $\mathcal{G}$.

In the case of translational invariance, the two Definitions 6.8 and 6.9 can be compared and are simply related by the identity $\pi_0(\mathcal{G}_{\mathcal{H}}) = \pi_0(\mathcal{G})$, since the Bloch Hamiltonian $Q(\mathbf{k})$ is uniquely obtained from H.

In Section 6.3, symmetries that one can impose on a Hamiltonian are discussed at length. These symmetries are essential to the study of topology, since enforcing a certain symmetry changes the space $\mathcal{G}_{\mathcal{H}}$. Finally, in Section 6.4, a complete classification of the spaces $\mathcal{G}_{\mathcal{H}}$ is presented.

6.2.2. The Bulk-Boundary Correspondence

Until now, we have assumed the existence of a gap in the band structure of the bulk system, which is necessary for the system to be an insulator. Now, consider a bulk topological insulator that shares a boundary with vacuum, as is the case in Fig. 6.3. If we think of the material and the boundary to be macroscopic, the quantum mechanical properties can locally be modeled by a Hamiltonian $\hat{H}(\mathbf{x})$ that describes an infinite, translationally invariant system. For any $\mathbf{x}_b \in$ bulk, the Hamiltonian $\hat{H}(\mathbf{x}_b)$ is topological. Similarly for any $\mathbf{x}_v \in$ vacuum, the Hamiltonian $\hat{H}(\mathbf{x}_v)$ is trivial. Additionally, for every path from $\mathbf{x}_b$ to $\mathbf{x}_v$, the boundary is crossed at some point $\mathbf{x}_\partial \in$ boundary.

Since space is continuous and $\hat{H}(\mathbf{x}_b)$ and $\hat{H}(\mathbf{x}_v)$ are not topologically equivalent, the map $\mathbf{x} \mapsto \hat{H}(\mathbf{x})$ must be discontinuous at $\mathbf{x}_\partial$. In terms of the Bloch Hamiltonian described by $\mathcal{G} \ni \gamma(\mathbf{x}) : \mathbf{k} \mapsto Q(\mathbf{k}, \mathbf{x})$, this means that the map $\mathbf{x} \mapsto \gamma(\mathbf{x}) \in \mathcal{G}$ has a discontinuity at $\mathbf{x} = \mathbf{x}_\partial$. It turns out that at such a discontinuity, *the band gap vanishes*. This results in a gapless, hence conducting, boundary mode at the Fermi energy, which is a hallmark of topological insulators.

Note that if $\hat{H}(\mathbf{x}_b)$ and $\hat{H}(\mathbf{x}_v)$ are topologically equivalent, the band gap never closes as they can be continuously deformed into each other. Therefore, the topology of the bulk Hamiltonian dictates the boundary behaviour; this is the *bulk-boundary correspondence*. Here, we prove the bulk-boundary correspondence in terms of the Bloch Hamiltonian. An important alternative way is to use the formalism of (non-abelian) Wilson loops, which are treated in detail in Ref. [102].

The remainder of this section is devoted to proving that the band gap closes at the interface between two topologically distinct materials. More generally:

Theorem 6.10. *If two Hamiltonians $\hat{H}_0$ and $\hat{H}_1$ are not topologically equivalent, the band gap closes at some point during any continuous deformation of the spectrum from $\hat{H}_0$ to $\hat{H}_1$.*

For the proof, we need the following theorem.

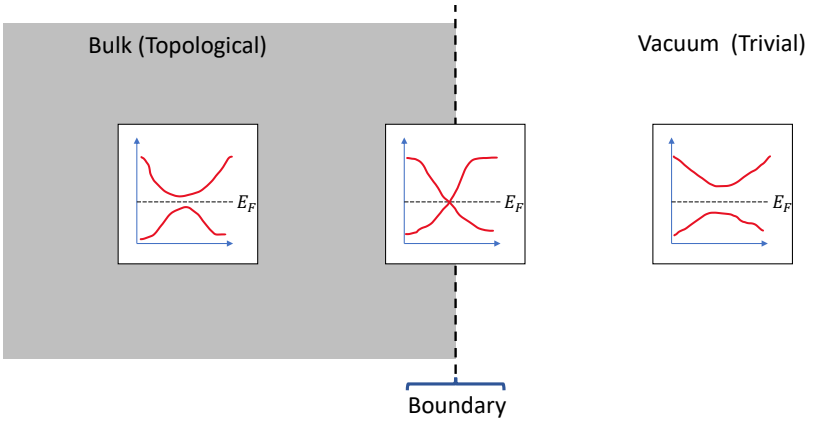

Figure 6.3.: A material that has a topological bulk Hamiltonian (grey), with a boundary (dashed line) that is in contact with vacuum (white) - a topologically trivial insulator. The band gap closes at the boundary of the material at the Fermi energy.

Theorem 6.11. *(Theorem 8 (p. 130) in Ref. [103]) Let $A(t)$ be a continuous (differentiable) complex matrix-valued function of t, $\lambda(t)$ an eigenvalue of $A(t)$ of multiplicity one. Then we can choose an eigenvector $h(t)$ of $A(t)$ pertaining to the eigenvalue $\lambda(t)$ to depend continuously (differentiably) on t.*

To show the non-triviality of Theorem 6.11, we show an example of a continuous matrix-valued function that has discontinuous eigenvectors at the point where the eigenvalues become degenerate.

Example 6.12. *(Example of discontinuous eigenvectors of a continuous matrix-valued function) Consider the matrix-valued function*

$$A(t) = \begin{cases} \begin{pmatrix} 1-t^2 & 0 \\ 0 & 1+t^2 \end{pmatrix} & for \quad t < 0, \\ \begin{pmatrix} 1 & t^2 \\ t^2 & 1 \end{pmatrix} & for \quad t \geq 0, \end{cases}$$

where $t \in \mathbb{R}$. This matrix is continuous and differentiable at $t = 0$ since $\lim_{\epsilon\to 0} A(\epsilon) = A(-\epsilon)$ and $\lim_{\epsilon\to 0} \frac{\mathrm{d}A}{\mathrm{d}t}(\epsilon) = \frac{\mathrm{d}A}{\mathrm{d}t}(-\epsilon) = \begin{pmatrix} 0 & 0 \\ 0 & 0 \end{pmatrix}$. Solving the eigenvalue problem $A(t)v_i(t) = \lambda_i(t)v_i(t)$ yields $\lambda_1(t) = 1 + t^2$ and $\lambda_2(t) = 1 - t^2$ for all $t \in \mathbb{R}$, and eigenvalues

$$\begin{cases} v_1(t) = (0,1)^T, & v_2(t) = (1,0)^T, \quad for \quad t \leq 0, \\ v_1(t) = (1,1)^T, & v_2(t) = (1,-1)^T \quad for \quad t \geq 0, \end{cases}$$

which are clearly not continuous at $t = 0$, which is the only value of t for which the eigenvalues are degenerate.

Proof of Theorem 6.10. Let $H_0(\mathbf{k}), H_1(\mathbf{k})$ be the single-particle Bloch Hamiltonians of $\hat{H}_0, \hat{H}_1$, respectively. By assumption, any allowed map $[0,1] \ni t \mapsto H(t,\mathbf{k})$ where $H(0,\mathbf{k}) = H_0(\mathbf{k})$ and $H(1,\mathbf{k}) = H_1(\mathbf{k})$ must be discontinuous in t at some value $(t',\mathbf{k}')$. We assume that the eigenvalues $\lambda_i(t,\mathbf{k})$ are continuous, such that the energy bands are a continuous function of t (a natural assumption in physics).

$$\Rightarrow$$

There exists at least one eigenvector $v_i(t,\mathbf{k})$ that is discontinuous in t at $(t',\mathbf{k}')$.

$$\Longleftrightarrow$$

¬(all eigenvectors $v_i(t, \mathbf{k})$ are continuous in t).

$$\Rightarrow \text{(using Theorem 6.11)}$$

¬(all eigenvalues $\lambda_i(t, \mathbf{k})$ are continuous in t and isolated.)

$$\Rightarrow$$

There exists at least one eigenvalue $\lambda_i(t, \mathbf{k})$ that has multiplicity > 1 for some $(t', \mathbf{k}')$. □

6.3. Symmetry Protected Topological States

In Section 6.1.2, the Hamiltonians for insulators and superconductors were introduced, which are the relevant models in this chapter. This section aims to describe symmetry protected topological (SPT) states, hosted by these models. These are short-range entangled (SRE) states of $\hat{H}$ that have topological properties that are protected by symmetry conditions imposed on $\hat{H}$. SRE states are eigenstates of $\hat{H}$ that can be continuously transformed to a direct product state by applying infinitesimal local unitary transformations. See part II of Ref. [10] for details.

The rest of this chapter is devoted to the relevant symmetries that can be imposed on $\hat{H}$. Most importantly, we discuss how these imposed symmetries affect the space $\mathcal{G}$ (see Eq. 6.7) of allowed Bloch Hamiltonians.

6.3.1. Symmetries in Quantum Mechanics

An operator $\hat{S} : \mathcal{H} \to \mathcal{H}$ that is either unitary or anti-unitary (i.e. $\hat{S}i\hat{S}^{-1} = -i$) is called a symmetry of a second-quantised Hamiltonian $\hat{H} \in L(\mathcal{H})$ if

$$\hat{S}\hat{H}\hat{S}^{-1} = \hat{H}, \tag{6.8}$$

i.e. if $\hat{S}$ commutes with the Hamiltonian. A natural question is now; how does $\hat{S}$ act on the single-particle Hamiltonian H? The answer is that there exists a (anti-)unitary matrix U such that $UHU^{-1} = \pm H$ and acts on the creation/annihilation operators as

$$\hat{S}\hat{\psi}_I\hat{S}^{-1} = \sum_J (U^\dagger)_{I,J}\hat{\psi}_J.$$

The question is now: what symmetries $\hat{S}$ do we need to consider. It turns out that the simplest and most fundamental approach is to consider the symmetries that are *anti-unitarily* realised on the first-quantised and/or the second-quantised Hilbert space:

- Time-reversal (TR) symmetry (TRS),
- Charge-conjugation/particle-hole (PH) symmetry (PHS),
- Chiral/sublattice symmetry (CS) (combination of TRS and PHS).

We refer the reader to Ref. [11] for a proof that these three symmetries indeed exhaust all anti-unitarily realised symmetries.

6.3.2. Fundamental Symmetries

In this section, we showcase the most important properties of the three fundamental anti-unitary symmetries, and therefore, skip the derivation of most results. The reader can consult Refs. [10] and [11] for all missing details.

Time-Reversal Symmetry

The first symmetry we discuss is *time-reversal* symmetry $\hat{\mathcal{T}}$, acting on the time-evolution operator $\hat{U}(t) := \exp\{it\hat{H}\}$ as $\hat{\mathcal{T}}\hat{U}(t)\hat{\mathcal{T}}^{-1} = \hat{U}(-t)$. Using Eq. 6.8 and that fact that $\hat{\mathcal{T}}$ is anti-unitary, one can see that TR acts on the single-particle Hamiltonian as

$$U_T H^* U_T^\dagger = H,$$

where U_T is a $N \times N$ unitary matrix and H^* denotes the complex conjugation of H. Let K denote the anti-unitary complex conjugation operator $KHK^{-1} = H^*$ with $K^2 = 1$, then one can define $\mathbf{T} = U_T \cdot K$ such that

$$\mathbf{T}H\mathbf{T}^{-1} = H.$$

If $\hat{\mathcal{T}}$ were to be applied twice, the resulting action on the single-particle Hamiltonian reads

$$U_T U_T^* H^* (U_T U_T^*)^\dagger = H,$$

where we define $\mathbf{T}^2 := U_T U_T^*$. There turn out to be two possibilities $\mathbf{T}^2 = \pm\mathbf{1}$, which can be proven using Schur's lemma [10]. We summarise the three possible ways that TR can be present as

$$T = \begin{cases} 0, & \text{when } H \text{ is not TR invariant,} \\ +1, & \text{when } H \text{ is TR invariant and } \mathbf{T}^2 = \mathbf{1}, \\ -1, & \text{when } H \text{ is TR invariant and } \mathbf{T}^2 = -\mathbf{1}. \end{cases}$$

Finally, by noting that TR acts on Fourier space operators as

$$\hat{\mathcal{T}}\hat{\psi}^{(\dagger)}(\mathbf{k})\hat{\mathcal{T}}^{-1} = \hat{\psi}^{(\dagger)}(-\mathbf{k}),$$

where $\hat{\psi}(\mathbf{k})$ is defined in Eq. 6.6, it can be shown that the action on the Bloch Hamiltonian reads

$$U_T H^*(\mathbf{k}) U_T^\dagger = H(-\mathbf{k}), \qquad \mathbf{T}H(\mathbf{k})\mathbf{T}^{-1} = H(-\mathbf{k}),$$

where now $U_T, \mathbf{T}$ are $M \times M$ matrices. This has the implication that the spectrum of $H(\mathbf{k})$ is reflection symmetric w.r.t. $\mathbf{k} = 0$. If $\psi(\mathbf{k})$ is an eigenstate of $H(\mathbf{k})$ such that $H(\mathbf{k})\psi(\mathbf{k}) = E(\mathbf{k})\psi(\mathbf{k})$, then

$$H(\mathbf{k})\mathbf{T}^{-1}\psi(-\mathbf{k}) = \mathbf{T}^{-1}H(-\mathbf{k})\psi(-\mathbf{k}) = E(-\mathbf{k})\mathbf{T}^{-1}\psi(-\mathbf{k}).$$

Particle-Hole Symmetry

The next symmetry is *particle-hole* symmetry $\hat{\mathcal{C}}$, which physically means that there are equally many filled and vacant states, and that the system is invariant under the exchange of filled and vacant states. PHS is a *unitary* operator on the second-quantised Hamiltonian acting as

$$\hat{\mathcal{C}}\hat{\psi}_I\hat{\mathcal{C}}^{-1} = \sum_J (U_C^{*\dagger})_{I,J}\hat{\psi}_J^\dagger, \qquad \hat{\mathcal{C}}\hat{\psi}_{\mathbf{k}}\hat{\mathcal{C}}^{-1} = \hat{\psi}_{-\mathbf{k}}^\dagger, \tag{6.9}$$

where U_C is a unitary $N \times N$ matrix. From Eq. 6.8 and Eq. 6.9, one can derive that the action on the single-particle Hamiltonian reads

$$U_C H^* U_C^\dagger = -H.$$

Entirely analogous to TR, we define $\mathbf{C} = U_C \cdot K$ and the operator $\mathbf{C}^2$ such that there exist three ways that PHS can manifest itself

$$C = \begin{cases} 0, & \text{when } H \text{ is not PH invariant,} \\ +1, & \text{when } H \text{ is PH invariant and } \mathbf{C}^2 = \mathbf{1}, \\ -1, & \text{when } H \text{ is PH invariant and } \mathbf{C}^2 = -\mathbf{1}. \end{cases}$$

The action of PHS on the Bloch Hamiltonian reads

$$\mathbf{C}H(\mathbf{k})\mathbf{C}^{-1} = -H(-\mathbf{k}),$$

where $\mathbf{C} = U_C \cdot K$ and U_C is now a $M \times M$ unitary matrix.

Chiral Symmetry

The last symmetry, *chiral* symmetry $\hat{\mathcal{S}} \equiv \hat{\mathcal{T}} \cdot \hat{\mathcal{C}}$, is a anti-unitary symmetry on the second-quantised Hilbert space. This symmetry has the physical interpretation that the system can be split up into two non-interacting systems

$$\hat{H} = \begin{pmatrix} 0 & \hat{H}_{12} \\ \hat{H}_{12}^\dagger & 0 \end{pmatrix}.$$

The action of CS on the second-quantised Hamiltonian reads

$$\hat{\mathcal{S}} \hat{\psi}_I \hat{\mathcal{S}}^{-1} = \sum_J (U_S^{*\dagger})_{I,J} \hat{\psi}_J^\dagger, \qquad \hat{\mathcal{S}} i \hat{\mathcal{S}}^{-1} = -i.$$

The action on the single-particle Hamiltonian therefore is

$$U_S H U_S^\dagger = -H, \qquad U_S = U_T U_C^* = \mathbf{S},$$

where U_S is a unitary $N \times N$ matrix. Finally, the action on the Bloch Hamiltonian is

$$\mathbf{S} H(\mathbf{k}) \mathbf{S}^{-1} = -H(\mathbf{k}),$$

where now $\mathbf{S} = U_S$ is a $M \times M$ unitary matrix. To conclude, there exist two ways that CS can manifest itself, being $S = 0, 1$, denoting that CS is either present ($S = 1$) or not ($S = 0$).

Summary

To summarise, there are three fundamental symmetries $\hat{\mathcal{T}}, \hat{\mathcal{C}}$ and $\hat{\mathcal{S}}$, with their single-particle versions $\mathbf{T}, \mathbf{C}$ and $\mathbf{S}$ that are not unitarily realised on both the second-quantised and first-quantised Hilbert space. Table 6.1 summarises the possible (anti-)unitary action of a symmetry on both the first- and second-quantised Hamiltonian.

Table 6.1.: For all fundamental symmetries T, C, S, and general unitary symmetries U, the table indicates if the symmetry is realised unitarily (U) or anti-unitarily (K) on the relevant Hilbert space.

	T	C	S	U
Second-quantised	K	U	K	U
First-quantised	K	K	U	U

The three symmetries act on the first-quantised Hamiltonian as

$$U_T H^* U_T^\dagger = H, \quad U_C H^* U_C^\dagger = -H, \quad U_S H U_S^\dagger = -H,$$

and on the Bloch Hamiltonian as

$$U_T H^*(\mathbf{k}) U_T^\dagger = H(-\mathbf{k}), \quad U_C H^*(\mathbf{k}) U_C^\dagger = -H(-\mathbf{k}), \quad U_S H(\mathbf{k}) U_S^\dagger = -H(\mathbf{k}).$$

6.3.3. Topological Protection

In this section, we explain how the fundamental symmetries discussed in Section 6.3.2 can lead to an SPT state. For any $\hat{H}$, let H denote the single-particle Hamiltonian and $U(t) = \exp\{itH\}$ the corresponding time-evolution operator. Suppose the system possesses no symmetry, i.e. $T = C = S = 0$, then H is a general Hermitian matrix, so the time-evolution operator is a general $N \times N$ unitary matrix, i.e. $U(t) \in U(N)$. Now suppose the system possesses only TRS, so $T = +1, C = S = 0$. By anti-unitarity of $\mathbf{T}$, the matrix H must be real and symmetric. Since any hermitian matrix can be written as $H = H_s + H_a$, where H_s symmetric and H_a anti-symmetric,

we can write our TR symmetric matrix as $H_s = H - H_a$. Since for any anti-symmetric H_a, the operator $\exp\{itH_a\} \in O(N)$, one can see that the time-evolution operator of a real symmetric H_s must lie in $U(N)/O(N)$, since it is defined by the time-evolution operator of any Hermitian matrix modulo the anti-symmetric part.

Topological protection arises as follows. If one demands $T = +1, C = S = 0$, then $\hat{H}$ is topologically equivalent to all other Hamiltonians $\hat{H}'$ for which the time-evolution operator $U(t)'$ lies in the same path-connected component of $U(N)/O(N)$ as $U(t)$. Moreover, if $\pi_0(U(N)/O(N))) = \{1\}$, the system is topologically trivial. If $U(N)/O(N)$ has more than one path-connected component, enforcing $T = +1, C = S = 0$ ensures that two Hamiltonians from different components cannot deform continuously into each other without closing the bulk gap. Hence, if there is a physical property that depends on the connected component, this property is topologically protected by the enforced symmetries.

Now consider the $M \times M$ Bloch Hamiltonian $Q(\mathbf{k})$ that has n filled and m empty bands, where $M = n + m$ and no symmetry requirements, i.e. $T = C = S = 0$. Since $Q(\mathbf{k})$ is Hermitian, for all $\mathbf{k} \in BZ$, there exists a unitary $U(\mathbf{k}) \in U(n+m)$ such that $Q(\mathbf{k}) = U(\mathbf{k})\Lambda U^\dagger(\mathbf{k})$ where

$$\Lambda = \begin{pmatrix} \mathbf{1}_n & 0 \\ 0 & -\mathbf{1}_m \end{pmatrix},$$

where $\mathbf{1}_k$ denotes the $k \times k$ identity matrix. If we assume that

$$U(\mathbf{k}) = \begin{pmatrix} U_1(\mathbf{k}) & 0 \\ 0 & U_2(\mathbf{k}) \end{pmatrix}, \qquad U_1(\mathbf{k}) \in U(n), \qquad U_2(\mathbf{k}) \in U(m),$$

then $Q(\mathbf{k}) = U(\mathbf{k})\Lambda U^\dagger(\mathbf{k}) = \Lambda$. By observing that $Q(\mathbf{k})$ is unitary, and unique up to U_1, U_2, the space of possible Bloch Hamiltonians reads

$$Q(\mathbf{k}) \in U(n+m)/U(n) \times U(m) = G.$$

By enforcing one or more of the fundamental symmetries, the space G becomes more restricted, as well as the space $\mathcal{G}$. An example of such a restriction on $\mathcal{G}$ is the requirement $Q^*(\mathbf{k}) = Q(-\mathbf{k})$, since this is a restriction on the map $\gamma : BZ \to G$ rather than on the space G itself. The result of enforcing symmetries on maps $\gamma : BZ \to G$ is the space $\mathcal{G}$. Table 6.4 gives this space $\mathcal{G}$ for all possible combinations of T, C and S.

The reason for using the Bloch Hamiltonian instead of the single-particle Hamiltonian H, is that the map $\gamma : BZ \to G$ naturally leads to a *topological invariant*, such as Chern numbers, Chern-Simons invariants, Zak phases and winding numbers [11]. Additionally, these winding numbers are often naturally related to physical properties, such as the quantum Hall conductance [8]. We do not review invariants of topological phases of matter here. Instead, we refer the reader to Ref. [11] for an extensive overview, and show an example of a winding number as topological invariant for the Su-Schrieffer-Heeger (SSH) model in Section 6.3.5.

6.3.4. Spaces of Allowed Hamiltonians

In this section we discuss the important notion of the space of allowed single-particle Hamiltonians $\mathcal{G}_\mathcal{H}$ and Bloch Hamiltonians $\mathcal{G}$. Any space of allowed Hamiltonians must obey the following two requirements:

1. The space must contain only Hamiltonians that obey the symmetry requirements from Section 6.3.1,
2. Any two Hamiltonians are path connected in the space if and only if they can be deformed into each other without closing the gap in which the Fermi energy lies.

The first requirement is easy to implement, which is shown in Section 6.3.3.

The power of Bloch Hamiltonians is that by Theorem 6.10, any of the spaces $\mathcal{G}$ in Table 6.4 automatically satisfies the second requirement. It is precisely the second requirement that is extremely hard to account for in determining $\mathcal{G}_{\mathcal{H}}$ for systems with $N \to \infty$ lattice sites, in the absence of a Bloch Hamiltonian. Since the spectrum of a tight-binding lattice model is typically bounded, the spectrum must have accumulation points (Bolzano-Weierstrass), hence Theorem 6.10 is not applicable anymore. The unavailability of such a theorem makes it hard to construct a space in which the second requirement is satisfied.

6.3.5. Topology in the SSH Model

The SSH model [18] is a one-dimensional tight-binding lattice model with $2N$ lattice sites, defined by the second-quantised Hamiltonian

$$\hat{H} = v \sum_{n=0}^{N-1} \hat{a}_n^\dagger \hat{b}_n + w \sum_{n=0}^{N-1} \hat{b}_n^\dagger \hat{a}_{n+1} + H.c., \tag{6.10}$$

where $v, w \in \mathbb{R}$ are parameters and $\hat{a}_n, \hat{b}_n$ are fermionic creation/annihilation operators where the only nonzero anti-commutators are $\{\hat{a}_n, \hat{a}_m^\dagger\} = \{\hat{b}_n, \hat{b}_m^\dagger\} = \delta_{n,m}$. Upon taking periodic boundary conditions (PBC) one defines $\hat{a}_N^{(\dagger)} = \hat{a}_0^{(\dagger)}$, and for open boundary conditions (OBC) one takes $\hat{a}_N^{(\dagger)} = 0$.

To obtain the single-particle Hamiltonian as a $2N \times 2N$ matrix, define

$$\hat{\Psi} = (\hat{a}_0, \hat{b}_0, \hat{a}_1, \hat{b}_1, \ldots, \hat{a}_{N-1}, \hat{b}_{N-1})^T,$$

such that Eq. 6.10 can be rewritten as $\hat{H} = \hat{\Psi}^\dagger H \hat{\Psi}$ with

$$H_{PBC} = \begin{pmatrix} 0 & v & & & & w \\ v & 0 & w & & & \\ & w & \ddots & \ddots & & \\ & & \ddots & \ddots & w & \\ & & & w & 0 & v \\ w & & & & v & 0 \end{pmatrix}, \qquad H_{OBC} = \begin{pmatrix} 0 & v & & & & \\ v & 0 & w & & & \\ & w & \ddots & \ddots & & \\ & & \ddots & \ddots & w & \\ & & & w & 0 & v \\ & & & & v & 0 \end{pmatrix},$$

for PBC and OBC, respectively. The energy spectra of H_{PBC} and H_{OBC}, i.e. the eigenvalues, are plotted in Fig. 6.4 as function of the parameter v/w. Note that for approximately $v/w \in [-1, 1]$, the SSH model with open boundary conditions in Fig. 6.4b has two $E = 0$ states, located at the edges. These states do not exist in the SSH model with periodic boundary conditions (see Fig. 6.4a). In fact, these edge modes are topological, as will be shown in this section, and are the result of the bulk-boundary correspondence from Section 6.2.2 in the SSH model.

The starting point for studying the topological properties of a model, is the Bloch Hamiltonian representation. By defining $\hat{\psi}_n = (\hat{a}_n, \hat{b}_n)^T$ and the Fourier transform over the N unit cells

$$\hat{\psi}_n = \frac{1}{\sqrt{N}} \sum_{m=0}^{N-1} e^{ik_m n} \hat{\psi}_{k_m},$$

with $k_m = 2\pi m/N$, the Hamiltonian in Eq. 6.10 with PBC can be rewritten as $\hat{H} = \sum_k \hat{\psi}_k^\dagger H(k) \hat{\psi}_k$ where

$$H(k) = \begin{pmatrix} 0 & v + we^{-ik} \\ v + we^{ik} & 0 \end{pmatrix} = d_0(k)\,\mathrm{Id} + \mathbf{d}(k) \cdot \vec{\sigma}$$

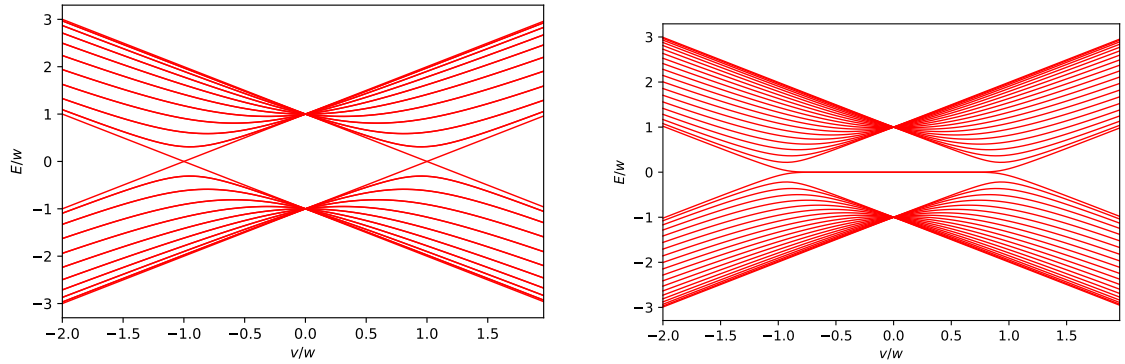

(a) Periodic boundary conditions.

(b) Open boundary conditions.

Figure 6.4.: The energy spectrum of the SSH model with $N = 20$ unit cells, for various values of v/w.

is the Bloch Hamiltonian, which can be written in terms of Pauli matrices $\vec{\sigma} = (\sigma_x, \sigma_y, \sigma_z)^T$ with $d_0(k) = d_z(k) = 0$ and $d_x(k) = v + w\cos k$, $d_y(k) = w \sin k$. Furthermore, the BZ is the interval $[0, 2\pi]$, where periodic boundary conditions are imposed such that $0 \sim 2\pi$ are identified as the same point. Now, one can view the Bloch Hamiltonian as a map $\gamma : BZ \to G$, where $G = \mathbb{R}^2$ is the space where the vector $\mathbf{d}(k)$ lives in.

Solving the time-independent Schrödinger equation $H(k)\,|\psi_\pm(k)\rangle = E_\pm(k)\,|\psi_\pm(k)\rangle$ yields the eigenvalues of the Bloch Hamiltonian $E(k) = \pm\sqrt{v^2 + w^2 + 2vw\cos k}$, which constitute the band structure. Furthermore, the eigenstates read

$$|\psi_\pm(k)\rangle = \frac{1}{\sqrt{2}} \begin{pmatrix} \frac{v+we^{-ik}}{E_\pm(k)} \\ 1 \end{pmatrix} = \frac{1}{\sqrt{2}} \begin{pmatrix} \pm\frac{d_x(k)-id_y(k)}{|\mathbf{d}(k)|} \\ 1 \end{pmatrix}.$$

The band structure of the SSH model is plotted in the top part of Fig. 6.5 for various v, w values. In the bottom row of Fig. 6.5, the loop traced out by the vector $\mathbf{d}(k)$ is shown for the v, w values of the corresponding band structure in the top row. Note that for $v = w = 1$, the band gap closes, which is not allowed according to Section 6.3.4. This happens precisely when $H(k) = 0$, which is equivalent to $\mathbf{d}(k) = \mathbf{0}$. Therefore, the space G should be adapted to $G = \mathbb{R}^2 \setminus \{\mathbf{0}\}$

By observing that Eq. 6.10 has a real and symmetric single-particle Hamiltonian, and that there exists CS, represented by the unitary

$$\Gamma = \sum_{n\in\mathbb{Z}} |2n\rangle\langle 2n| - \sum_{n\in\mathbb{Z}} |2n+1\rangle\langle 2n+1|,$$

it is clear that the SSH model has all three fundamental symmetries, i.e. $T = C = S = 1$. Let us further assume that the only allowed deformations of the SSH model are variations in the parameters v, w. Under these assumptions, the space of allowed Bloch Hamiltonians reads

$$\mathcal{G} = \{\gamma : BZ \to \mathbb{R}^2 \setminus \{\mathbf{0}\} \mid \gamma(k) = \mathbf{d}(k) = (v + w\cos k, w\sin k)^T\}.$$

Now, we have reduced the study of topology of the SSH model to the problem of loops in the punctured plane that have the specific form $\gamma(x) = (v + w\cos 2\pi x, w\sin 2\pi x)^T$, where $x \in \mathbb{S}^1$. By a change of coordinates, we can set $w \to 1$ and $v \to v/w$, which gives us the simple problem of determining whether the loop

$$\gamma(x) = \begin{pmatrix} v/w + \cos 2\pi x \\ \sin 2\pi x \end{pmatrix}$$

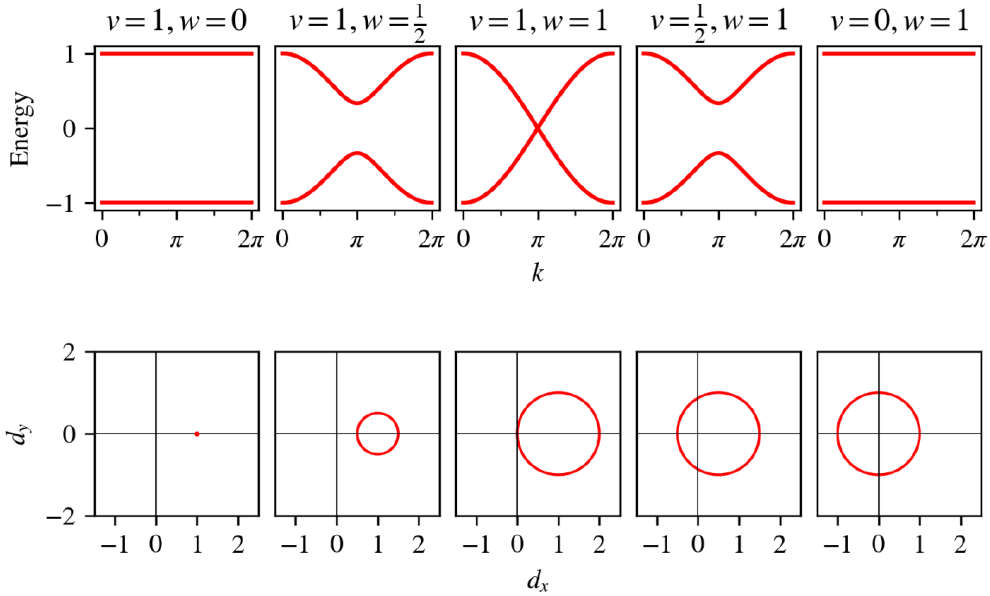

Figure 6.5.: Top: band structure of the SSH model Eq. 6.10 for various v, w values. Bottom: closed loop of the vector $\mathbf{d}(k)$ in the (d_x, d_y)-plane (figure from Ref. [104]).

winds around the origin. Clearly, for precisely $v/w = 1, -1$, the loop hits the origin at $x = 1/2, 0$. Moreover, for $|v/w| < 1$, the loop is homotopic to the $v/w = 0$ case, hence has $\nu(\gamma) = 1$ by Eq. 6.3. For $|v/w| > 1$, the winding number is zero.

A more general way to compute the winding number is to write $\mathbf{d}(k)$ as the complex number $h(k) := d_x(k) + id_y(k)$. When writing $h(k) = r(k)e^{i\theta(k)}$ in polar form, the differential $\mathrm{d}h/h$ reads $\frac{\mathrm{d}h}{h} = \mathrm{d}\ln r + i\mathrm{d}\theta$. Since the term $\mathrm{d}\ln r$ vanishes for closed loops, one can use the winding number formula

$$\nu(\gamma) = \frac{1}{2\pi i}\int_\gamma \frac{\mathrm{d}h}{h} = \frac{1}{2\pi i}\int_0^{2\pi} \mathrm{d}k \frac{\mathrm{d}}{\mathrm{d}k}\ln h(k). \tag{6.11}$$

Another way to view topology in the SSH chain, and in many other models, is to consider the winding of the wavefunction of the filled bands across the BZ. This winding can be quantified using the *Berry phase*, also known as the geometric phase, which reads

$$\gamma_{\text{Berry}} = i\int_0^{2\pi} \langle\psi_-(k)| \frac{\mathrm{d}}{\mathrm{d}k} |\psi_-(k)\rangle \,. \tag{6.12}$$

The winding number Eq. 6.11 and the Berry phase Eq. 6.12 are in fact related. Note that $|\psi_-(k)\rangle = \sqrt{2}^{-1}(-h(k)^*/|h(k)|, 1)^T$, then the integrand of Eq. 6.12 can be written as

$$\begin{aligned} 2\langle\psi_-(k)| \frac{\mathrm{d}}{\mathrm{d}k} |\psi_-(k)\rangle = \frac{h(k)}{|h(k)|}\frac{\mathrm{d}}{\mathrm{d}k}\frac{h(k)^*}{|h(k)|} &= \underbrace{\frac{\mathrm{d}}{\mathrm{d}k}\left(\frac{h(k)}{|h(k)|}\frac{h(k)^*}{|h(k)|}\right)}_{=0} - \frac{h(k)^*}{|h(k)|}\frac{\mathrm{d}}{\mathrm{d}k}\frac{h(k)}{|h(k)|} \\ &= -\frac{\mathrm{d}}{\mathrm{d}k}\ln h(k) + \frac{\mathrm{d}}{\mathrm{d}k}\ln|h(k)|, \end{aligned} \tag{6.13}$$

by using partial integration twice. Now plugging Eq. 6.13 into Eq. 6.12, one obtains the identity

$$\gamma_{\text{Berry}} = \frac{1}{2i}\int_0^{2\pi} \mathrm{d}d\frac{\mathrm{d}}{\mathrm{d}k}\ln h(k) = \pi\nu(\gamma).$$

The topological invariant is in this case a winding number that is also the Berry phase over the one-dimensional BZ. This type of topological invariant is an example of a Zak phase [92].

To summarise, the SSH model is a topologically nontrivial model, characterised by a Zak phase topological invariant. This invariant can be studied via the Bloch Hamiltonian as a loop in the punctured plane, as well as via the Berry phase of the filled eigenstate. Moreover, in the regime $|v/w| < 1$ where the winding number is nonzero, there exist $E = 0$ edge modes, as can be seen in Fig. 6.4b. These modes vanish for $|v/w| > 1$ since the bulk Hamiltonian is now topologically equivalent to the trivial/vacuum case, as explained in Section 6.2.2.

6.4. Classification of Topological States of Matter

6.4.1. Tenfold Way

The starting point of the classification of SPT states of matter is the so-called *tenfold way*, which use in physics originates from the classification of random matrices by Altland and Zirnbauer [9]. Recall that there are three ways to realise both TRS and PHS: $T = 0, \pm 1$ and $C = 0, \pm 1$. This already gives a total of nine different classes. The third symmetry, CS, is present if both TR and PH are symmetries, and is absent if either TRS or PHS is missing. However, when both TRS and PHS are missing, CS can be either present or absent. The case $T = C = 0, S = 1$ gives us the $9 + 1 = 10$ possible ways that the three fundamental symmetries can appear.

The second ingredient of the tenfold way is the spatial *dimension* of the model, which is equal to the dimension d of the Brillouin zone manifold. For each of these ten combinations of symmetries and dimension d, there is a certain space $\mathcal{G}_{\mathcal{H}}$ in which H must be contained, or equivalently, a space $\mathcal{G}$ in which the Bloch Hamiltonian $\gamma : BZ \to G$ must be contained.

Table 6.2.: The tenfold way of classifying topological insulators and superconductors.

T	C	S	Cartan Label	$d=0$	$d=1$	$d=2$	$d=3$	$d=4$	$d=5$	$d=6$	$d=7$
0	0	0	A	$\mathbb{Z}$	0	$\mathbb{Z}$	0	$\mathbb{Z}$	0	$\mathbb{Z}$	0
0	0	1	**AIII**	0	$\mathbb{Z}$	0	$\mathbb{Z}$	0	$\mathbb{Z}$	0	$\mathbb{Z}$
+	0	0	AI	$\mathbb{Z}$	0	0	0	$2\mathbb{Z}$	0	$\mathbb{Z}_2$	$\mathbb{Z}_2$
+	+	1	**BDI**	$\mathbb{Z}_2$	$\mathbb{Z}$	0	0	0	$2\mathbb{Z}$	0	$\mathbb{Z}_2$
0	+	0	D	$\mathbb{Z}_2$	$\mathbb{Z}_2$	$\mathbb{Z}$	0	0	0	$2\mathbb{Z}$	0
−	+	1	**DIII**	0	$\mathbb{Z}_2$	$\mathbb{Z}_2$	$\mathbb{Z}$	0	0	0	$2\mathbb{Z}$
−	0	0	AII	$2\mathbb{Z}$	0	$\mathbb{Z}_2$	$\mathbb{Z}_2$	$\mathbb{Z}$	0	0	0
−	−	1	**CII**	0	$2\mathbb{Z}$	0	$\mathbb{Z}_2$	$\mathbb{Z}_2$	$\mathbb{Z}$	0	0
0	−	0	C	0	0	$2\mathbb{Z}$	0	$\mathbb{Z}_2$	$\mathbb{Z}_2$	$\mathbb{Z}$	0
+	−	1	**CI**	0	0	0	$2\mathbb{Z}$	0	$\mathbb{Z}_2$	$\mathbb{Z}_2$	$\mathbb{Z}$

Table 6.2 displays the most common representation of the tenfold way in physics. For each spatial dimension d, the table indicated whether a given combination of symmetries yields a topologically trivial model (indicated by a zero) or a topological model. The labels $\mathbb{Z}, 2\mathbb{Z}$ and $\mathbb{Z}_2$ indicate a topological state for which the topological invariant is represented by integers, even integers, or a binary value (e.g. $\pm$), respectively. Furthermore, the table turns out to be periodic in d with period 8 for the "real" symmetry classes, which is called the *Bott periodicity* of the tenfold way, and periodic with period two for the "complex" symmetry classes A and AIII. By examining the dimensionality and symmetries of the model, the tenfold way immediately answers the question whether the model can host a topological phase or not. The remainder of this chapter is devoted to deriving the entries in Table 6.2, for which K-Theory is the central tool.

6.4.2. Cartan Classes, Classifying Spaces, and K-Theory

To introduce the remarkable mathematical structures that we will showcase in this section, we start by asking the following question: what are all possible generalizations of the sphere, i.e. spaces with constant curvature. The mathematician Elie Cartan solved the problem in 1926, and those turned out to exactly be the ten coset spaces in the time-evolution operator column in Table 6.3. A peculiar feature of the Bloch Hamiltonian for $d = 0$ in column in Table 6.3, is that it is obtained by shifting the time-evolution column one downwards, and taking periodic boundary conditions in both the complex and real sector separately.

Table 6.3.: For each Cartan label (see Table 6.2 for corresponding symmetries), this table shows the space in which the time-evolution operator must lie and the space in which the Bloch Hamiltonian must lie when $d = 0$. The classifying space, corresponding to each Cartan label, is given in the last column. Finally, the two spaces C_0, C_1 constitute the complex sector, where all other spaces R_i constitute the real sector.

Cartan Label	Time-evolution operator $U(t) = \exp\{itH\}$	Bloch Hamiltonian	Classifying Space
A	$U(N)$	$U(N+M)/U(N) \times U(M)$	$= C_0$
AIII	$U(N+M)/U(N) \times U(M)$	$U(N)$	$= C_1$
AI	$U(N)/O(N)$	$O(N+M)/O(N) \times O(M)$	$= R_0$
BDI	$O(N+M)/O(N) \times O(M)$	$O(N)$	$= R_1$
D	$O(N)$	$O(2N)/U(N)$	$= R_2$
DIII	$SO(2N)/U(N)$	$U(2N)/Sp(2N)$	$= R_3$
AII	$U(2N)/Sp(2N)$	$Sp(N+M)/Sp(N) \times Sp(M)$	$= R_4$
CII	$Sp(N+M)/Sp(N) \times Sp(M)$	$Sp(N)$	$= R_5$
C	$Sp(2N)$	$Sp(2N)/U(N)$	$= R_6$
CI	$Sp(2N)/U(N)$	$U(N)/O(N)$	$= R_7$

The next step towards a full classification of topological matter, the tenfold way in Table 6.2, is to extend Table 6.3 to the spaces of Bloch Hamiltonians when $d > 0$. For each Cartan class, the result is shown in Table 6.4. Now we are in shape to answer the question: how to distinguish all topologically distinct Bloch Hamiltonians, given a certain symmetry class? The answer for the real sector, obtained by Kitaev [105] using K-theory, is to compute the generalised homotopy group

$$\pi(\overline{T^d}, R_q) = \pi_0(R_{q-d}) \oplus \bigoplus_{s=0}^{d-1} \binom{d}{s} \pi_0(R_{q-s}), \tag{6.14}$$

where T^d is the d-dimensional torus (homeomorphic to the BZ [10]), and the bar denotes that the constrains on R_q in Table 6.4 are taken into account. Note that the generalised homotopy group satisfies $\pi_0(\mathcal{G}) = \pi(\overline{BZ}, G)$ in view of Eq. 6.7. It turns out that only the first part $\pi_0(R_{q-d})$, also denoted as $\tilde{\pi}(\mathcal{G})$ in this chapter, is of relevance for the tenfold way of classifying topological materials. If the first part $\tilde{\pi}(\mathcal{G}) \neq 0$, the system is a strong topological insulator/superconductor, which are exactly the systems described by the tenfold way. The second part $\bigoplus_{s=0}^{d-1} \binom{d}{s} \pi_0(R_{q-s})$ can be shown to be a result of translational invariance, which is a unitarily realised symmetry, hence irrelevant. A nonzero second part indicates if the system is a weak topological insulator/superconductor.

This has the implication that if a d-dimensional system corresponding to a symmetry class R_q (or C_q) is not translationally invariant, the zeroth homotopy group of the space of allowed single-particle Hamiltonians $\mathcal{G}_\mathcal{H}$ satisfies $\pi_0(\mathcal{G}_\mathcal{H}) = \pi_0(R_{q-d})$ (or $\pi_0(C_{q-d})$). Note, however, that the space $\mathcal{G}_\mathcal{H}$ is very complicated, as argued in Section 6.3.4, and not simply one of the spaces in Table 6.3.

The final step is to invoke the real K-theoretic result that $\pi_0(R_{q-d}) \in \{0, \mathbb{Z}, 2\mathbb{Z}, \mathbb{Z}_2\}$ with Bott

Table 6.4.: The ten spaces $\mathcal{G}$ of Bloch Hamiltonians $Q(\mathbf{k})$ as maps $BZ \to G$. Note that σ, τ are Pauli matrices (the difference in notation is used to emphasise that the Pauli matrices act in different sectors) and $q(\mathbf{k})$ denotes the matrix that uniquely defines Q in the presence of chiral symmetry.

Cartan label	Bloch Hamiltonian Space $\mathcal{G}$
A	$\{Q(\mathbf{k}) \in G_{m,n+m}(\mathbb{C}) = U(n+m)/U(n) \times U(m)\}$
AI	$\{Q(\mathbf{k}) \in G_{m,n+m}(\mathbb{C}) \mid Q(\mathbf{k})^* = Q(-\mathbf{k})\}$
AII	$\{Q(\mathbf{k}) \in G_{2m,2(n+m)}(\mathbb{C}) \mid (i\sigma_y)Q(\mathbf{k})^*(-i\sigma_y) = Q(-\mathbf{k})\}$
AIII	$\{q(\mathbf{k}) \in U(m)\}$
BDI	$\{q(\mathbf{k}) \in U(m) \mid q(\mathbf{k})^* = q(-\mathbf{k})\}$
CII	$\{q(\mathbf{k}) \in U(2m) \mid (i\sigma_y)q(\mathbf{k})^*(-i\sigma_y) = q(-\mathbf{k})\}$
D	$\{Q(\mathbf{k}) \in G_{m,2m}(\mathbb{C}) \mid \tau_x Q(\mathbf{k})^* \tau_x = -Q(-\mathbf{k})\}$
C	$\{Q(\mathbf{k}) \in G_{m,2m}(\mathbb{C}) \mid \tau_y Q(\mathbf{k})^* \tau_y = -Q(-\mathbf{k})\}$
DIII	$\{q(\mathbf{k}) \in U(2m) \mid q(\mathbf{k})^T = -q(-\mathbf{k})\}$
CI	$\{q(\mathbf{k}) \in U(m) \mid q(\mathbf{k})^T = q(-\mathbf{k})\}$

periodicity $\pi_0(R_i) = \pi_0(R_{i \bmod 8})$, and the analogous complex K-theoretic result $\pi_0(C_{q-d}) \in \{0, \mathbb{Z}\}$ with Bott periodicity $\pi_0(C_i) = \pi_0(C_{i \bmod 2}) \in \{0, \mathbb{Z}\}$. Evaluating the homotopy groups $\pi_0(C_{q-d})$ and $\pi_0(R_{q-d})$ for all values of q and $d = 0, \ldots, 7$, one obtains the tenfold way Table 6.2.

6.4.3. A Final Note on Topological Triviality

In our definition of topology for SPT states in Section 6.2.1, a system is defined as *topological* if and only if $\tilde{\pi}(\mathcal{G}) \neq 0$. Now that we are familiar with the groups that $\tilde{\pi}(\mathcal{G})$ can be, we are obliged to add a confusion nuance to our definition.

Suppose a d-dimensional system $\gamma \in \mathcal{G} = \{\text{allowed maps } BZ \to G\}$ belongs to a symmetry class such that w.l.o.g. $\tilde{\pi}(\mathcal{G}) = \mathbb{Z}$ (no loss of generality since we could have taken any other nonzero group from Table 6.2), then each path-connected component $\mathcal{G}_n$ of $\tilde{\pi}(\mathcal{G})$ is associated to some $n \in \mathbb{Z}$. If γ lies in $\mathcal{G}_0$, i.e. the path-connected component associated to the identity element $0 \in \mathbb{Z}$ (or $2\mathbb{Z}, \mathbb{Z}_2$), we say that the system γ is in a *topologically trivial phase*.

This subtle distinction can be understood in light of the SSH model from Section 6.3.5. The SSH model has symmetry class BDI and dimension $d = 1$. Therefore, the tenfold way tells us that $\mathcal{G} = \mathbb{Z}$, i.e. the system is topological. When $|v| > |w|$, we saw that the chain has winding number one, hence a topologically nontrivial phase. On the other hand, when $|v| < |w|$, the winding number is zero, hence the phase is trivial.

6.5. Conclusion and Outlook

This section treated the topology of SPT states in condensed matter physics. More specifically, we identified the three fundamental symmetries TRS, PHS and CS, and studied the topology of the space of allowed Hamiltonians for each symmetry class. The answer is given by the tenfold way in Table 6.2, which can be derived using K-theory when translational invariance is assumed. The tenfold way gives the relevant homotopy group for each of the ten symmetry classes and every spatial dimension $d \geq 0$.

Studying the topology of allowed Bloch Hamiltonians $\mathcal{G}$ is an equivalent approach to studying the topology of $\mathcal{G}_\mathcal{H}$, which has the advantage that it allows for a natural explanation of the bulk-boundary correspondence. Moreover, since the space $\mathcal{G}_\mathcal{H}$ is very complicated to construct (see Section 6.3.4), the Bloch Hamiltonian is the canonical way right now. However, one must discard the second part of the generalised homotopy group in Eq. 6.14 when studying its topology. This

is actually the case for the SSH model in Section 6.3.5: despite being a good educational model, it is a weak topological insulator and the quantisation of the winding number is due to the unitary symmetries of the lattice instead of its symmetry class [102] in the tenfold classification. This is an example where the full homotopy group becomes richer in presence of additional unitary symmetries, in this case (lattice) translational invariance. Upon taking the effect of additional unitary symmetries into account, the tenfold classification can be extended, which is precisely the topic of topological *crystalline* insulators/superconductors [11]. An example of a true strong topological insulator that fits within the tenfold framework is the Haldane model [106]. This is a two-dimensional insulator, characterised by a topological invariant called the Chern number.

An entirely different way of studying the topological properties of SPT states is the framework of quantum geometry [107]. The idea is to parameterise the Hamiltonian $H = H(\lambda)$ with λ^μ being a vector in parameter space. The eigenstates $\psi(\lambda)$ vary with the parameterisation as well, and we denote $\partial_\mu \psi = \frac{\partial \psi}{\partial \lambda^\mu}$. The quantum geometric tensor is then defined as

$$\chi_{\mu\nu} = \langle \partial_\mu \psi | \partial_\nu \psi \rangle - \langle \partial_\mu \psi | \psi \rangle \langle \psi | \partial_\nu \psi \rangle ,$$

and the Berry connection $A_\mu = i \langle \psi | \partial_\mu \psi \rangle$, yielding the Berry curvature

$$F_{\mu\nu} = \partial_\mu A_\nu - \partial_\nu A_\mu = i(\chi_{\mu\nu} - \chi_{\nu\mu}).$$

Analogous to the Berry phase being related to a topological invariant, the winding number for the SSH in Section 6.3.5, the Berry connection A_μ in the context of quantum geometry is used to study the topological properties of the Hamiltonian. In fact, the quantum geometry framework can be applied to non-Hermitian system as well [108]. This has the advantage is that it allows to distinguish phases which are not distinguishable within the Bloch Hamiltonian framework.

Finally, we would like to point out that there are two main open questions regarding the framework of non-interacting (crystalline) topological insulators/superconductors.

- How to implement interactions into the classification scheme?
- How to extend the classification of topological matter to non-integer dimensions?

7. Conclusion

7.1. Conclusion

To conclude, this thesis started with the study of ordered, non-periodic mathematical structures in Chapter 3. These include substitution sequences, tilings, CPS, (multi)fractals and L-systems. More specifically, we zoomed in on a class of aperiodic structures, called quasicrystals, that are mathematically described via a CPS. The most important quasicrystal in this thesis is the Tribonacci word, obtained by projecting a 3D cubic lattice onto a 1D line. In the internal space of two dimensions lies a compact domain with fractal boundary, the Rauzy fractal, which acts as the acceptance set.

To show the relevance of aperiodic order outside the realm of mathematics and theoretical physics, we briefly touched upon experimental realisations of aperiodic structures in Chapter 4. The experiments discussed involve photonic quantum simulators, ultracold quantum simulators and twisted bilayer graphene.

In Chapter 5, the bulk of original work in this thesis, we zoom in on a new quasicrystal called the Tribonacci chain. Analogous to the Fibonacci chain, we define a hopping and on-site Tribonacci chain. These models are based on the Tribonacci numbers that generalise the Fibonacci numbers, hence the model is a generalisation of the Fibonacci chain. First we discuss some non-perturbative properties, such as the trace map, the $E = 0$ eigenstate and the multifractal properties of the Tribonacci chain. Subsequently, we develop the perturbative real-space renormalisation scheme for the Tribonacci chains based on the self-similar properties of the Tribonacci word. The perturbative calculations were carried out using the framework of Brillouin-Wigner Perturbation Theory. This scheme can be used to explain the fractal structure of the energy spectrum and show that the hopping and on-site model are equivalent. When plotting the eigenstates onto Rauzy fractal in the internal space of the Tribonacci word, the renormalisation scheme is shown to dictate the structure of the eigenstates. The renormalisation scheme can be seen to subdivide the Rauzy fractal, where each domain of the subdivision corresponds to a branch of the energy spectrum. We also show that the renormalisation scheme precisely explains the Local Resonator Mode structure of the Tribonacci chains, which is a new insight as well, and that Local Resonator Modes correspond to subdivisions of the Rauzy fractal. Because the details of the Rauzy fractal are relevant to our work, we explain the difference between two common ways in mathematics literature to generate the Rauzy fractal. These methods are the projection method and the valuation map method. They are equivalent, and we derive the relation between them. After a brief analysis of edge modes in the hopping Tribonacci chain with open boundary conditions, we turn to the study of a topological charge pump with a Tribonacci structure. We show that the charge pumping behaviour is analogous to that of the Fibonacci chain, being multilevel. Upon studying the pumping behaviour of more general aperiodic structures, we find that the silver mean and Rudin-Shapiro also behave in a similar way, despite being of a different class of aperiodic order. The Thue-Morse charge pump behaves quite differently, and requires some further investigation.

As a final part of this thesis, we study the tenfold classification of symmetry protected topological states in non-interacting fermionic gapped systems in Chapter 6. The aim is not to give a comprehensive overview, but rather bridge the gap between the mathematical formulation and the canonical approach in physics. Therefore, this section is designed to be accessible to both mathematicians and physicists with minimal preknowledge. After introducing essential preliminaries from mathematics and physics, we define the relevant notion of topology, the fundamental non-

unitary symmetries, and prove the bulk-boundary correspondence. Subsequently, we turn to the tenfold classification using K-theory and end with a summary pointing to alternative descriptions and open questions.

7.2. Outlook

In this final section, we point towards remaining open questions and relevant further directions of research that are connected to the work in this thesis. We start by mentioning some small and relatively straightforward tasks that could not be included in the thesis due to time constraints.

First of all, it could be interesting to develop the trace map of the Tribonacci chain in Section 5.1.1 by deriving the intial conditions and studying its dynamics. A starting point would be Ref. [109] together with the work in this thesis. A more mathematically oriented task would be to study invariants of this trace map, analogous to the Fricke characters for binary trace maps in Ref. [110].

To expand on the second exact result, the $E = 0$ wavefunction in Section 5.1.2, is interesting to see if the method of renormalisation paths developed by Macé et al. [111] can be used to explain all Tribonacci eigenstates as well. Additionally, this framework could be used to study the effect of disorder in the Tribonacci chain, analogous to the work in Ref. [82].

To obtain analytic results next to the numerical results in Section 5.1.3 on the multifractal properties of the spectrum, one could attempt to evaluate Eq. 3.25 for the renormalisation scheme in Eq. 5.33. This is done in Ref. [20] for the Fibonacci chain, which could serve as a guiding example. If this turns out to be unfeasible, one could study and implement more reliable methods of numerically computing the multifractal dimension. This would be a relevant improvement, since the currently used method from Section 3.3.3 does not work for $q < 0$.

In order to strengthen the claims in Section 5.1.3 about the criticality of eigenstates, the inverse participation ratio of the eigenstates should be studied. This is necessary, as the current argument relies on the average over all states, which yields skewed results if one part of the eigenstates is localised and the rest is extended.

Finally, it is interesting to study the anomalous behaviour of the Thue-Morse charge pump in Section 5.5.4. Additionally, the Rudin-Shapiro pump behaves as all other quasicrystalline charge pumps, which is not straightforward. Since self-similarity is a reason to expect multilevel pumping according to Yoshii et al. [89], a starting point could be to compare the self-similar properties of general quasicrystals, the Thue-Morse and Rudin-Shapiro chains. Additionally, the apparent dichotomy between Fig. 5.17c, where charge is pumped without an energy level crossing the Fermi energy, and the intuitive explanation of charge pumps in Ref. [92] could be studied.

Now, we turn to more ambitious and impactful open questions.

7.2.1. Complete the Generalisation of the Fibonacci Chain

One could generalize the Tribonacci substitution to any Pisot substitution, or consider the general k-bonacci substitution $0 \to 01, 1 \to 02, \ldots, (k-1) \to 0$, as explained in Section 3.1.5. The latter would make the generalization of the Fibonacci chain as complete as the complementary generalization in Refs. [73–75]. The generalisation would be complete in the sense that both the cases fixing the internal dimension $d' = 1$ while increasing the real space dimension d, and, fixing the real space dimension $d = 1$ while increasing the dimension d' of the internal space (this is the k-bonacci approach), would have been explored for all dimensions d and d'.

7.2.2. Topological Classification of the Tribonacci Chains

Kraus and Zilberberg [25] have constructed an explicit equivalence between the Fibonacci chain and a topological model in 2D. It would be interesting to study the ramifications of the Tribonacci word on the topological properties of the HTC and OTC. Constructing an equivalence between the Tribonacci chain, hopping and/or on-site, and some other model in higher dimensions for which the topology is well known, would be key to understanding the topological properties.

7.2.3. Tribonacci Spin Chains

To gain more insight into the aperiodic effect of the Tribonacci word, one could consider the spin chain

$$H = -\sum_i J_i \left(\sigma_i^x \sigma_{i+1}^x + \sigma_i^y \sigma_{i+1}^y\right), \tag{7.1}$$

where the couplings $\{J_i\}$ can depend on the site index and follows the Tribonacci word. Under the Jordan-Wigner transform, this maps to the Hamiltonian of a free fermionic hopping model with couplings $J_i/2$:

$$H = -\sum_i \frac{J_i}{2}\left(c_i^\dagger c_{i+1} + c_{i+1}^\dagger c_i\right) \tag{7.2}$$

$$a_j^\dagger = \sigma_j^x + i\sigma_j^y, \qquad c_j = e^{\pi i \sum_{k=0}^{j-1} a_k^\dagger a_k} a_j$$

Since the Jordan-Wigner transformation implies

$$\sigma_j^z = c_j^\dagger c_j - 1/2,$$

a transverse field term $h_j\sigma_j^z$, changing the XY model to a transverse field Ising model, amounts to adding an on-site energy term to Eq. 7.2. One can make the XY model anisotropic by introducing a nonzero γ_i on each site, changing Eq. 7.1 to

$$H = -\frac{1}{2}\sum_i J_i[(1+\gamma_i)\sigma_i^x\sigma_{i+1}^x + (1-\gamma_i)\sigma_i^y\sigma_{i+1}^y] - \sum_i h_i\sigma_i^z, \tag{7.3}$$

which gives the isotropic XY model for $\gamma_i = h_i = 0$ and the transverse-field Ising model for $\gamma_i = 1$. As Hermisson [112] and Luck and Nieuwenhuizen [113] point out, the $h_i = 0$ isotropic XY model has non-universal scaling behaviour for the Fibonacci substitution. The critical exponents interpolate between the uniform and the random case. Lee and Tong [114] claim that the quantum phase transition of isotropic and anisotropic XY models sit in a different universality class. It would be interesting to understand how these implications change, or not, for the Tribonacci chain.

The take-away is that the relevance of the Tribonacci aperiodicity depends on the model taken, and it would be interesting to find out how exactly. The starting point would be the renormalisation framework by Hermisson et al. [112, 115], or the strong disorder renormalisation as in Ref. [116]. The study of aperiodic spin chains is relevant in holography, as they also occur at the boundaries of discrete Anti-de Sitter spaces [117].

7.2.4. Experimental Realisations

Finally, experimental setups, such as polaritonic waveguides [59] and dielectric resonators [118], which were employed to study the Fibonacci chain, can be used to probe the electronic and multifractal properties of the hopping and on-site Tribonacci chain. In this way, the Fibonacci and Tribonacci chains can be compared in an experimental set-up, validating the analysis in Section 5.1.3.

7.2.5. Topological Classification of Fractal Systems

Perhaps the most ambitious topic for further research, is generalising the classification of topological matter to systems that have *fractional real space dimension*, hence they are fractals. We present the following possible starting points. We note that some (or all) of them could turn out to be ill-posed or simply proved unfeasible after little investigation.

- Since the tenfold framework relies ultimately on the computation of the generalised homotopy group in Eq. 6.14, one could try to formulate the problem with d non-integer. This would require one to come up with a well-defined notion of a non-integer dimensional torus, or sphere.
- Another approach is to directly generalise the concept of a homotopy group $\pi_d(X)$ of some space to non-integer d. It is, however, unclear how one would start attacking problem and no work has been done on it yet, to the best of our knowledge.
- Yet another approach is to generalise the Bloch transformation. If some discrete lattice translational invariance is present, one can apply Bloch's theorem. This is linked to the fact that momentum $\mathbf{k}$ is the conserved charge of translations. In a fractal, translational invariance is swapped for scale invariance. One could try to identify the conserved charge of the discrete scale invariance at hand, and attempt to construct a transformation analogous to the Bloch transformation. The analog of the Brillouin zone for this transform would then serve as the space BZ in Chapter 6, which allows for the study of topology of the analog Bloch Hamiltonian.

Yet another proposition to check is whether quasicrystals can generally be studied via their internal space, which is conumbering for the Fibonacci chain and the Rauzy fractal for the Tribonacci chain, and how the renormalisation scheme can be applied in the internal space to understand the eigenstates. Since the renormalisation scheme originates from the self-similar structure, it could be interesting to study if self-similarity can replace translational invariance in the topological classification of quasicrystals and/or fractals.

A. Supplementary Material for the Tribonacci Chain

For further reference, we start by writing down all the orders of Eq. 5.30 that we need in this appendix:

$$
\begin{aligned}
H_{\text{eff}}^{(0)} =& QH_0Q, \\
H_{\text{eff}}^{(1)} =& H_{\text{eff}}^{(0)} + QH_1Q, \\
H_{\text{eff}}^{(2)} =& H_{\text{eff}}^{(1)} + QH_1P\frac{1}{E-H_0}H_1Q, \\
H_{\text{eff}}^{(3)} =& H_{\text{eff}}^{(2)} + QH_1P\frac{1}{E-H_0}H_1P\frac{1}{E-H_0}H_1Q, \\
&\vdots \\
H_{\text{eff}}^{(n)} =& H_{\text{eff}}^{(n-1)} + QH_1\left(P\frac{1}{E-H_0}H_1\right)^{n-1}Q.
\end{aligned}
$$

A.1. BWPT Calculations for the Hopping Model

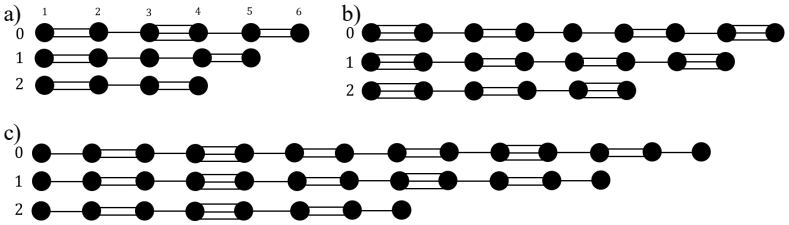

Figure A.1.: The different chains occurring in the HTC. The black dots denote the lattice sites, a single/double/triple line denotes a $t_0/t_1/t_2$ bond. a) the molecular-1 chains, b) molecular-2 chains and c) atomic chains. The vertical numbers $0, 1, 2$ denote the letter to which that chain renormalizes, the horizontal numbers $1, 2, \ldots$ denote the lattice site labeling in the perturbative calculations in Section A.1.

The results of the perturbative calculations for the renormalized couplings t_i' are summarized in Table 5.2. In this table, the function $c(p, q)$ is the leading order in ρ in $t_i' = c(p, q)t_i$. The last two columns give the new $\rho^{p_i} = |t_0'/t_1'|$ and $\rho^{q_i} = |t_1'/t_2'|$.

We can now explain how Eq. 5.33 is obtained. Let $t_0 = 0$, take one of the five unperturbed energies $E_0 = 0, \pm t_1, \pm t_2$, and consider the chain formed by the unperturbed eigenstates with that energy. Firstly, the p_i and q_i corresponding to that chain are exactly the exponents in the block $z_i H_{N-k}^{(p_i,q_i)} + E_0$. The value k corresponding to E_0 can be read off from the last column of Table 5.1, and is given by $k = 2, 3, 4$ for $E_0 = \pm t_1, \pm t_2, 0$ for the HTC, respectively. The value of z_i is the ratio between the chain under consideration and $H_{N-k}^{(p_i,q_i)}$. Note that if all bonds in $H_{N-k}^{(p_i,q_i)}$ are divided by t_2, the spectrum is bounded and of size $\mathcal{O}(1)$. So in order to match the

energy scale of the chain under consideration and $H_{N-k}^{(p_i,q_i)}$, we divide all renormalized couplings in the chain by t_2' and all couplings in $H_{N-k}^{(p_i,q_i)}$ by t_2. This is equivalent to multiplying $H_{N-k}^{(p_i,q_i)}$ by $t_2'/t_2 = c_2(p,q) = z_i$, which means that $z_i H_{N-k}^{(p_i,q_i)}$ is now an approximation of the HTC with renormalized couplings t_i'. Finally, the result is shifted by the value of E_0, since the new lattice sites of each chain have the on-site energy E_0. This procedure is carried out for each of the five E_0 values, thereby obtaining five blocks in Eq. 5.33.

The remainder of this section is devoted to computing the t_i' values in Table 5.2. All calculations are done for the HTC $H_N^{(p,q)}$, where $p, q > 0$ are assumed to be integers. It turns out that the order of perturbation theory needed is equal to the amount of t_0 in the chain that is considered in Fig. A.1. This means that in the worst case, which is the top chain in Fig. A.1(c), one needs seven orders of perturbation theory. We show all computational details for the type-1 molecular chain. For the other chains, the computational steps are identical, but we give only the operators H_1, $\frac{1}{E-H_0}P$ and eigenstates, and skip the computational steps of repeatedly applying these operators. This is enough, because if the operators and eigenstates are known, the computation can be carried out using a computer algebra program such as Mathematica.

A.1.1. Type-1 Molecules

Computation of t_0'

Consider the top chain in Fig. A.1(a), for which the Hamiltonian $H = H_0 + H_1$ reads

$$\begin{aligned} H_0 &= t_1 |1\rangle \langle 2| + t_2 |3\rangle \langle 4| + t_1 |5\rangle \langle 6| + H.c., \\ H_1 &= t_0 |2\rangle \langle 3| + t_0 |4\rangle \langle 5| + H.c., \end{aligned}$$

and the six eigenstates of H_0 read

$$\begin{aligned} |\pm\rangle_1 &= (|1\rangle \pm |2\rangle)/\sqrt{2}, \qquad E_0 = \pm t_1, \\ |\pm\rangle_2 &= (|3\rangle \pm |4\rangle)/\sqrt{2}, \qquad E_0 = \pm t_2, \\ |\pm\rangle_3 &= (|5\rangle \pm |6\rangle)/\sqrt{2}, \qquad E_0 = \pm t_1, \end{aligned}$$

from which we can read off

$$Q = |\pm\rangle_1 \langle\pm|_1 + |\pm\rangle_3 \langle\pm|_3 .$$

The perturbation theory gives

$$\begin{aligned} \langle\pm|_1 H_{\text{eff}}^{(0)} |\pm\rangle_3 &= \langle\pm|_1 H_0 |\pm\rangle_3 = \pm t_1 \langle\pm|_1 |\pm\rangle_3 = 0, \\ \langle\pm|_1 H_{\text{eff}}^{(1)} |\pm\rangle_3 &= \langle\pm|_1 H_1 |\pm\rangle_3 = \pm \frac{t_0}{\sqrt{2}} \langle 3|\pm\rangle_3 = 0, \\ \langle\pm|_1 H_{\text{eff}}^{(2)} |\pm\rangle_3 &= \langle\pm|_1 H_1 P \frac{1}{\pm t_1 - H_0} H_1 |\pm\rangle_3 \\ &= \pm \frac{t_0^2}{2} \langle 3| P \frac{1}{\pm t_1 - H_0} |4\rangle . \end{aligned}$$

We can write $\frac{1}{\pm t_1 - H_0} P$ as

$$\frac{1}{\pm t_1 - H_0} P = \frac{1}{\pm 2t_1} |\mp\rangle_1 \langle\mp|_1 + \frac{1}{\pm t_1 \mp t_2} |\pm\rangle_2 \langle\pm|_2 + \frac{1}{\pm t_1 \pm t_2} |\mp\rangle_2 \langle\mp|_2 + \frac{1}{\pm 2t_1} |\mp\rangle_3 \langle\mp|_3 ,$$

and by using $|4\rangle = \pm \frac{|\pm\rangle_2 - |\mp\rangle_2}{\sqrt{2}}$ we can proceed as

$$\begin{aligned} \langle\pm|_1 H_{\text{eff}}^{(2)} |\pm\rangle_3 &= \frac{t_0^2}{2\sqrt{2}} \langle 3| \frac{1}{\pm t_1 - H_0} P(|\pm\rangle_2 - |\mp\rangle_2) \\ &= \pm \frac{t_0^2}{2\sqrt{2}} \langle 3| \left(\frac{1}{t_1 - t_2} |\pm\rangle_2 - \frac{1}{t_1 + t_2} |\mp\rangle_2 \right) = \mp \frac{t_0^2}{2} \frac{t_2}{t_2^2 - t_1^2} = t_0'. \end{aligned}$$

This can be approximated as

$$t_0' = \mp\frac{t_0^2}{2t_2}\left(1+\mathcal{O}\left(\frac{t_1^2}{t_2^2}\right)\right) \approx \mp\frac{t_0^2}{2t_2} = \mp\frac{\rho^{p+q}}{2}t_0,$$

such that $c_0(p,q) = \rho^{p+q}/2$ can be read off.

Computation of t_1'

Consider the middle chain in Fig. A.1(a), for which the Hamiltonian $H = H_0 + H_1$ reads

$$\begin{aligned} H_0 &= t_1 \left|1\right\rangle \left\langle 2\right| + t_1 \left|4\right\rangle \left\langle 5\right| + H.c., \\ H_1 &= t_0 \left|2\right\rangle \left\langle 3\right| + t_0 \left|3\right\rangle \left\langle 4\right| + H.c., \end{aligned}$$

and the five eigenstates of H_0 read

$$\begin{aligned} \left|\pm\right\rangle_1 &= \left(\left|1\right\rangle \pm \left|2\right\rangle\right)/\sqrt{2}, & E_0 &= \pm t_1, \\ \left|\psi\right\rangle_2 &= \left|3\right\rangle, & E_0 &= 0, \\ \left|\pm\right\rangle_3 &= \left(\left|4\right\rangle \pm \left|5\right\rangle\right)/\sqrt{2}, & E_0 &= \pm t_1, \end{aligned}$$

from which we can read off

$$Q = \left|\pm\right\rangle_1 \left\langle\pm\right|_1 + \left|\pm\right\rangle_3 \left\langle\pm\right|_3.$$

Since the chain consists of two t_0 bonds, we need two orders of perturbation theory for a nonzero result. For that we need

$$\frac{1}{\pm t_1 - H_0}P = \frac{1}{\pm 2t_1}\left|\mp\right\rangle_1 \left\langle\mp\right|_1 + \frac{1}{\pm t_1}\left|\psi\right\rangle_2 \left\langle\psi\right|_2 + \frac{1}{\pm 2t_1}\left|\mp\right\rangle_3 \left\langle\mp\right|_3,$$

which can be used to compute

$$t_1' = \left\langle\pm\right|_1 H_{\text{eff}}^{(2)} \left|\pm\right\rangle_3 = \left\langle\pm\right|_1 H_1 \frac{1}{\pm t_1 - H_0} P H_1 \left|\pm\right\rangle_3 = \pm\frac{t_0^2}{2}\left\langle 3\right| \frac{1}{\pm t_1 - H_0} P \left|3\right\rangle = \frac{t_0^2}{2t_1}.$$

Finally, we can compute the ratio

$$|t_0'/t_1'| = \frac{t_0^2 t_2}{2(t_2^2 - t_1^2)}\frac{2t_1}{t_0^2} = \frac{t_1}{t_2}\frac{1}{1-\frac{t_1^2}{t_2^2}} \approx \rho^q,$$

to leading order in ρ.

Computation of t_2'

Consider the bottom chain in Fig. A.1(a), for which the Hamiltonian $H = H_0 + H_1$ reads

$$\begin{aligned} H_0 &= t_1 \left|1\right\rangle \left\langle 2\right| + t_1 \left|3\right\rangle \left\langle 4\right|) + H.c., \\ H_1 &= t_0 \left|2\right\rangle \left\langle 3\right| + H.c., \end{aligned}$$

and the four eigenstates of H_0 read

$$\begin{aligned} \left|\pm\right\rangle_1 &= \left(\left|1\right\rangle \pm \left|2\right\rangle\right)/\sqrt{2}, & E_0 &= \pm t_1, \\ \left|\pm\right\rangle_2 &= \left(\left|4\right\rangle \pm \left|5\right\rangle\right)/\sqrt{2}, & E_0 &= \pm t_1, \end{aligned}$$

from which we can read off

$$Q = \left|\pm\right\rangle_1 \left\langle\pm\right|_1 + \left|\pm\right\rangle_2 \left\langle\pm\right|_2.$$

Since the chain consists of one t_0 bond, we need one order of perturbation theory for a nonzero result. Hence we can directly compute

$$t_2' = \langle\pm|_1 H_{\text{eff}}^{(1)} |\pm\rangle_2 = \langle\pm|_1 H_1 |\pm\rangle_2 = \frac{t_0}{\sqrt{2}} \langle\pm|_1 |2\rangle = \pm\frac{t_0}{2}.$$

Finally, we can compute the ratio

$$|t_1'/t_2'| = \frac{t_0^2}{2t_1}\frac{2}{t_0} = \frac{t_0}{t_1} = \rho^p.$$

A.1.2. Type-2 Molecules

Computation of t_0'

Consider the top chain in Fig. A.1(b), for which the Hamiltonian $H = H_0 + H_1$ reads

$$\begin{aligned} H_0 &= t_2 |1\rangle\langle 2| + t_1 |3\rangle\langle 4| + t_1 |6\rangle\langle 7| + t_2 |8\rangle\langle 9| + H.c., \\ H_1 &= t_0 \left(|2\rangle\langle 3| + |4\rangle\langle 5| + |5\rangle\langle 6| + |7\rangle\langle 8|\right) + H.c., \end{aligned}$$

and the nine eigenstates of H_0 read

$$\begin{aligned} |\pm\rangle_1 &= \left(|1\rangle \pm |2\rangle\right)/\sqrt{2}, & E_0 &= \pm t_2, \\ |\pm\rangle_2 &= \left(|3\rangle \pm |4\rangle\right)/\sqrt{2}, & E_0 &= \pm t_1, \\ |\psi\rangle_3 &= |5\rangle, & E_0 &= 0, \\ |\pm\rangle_4 &= \left(|6\rangle \pm |7\rangle\right)/\sqrt{2}, & E_0 &= \pm t_1, \\ |\pm\rangle_5 &= \left(|8\rangle \pm |9\rangle\right)/\sqrt{2}, & E_0 &= \pm t_2, \end{aligned}$$

from which we can read off

$$Q = |\pm\rangle_1 \langle\pm|_1 + |\pm\rangle_5 \langle\pm|_5,$$

and

$$\begin{aligned} \frac{1}{\pm t_2 - H_0} P = {} & \frac{1}{\pm 2t_2} |\mp\rangle_1 \langle\mp|_1 + \frac{1}{\pm t_2 \mp t_1} |\pm\rangle_2 \langle\pm|_2 + \frac{1}{\pm t_2 \pm t_1} |\mp\rangle_2 \langle\mp|_2 \\ & + \frac{1}{\pm t_2} |\psi\rangle_3 \langle\psi|_3 + \frac{1}{\pm t_2 \mp t_1} |\pm\rangle_4 \langle\pm|_4 + \frac{1}{\pm t_2 \pm t_1} |\mp\rangle_4 \langle\mp|_4 + \frac{1}{\pm 2t_2} |\mp\rangle_5 \langle\mp|_5. \end{aligned}$$

Now we can compute

$$t_0' = \langle\pm|_1 H_{\text{eff}}^{(4)} |\pm\rangle_5 = \langle\pm|_1 H_1 \left(P \frac{1}{\pm t_2 - H_0} H_1\right)^3 |\pm\rangle_5 = \frac{t_0^4 t_1^2}{2t_2(t_1^2 - t_2^2)^2}.$$

To leading order in ρ this can be expanded as

$$t_0' = \frac{t_0^3 t_1^2}{2t_2(t_1^2 - t_2^2)^2} t_0 \approx \frac{t_0^3 t_1^2}{2t_2^5} t_0 = \frac{\rho^{3p+5q}}{2} t_0,$$

from which we can read off $c_0(p,q) = \rho^{3p+5q}/2$.

Computation of t_1'

Consider the middle chain in Fig. A.1(b), for which the Hamiltonian $H = H_0 + H_1$ reads

$$\begin{aligned} H_0 &= t_2 |1\rangle\langle 2| + t_1 |3\rangle\langle 4| + t_1 |5\rangle\langle 6| + t_2 |7\rangle\langle 8| + H.c., \\ H_1 &= t_0 \left(|2\rangle\langle 3| + |4\rangle\langle 5| + |6\rangle\langle 7|\right) + H.c., \end{aligned}$$

and the eight eigenstates of H_0 read

$$\begin{aligned}
|\pm\rangle_1 &= (|1\rangle \pm |2\rangle)/\sqrt{2}, & E_0 &= \pm t_2,\\
|\pm\rangle_2 &= (|3\rangle \pm |4\rangle)/\sqrt{2}, & E_0 &= \pm t_1,\\
|\pm\rangle_3 &= (|5\rangle \pm |6\rangle)/\sqrt{2}, & E_0 &= \pm t_1,\\
|\pm\rangle_4 &= (|7\rangle \pm |8\rangle)/\sqrt{2}, & E_0 &= \pm t_2,
\end{aligned}$$

from which we can read off

$$Q = |\pm\rangle_1 \langle\pm|_1 + |\pm\rangle_4 \langle\pm|_4 ,$$

and

$$\begin{aligned}
\frac{1}{\pm t_2 - H_0} P = \frac{1}{\pm 2t_2} |\mp\rangle_1 \langle\mp|_1 + \frac{1}{\pm t_2 \mp t_1} |\pm\rangle_2 \langle\pm|_2 + \frac{1}{\pm t_2 \pm t_1} |\mp\rangle_2 \langle\mp|_2 \\
+ \frac{1}{\pm t_2 \mp t_1} |\pm\rangle_3 \langle\pm|_3 + \frac{1}{\pm t_2 \pm t_1} |\mp\rangle_3 \langle\mp|_3 + \frac{1}{\pm 2t_2} |\mp\rangle_4 \langle\mp|_4 .
\end{aligned}$$

Now we can compute

$$t_1' = \langle\pm|_1 H_{\text{eff}}^{(3)} |\pm\rangle_4 = \langle\pm|_1 H_1 \left(P \frac{1}{\pm t_2 - H_0} H_1 \right)^2 |\pm\rangle_4 = \pm \frac{t_0^3 t_1^2}{2(t_1^2 - t_2^2)^2}.$$

To leading order in ρ this can be expanded as

$$t_1' = \pm \frac{t_0^3 t_1}{2(t_1^2 - t_2^2)^2} t_1 \approx \frac{t_0^3 t_1}{2t_2^4} \pm t_1 = \pm \frac{\rho^{3p+4q}}{2} t_1,$$

from which we can read off $c_1(p,q) = \rho^{3p+4q}/2$. Finally, we can compute the ratio

$$|t_0'/t_1'| = \frac{t_0^4 t_1^2}{2t_2(t_1^2 - t_2^2)^2} \frac{2(t_1^2 - t_2^2)^2}{t_0^3 t_1^2} = \frac{t_0}{t_2} = \rho^{p+q}.$$

Computation of t_2'

Consider the bottom chain in Fig. A.1(b), for which the Hamiltonian $H = H_0 + H_1$ reads

$$\begin{aligned}
H_0 &= t_2 |1\rangle \langle 2| + t_1 |3\rangle \langle 4| + t_2 |5\rangle \langle 6| + H.c.,\\
H_1 &= t_0 |2\rangle \langle 3| + t_0 |4\rangle \langle 5| + H.c.,
\end{aligned}$$

and the six eigenstates of H_0 read

$$\begin{aligned}
|\pm\rangle_1 &= (|1\rangle \pm |2\rangle)/\sqrt{2}, & E_0 &= \pm t_2,\\
|\pm\rangle_2 &= (|3\rangle \pm |4\rangle)/\sqrt{2}, & E_0 &= \pm t_1,\\
|\pm\rangle_3 &= (|5\rangle \pm |6\rangle)/\sqrt{2}, & E_0 &= \pm t_2,
\end{aligned}$$

from which we can read off

$$Q = |\pm\rangle_1 \langle\pm|_1 + |\pm\rangle_3 \langle\pm|_3 ,$$

and

$$\frac{1}{\pm t_2 - H_0} P = \frac{1}{\pm 2t_2} |\mp\rangle_1 \langle\mp|_1 + \frac{1}{\pm t_2 \mp t_1} |\pm\rangle_2 \langle\pm|_2 + \frac{1}{\pm t_2 \pm t_1} |\mp\rangle_2 \langle\mp|_2 + \frac{1}{\pm 2t_2} |\mp\rangle_3 \langle\mp|_3 .$$

Now we can compute

$$t_2' = \langle\pm|_1 H_{\text{eff}}^{(2)} |\pm\rangle_3 = \langle\pm|_1 H_1 P \frac{1}{\pm t_2 - H_0} H_1 |\pm\rangle_3 = \pm \frac{t_0^2 t_1}{2(t_2^2 - t_1^2)}.$$

To leading order in ρ this can be expanded as

$$t_2' = \pm\frac{t_0^2 t_1}{2t_2(t_2^2 - t_1^2)} t_2 \approx \pm\frac{t_0^2 t_1}{2t_2^3} t_2 = \pm\frac{\rho^{2p+3q}}{2} t_2,$$

from which we can read off $c_2(p,q) = \rho^{2p+3q}/2$. Finally, we can compute the ratio

$$|t_1'/t_2'| = \frac{t_0^3 t_1^2}{2(t_1^2 - t_2^2)^2} \frac{2(t_2^2 - t_1^2)}{t_0^2 t_1} = \frac{t_0 t_1}{t_2^2 - t_1^2} \approx \frac{t_0 t_1}{t_2^2} = \rho^{p+2q},$$

up to leading order in ρ.

A.1.3. Atoms

Computation of t_0'

Consider the top chain in Fig. A.1(c), for which the Hamiltonian $H = H_0 + H_1$ reads

$$\begin{aligned} H_0 =& t_1 \left(|2\rangle\langle 3| + |6\rangle\langle 7| + |8\rangle\langle 9| + |12\rangle\langle 13|\right) \\ &+ t_2 |4\rangle\langle 5| + t_2 |10\rangle\langle 11| + H.c., \\ H_1 =& t_0\big(|1\rangle\langle 2| + |3\rangle\langle 4| + |5\rangle\langle 6| + |7\rangle\langle 8| \\ &+ |9\rangle\langle 10| + |11\rangle\langle 12| + |13\rangle\langle 14|\big) + H.c., \end{aligned}$$

and the fourteen eigenstates of H_0 read

$$\begin{aligned} |\psi\rangle_1 &= |1\rangle, & E_0 &= 0, \\ |\pm\rangle_2 &= (|2\rangle \pm |3\rangle)/\sqrt{2}, & E_0 &= \pm t_1, \\ |\pm\rangle_3 &= (|4\rangle \pm |5\rangle)/\sqrt{2}, & E_0 &= \pm t_2, \\ |\pm\rangle_4 &= (|6\rangle \pm |7\rangle)/\sqrt{2}, & E_0 &= \pm t_1, \\ |\pm\rangle_5 &= (|8\rangle \pm |9\rangle)/\sqrt{2}, & E_0 &= \pm t_1, \\ |\pm\rangle_6 &= (|10\rangle \pm |11\rangle)/\sqrt{2}, & E_0 &= \pm t_2, \\ |\pm\rangle_7 &= (|12\rangle \pm |13\rangle)/\sqrt{2}, & E_0 &= \pm t_1, \\ |\psi\rangle_8 &= |14\rangle, & E_0 &= 0, \end{aligned}$$

from which we can read off

$$Q = |\psi\rangle_1 \langle\psi|_1 + |\psi\rangle_8 \langle\psi|_8,$$

and

$$\frac{1}{-H_0} P = \sum_{i=2,4,5,7} \frac{1}{\mp t_1} |\pm\rangle_i \langle\pm|_i + \frac{1}{\pm t_1} |\mp\rangle_i \langle\mp|_i + \sum_{j=3,6} \frac{1}{\mp t_2} |\pm\rangle_j \langle\pm|_j + \frac{1}{\pm t_2} |\mp\rangle_j \langle\mp|_j$$

Now we can compute

$$t_0' = \langle\psi|_1 H_{\text{eff}}^{(7)} |\psi\rangle_8 = \langle\psi|_1 H_1 \left(P \frac{1}{-H_0} H_1\right)^6 |\psi\rangle_8 = \frac{t_0^7}{t_1^4 t_2^2},$$

from which we can read off $c_0(p,q) = \frac{t_0^6}{t_1^4 t_2^2} = \rho^{6p+2q}$.

Computation of t_1'

Consider the middle chain in Fig. A.1(c), for which the Hamiltonian $H = H_0 + H_1$ reads

$$\begin{aligned} H_0 =& t_1 \left(|2\rangle\langle 3| + |6\rangle\langle 7| + |10\rangle\langle 11|\right) \\ &+ t_2 |4\rangle\langle 5| + t_2 |8\rangle\langle 9| + H.c., \\ H_1 =& t_0 \big(|1\rangle\langle 2| + |3\rangle\langle 4| + |5\rangle\langle 6| + |7\rangle\langle 8| \\ &+ |9\rangle\langle 10| + |11\rangle\langle 12| \big) + H.c., \end{aligned}$$

and the twelve eigenstates of H_0 read

$$\begin{aligned} |\psi\rangle_1 &= |1\rangle, & E_0 &= 0, \\ |\pm\rangle_2 &= \left(|2\rangle \pm |3\rangle\right)/\sqrt{2}, & E_0 &= \pm t_1, \\ |\pm\rangle_3 &= \left(|4\rangle \pm |5\rangle\right)/\sqrt{2}, & E_0 &= \pm t_2, \\ |\pm\rangle_4 &= \left(|6\rangle \pm |7\rangle\right)/\sqrt{2}, & E_0 &= \pm t_1, \\ |\pm\rangle_5 &= \left(|8\rangle \pm |9\rangle\right)/\sqrt{2}, & E_0 &= \pm t_2, \\ |\pm\rangle_6 &= \left(|10\rangle \pm |11\rangle\right)/\sqrt{2}, & E_0 &= \pm t_1, \\ |\psi\rangle_7 &= |12\rangle, & E_0 &= 0, \end{aligned}$$

from which we can read off

$$Q = |\psi\rangle_1 \langle\psi|_1 + |\psi\rangle_7 \langle\psi|_7,$$

and

$$\frac{1}{-H_0} P = \sum_{i=2,4,6} \frac{1}{\mp t_1} |\pm\rangle_i \langle\pm|_i + \frac{1}{\pm t_1} |\mp\rangle_i \langle\mp|_i + \sum_{j=3,5} \frac{1}{\mp t_2} |\pm\rangle_j \langle\pm|_j + \frac{1}{\pm t_2} |\mp\rangle_j \langle\mp|_j$$

Now we can compute

$$t_1' = \langle\psi|_1 H_{\text{eff}}^{(6)} |\psi\rangle_7 = \langle\psi|_1 H_1 \left(P \frac{1}{-H_0} H_1\right)^5 |\psi\rangle_7 = -\frac{t_0^6}{t_1^3 t_2^2},$$

from which we can read off $c_1(p,q) = \frac{t_0^6}{t_1^4 t_2^2} = \rho^{6p+2q}$. Finally, we can compute the ratio

$$|t_0'/t_1'| = \frac{t_0^7}{t_1^4 t_2^2} \frac{t_1^3 t_2^2}{t_0^6} = \frac{t_0}{t_1} = \rho^p.$$

Computation of t_2'

Consider the bottom chain in Fig. A.1(c), for which the Hamiltonian $H = H_0 + H_1$ reads

$$\begin{aligned} H_0 =& t_1 |2\rangle\langle 3| + t_1 |6\rangle\langle 7| \\ &+ t_2 |4\rangle\langle 5| + H.c., \\ H_1 =& t_0 \big(|1\rangle\langle 2| + |3\rangle\langle 4| + |5\rangle\langle 6| + |7\rangle\langle 8| \big) + H.c., \end{aligned}$$

and the eight eigenstates of H_0 read

$$\begin{aligned} |\psi\rangle_1 &= |1\rangle, & E_0 &= 0, \\ |\pm\rangle_2 &= \left(|2\rangle \pm |3\rangle\right)/\sqrt{2}, & E_0 &= \pm t_1, \\ |\pm\rangle_3 &= \left(|4\rangle \pm |5\rangle\right)/\sqrt{2}, & E_0 &= \pm t_2, \\ |\pm\rangle_4 &= \left(|6\rangle \pm |7\rangle\right)/\sqrt{2}, & E_0 &= \pm t_1, \\ |\psi\rangle_5 &= |8\rangle, & E_0 &= 0, \end{aligned}$$

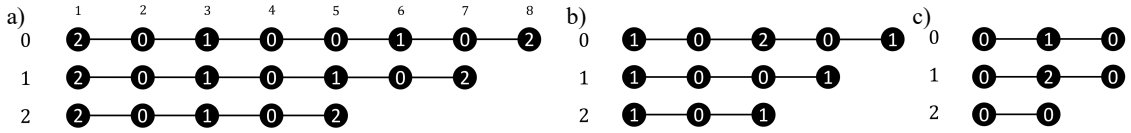

Figure A.2.: The different chains occurring in the OTC. The black dots denote the lattice sites, the black lines a bond t and the number in the black dot denotes ϵ_i, the on-site potential . a) the type-2 atomic chains, b) type-1 atomic chains and c) type-0 atomic chains. The vertical numbers $0, 1, 2$ denote the letter to which that chain renormalizes, the horizontal numbers $1, 2, \ldots$ denote the lattice site labeling in the perturbative calculations in Section A.2.

from which we can read off

$$Q = |\psi\rangle_1 \langle\psi|_1 + |\psi\rangle_5 \langle\psi|_5 ,$$

and

$$\frac{1}{-H_0}P = \sum_{i=2,4} \frac{1}{\mp t_1} |\pm\rangle_i \langle\pm|_i + \frac{1}{\pm t_1} |\mp\rangle_i \langle\mp|_i + \frac{1}{\mp t_2} |\pm\rangle_3 \langle\pm|_3 + \frac{1}{\pm t_2} |\mp\rangle_3 \langle\mp|_3$$

Now we can compute

$$t_2' = \langle\psi|_1 H_{\text{eff}}^{(4)} |\psi\rangle_5 = \langle\psi|_1 H_1 \left(P\frac{1}{-H_0}H_1\right)^3 |\psi\rangle_5 = -\frac{t_0^4}{t_1^2 t_2},$$

from which we can read off $c_2(p,q) = \frac{t_0^4}{t_1^2 t_2^2} = \rho^{4p+2q}$. Finally, we can compute the ratio

$$|t_1'/t_2'| = \frac{t_0^6}{t_1^3 t_2^2}\frac{t_1^2 t_2}{t_0^4} = \frac{t_0^2}{t_1 t_2} = \rho^{2p+q}.$$

A.2. BWPT Calculations for the On-site Model

The results of the perturbative calculations for the renormalized couplings t_i' are summarized in Table 5.3. The construction of Eq. 5.36 from Tables 5.3 and 5.4 is entirely analogous to the HTC case. Since the values a_i, b_i in Table 5.4 are not represented as powers of ρ, we use the mathematical identity $a = \rho^{\log a/\log\rho}$ for any real number $a > 0$. Using this trick, the values a_i, b_i can be converted to the exponents $p_i = \log a_i/\log\rho$ and $q_i = \log b_i/\log\rho$ in Eq. 5.36.

The remainder of this section is devoted to computing the t_i' values in Tables 5.3 and 5.4. All calculations are done for the OTC H_N^o, for arbitrary real c_1 and c_2 that satisfy $|c_1| \gg 1, |c_2| \gg 1$ and $|c_2 - c_1| \gg 1$. The perturbative calculations will be easier than for the hopping model, since the unperturbed OTC is diagonal.

A.2.1. Type-2 Atoms

Computation of t_0'

Consider the top chain in Fig. A.2(a), for which the Hamiltonian $H = H_0 + H_1$ reads

$$\begin{aligned} H_0 &= \epsilon_2 |1\rangle\langle 1| + \epsilon_0 |2\rangle\langle 2| + \epsilon_1 |3\rangle\langle 3| + \epsilon_0 |4\rangle\langle 4| \\ &+ \epsilon_0 |5\rangle\langle 5| + \epsilon_1 |6\rangle\langle 6| + \epsilon_0 |7\rangle\langle 7| + \epsilon_2 |8\rangle\langle 8| + H.c., \\ H_1 &= \sum_{i=1}^{7} t |i\rangle\langle i+1| + H.c., \end{aligned}$$

and the eight eigenstates of H_0 read $H_0 |i\rangle = E_0 |i\rangle$, from which we can read off

$$Q = |1\rangle\langle 1| + |8\rangle\langle 8|,$$

and the operator

$$\frac{1}{\epsilon_2 - H_0}P = \frac{1}{\epsilon_2-\epsilon_0}|2\rangle\langle 2| + \frac{1}{\epsilon_2-\epsilon_1}|3\rangle\langle 3| + \frac{1}{\epsilon_2-\epsilon_0}|4\rangle\langle 4| + \frac{1}{\epsilon_2-\epsilon_0}|5\rangle\langle 5| + \frac{1}{\epsilon_2-\epsilon_1}|6\rangle\langle 6| + \frac{1}{\epsilon_2-\epsilon_0}|7\rangle\langle 7|,$$

which is also diagonal. Now we can compute

$$t_0' = \langle 1| H_{\text{eff}}^{(7)} |8\rangle = \langle 1| H_1 \left(P\frac{1}{\epsilon_2 - H_0}H_1\right)^6 |8\rangle = \frac{t^7}{(\epsilon_2-\epsilon_0)^4(\epsilon_2-\epsilon_1)^2} = \frac{t}{c_2^4(c_2-c_1)^2}.$$

Computation of t_1'

Consider the middle chain in Fig. A.2(a), for which the Hamiltonian $H = H_0 + H_1$ reads

$$\begin{aligned} H_0 =& \epsilon_2|1\rangle\langle 1| + \epsilon_0|2\rangle\langle 2| + \epsilon_1|3\rangle\langle 3| + \epsilon_0|4\rangle\langle 4| \\ &+ \epsilon_1|5\rangle\langle 5| + \epsilon_0|6\rangle\langle 6| + \epsilon_2|7\rangle\langle 7| + H.c., \\ H_1 =& \sum_{i=1}^{6} t|i\rangle\langle i+1| + H.c., \end{aligned}$$

and the seven eigenstates of H_0 read $H_0 |i\rangle = E_0 |i\rangle$, from which we can read off

$$Q = |1\rangle\langle 1| + |7\rangle\langle 7|,$$

and the operator

$$\frac{1}{\epsilon_2 - H_0}P = \frac{1}{\epsilon_2-\epsilon_0}|2\rangle\langle 2| + \frac{1}{\epsilon_2-\epsilon_1}|3\rangle\langle 3| + \frac{1}{\epsilon_2-\epsilon_0}|4\rangle\langle 4| + \frac{1}{\epsilon_2-\epsilon_1}|5\rangle\langle 5| + \frac{1}{\epsilon_2-\epsilon_0}|6\rangle\langle 6|,$$

which is also diagonal. Now we can compute

$$t_1' = \langle 1| H_{\text{eff}}^{(6)} |7\rangle = \langle 1| H_1 \left(P\frac{1}{\epsilon_2 - H_0}H_1\right)^5 |7\rangle = \frac{t^6}{(\epsilon_2-\epsilon_0)^3(\epsilon_2-\epsilon_1)^2} = \frac{t}{c_2^3(c_2-c_1)^2}.$$

Finally, we can compute the ratio

$$|t_0'/t_1'| = \left|\frac{t}{c_2^4(c_2-c_1)^2}\frac{c_2^3(c_2-c_1)^2}{t}\right| = \frac{1}{|c_2|}.$$

Computation of t_2'

Consider the bottom chain in Fig. A.2(a), for which the Hamiltonian $H = H_0 + H_1$ reads

$$\begin{aligned} H_0 =& \epsilon_2|1\rangle\langle 1| + \epsilon_0|2\rangle\langle 2| + \epsilon_1|3\rangle\langle 3| + \epsilon_0|4\rangle\langle 4| \\ &+ \epsilon_2|5\rangle\langle 5| + H.c., \\ H_1 =& \sum_{i=1}^{4} t|i\rangle\langle i+1| + H.c., \end{aligned}$$

and the five eigenstates of H_0 read $H_0 |i\rangle = E_0 |i\rangle$, from which we can read off

$$Q = |1\rangle\langle 1| + |5\rangle\langle 5|,$$

and the operator

$$\frac{1}{\epsilon_2 - H_0} P = \frac{1}{\epsilon_2 - \epsilon_0} |2\rangle\langle 2| + \frac{1}{\epsilon_2 - \epsilon_1} |3\rangle\langle 3| + \frac{1}{\epsilon_2 - \epsilon_0} |4\rangle\langle 4|,$$

which is also diagonal. Now we can compute

$$t_2' = \langle 1| H_{\text{eff}}^{(4)} |5\rangle = \langle 1| H_1 \left(P \frac{1}{\epsilon_2 - H_0} H_1 \right)^3 |5\rangle = \frac{t^4}{(\epsilon_2 - \epsilon_0)^2 (\epsilon_2 - \epsilon_1)} = \frac{t}{c_2(c_2 - c_1)}.$$

Finally, we can compute the ratio

$$|t_1'/t_2'| = \left| \frac{t}{c_2^3 (c_2 - c_1)^2} \frac{c_2(c_2 - c_1)}{t} \right| = \frac{1}{|c_2(c_2 - c_1)|}.$$

A.2.2. Type-1 Atoms

Computation of t_0'

Consider the top chain in Fig. A.2(b), for which the Hamiltonian $H = H_0 + H_1$ reads

$$\begin{aligned} H_0 =& \epsilon_1 |1\rangle\langle 1| + \epsilon_0 |2\rangle\langle 2| + \epsilon_2 |3\rangle\langle 3| + \epsilon_0 |4\rangle\langle 4| \\ &+ \epsilon_1 |5\rangle\langle 5| + H.c., \\ H_1 =& \sum_{i=1}^{4} t |i\rangle\langle i+1| + H.c., \end{aligned}$$

and the five eigenstates of H_0 read $H_0 |i\rangle = E_0 |i\rangle$, from which we can read off

$$Q = |1\rangle\langle 1| + |5\rangle\langle 5|,$$

and the operator

$$\frac{1}{\epsilon_1 - H_0} P = \frac{1}{\epsilon_1 - \epsilon_0} |2\rangle\langle 2| + \frac{1}{\epsilon_1 - \epsilon_2} |3\rangle\langle 3| + \frac{1}{\epsilon_1 - \epsilon_0} |4\rangle\langle 4|,$$

which is also diagonal. Now we can compute

$$t_0' = \langle 1| H_{\text{eff}}^{(4)} |5\rangle = \langle 1| H_1 \left(P \frac{1}{\epsilon_1 - H_0} H_1 \right)^3 |5\rangle = \frac{t^4}{(\epsilon_1 - \epsilon_0)^2 (\epsilon_1 - \epsilon_2)} = -\frac{t}{c_1^2 (c_2 - c_1)}.$$

Computation of t_1'

Consider the middle chain in Fig. A.2(b), for which the Hamiltonian $H = H_0 + H_1$ reads

$$\begin{aligned} H_0 =& \epsilon_1 |1\rangle\langle 1| + \epsilon_0 |2\rangle\langle 2| + \epsilon_0 |3\rangle\langle 3| + \epsilon_1 |4\rangle\langle 4| + H.c., \\ H_1 =& \sum_{i=1}^{3} t |i\rangle\langle i+1| + H.c., \end{aligned}$$

and the four eigenstates of H_0 read $H_0 |i\rangle = E_0 |i\rangle$, from which we can read off

$$Q = |1\rangle\langle 1| + |4\rangle\langle 4|,$$

and the operator

$$\frac{1}{\epsilon_1 - H_0} P = \frac{1}{\epsilon_1 - \epsilon_0} |2\rangle \langle 2| + \frac{1}{\epsilon_1 - \epsilon_0} |3\rangle \langle 3|$$

which is also diagonal. Now we can compute

$$t_1' = \langle 1| H_{\text{eff}}^{(3)} |4\rangle = \langle 1| H_1 \left(P \frac{1}{\epsilon_1 - H_0} H_1 \right)^2 |4\rangle = \frac{t^3}{(\epsilon_1 - \epsilon_0)^2} = \frac{t}{c_1^2}.$$

Finally, we can compute the ratio

$$|t_0'/t_1'| = \left| \frac{t}{c_1^2(c_2 - c_1)} \frac{c_1^2}{t} \right| = \frac{1}{|c_2 - c_1|}.$$

Computation of t_2'

Consider the bottom chain in Fig. A.2(b), for which the Hamiltonian $H = H_0 + H_1$ reads

$$\begin{aligned} H_0 =& \epsilon_1 |1\rangle \langle 1| + \epsilon_0 |2\rangle \langle 2| + \epsilon_1 |3\rangle \langle 3| + H.c., \\ H_1 =& t |1\rangle \langle 2| + t |2\rangle \langle 3| + H.c., \end{aligned}$$

and the three eigenstates of H_0 read $H_0 |i\rangle = E_0 |i\rangle$, from which we can read off

$$Q = |1\rangle \langle 1| + |3\rangle \langle 3|,$$

and the operator

$$\frac{1}{\epsilon_1 - H_0} P = \frac{1}{\epsilon_1 - \epsilon_0} |2\rangle \langle 2|,$$

which is also diagonal. Now we can compute

$$t_2' = \langle 1| H_{\text{eff}}^{(2)} |3\rangle = \langle 1| H_1 P \frac{1}{\epsilon_1 - H_0} H_1 |3\rangle = \frac{t^2}{\epsilon_1 - \epsilon_0} = \frac{t}{c_1}.$$

Finally, we can compute the ratio

$$|t_1'/t_2'| = \left| \frac{t}{c_1^2} \frac{c_1}{t} \right| = \frac{1}{|c_1|}.$$

A.2.3. Type-0 Atoms

Computation of t_0'

Consider the top chain in Fig. A.2(c), for which the Hamiltonian $H = H_0 + H_1$ reads

$$\begin{aligned} H_0 =& \epsilon_0 |1\rangle \langle 1| + \epsilon_1 |2\rangle \langle 2| + \epsilon_0 |3\rangle \langle 3| + H.c., \\ H_1 =& t |1\rangle \langle 2| + t |2\rangle \langle 3| + H.c., \end{aligned}$$

and the three eigenstates of H_0 read $H_0 |i\rangle = E_0 |i\rangle$, from which we can read off

$$Q = |1\rangle \langle 1| + |3\rangle \langle 3|,$$

and the operator

$$\frac{1}{\epsilon_0 - H_0} P = \frac{1}{\epsilon_0 - \epsilon_1} |2\rangle \langle 2|,$$

which is also diagonal. Now we can compute

$$t_0' = \langle 1| H_{\text{eff}}^{(2)} |3\rangle = \langle 1| H_1 P \frac{1}{\epsilon_0 - H_0} H_1 |3\rangle = \frac{t^2}{\epsilon_0 - \epsilon_1} = -\frac{t}{c_1}.$$

Computation of t_1'

Consider the middle chain in Fig. A.2(c), for which the Hamiltonian $H = H_0 + H_1$ reads

$$\begin{aligned} H_0 =& \epsilon_0 |1\rangle\langle 1| + \epsilon_2 |2\rangle\langle 2| + \epsilon_0 |3\rangle\langle 3| + H.c., \\ H_1 =& t |1\rangle\langle 2| + t |2\rangle\langle 3| + H.c., \end{aligned}$$

and the three eigenstates of H_0 read $H_0 |i\rangle = E_0 |i\rangle$, from which we can read off

$$Q = |1\rangle\langle 1| + |3\rangle\langle 3|,$$

and the operator

$$\frac{1}{\epsilon_0 - H_0} P = \frac{1}{\epsilon_0 - \epsilon_2} |2\rangle\langle 2|,$$

which is also diagonal. Now we can compute

$$t_1' = \langle 1| H_{\text{eff}}^{(2)} |3\rangle = \langle 1| H_1 P \frac{1}{\epsilon_0 - H_0} H_1 |3\rangle = \frac{t^2}{\epsilon_0 - \epsilon_2} = -\frac{t}{c_2}.$$

Finally, we can compute the ratio $|t_0'/t_1'| = |c_2/c_1|$.

Computation of t_2'

Consider the bottom chain in Fig. A.2(c), for which the Hamiltonian $H = H_0 + H_1$ reads

$$\begin{aligned} H_0 =& \epsilon_0 |1\rangle\langle 1| + \epsilon_0 |2\rangle\langle 2| + H.c., \\ H_1 =& t |1\rangle\langle 2| + H.c., \end{aligned}$$

and the two eigenstates of H_0 read $H_0 |i\rangle = \epsilon_0 |i\rangle$, from which we can read off

$$Q = |1\rangle\langle 1| + |2\rangle\langle 2| = \text{Id}, \qquad \frac{1}{\epsilon_0 - H_0} P = 0,$$

which are not needed anyway. Now we can compute

$$t_2' = \langle 1| H_{\text{eff}}^{(1)} |2\rangle = \langle 1| H_1 |2\rangle = t,$$

and the ratio $|t_1'/t_2'| = 1/|c_2|$.

A.3. BWPT Results for the Hopping Model with Different Energy Scale

Table A.1.: Renormalised couplings for the tribonacci chain, new definition of p', q'.

Lattice	t_0'	$c_0'(p', q')$	t_1'	$c_1'(p', q')$	t_2'	$c_2'(p', q')$
00	$\frac{t_0^7}{t_1^4 t_2^2}$	$\rho^{6p'-4q'}$	$-\frac{t_0^6}{t_1^3 t_2^2}$	$\rho^{6p'-4q'}$	$-\frac{t_0^4}{t_1^2 t_2}$	$\rho^{4p'-2q'}$
1	$\mp\frac{t_0^2 t_2}{2(t_2^2-t_1^2)}$	$\rho^{p'}/2$	$\frac{t_0^2}{2t_1}$	$\rho^{2p'-2q'}/2$	$\pm\frac{t_0}{2}$	$\rho^{p'}/2$
2	$\frac{t_0^4 t_1^2}{2t_2(t_1^2-t_2^2)^2}$	$\rho^{3p'+2q'}/2$	$\pm\frac{t_0^3 t_1^2}{2(t_1^2-t_2^2)^2}$	$\rho^{3p'+q'}/2$	$\pm\frac{t_0^2 t_1}{2(t_2^2-t_1^2)}$	$\rho^{2p'+q'}/2$

In the analysis in Section 5.2, we set $t_0/t_1 = \rho^p, t_1/t_2\rho^q$. Now, is it more common practice to take one energy scale, t_2 and describe $t_0/t_2 = \rho^{p'}, t_1/t_2 = \rho^{q'}$. We immediately see $p' = p + q, q' = q$. So to obtain these results, replace every p in Table 5.2 with $p' - q$. This yields Table A.1, which does not seem to be a big improvement in terms of conciseness of expressions.

A.4. Additional Analysis of Edge Modes in the HTC

A.4.1. N=8

The main thing to note is that for $\Delta = -2, 0$, there is a pronounced in-gap state between the second/third and third/fourth branch of the spectrum, which are right edge modes. Additionally, for all Δ, there is a state sitting in the gap of the second (fourth) branch of the spectrum, corresponding to a left-edge state. This one is always present because the left side of the chain is always the same.

$\Delta = -2$

Looking at the first and last bond of the chain, we denote all the bonds from the left and from the right inward, up the bond at which the first difference occurs. This results in $01 \cdots 00$, i.e. the first and last bond are a t_0, the second bond is a t_1 and the second to last bond is a t_0. This means that the first difference occurs at the second bond.

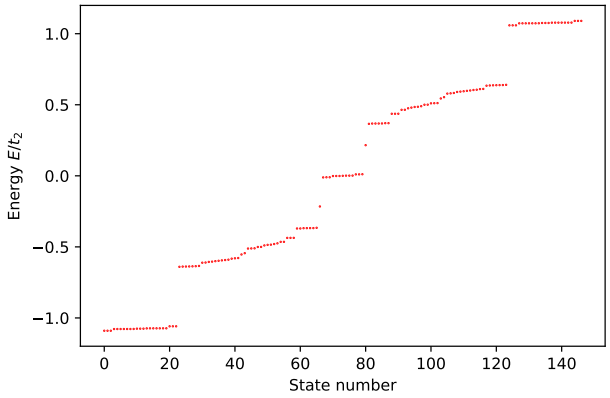

Figure A.3.: $N = 8, \Delta = -2$.

Below we show all eigenstates that behave like edge modes.

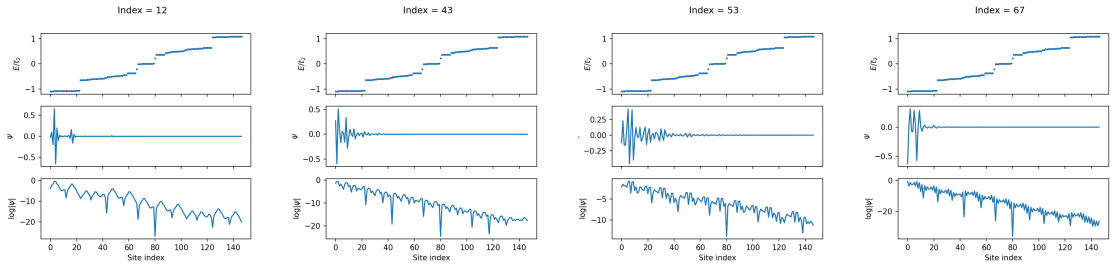

(a) (b) (c) (d)

Figure A.4.: All left modes of $N = 8, \Delta = -2$.

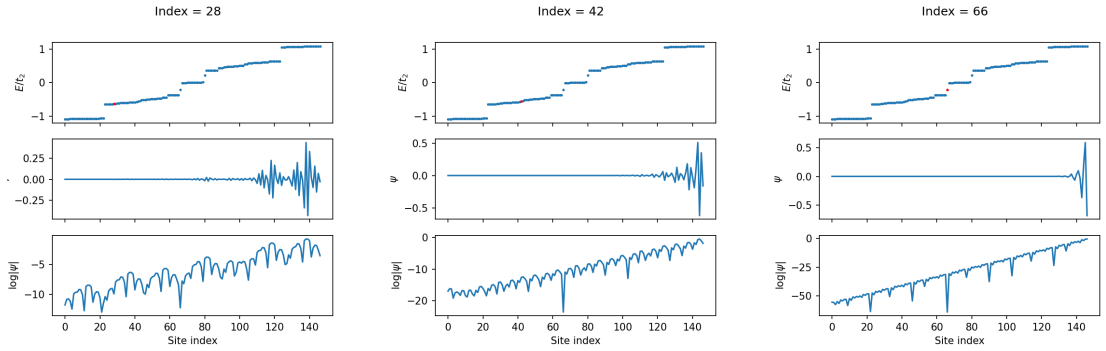

(a) (b) (c)

Figure A.5.: All right edge modes of $N = 8, \Delta = -2$.

A.4.2. N=9

Now we consider $N = 9$, to have a slightly better resolution, while it is still feasible to manually inspect all eigenstates.

$\Delta = 0$

Looking at the first and last bond of the chain, we denote all the bonds from the left and from the right inward, up the bond at which the first difference occurs. This results in $0 \cdots 1$.

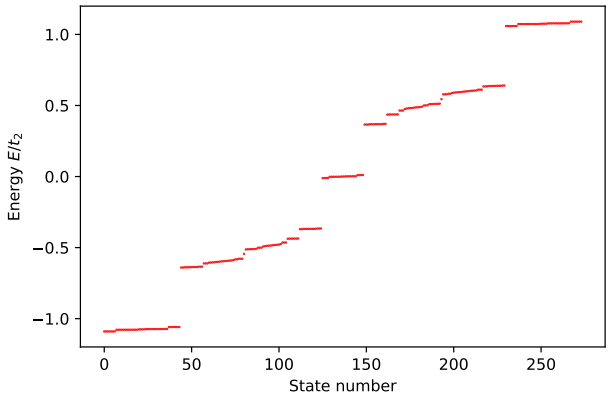

Figure A.6.: $N = 9, \Delta = 0$.

Below we show all eigenstates that behave like edge modes.

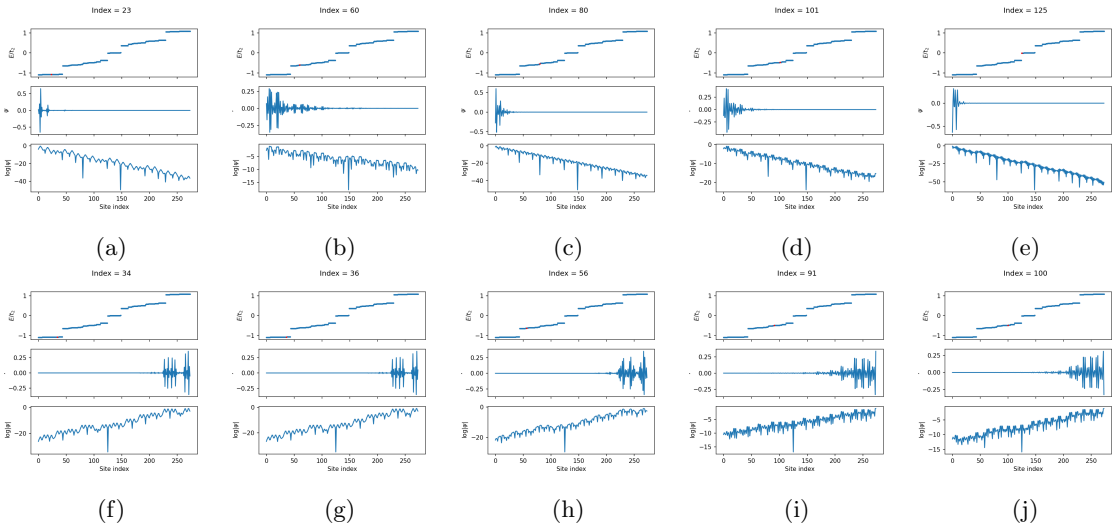

Figure A.7.: All edge modes of $N = 9, \Delta = 0$.

$\Delta = 1$

Looking at the first and last bond of the chain, we denote all the bonds from the left and from the right inward, up the bond at which the first difference occurs. This results in $01020100 \cdots 10102010$. Note that the difference occurs here at the ninth symbol. This means that the left and right modes must sit quite close in the spectrum, which is indeed the case. Those modes correspond to index 80 and 81 in Figs. A.9c and A.9h, respectively.

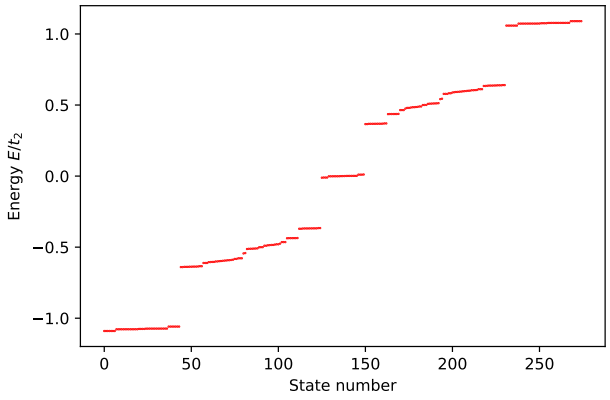

Figure A.8.: $N = 9, \Delta = 1$.

Below we show all eigenstates that behave like edge modes.

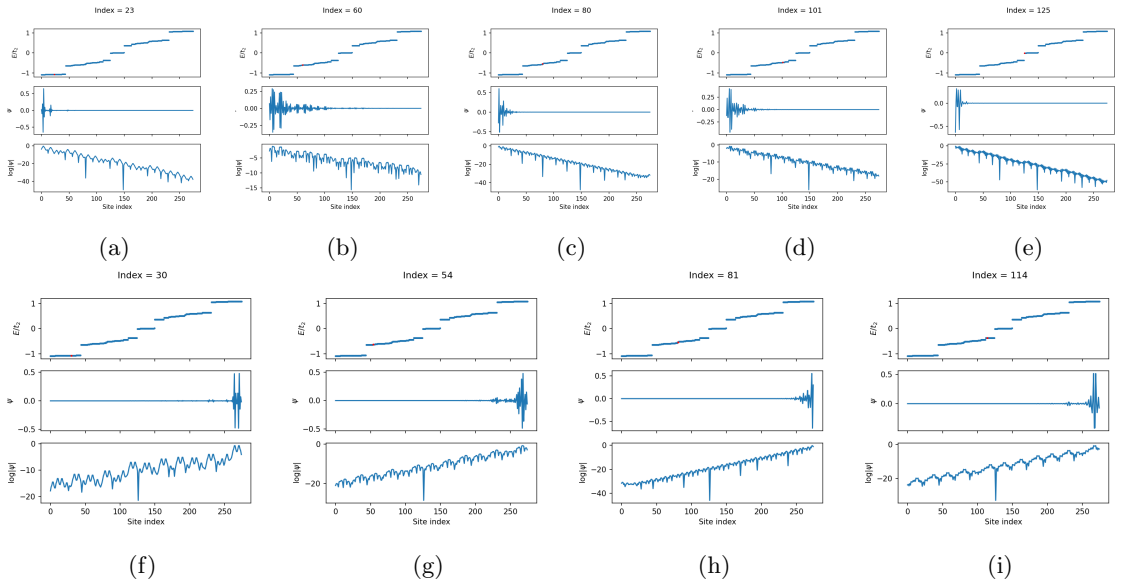

Figure A.9.: All edge modes of $N = 9, \Delta = 1$.

$\Delta = -2$

Looking at the first and last bond of the chain, we denote all the bonds from the left and from the right inward, up the bond at which the first difference occurs. This results in $0 \cdots 2$.

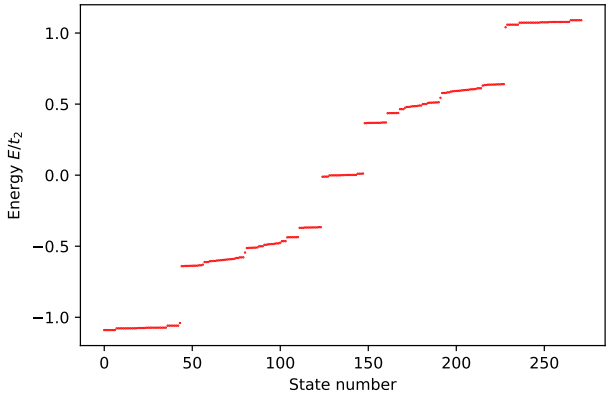

Figure A.10.: $N = 9, \Delta = -2$.

Below we show all eigenstates that behave like edge modes.

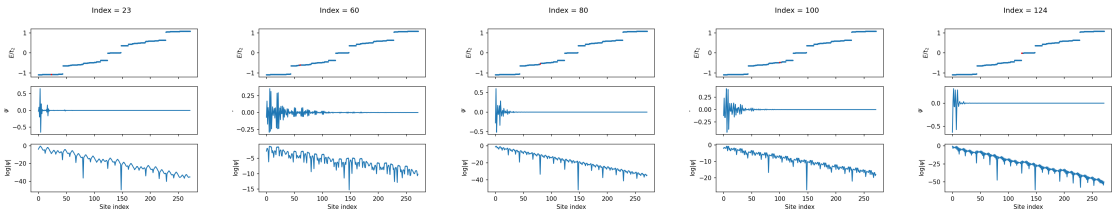

(a) (b) (c) (d) (e)

Figure A.11.: All left edge modes of $N = 9, \Delta = -2$.

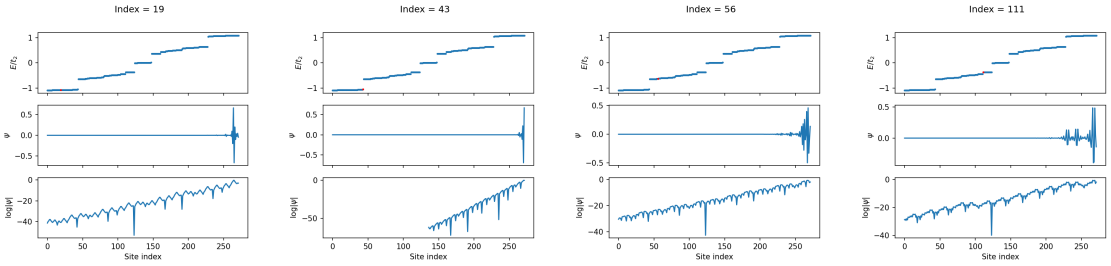

(a) (b) (c) (d)

Figure A.12.: All right edge modes of $N = 9, \Delta = -2$.

A.4.3. Larger Approximants

Below we show spectra of Eq. 5.51 for higher values of N. Note that the pronounced in-gap modes between second/third and third/fourth branch occur at $N = 3k + 2$. These correspond to right edge modes, and since the termination of W_N is the same with period three in N, this is expected.

Furthermore, the in-gap states within the second and fourth branch (e.g. the in-gap state between index 200 and 400 or 600 and 800 in Fig. A.13a) are present for all N. This is no surprise, since these correspond to left edge modes.

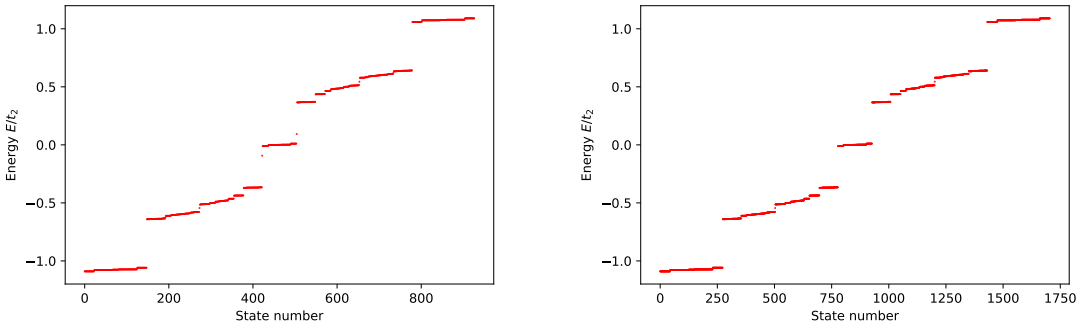

(a) $N = 11, \Delta = 0$. (b) $N = 12, \Delta = 0$.

Figure A.13.: More spectra of Eq. 5.51.

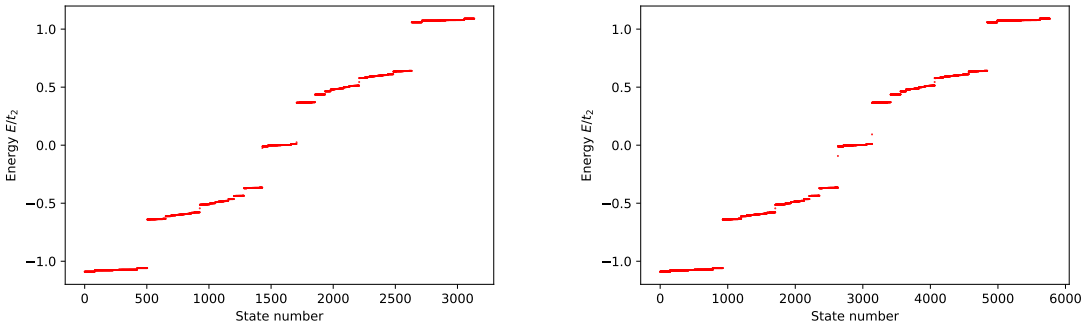

(a) $N = 13, \Delta = 0$.

(b) $N = 14, \Delta = 0$.

Figure A.14.: More spectra of Eq. 5.51.

A.5. Wavefunctions on the Rauzy Fractal

Figs. A.15 and A.16 contain more examples of eigenstates plotted on the Rauzy fractal, where the Rauzy fractal is subdivided again according to environments of the local structures. These figures give more evidence for the observation that the eigenstates localize on the Rauzy fractal in regions that correspond to the branch of the spectrum of the eigenstate. For example, in Fig. A.16(a)/(b)/(c), the state belongs to the bottom/middle/top branch of the spectrum, hence localizes on the red/green/blue area of the Rauzy fractal.

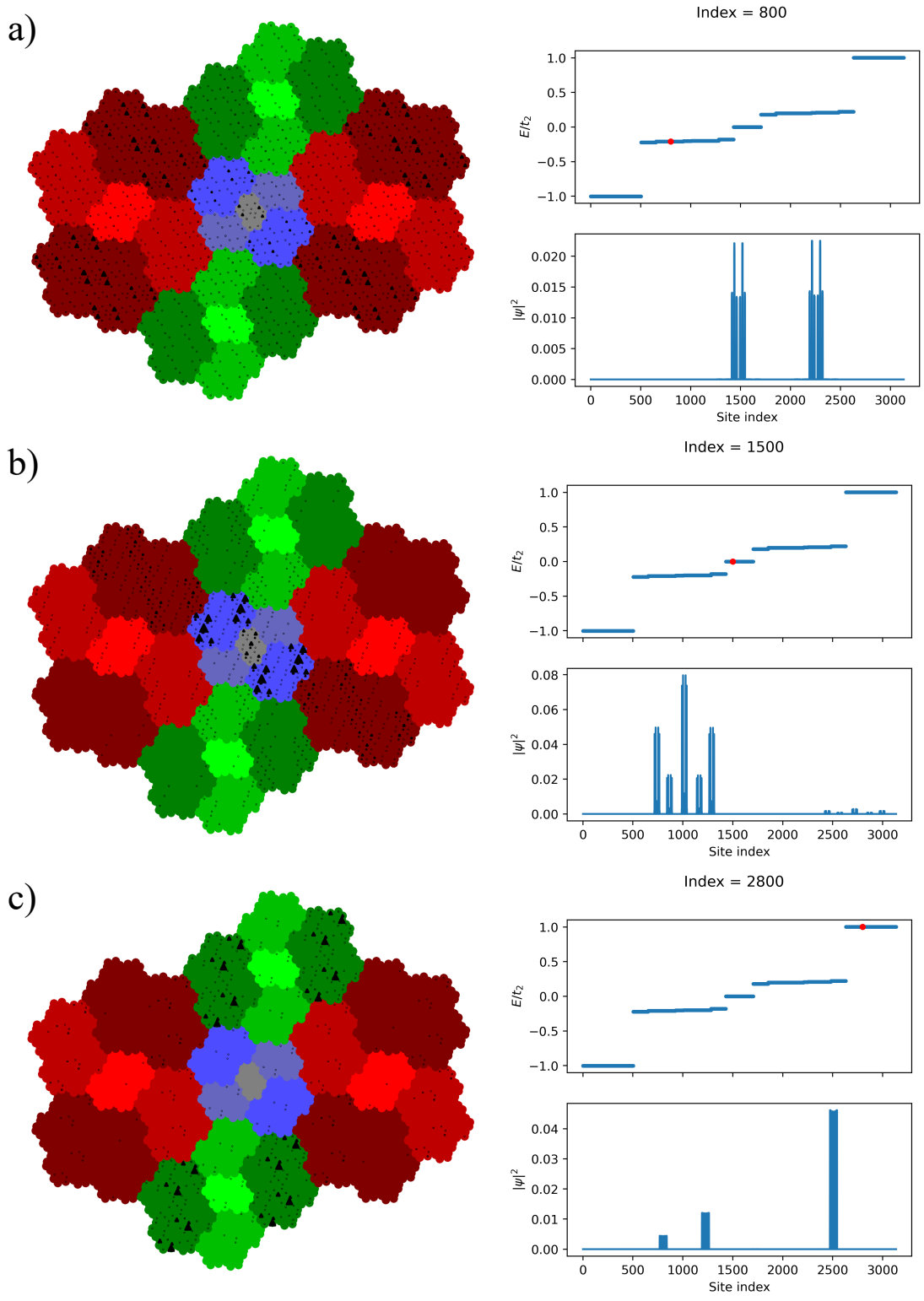

Figure A.15.: (Color online) Three eigenstates of the HTC H_{13}, plotted on the subdivided Rauzy fractal. The height of the black triangles on site n are proportional to $|\psi_i(n)|^2$. On the right hand side, the eigenstate is plotted, together with the state (red dot) in the spectrum (blue). a) $i = 800$, b) $i = 1500$ and c) $i = 2800$.

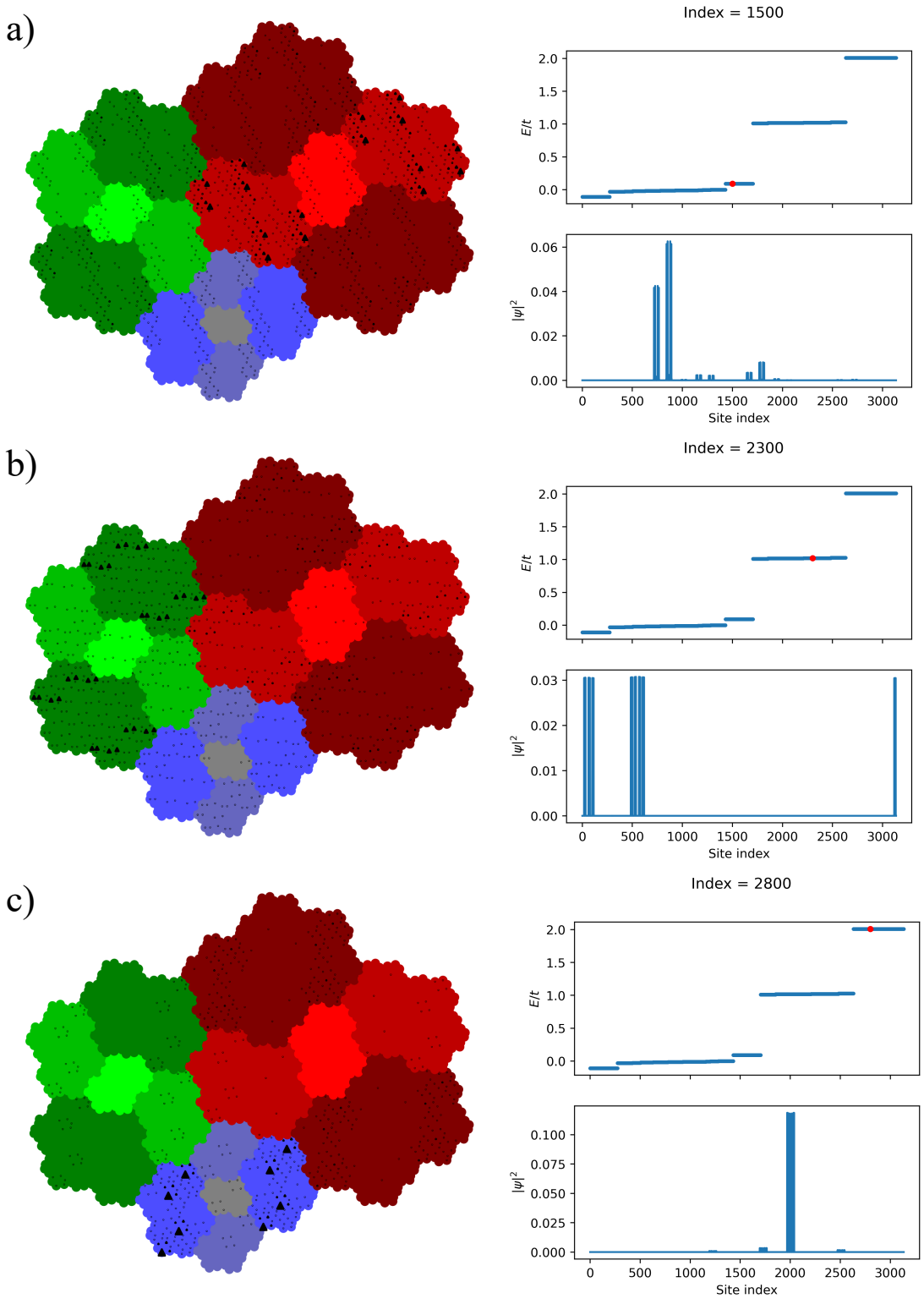

Figure A.16.: (Color online) Three eigenstates of the OTC H^o_{13}, plotted on the subdivided Rauzy fractal. The height of the black triangles on site n are proportional to $|\psi_i(n)|^2$. On the right hand side, the eigenstate is plotted, together with the state (red dot) in the spectrum (blue). a) $i = 1500$, b) $i = 2300$ and c) $i = 2800$.

B. Appendix

B.1. Symmetric spectrum for hopping models

Consider a chain with N sites, described by a tight-binding Hamiltonian

$$H = \sum_{i=1}^{N-1} a_i \left|i\right\rangle \left\langle i+1\right| + b_i \left|i+1\right\rangle \left\langle i\right| = \begin{pmatrix} 0 & a_1 & & & \\ b_1 & 0 & a_2 & & \\ & b_2 & \ddots & \ddots & \\ & & \ddots & \ddots & a_{N-1} \\ & & & b_{N-1} & 0 \end{pmatrix} \in \mathrm{GL}(N, \mathbb{C}), \tag{B.1}$$

which need not be Hermitian. The energy spectrum consists of the roots of the characteristic polynomial $p(\lambda) = \det(H - \lambda \,\mathrm{Id})$, where Id is the identity matrix. We will prove that for any Hamiltonian Eq. B.1, it is true that for all $\lambda \in \mathbb{C}$ such that $p(\lambda) = 0$, one also has $p(-\lambda) = 0$. More precisely:

Theorem B.1. *For any $N \times N$ tridiagonal matrix $A \in \mathrm{GL}(N, \mathbb{C})$, where $N \in \mathbb{N}$, with zero diagonal, it is true that*

$$\lambda \in \sigma(A) \iff -\lambda \in \sigma(A).$$

Proof. The determinant of a general tridiagonal matrix

$$T = \begin{pmatrix} c_1 & a_1 & & & \\ b_1 & c_2 & a_2 & & \\ & b_2 & \ddots & \ddots & \\ & & \ddots & \ddots & a_{N-1} \\ & & & b_{N-1} & c_N \end{pmatrix} \in \mathrm{GL}(N, \mathbb{C}),$$

can be obtained using the following recursion relation [119]. Let $f_{-1} = 0, f_0 = 1$, where the recurrence relation reads

$$f_n = c_n f_{n-1} - a_{n-1} b_{n-1} f_{n-2}.$$

The determinant is then the Nth iteration, i.e. $\det T = f_N$.

Now let A be the matrix in Eq. B.1, which is a general $N \times N$ tridiagonal matrix with zero diagonal. Observe that $T = A - \lambda \,\mathrm{Id}$ is a tridiagonal matrix, for which the recurrence relation reads

$$f_n(\lambda) = -\lambda f_{n-1}(\lambda) - a_{n-1} b_{n-1} f_{n-2}(\lambda),$$

where the λ dependence is implemented as a function property. The key to proving the theorem is the observation that for n even (odd), $f_n(\lambda)$ is an even (odd) function of λ for $n \geq 1$. We will show this using strong induction.

- For $n = 1$, one has $f_1(\lambda) = -\lambda$, which is an odd function.
- For $n = 2$, one has $f_2(\lambda) = \lambda^2 - a_1 b_1$, which is an even function.

- Now suppose that for all $1 \leq k < n$, it holds that $f_k(\lambda)$ is an even (odd) function of λ if k is even (odd). Suppose that n is even (odd), then $-\lambda f_{n-1}(\lambda)$ and $f_{n-2}(\lambda)$ are both even (odd) functions, which makes $f_n(\lambda) = -\lambda f_{n-1}(\lambda) - a_{n-1}b_{n-1}f_{n-2}(\lambda)$ an even (odd) function, which completes the induction step, and hence the proof.

From this we can conclude that $\det(A - \lambda \,\mathrm{Id}) = f_N(\lambda) = \pm f_N(-\lambda)$, where it is $+$ for N even and $-$ for N odd. For $\lambda \in \sigma(A)$ to hold, $f_N(\lambda) = \pm f_N(-\lambda) = 0$ must be true, which implies $-\lambda \in \sigma(A)$, proving the statement. □

An alternative way to prove Theorem B.1 is based on chiral symmetry, also known as sublattice symmetry: the sites with an even label only interact with odd labeled sites, and vice versa. This leads one to introduce the operator

$$\Gamma = \sum_{j=1}^{\lceil N/2 \rceil} |2j-1\rangle \langle 2j-1| - \sum_{j=1}^{\lfloor N/2 \rfloor} |2j\rangle \langle 2j|,$$

which acts as the identity on the odd sites and as minus the identity on the even sites. One can check that for any H as in Eq. B.1, it is true that $H\Gamma = -\Gamma H$. Now suppose $H|\psi\rangle = E|\psi\rangle$ for some $E \in \mathbb{C}$, then $H|\phi\rangle = H\Gamma|\psi\rangle = -\Gamma H|\psi\rangle = -E\Gamma|\psi\rangle = -E|\phi\rangle$. This means that for every $E \in \sigma(H)$ with eigenstate $|\psi\rangle$, the state $|\phi\rangle = \Gamma|\psi\rangle$ has energy $-E$, which proves Theorem B.1.

B.2. Biorthogonal Bases

Let M be a diagonalisable $n \times n$ matrix with elements in a field F. This means that there exist n eigenvalues λ_n and eigenvectors $|v_n\rangle$ such that $M|v_n\rangle = \lambda_n |v_n\rangle$ and $\{|v_i\rangle\}_i$ spans F^n. If one arranges the vectors as columns of a matrix

$$V = \begin{pmatrix} | & & | \\ |v_1\rangle & \cdots & |v_n\rangle \\ | & & | \end{pmatrix},$$

it is known that these matrices diagonalise the matrix as

$$D = V^{-1}MV = \begin{pmatrix} \lambda_1 & & \\ & \lambda_2 & \\ & & \ddots \end{pmatrix}.$$

The columns $|v_i\rangle$ of V are the *right* eigenvectors. Similarly, there exist *left* eigenvectors $\langle w_i|$ such that $\langle w_i| M = \gamma_i \langle w_i|$. For Hermitian matrices, $\langle w_i| = |v_i\rangle^\dagger$ and $\gamma_i = \lambda_i$ holds, and the eigenvectors are orthogonal.

In general, eigenvectors are not orthogonal and the left- and right eigenvectors are different. It turns out, however, that the left eigenvectors is the dual basis of the right eigenvectors. Consider

$$V^{-1} = \begin{pmatrix} — & \langle u_1| & — \\ & \vdots & \\ — & \langle u_n| & — \end{pmatrix},$$

now we can show that $\langle u_i|$ are left eigenvectors of M:

$$V^{-1}M = V^{-1}MVV^{-1} = DV^{-1} = \begin{pmatrix} — & \lambda_1 \langle u_1| & — \\ & \vdots & \\ — & \lambda_n \langle u_n| & — \end{pmatrix}.$$

This shows that the left eigenvectors are the rows of V^{-1}, the inverted matrix where the columns are the right eigenvectors, and that the left- and right eigenvectors have the same eigenvalues. Moreover, since $V^{-1}V = \mathrm{Id}$, the left- and right eigenvectors form a *biorthogonal system*, i.e. $\langle u_i | v_j \rangle = \delta_{ij}$.

It is important to note that this is not a biorthonormal system. Even when the right eigenvectors $|v_i\rangle$ are chosen to be unit vectors, the corresponding left eigenvectors $\langle u_i|$ are not of unit length in general. This is an important notion in non-Hermitian quantum mechanics, where the resolution of identity is written as

$$\mathrm{Id} = \sum_n \frac{|v_n\rangle \langle u_n|}{\langle u_n | v_n \rangle},$$

where the eigenvectors are chosen to be of unit length, such that $\langle u_n | v_n \rangle$ need not be unity.

C. Overview of Original Results

This appendix presents an overview of all original results in this thesis.

- Proving the correspondence between $S(\mathbf{q})$ and the Fourier Transform of the autocorrelation measure γ_Λ in Section 3.2.1.
- Explicit proof of the conumbering scheme for the Fibonacci chain in Section 3.2.2.
- All figures in this thesis that do not explicitly refer to a source from which they are taken. Notable examples are:
  - The 3D visualisation of the cut-and-project procedure for the Tribonacci word in Fig. 3.6a.
  - Plots of Moiré patterns in Figs. 4.7, 4.8a and 4.8b.
- The Tribonacci chain, Chapter 5, and all corresponding results, leading to the publication Ref. [27].
- The explicit correspondence between the two methods of obtaining the Rauzy fractal, treated in Section 5.3.1.
- Theorem 6.10 and its proof.

Bibliography

[1] Felix Bloch. Über die quantenmechanik der elektronen in kristallgittern. *Zeitschrift für physik*, 52(7-8):555–600, 1929. 7, 39, 88

[2] D. Shechtman, I. Blech, D. Gratias, and J. W. Cahn. Metallic phase with long-range orientational order and no translational symmetry. *Phys. Rev. Lett.*, 53:1951–1953, Nov 1984. 7, 9

[3] N. G. de Bruijn. Algebraic theory of Penrose's nonperiodic tilings of the plane. I, II. *Nederl. Akad. Wetensch. Indag. Math.*, 43(1):39–52, 53–66, 1981. 7, 11, 28

[4] David Smith, Joseph Samuel Myers, Craig S. Kaplan, and Chaim Goodman-Strauss. An aperiodic monotile, 2023. 7

[5] David Smith, Joseph Samuel Myers, Craig S. Kaplan, and Chaim Goodman-Strauss. A chiral aperiodic monotile, 2023. 7

[6] Konrad Viebahn, Matteo Sbroscia, Edward Carter, Jr-Chiun Yu, and Ulrich Schneider. Matter-wave diffraction from a quasicrystalline optical lattice. *Phys. Rev. Lett.*, 122:110404, Mar 2019. 7, 44, 45

[7] Valentin Goblot, Antonio Štrkalj, Nicolas Pernet, Jose L Lado, C Dorow, Aristide Lemaître, Luc Le Gratiet, Abdelmounaim Harouri, Isabelle Sagnes, Sylvain Ravets, et al. Emergence of criticality through a cascade of delocalization transitions in quasiperiodic chains. *Nature Physics*, 16(8):832–836, 2020. 7

[8] D. J. Thouless, M. Kohmoto, M. P. Nightingale, and M. den Nijs. Quantized Hall conductance in a two-dimensional periodic potential. *Phys. Rev. Lett.*, 49:405–408, Aug 1982. 7, 95

[9] Alexander Altland and Martin R. Zirnbauer. Nonstandard symmetry classes in mesoscopic normal-superconducting hybrid structures. *Phys. Rev. B*, 55:1142–1161, Jan 1997. 7, 99

[10] Andreas W W Ludwig. Topological phases: classification of topological insulators and superconductors of non-interacting fermions, and beyond. *Physica Scripta*, 2016(T168):014001, dec 2015. 7, 84, 89, 92, 93, 100

[11] Ching-Kai Chiu, Jeffrey C. Y. Teo, Andreas P. Schnyder, and Shinsei Ryu. Classification of topological quantum matter with symmetries. *Rev. Mod. Phys.*, 88:035005, Aug 2016. 7, 84, 92, 95, 102

[12] Jiahao Fan and Huaqing Huang. Topological states in quasicrystals. *Frontiers of Physics*, 17(1):13203, 2022. 7

[13] Duc-Thanh Tran, Alexandre Dauphin, Nathan Goldman, and Pierre Gaspard. Topological Hofstadter insulators in a two-dimensional quasicrystal. *Phys. Rev. B*, 91:085125, Feb 2015. 7, 51

[14] Jean-Noël Fuchs and Julien Vidal. Hofstadter butterfly of a quasicrystal. *Phys. Rev. B*, 94:205437, Nov 2016. 7, 51

[15] Shriya Pai and Abhinav Prem. Topological states on fractal lattices. *Phys. Rev. B*, 100:155135, Oct 2019. 7

[16] Archisman Panigrahi, Vladimir Juričić, and Bitan Roy. Projected topological branes. *Communications Physics*, 5(1):230, 2022. 7

[17] Anuradha Jagannathan. The fibonacci quasicrystal: Case study of hidden dimensions and multifractality. *Rev. Mod. Phys.*, 93:045001, Nov 2021. 7, 15, 41, 49

[18] W. P. Su, J. R. Schrieffer, and A. J. Heeger. Solitons in polyacetylene. *Phys. Rev. Lett.*, 42:1698–1701, Jun 1979. 7, 96

[19] Qian Niu and Franco Nori. Spectral splitting and wave-function scaling in quasicrystalline and hierarchical structures. *Phys. Rev. B*, 42:10329–10341, Dec 1990. 7, 40, 41, 49, 50, 53, 59, 64

[20] W. M. Zheng. Global scaling properties of the spectrum for the Fibonacci chains. *Phys. Rev. A*, 35:1467–1469, Feb 1987. 7, 49, 104

[21] T. Fujiwara, M. Kohmoto, and T. Tokihiro. Multifractal wave functions on a Fibonacci lattice. *Phys. Rev. B*, 40:7413–7416, Oct 1989. 7, 49

[22] Nicolas Macé, Anuradha Jagannathan, and Frédéric Piéchon. Fractal dimensions of wave functions and local spectral measures on the Fibonacci chain. *Phys. Rev. B*, 93:205153, May 2016. 7, 22, 40, 41, 53, 70

[23] Clément Sire and Rémy Mosseri. Excitation spectrum, extended states, gap closing: some exact results for codimension one quasicrystals. *Journal de Physique*, 51(15):1569–1583, 1990. 7, 22, 49

[24] M. Röntgen, C. V. Morfonios, R. Wang, L. Dal Negro, and P. Schmelcher. Local symmetry theory of resonator structures for the real-space control of edge states in binary aperiodic chains. *Phys. Rev. B*, 99:214201, Jun 2019. 7, 71, 72

[25] Yaacov E. Kraus and Oded Zilberberg. Topological equivalence between the Fibonacci quasicrystal and the Harper model. *Phys. Rev. Lett.*, 109:116404, Sep 2012. 7, 105

[26] G. Rauzy. Nombres algébriques et substitutions. *Bull. Soc. Math. France*, 110(2):147–178, 1982. 7, 66

[27] Julius Krebbekx, Anouar Moustaj, Karma Dajani, and Cristiane Morais Smith. Multifractal properties of Tribonacci chains. *arXiv preprint arXiv:2304.11144*, 2023. 8, 49, 130

[28] Enrique Maciá-Barber. *Quasicrystals: fundamentals and applications*. CRC Press, 2020. 9, 11

[29] Michael Baake and Uwe Grimm. *Aperiodic order. Vol. 1*, volume 149 of *Encyclopedia of Mathematics and its Applications*. Cambridge University Press, Cambridge, 2013. A mathematical invitation, With a foreword by Roger Penrose. 10, 11, 18, 19, 20, 21

[30] Dov Levine and Paul Joseph Steinhardt. Quasicrystals: A new class of ordered structures. *Phys. Rev. Lett.*, 53:2477–2480, Dec 1984. 10

[31] J-B Suck, Michael Schreiber, and Peter Häussler. *Quasicrystals: An introduction to structure, physical properties and applications*, volume 55. Springer Science & Business Media, 2013. 11

[32] Michael Brin and Garrett Stuck. *Introduction to dynamical systems*. Cambridge university press, 2002. 12

[33] N. Pytheas Fogg. *Substitutions in dynamics, arithmetics and combinatorics*, volume 1794 of *Lecture Notes in Mathematics*. Springer-Verlag, Berlin, 2002. Edited by V. Berthé, S. Ferenczi, C. Mauduit and A. Siegel. 13, 25, 66

[34] Jean Berstel. Fibonacci words—a survey. In *The book of L*, pages 13–27. Springer, 1986. 13, 15, 16

[35] Ethan M Coven and Gustav A Hedlund. Sequences with minimal block growth. *Mathematical Systems Theory*, 7(2):138–153, 1973. 14

[36] Parmanand Singh. The so-called Fibonacci numbers in ancient and medieval India. *Historia Mathematica*, 12(3):229–244, 1985. 14

[37] Dov Levine and Paul J. Steinhardt. Quasicrystals. I. definition and structure. *Phys. Rev. B*, 34:596–616, Jul 1986. 15

[38] Jean-Paul Allouche and Jeffrey Shallit. The ubiquitous prouhet-thue-morse sequence. In *Sequences and their applications*, pages 1–16. Springer, 1999. 16, 17

[39] Jun Ma and Judy Holdener. When Thue-Morse meets Koch. *Fractals*, 13(03):191–206, 2005. 17

[40] Alfred Brauer. On algebraic equations with all but one root in the interior of the unit circle. to my teacher and former colleague Erhard Schmidt on his 75th birthday. *Mathematische Nachrichten*, 4(1-6):250–257, 1950. 18

[41] Shin-Ichi Yasutomi. On Sturmian sequences which are invariant under some substitutions. *Number theory and its applications (Kyoto, 1997)*, 2:347–373, 1999. 25

[42] Michael Baake, Uwe Grimm, and Robert V Moody. What is aperiodic order? *arXiv preprint math/0203252*, 2002. 26, 27, 28

[43] David Austin. Penrose tilings tied up in ribbons. *American Mathematical Society: feature column, Providence*, 5, 2005. 28, 29

[44] René L Schilling. *Measures, integrals and martingales*. Cambridge University Press, 2017. 30

[45] Benoit B Mandelbrot and Benoit B Mandelbrot. *The fractal geometry of nature*, volume 1. WH freeman New York, 1982. 31

[46] Kenneth Falconer. *Fractal geometry: mathematical foundations and applications*. John Wiley & Sons, 2004. 32

[47] Thomas C. Halsey, Mogens H. Jensen, Leo P. Kadanoff, Itamar Procaccia, and Boris I. Shraiman. Fractal measures and their singularities: The characterization of strange sets. *Phys. Rev. A*, 33:1141–1151, Feb 1986. 32, 33

[48] H George E Hentschel and Itamar Procaccia. The infinite number of generalized dimensions of fractals and strange attractors. *Physica D: Nonlinear Phenomena*, 8(3):435–444, 1983. 33

[49] A. Block, W. von Bloh, and H. J. Schellnhuber. Efficient box-counting determination of generalized fractal dimensions. *Phys. Rev. A*, 42:1869–1874, Aug 1990. 34

[50] L. V. Meisel, Mark Johnson, and P. J. Cote. Box-counting multifractal analysis. *Phys. Rev. A*, 45:6989–6996, May 1992. 34, 35

[51] Aristid Lindenmayer. Mathematical models for cellular interactions in development I. filaments with one-sided inputs. *Journal of theoretical biology*, 18(3):280–299, 1968. 35

[52] Grzegorz Rozenberg and Arto Salomaa. *The mathematical theory of L systems*. Academic press, 1980. 35, 37

[53] Premshree Pillai. Fractal plants: https://disquiet.in/posts/2019/11/26/fractal-plants, Dec visited 11-11-2022. 38

[54] Nicolas Maceé. *Electronic properties of quasicrystals*. PhD thesis, Université Paris Saclay (COmUE), 2017. 40, 52, 53

[55] J Bellissard, B Iochum, E Scoppola, and D Testard. Spectral properties of one-dimensional quasi-crystals. *Communications in Mathematical Physics*, 125(3):527–543, 1989. 40

[56] Andreas Rüdinger and Frédéric Piéchon. On the multifractal spectrum of the Fibonacci chain. *Journal of Physics A: Mathematical and General*, 31(1):155, 1998. 41

[57] Ming-Guang Qin, Hong-ru Ma, and Chien-Hua Tsai. A renormalisation analysis of the one-dimensional Thue-Morse aperiodic chain. *Journal of Physics: Condensed Matter*, 2(5):1059, 1990. 41

[58] Jean Bellissard, Anton Bovier, and Jean-Michel Ghez. Gap labelling theorems for one dimensional discrete Schrödinger operators. *Reviews in Mathematical Physics*, 4(01):1–37, 1992. 41, 49

[59] Florent Baboux, Eli Levy, Aristide Lemaître, Carmen Gómez, Elisabeth Galopin, Luc Le Gratiet, Isabelle Sagnes, Alberto Amo, Jacqueline Bloch, and Eric Akkermans. Measuring topological invariants from generalized edge states in polaritonic quasicrystals. *Phys. Rev. B*, 95:161114, Apr 2017. 42, 43, 105

[60] Tomoki Ozawa, Hannah M. Price, Alberto Amo, Nathan Goldman, Mohammad Hafezi, Ling Lu, Mikael C. Rechtsman, David Schuster, Jonathan Simon, Oded Zilberberg, and Iacopo Carusotto. Topological photonics. *Rev. Mod. Phys.*, 91:015006, Mar 2019. 44

[61] Immanuel Bloch, Jean Dalibard, and Wilhelm Zwerger. Many-body physics with ultracold gases. *Rev. Mod. Phys.*, 80:885–964, Jul 2008. 44, 45

[62] Theodore A Corcovilos and Jahnavee Mittal. Two-dimensional optical quasicrystal potentials for ultracold atom experiments. *Applied optics*, 58(9):2256–2263, 2019. 44, 45

[63] Eva Y Andrei and Allan H MacDonald. Graphene bilayers with a twist. *Nature materials*, 19(12):1265–1275, 2020. 46, 47, 48

[64] Heather M Hill. Twisted bilayer graphene enters a new phase. *Physics Today*, 73(1):18–20, 2020. 47

[65] J. M. B. Lopes dos Santos, N. M. R. Peres, and A. H. Castro Neto. Graphene bilayer with a twist: Electronic structure. *Phys. Rev. Lett.*, 99:256802, Dec 2007. 46

[66] Wei Yao, Eryin Wang, Changhua Bao, Yiou Zhang, Kenan Zhang, Kejie Bao, Chun Kai Chan, Chaoyu Chen, Jose Avila, Maria C Asensio, et al. Quasicrystalline 30 twisted bilayer graphene as an incommensurate superlattice with strong interlayer coupling. *Proceedings of the National Academy of Sciences*, 115(27):6928–6933, 2018. 47, 48

[67] Ming-Guang Qin, Hong ru Ma, and Chien-Hua Tsai. A renormalisation analysis of the one-dimensional Thue-Morse aperiodic chain. *Journal of Physics: Condensed Matter*, 2(5):1059, feb 1990. 49

[68] Sheng-Feng Cheng and Guo-Jun Jin. Trace map and eigenstates of a Thue-Morse chain in a general model. *Phys. Rev. B*, 65:134206, Mar 2002. 49

[69] M Severin, M Dulea, and R Riklund. Periodic and quasiperiodic wavefunctions in a class of one-dimensional quasicrystals: an analytical treatment. *Journal of Physics: Condensed Matter*, 1(45):8851, nov 1989. 49

[70] S. Thiem and M. Schreiber. Photonic properties of metallic-mean quasiperiodic chains. *The European Physical Journal B*, 76(3):339–345, Aug 2010. 49

[71] Mihnea Dulea, Magnus Johansson, and Rolf Riklund. Localization of electrons and electromagnetic waves in a deterministic aperiodic system. *Phys. Rev. B*, 45:105–114, Jan 1992. 49

[72] Mihnea Dulea, Magnus Johansson, and Rolf Riklund. Trace-map invariant and zero-energy states of the tight-binding Rudin-Shapiro model. *Phys. Rev. B*, 46:3296–3304, Aug 1992. 49

[73] Julien Vidal and Rémy Mosseri. Generalized quasiperiodic rauzy tilings. *Journal of Physics A: Mathematical and General*, 34(18):3927, may 2001. 51, 104

[74] A. Jagannathan. Less singular quasicrystals: The case of low codimensions. *Phys. Rev. B*, 64:140201, Sep 2001. 51, 104

[75] Francois Triozon, Julien Vidal, Rémy Mosseri, and Didier Mayou. Quantum dynamics in two- and three-dimensional quasiperiodic tilings. *Phys. Rev. B*, 65:220202, Jun 2002. 51, 104

[76] Julien Vidal and Rémy Mosseri. Quasiperiodic tilings in a magnetic field. *Journal of Non-Crystalline Solids*, 334-335:130–136, 2004. 8th International Conference on Quasicrystals. 51

[77] Michael Baake, Uwe Grimm, and Dieter Joseph. Trace maps, invariants, and some of their applications. *International Journal of Modern Physics B*, 7(06n07):1527–1550, 1993. 51

[78] Mahito Kohmoto, Leo P. Kadanoff, and Chao Tang. Localization problem in one dimension: Mapping and escape. *Phys. Rev. Lett.*, 50:1870–1872, Jun 1983. 51

[79] Pavel Kalugin and André Katz. Electrons in deterministic quasicrystalline potentials and hidden conserved quantities. *Journal of Physics A: Mathematical and Theoretical*, 47(31):315206, 2014. 52

[80] A. D. Mirlin, Y. V. Fyodorov, A. Mildenberger, and F. Evers. Exact relations between multifractal exponents at the Anderson transition. *Phys. Rev. Lett.*, 97:046803, Jul 2006. 53

[81] Ferdinand Evers and Alexander D. Mirlin. Anderson transitions. *Rev. Mod. Phys.*, 80:1355–1417, Oct 2008. 53

[82] Anouar Moustaj, Sander Kempkes, and Cristiane Morais Smith. Effects of disorder in the Fibonacci quasicrystal. *Phys. Rev. B*, 104:144201, Oct 2021. 53, 104

[83] Valérie Berthé, Clelia De Felice, Francesco Dolce, Julien Leroy, Dominique Perrin, Christophe Reutenauer, and Giuseppina Rindone. Acyclic, connected and tree sets. *Monatshefte für Mathematik*, 176(4):521–550, 2015. 54

[84] Valérie Berthé, Clelia De Felice, Francesco Dolce, Julien Leroy, Dominique Perrin, Christophe Reutenauer, and Giuseppina Rindone. Acyclic, connected and tree sets. *Monatsh. Math.*, 176(4):521–550, 2015. 63

[85] Pierre Arnoux and Shunji Ito. *Pisot substitutions and Rauzy fractals*, volume 8. Simon Stevin, 2001. Journées Montoises d'Informatique Théorique (Marne-la-Vallée, 2000). 66

[86] Pierre Arnoux and Edmund Harriss. What is ... a Rauzy fractal? *Notices Amer. Math. Soc.*, 61(7):768–770, 2014. 66

[87] Milton Minervino. *Rauzy fractals and tilings*. PhD thesis, University of Leoben, 2014. 66

[88] Víctor F. Sirvent and Yang Wang. Self-affine tiling via substitution dynamical systems and Rauzy fractals. *Pacific J. Math.*, 206(2):465–485, 2002. 66

[89] Mao Yoshii, Sota Kitamura, and Takahiro Morimoto. Topological charge pumping in quasiperiodic systems characterized by the Bott index. *Phys. Rev. B*, 104:155126, Oct 2021. 74, 75, 76, 77, 78, 79, 104

[90] D. J. Thouless. Quantization of particle transport. *Phys. Rev. B*, 27:6083–6087, May 1983. 75

[91] Roberta Citro and Monika Aidelsburger. Thouless pumping and topology. *Nature Reviews Physics*, 5(2):87–101, Feb 2023. 81

[92] János K Asbóth, László Oroszlány, and András Pályi. A short course on topological insulators. *Lecture notes in physics*, 919:166, 2016. 75, 76, 77, 78, 98, 104

[93] Emil Prodan and Hermann Schulz-Baldes. *Bulk and boundary invariants for complex topological insulators*. Mathematical Physics Studies. Springer, [Cham], 2016. From K-theory to physics. 76, 77

[94] T. A. Loring and M. B. Hastings. Disordered topological insulators via C*-algebras. *Europhysics Letters*, 92(6):67004, jan 2011. 76

[95] Terry A Loring. A guide to the Bott index and localizer index. *arXiv preprint arXiv:1907.11791*, 2019. 76

[96] Daniele Toniolo. On the Bott index of unitary matrices on a finite torus. *Letters in Mathematical Physics*, 112(6), dec 2022. 77

[97] Zhong Wang, Xiao-Liang Qi, and Shou-Cheng Zhang. Equivalent topological invariants of topological insulators. *New Journal of Physics*, 12(6):065007, jun 2010. 86

[98] Allen Hatcher. *Algebraic topology*. Cambridge University Press, Cambridge, 2002. 87

[99] Mikio Nakahara. *Geometry, topology and physics*. Graduate Student Series in Physics. Institute of Physics, Bristol, second edition, 2003. 87

[100] Charles Kittel. *Introduction to solid state physics*. John Wiley & sons, inc, 2005. 88

[101] Ian Mondragon-Shem, Taylor L. Hughes, Juntao Song, and Emil Prodan. Topological criticality in the chiral-symmetric AIII class at strong disorder. *Phys. Rev. Lett.*, 113:046802, Jul 2014. 89

[102] Titus Neupert and Frank Schindler. *Topological Crystalline Insulators*, pages 31–61. Springer International Publishing, Cham, 2018. 90, 102

[103] Peter D Lax. *Linear algebra and its applications*, volume 78. John Wiley & Sons, 2007. 91

[104] Lumen Eek. Topology and disorder in non-Hermitian physics. Master's thesis, Institute for Theoretical Physics, Utrecht University, 2022. 98

[105] Alexei Kitaev. Periodic table for topological insulators and superconductors. In *AIP conference proceedings*, volume 1134, pages 22–30. American Institute of Physics, 2009. 100

[106] F. D. M. Haldane. Model for a quantum Hall effect without Landau levels: Condensed-matter realization of the "parity anomaly". *Phys. Rev. Lett.*, 61:2015–2018, Oct 1988. 102

[107] J. P. Provost and G. Vallee. Riemannian structure on manifolds of quantum states. *Communications in Mathematical Physics*, 76(3):289–301, Sep 1980. 102

[108] Chao Chen Ye, WL Vleeshouwers, S Heatley, V Gritsev, and C Morais Smith. Quantum geometry of non-Hermitian topological systems. *arXiv preprint arXiv:2305.17675*, 2023. 102

[109] M. K. Ali and Godfrey Gumbs. Quasiperiodic dynamics for a generalized third-order Fibonacci series. *Phys. Rev. B*, 38:7091–7093, Oct 1988. 104

[110] William M Goldman. Trace coordinates on Fricke spaces of some simple hyperbolic surfaces. *arXiv preprint arXiv:0901.1404*, 2009. 104

[111] Frédéric Piéchon, Mourad Benakli, and Anuradha Jagannathan. Analytical results for scaling properties of the spectrum of the Fibonacci chain. *Phys. Rev. Lett.*, 74:5248–5251, Jun 1995. 104

[112] Joachim Hermisson. Aperiodic and correlated disorder in XY chains: exact results. *Journal of Physics A: Mathematical and General*, 33(1):57, 2000. 105

[113] JM Luck and Th M Nieuwenhuizen. A soluble quasi-crystalline magnetic model: the XY quantum spin chain. *Europhysics Letters*, 2(4):257, 1986. 105

[114] Peiqing Tong and Xiaoxian Liu. Lee-Yang zeros of periodic and quasiperiodic anisotropic XY chains in a transverse field. *Phys. Rev. Lett.*, 97:017201, Jul 2006. 105

[115] Joachim Hermisson, Uwe Grimm, and Michael Baake. Aperiodic Ising quantum chains. *Journal of Physics A: Mathematical and General*, 30(21):7315, 1997. 105

[116] Fleury J Oliveira Filho, Maicon S Faria, and André P Vieira. Strong-disorder renormalization group study of aperiodic quantum Ising chains. *Journal of Statistical Mechanics: Theory and Experiment*, 2012(03):P03007, 2012. 105

[117] Pablo Basteiro, Giuseppe Di Giulio, Johanna Erdmenger, Jonathan Karl, René Meyer, and Zhuo-Yu Xian. Towards explicit discrete holography: Aperiodic spin chains from hyperbolic tilings. *SciPost Phys.*, 13:103, 2022. 105

[118] Mattis Reisner, Yanel Tahmi, Frédéric Piéchon, Ulrich Kuhl, and Fabrice Mortessagne. Experimental observation of multifractality in Fibonacci chains, 2022. 105

[119] Moawwad EA El-Mikkawy. On the inverse of a general tridiagonal matrix. *Applied Mathematics and Computation*, 150(3):669–679, 2004. 127